

Syracuse University

SURFACE

Dissertations - ALL

SURFACE

December 2014

ADVANCED IMPLEMENTATIONS OF THE ITERATIVE MULTI REGION TECHNIQUE

Fatih Kaburcuk
Syracuse University

Follow this and additional works at: <https://surface.syr.edu/etd>



Part of the [Engineering Commons](#)

Recommended Citation

Kaburcuk, Fatih, "ADVANCED IMPLEMENTATIONS OF THE ITERATIVE MULTI REGION TECHNIQUE" (2014).
Dissertations - ALL. 170.
<https://surface.syr.edu/etd/170>

This Dissertation is brought to you for free and open access by the SURFACE at SURFACE. It has been accepted for inclusion in Dissertations - ALL by an authorized administrator of SURFACE. For more information, please contact surface@syr.edu.

ABSTRACT

The integration of the finite-difference time-domain (FDTD) method into the iterative multi-region (IMR) technique, an iterative approach used to solve large-scale electromagnetic scattering and radiation problems, is presented in this dissertation. The idea of the IMR technique is to divide a large problem domain into smaller subregions, solve each subregion separately, and combine the solutions of subregions after introducing the effect of interaction to obtain solutions at multiple frequencies for the large domain. Solution of the subregions using the frequency domain solvers has been the preferred approach as such solutions using time domain solvers require computationally expensive bookkeeping of time signals between subregions. In this contribution we present an algorithm that makes it feasible to use the FDTD method, a time domain numerical technique, in the IMR technique to obtain solutions at a pre-specified number of frequencies in a single simulation. As a result, a considerable reduction in memory storage requirements and computation time is achieved.

A hybrid method integrated into the IMR technique is also presented in this work. This hybrid method combines the desirable features of the method of moments (MoM) and the FDTD method to solve large-scale radiation problems more efficiently. The idea of this hybrid method based on the IMR technique is to divide an original problem domain into unconnected subregions and use the more appropriate method in each domain.

The most prominent feature of this proposed method is to obtain solutions at multiple frequencies in a single IMR simulation by constructing time-limited waveforms. The performance of the proposed method is investigated numerically using different configurations composed of two, three, and four objects.

ADVANCED IMPLEMENTATIONS OF THE ITERATIVE MULTI REGION TECHNIQUE

By

Fatih Kaburcuk

B.S., Ondokuz Mayıs University, 2007

M.S., Syracuse University, 2011

DISSERTATION

Submitted in partial fulfillment of the requirements for the degree of
Doctor of Philosophy in Electrical and Computer Engineering
in the Graduate School of Syracuse University

Syracuse University
December 2014

Copyright © Fatih Kaburcuk 2014

All rights reserved

ACKNOWLEDGEMENTS

I would like to express my deepest appreciation and gratitude to my advisor, Dr. Veysel Demir, for his dedicated guidance, invaluable suggestions and everlasting friendly attitude throughout the development of this dissertation. I would like to express my deep appreciation to my co-advisors Dr. Atef Z. Elsherbeni and Dr. Ercument Arvas for their advice, support, and guidance throughout this research. I owe much to Dr. Arvas for his patience and mental support throughout the entire course of my graduate study.

I would like to extend my appreciation to Dr. Joseph R. Mautz, Dr. Jay Kyoony Lee, and Dr. Amit Agrawal for serving on my dissertation committee and Dr. Thong Quoc Dang for chairing the committee.

Finally, I express my special thanks to my family for their endless understanding, love, and support throughout my entire educational career. I am also indebted to all my friends who have supporting and motivating me to complete this dissertation.

TABLE OF CONTENTS

| | | |
|-------|--|-----|
| 1 | INTRODUCTION | 1 |
| 2 | IMR TECHNIQUE USING THE FDTD METHOD | 7 |
| 2.1 | Iterative Procedure Using the FDFD method..... | 8 |
| 2.2 | Iterative Procedure Using the FDTD method | 12 |
| 2.3 | Time-Limited Waveform Construction (TWC) Algorithm | 20 |
| 2.4 | IMR Procedure for Radiation Problems..... | 24 |
| 2.5 | Speeding up Techniques..... | 28 |
| 2.5.1 | Total-Field Scattered-Field (TF/SF) Formulation | 29 |
| 2.5.2 | Interpolation Process..... | 29 |
| 3 | NUMERICAL RESULTS FOR SCATTERING PROBLEMS | 31 |
| 3.1 | Electromagnetic Scattering from Two Objects-1 | 32 |
| 3.2 | Electromagnetic Scattering from Two Objects-2..... | 46 |
| 3.3 | Electromagnetic Scattering from Three Objects-1 | 60 |
| 3.4 | Electromagnetic Scattering from Three Objects-2..... | 73 |
| 3.5 | Electromagnetic Scattering from Four Objects | 87 |
| 4 | NUMERICAL RESULTS FOR RADIATION PROBLEMS | 101 |
| 4.1 | Radiation from a Dipole Antenna in the Presence of an Object | 103 |
| 4.2 | Radiation from a Dipole Antenna in the Presence of Two Objects-1 | 117 |
| 4.3 | Radiation from a Dipole Antenna in the Presence of Two Objects-2 | 131 |
| 4.4 | Radiation from a Dipole Antenna in the Presence of Two Objects-3 | 145 |

| | | |
|-------------------|--|-----|
| 4.5 | Radiation from a Dipole Antenna in the Presence of Three Objects | 159 |
| 4.6 | Radiation from a Dipole Antenna in the Presence of Four Objects | 173 |
| 5 | IMR ALGORITHM AS HYBRID TECHNIQUE | 187 |
| 5.1 | Hybrid (MoM/FDTD) Method..... | 188 |
| 5.2 | Numerical Results | 192 |
| 5.2.1 | Current Distributions on an Antenna in the Presence of an Obstacle-1 ... | 193 |
| 5.2.2 | Current Distributions on an Antenna in the Presence of an Obstacle-2 ... | 197 |
| 5.2.3 | Antenna Input Impedance in the Presence of Two Obstacles..... | 201 |
| 6 | CONCLUSION..... | 204 |
| Appendix A | Near-Field to Near-Field (NF/NF) Transformation | 206 |
| Appendix B | The Computing System Information..... | 210 |
| Appendix C | Moment Matrix of a Thin Wire Antenna | 211 |
| Appendix D | Near Fields of a Thin Wire Antenna | 213 |
| BIBLIOGRAPHY..... | | 215 |
| VITA..... | | 219 |

LIST OF FIGURES

| | |
|---|----|
| Figure 2.1: Scattering from multiple objects: a) original problem and b) subregions. (dotted line: imaginary surface and dashed line: TF/SF boundary) | 9 |
| Figure 2.2: Iterative procedure between subregions. | 10 |
| Figure 2.3: Imaginary surface in subregion- d | 11 |
| Figure 2.4: a) Iterative procedure between subregions and b) NF/NF-TWC algorithm. . | 14 |
| Figure 2.5: Radiation from multiple objects: a) original problem and b) source and scatterer subregions. (dotted line: imaginary surface and dashed line: TF/SF boundary) | 25 |
| Figure 2.6: Iterative procedure between source subregion and scatterer subregions. | 27 |
| Figure 2.7: Configuration for the averaging process of current points on the imaginary surface..... | 30 |
| Figure 2.8: Configuration for the averaging process of field points along the x direction on the TF/SF boundary. | 30 |
| Figure 3.1: Geometry of the first problem. | 33 |
| Figure 3.2: Convergence (ϵ_k) between iteration steps for the first problem. | 33 |
| Figure 3.3: Bistatic RCS_θ for xy -plane cuts at frequencies: a) 200 MHz, b) 225 MHz, c) 250 MHz, d) 275 MHz, and e) 300 MHz. | 35 |
| Figure 3.4: Bistatic RCS_θ for xz -plane cuts at frequencies: a) 200 MHz, b) 225 MHz, c) 250 MHz, d) 275 MHz, and e) 300 MHz. | 37 |
| Figure 3.5: Bistatic RCS_θ for yz -plane cuts at frequencies: a) 200 MHz, b) 225 MHz, c) 250 MHz, d) 275 MHz, and e) 300 MHz. | 38 |
| Figure 3.6: Bistatic RCS_ϕ for xy -plane cuts at frequencies: a) 200 MHz, b) 225 MHz, c) 250 MHz, d) 275 MHz, and e) 300 MHz. | 40 |
| Figure 3.7: Bistatic RCS_ϕ for xz -plane cuts at frequencies: a) 200 MHz, b) 225 MHz, c) 250 MHz, d) 275 MHz, and e) 300 MHz. | 42 |
| Figure 3.8: Bistatic RCS_ϕ for yz -plane cuts at frequencies: a) 200 MHz, b) 225 MHz, c) 250 MHz, d) 275 MHz, and e) 300 MHz. | 43 |
| Figure 3.9: Normalized average errors for RCS_θ in the three plane cuts: a) xy -plane, b) xz - plane, and c) yz -plane. | 44 |
| Figure 3.10: Normalized average errors for RCS_ϕ in the three plane cuts: a) xy -plane, b) xz -plane, and c) yz -plane..... | 45 |

| | |
|--|----|
| Figure 3.11: Geometry of the second problem. | 47 |
| Figure 3.12: Convergence (ϵ_k) between iteration steps for the second problem..... | 47 |
| Figure 3.13: Bistatic RCS_θ for xy -plane cuts at frequencies: a) 200 MHz, b) 225 MHz, c) 250 MHz, d) 275 MHz, and e) 300 MHz. | 49 |
| Figure 3.14: Bistatic RCS_θ for xz -plane cuts at frequencies: a) 200 MHz, b) 225 MHz, c) 250 MHz, d) 275 MHz, and e) 300 MHz. | 51 |
| Figure 3.15: Bistatic RCS_θ for yz -plane cuts at frequencies: a) 200 MHz, b) 225 MHz, c) 250 MHz, d) 275 MHz, and e) 300 MHz. | 52 |
| Figure 3.16: Bistatic RCS_ϕ for xy -plane cuts at frequencies: a) 200 MHz, b) 225 MHz, c) 250 MHz, d) 275 MHz, and e) 300 MHz. | 54 |
| Figure 3.17: Bistatic RCS_ϕ for xz -plane cuts at frequencies: a) 200 MHz, b) 225 MHz, c) 250 MHz, d) 275 MHz, and e) 300 MHz. | 56 |
| Figure 3.18: Bistatic RCS_ϕ for yz -plane cuts at frequencies: a) 200 MHz, b) 225 MHz, c) 250 MHz, d) 275 MHz, and e) 300 MHz. | 57 |
| Figure 3.19: Normalized average errors for RCS_θ in the three plane cuts: a) xy -plane, b) xz -plane, and c) yz -plane..... | 58 |
| Figure 3.20: Normalized average errors for RCS_ϕ in the three plane cuts: a) xy -plane, b) xz -plane, and c) yz -plane..... | 59 |
| Figure 3.21: Geometry of the third problem. | 61 |
| Figure 3.22: Convergence (ϵ_k) between iteration steps for the third problem. | 61 |
| Figure 3.23: Bistatic RCS_θ for xy -plane cuts at frequencies: a) 200 MHz, b) 225 MHz, c) 250 MHz, d) 275 MHz, and e) 300 MHz. | 63 |
| Figure 3.24: Bistatic RCS_θ for xz -plane cuts at frequencies: a) 200 MHz, b) 225 MHz, c) 250 MHz, d) 275 MHz, and e) 300 MHz. | 64 |
| Figure 3.25: Bistatic RCS_θ for yz -plane cuts at frequencies: a) 200 MHz, b) 225 MHz, c) 250 MHz, d) 275 MHz, and e) 300 MHz. | 66 |
| Figure 3.26: Bistatic RCS_ϕ for xy -plane cuts at frequencies: a) 200 MHz, b) 225 MHz, c) 250 MHz, d) 275 MHz, and e) 300 MHz. | 68 |
| Figure 3.27: Bistatic RCS_ϕ for xz -plane cuts at frequencies: a) 200 MHz, b) 225 MHz, c) 250 MHz, d) 275 MHz, and e) 300 MHz. | 69 |
| Figure 3.28: Bistatic RCS_ϕ for yz -plane cuts at frequencies: a) 200 MHz, b) 225 MHz, c) 250 MHz, d) 275 MHz, and e) 300 MHz. | 71 |
| Figure 3.29: Normalized average errors for RCS_θ in the three plane cuts: a) xy -plane, b) xz -plane, and c) yz -plane..... | 72 |

| | |
|---|----|
| Figure 3.30: Normalized average errors for RCS_ϕ in the three plane cuts: a) xy -plane, b) xz -plane, and c) yz -plane. | 73 |
| Figure 3.31: Convergence (ϵ_k) between iteration steps for the fourth problem. | 74 |
| Figure 3.32: Bistatic RCS_θ for xy -plane cut at frequencies: a) 200 MHz, b) 225 MHz, c) 250 MHz, d) 275 MHz, and e) 300 MHz. | 76 |
| Figure 3.33: Bistatic RCS_θ for xz -plane cut at frequencies: a) 200 MHz, b) 225 MHz, c) 250 MHz, d) 275 MHz, and e) 300 MHz. | 78 |
| Figure 3.34: Bistatic RCS_θ for yz -plane cut at frequencies: a) 200 MHz, b) 225 MHz, c) 250 MHz, d) 275 MHz, and e) 300 MHz. | 79 |
| Figure 3.35: Bistatic RCS_ϕ for xy -plane cut at frequencies: a) 200 MHz, b) 225 MHz, c) 250 MHz, d) 275 MHz, and e) 300 MHz. | 81 |
| Figure 3.36: Bistatic RCS_ϕ for xz -plane cut at frequencies: a) 200 MHz, b) 225 MHz, c) 250 MHz, d) 275 MHz, and e) 300 MHz. | 83 |
| Figure 3.37: Bistatic RCS_ϕ for yz -plane cut at frequencies: a) 200 MHz, b) 225 MHz, c) 250 MHz, d) 275 MHz, and e) 300 MHz. | 84 |
| Figure 3.38: Normalized average errors for RCS_θ in the three plane cuts: a) xy -plane, b) xz -plane, and c) yz -plane. | 85 |
| Figure 3.39: Normalized average errors for RCS_ϕ in the three plane cuts: a) xy -plane, b) xz -plane, and c) yz -plane. | 86 |
| Figure 3.40: Geometry of the fifth problem. | 88 |
| Figure 3.41: Convergence (ϵ_k) between iteration steps for the fifth problem. | 88 |
| Figure 3.42: Bistatic RCS_θ for xy -plane cut at frequencies: a) 200 MHz, b) 225 MHz, c) 250 MHz, d) 275 MHz, and e) 300 MHz. | 90 |
| Figure 3.43: Bistatic RCS_θ for xz -plane cut at frequencies: a) 200 MHz, b) 225 MHz, c) 250 MHz, d) 275 MHz, and e) 300 MHz. | 92 |
| Figure 3.44: Bistatic RCS_θ for yz -plane cut at frequencies: a) 200 MHz, b) 225 MHz, c) 250 MHz, d) 275 MHz, and e) 300 MHz. | 93 |
| Figure 3.45: Bistatic RCS_ϕ for xy -plane cut at frequencies: a) 200 MHz, b) 225 MHz, c) 250 MHz, d) 275 MHz, and e) 300 MHz. | 95 |
| Figure 3.46: Bistatic RCS_ϕ for xz -plane cut at frequencies: a) 200 MHz, b) 225 MHz, c) 250 MHz, d) 275 MHz, and e) 300 MHz. | 97 |
| Figure 3.47: Bistatic RCS_ϕ for yz -plane cut at frequencies: a) 200 MHz, b) 225 MHz, c) 250 MHz, d) 275 MHz, and e) 300 MHz. | 98 |
| Figure 3.48: Normalized average errors for RCS_θ in the three plane cuts: a) xy -plane, b) xz -plane, and c) yz -plane. | 99 |

| | |
|---|-----|
| Figure 3.49: Normalized average errors for RCS_ϕ in the three plane cuts: a) xy -plane, b) xz -plane, and c) yz -plane. | 100 |
| Figure 4.1: a) Configuration of the 0.5 m active dipole antenna and b) Configuration of the 0.5 m inactive dipole antenna. | 102 |
| Figure 4.2: Magnitude of the reflection coefficient of a single 0.5 m dipole antenna. | 103 |
| Figure 4.3: Geometry of the first problem. | 104 |
| Figure 4.4: Convergence (ϵ_k) between iteration steps for the first problem. | 105 |
| Figure 4.5: Radiation pattern ($Gain_\theta$) for xy -plane cut at frequencies: a) 230 MHz, b) 240 MHz, c) 250 MHz, d) 260 MHz, and e) 270 MHz. | 106 |
| Figure 4.6: Radiation pattern ($Gain_\theta$) for xz -plane cut at frequencies: a) 230 MHz, b) 240 MHz, c) 250 MHz, d) 260 MHz, and e) 270 MHz. | 108 |
| Figure 4.7: Radiation pattern ($Gain_\theta$) for yz -plane cut at frequencies: a) 230 MHz, b) 240 MHz, c) 250 MHz, d) 260 MHz, and e) 270 MHz. | 110 |
| Figure 4.8: Radiation pattern ($Gain_\phi$) for xy -plane cut at frequencies: a) 230 MHz, b) 240 MHz, c) 250 MHz, d) 260 MHz, and e) 270 MHz. | 111 |
| Figure 4.9: Radiation pattern ($Gain_\phi$) for xz -plane cut at frequencies: a) 230 MHz, b) 240 MHz, c) 250 MHz, d) 260 MHz, and e) 270 MHz. | 113 |
| Figure 4.10: Radiation pattern ($Gain_\phi$) for yz -plane cut at frequencies: a) 230 MHz, b) 240 MHz, c) 250 MHz, d) 260 MHz, and e) 270 MHz. | 115 |
| Figure 4.11: Normalized average errors for $Gain_\theta$ components in the three plane cuts: a) xy -plane, b) xz -plane, and c) yz -plane. | 116 |
| Figure 4.12: Normalized average errors for $Gain_\phi$ components in the three plane cuts: a) xy -plane, b) xz -plane, and c) yz -plane. | 117 |
| Figure 4.13: a) Geometry of the second problem and b) Geometry of the conducting box-B on the yz -plane. | 118 |
| Figure 4.14: Convergence (ϵ_k) between iteration steps for the second problem. | 119 |
| Figure 4.15: Radiation pattern ($Gain_\theta$) for xy -plane cut at frequencies: a) 230 MHz, b) 240 MHz, c) 250 MHz, d) 260 MHz, and e) 270 MHz. | 121 |
| Figure 4.16: Radiation pattern ($Gain_\theta$) for xz -plane cut at frequencies: a) 230 MHz, b) 240 MHz, c) 250 MHz, d) 260 MHz, and e) 270 MHz. | 122 |
| Figure 4.17: Radiation pattern ($Gain_\theta$) for yz -plane cut at frequencies: a) 230 MHz, b) 240 MHz, c) 250 MHz, d) 260 MHz, and e) 270 MHz. | 124 |
| Figure 4.18: Radiation pattern ($Gain_\phi$) for xy -plane cut at frequencies: a) 230 MHz, b) 240 MHz, c) 250 MHz, d) 260 MHz, and e) 270 MHz. | 126 |

| | |
|--|-----|
| Figure 4.19: Radiation pattern (Gain_ϕ) for xz -plane cut at frequencies: a) 230 MHz, b) 240 MHz, c) 250 MHz, d) 260 MHz, and e) 270 MHz. | 127 |
| Figure 4.20: Radiation pattern (Gain_ϕ) for yz -plane cut at frequencies: a) 230 MHz, b) 240 MHz, c) 250 MHz, d) 260 MHz, and e) 270 MHz. | 129 |
| Figure 4.21: Normalized average errors for Gain_θ components in the three plane cuts: a) xy -plane, b) xz -plane, and c) yz -plane. | 130 |
| Figure 4.22: Normalized average errors for Gain_ϕ components in the three plane cuts: a) xy -plane, b) xz -plane, and c) yz -plane. | 131 |
| Figure 4.23: Convergence (ϵ_k) between iteration steps for the third problem. | 132 |
| Figure 4.24: Radiation pattern (Gain_θ) for xy -plane cut at frequencies: a) 230 MHz, b) 240 MHz, c) 250 MHz, d) 260 MHz, and e) 270 MHz. | 134 |
| Figure 4.25: Radiation pattern (Gain_θ) for xz -plane cut at frequencies: a) 230 MHz, b) 240 MHz, c) 250 MHz, d) 260 MHz, and e) 270 MHz. | 136 |
| Figure 4.26: Radiation pattern (Gain_θ) for yz -plane cut at frequencies: a) 230 MHz, b) 240 MHz, c) 250 MHz, d) 260 MHz, and e) 270 MHz. | 137 |
| Figure 4.27: Radiation pattern (Gain_ϕ) for xy -plane cut at frequencies: a) 230 MHz, b) 240 MHz, c) 250 MHz, d) 260 MHz, and e) 270 MHz. | 139 |
| Figure 4.28: Radiation pattern (Gain_ϕ) for xz -plane cut at frequencies: a) 230 MHz, b) 240 MHz, c) 250 MHz, d) 260 MHz, and e) 270 MHz. | 141 |
| Figure 4.29: Radiation pattern (Gain_ϕ) for yz -plane cut at frequencies: a) 230 MHz, b) 240 MHz, c) 250 MHz, d) 260 MHz, and e) 270 MHz. | 142 |
| Figure 4.30: Normalized average errors for Gain_θ components in the three plane cuts: a) xy -plane, b) xz -plane, and c) yz -plane. | 143 |
| Figure 4.31: Normalized average errors for Gain_ϕ components in the three plane cuts: a) xy -plane, b) xz -plane, and c) yz -plane. | 144 |
| Figure 4.32: Geometry of the fourth problem. | 146 |
| Figure 4.33: Convergence (ϵ_k) between iteration steps for the fourth problem. | 146 |
| Figure 4.34: Radiation pattern (Gain_θ) for xy -plane cut at frequencies: a) 230 MHz, b) 240 MHz, c) 250 MHz, d) 260 MHz, and e) 270 MHz. | 148 |
| Figure 4.35: Radiation pattern (Gain_θ) for xz -plane cut at frequencies: a) 230 MHz, b) 240 MHz, c) 250 MHz, d) 260 MHz, and e) 270 MHz. | 150 |
| Figure 4.36: Radiation pattern (Gain_θ) for yz -plane cut at frequencies: a) 230 MHz, b) 240 MHz, c) 250 MHz, d) 260 MHz, and e) 270 MHz. | 151 |
| Figure 4.37: Radiation pattern (Gain_ϕ) for xy -plane cut at frequencies: a) 230 MHz, b) 240 MHz, c) 250 MHz, d) 260 MHz, and e) 270 MHz. | 153 |

| | |
|--|-----|
| Figure 4.38: Radiation pattern (Gain_ϕ) for xz -plane cut at frequencies: a) 230 MHz, b) 240 MHz, c) 250 MHz, d) 260 MHz, and e) 270 MHz. | 155 |
| Figure 4.39: Radiation pattern (Gain_ϕ) for yz -plane cut at frequencies: a) 230 MHz, b) 240 MHz, c) 250 MHz, d) 260 MHz, and e) 270 MHz. | 156 |
| Figure 4.40: Normalized average errors for Gain_θ components in the three plane cuts: a) xy -plane, b) xz -plane, and c) yz -plane. | 157 |
| Figure 4.41: Normalized average errors for Gain_ϕ components in the three plane cuts: a) xy -plane, b) xz -plane, and c) yz -plane. | 158 |
| Figure 4.42: Geometry of the fifth problem. | 160 |
| Figure 4.43: Convergence (ϵ_k) between iteration steps for the fifth problem. | 160 |
| Figure 4.44: Radiation pattern (Gain_θ) for xy -plane cut at frequencies: a) 230 MHz, b) 240 MHz, c) 250 MHz, d) 260 MHz, and e) 270 MHz. | 162 |
| Figure 4.45: Radiation pattern (Gain_θ) for xz -plane cut at frequencies: a) 230 MHz, b) 240 MHz, c) 250 MHz, d) 260 MHz, and e) 270 MHz. | 164 |
| Figure 4.46: Radiation pattern (Gain_θ) for yz -plane cut at frequencies: a) 230 MHz, b) 240 MHz, c) 250 MHz, d) 260 MHz, and e) 270 MHz. | 165 |
| Figure 4.47: Radiation pattern (Gain_ϕ) for xy -plane cut at frequencies: a) 230 MHz, b) 240 MHz, c) 250 MHz, d) 260 MHz, and e) 270 MHz. | 167 |
| Figure 4.48: Radiation pattern (Gain_ϕ) for xz -plane cut at frequencies: a) 230 MHz, b) 240 MHz, c) 250 MHz, d) 260 MHz, and e) 270 MHz. | 169 |
| Figure 4.49: Radiation pattern (Gain_ϕ) for yz -plane cut at frequencies: a) 230 MHz, b) 240 MHz, c) 250 MHz, d) 260 MHz, and e) 270 MHz. | 170 |
| Figure 4.50: Normalized average errors for Gain_θ components in the three plane cuts: a) xy -plane, b) xz -plane, and c) yz -plane. | 171 |
| Figure 4.51: Normalized average errors for Gain_ϕ components in the three plane cuts: a) xy -plane, b) xz -plane, and c) yz -plane. | 172 |
| Figure 4.52: Geometry of the sixth problem. | 174 |
| Figure 4.53: Convergence (ϵ_k) between iteration steps for the sixth problem. | 174 |
| Figure 4.54: Radiation pattern (Gain_θ) for xy -plane cut at frequencies: a) 230 MHz, b) 240 MHz, c) 250 MHz, d) 260 MHz, and e) 270 MHz. | 176 |
| Figure 4.55: Radiation pattern (Gain_θ) for xz -plane cut at frequencies: a) 230 MHz, b) 240 MHz, c) 250 MHz, d) 260 MHz, and e) 270 MHz. | 178 |
| Figure 4.56: Radiation pattern (Gain_θ) for yz -plane cut at frequencies: a) 230 MHz, b) 240 MHz, c) 250 MHz, d) 260 MHz, and e) 270 MHz. | 179 |

| | |
|--|-----|
| Figure 4.57: Radiation pattern (Gain_ϕ) for xy -plane cut at frequencies: a) 230 MHz, b) 240 MHz, c) 250 MHz, d) 260 MHz, and e) 270 MHz. | 181 |
| Figure 4.58: Radiation pattern (Gain_ϕ) for xz -plane cut at frequencies: a) 230 MHz, b) 240 MHz, c) 250 MHz, d) 260 MHz, and e) 270 MHz. | 183 |
| Figure 4.59: Radiation pattern (Gain_ϕ) for yz -plane cut at frequencies: a) 230 MHz, b) 240 MHz, c) 250 MHz, d) 260 MHz, and e) 270 MHz. | 184 |
| Figure 4.60: Normalized average errors for Gain_θ components in the three plane cuts: a) xy -plane, b) xz -plane, and c) yz -plane. | 185 |
| Figure 4.61: Normalized average errors for Gain_ϕ components in the three plane cuts: a) xy -plane, b) xz -plane, and c) yz -plane. | 186 |
| Figure 5.1: Radiation from multiple objects: a) original problem and b) MoM and FDTD subregions. (dotted line: imaginary surface, dashed line: TF/SF boundary) | 189 |
| Figure 5.2: Iterative procedure between subregions using the hybrid method. | 190 |
| Figure 5.3: Magnitude of the reflection coefficient of a single thin wire antenna..... | 193 |
| Figure 5.4: The geometry of the first problem..... | 194 |
| Figure 5.5: Convergence (ϵ_k) between iteration steps..... | 194 |
| Figure 5.6: Convergence of current distribution versus segment number at frequencies: a) 840, b) 860, and c) 880 MHz. (0-4): represents the iteration number. | 195 |
| Figure 5.7: The geometry of the second problem. | 198 |
| Figure 5.8: Convergence (ϵ_k) between iteration steps..... | 198 |
| Figure 5.9: Convergence of current distribution versus segment number at frequencies: a) 840, b) 860, and c) 880 MHz. (0-4): represents the iteration number. | 199 |
| Figure 5.10: The geometry of the third problem..... | 202 |
| Figure 5.11: Convergence (ϵ_k) between iteration steps..... | 203 |
| Figure A.1: NF/NF transformation between two subregions..... | 206 |
| Figure C.1: Geometry of a thin wire antenna for the moment matrix calculation..... | 212 |
| Figure C.2: The delta gap source model with impressed field. | 212 |
| Figure D.1: The electric dipole (ideal dipole)..... | 213 |

LIST OF TABLES

| | |
|--|-----|
| Table 3-1: Simulation parameters and computer resources used by the IMR and full domain simulations..... | 33 |
| Table 3-2: Simulation parameters and computer resources used by the IMR and full domain simulation. | 47 |
| Table 3-3: Simulation parameters and computer resources used by the IMR and full domain simulation. | 60 |
| Table 3-4: Simulation parameters and computer resources used by the IMR and full domain simulation. | 74 |
| Table 3-5: Simulation parameters and computer resources used by the IMR and full domain simulation. | 88 |
| Table 4-1: Simulation parameters and computer resources used by the IMR and full domain simulations..... | 104 |
| Table 4-2: Simulation parameters and computer resources used by the IMR and full domain simulations..... | 119 |
| Table 4-3: Simulation parameters and computer resources used by the IMR and full domain simulations..... | 132 |
| Table 4-4: Simulation parameters and computer resources used by the IMR and full domain simulations..... | 145 |
| Table 4-5: Simulation parameters and computer resources used by the IMR and full domain simulations..... | 160 |
| Table 4-6: Simulation parameters and computer resources used by the IMR and full domain simulations..... | 174 |
| Table 5-1: Antenna input impedances at frequencies of interest of a single thin wire... | 193 |
| Table 5-2: Antenna input impedances at the frequencies of interest. | 194 |
| Table 5-3: Simulation parameters and computer resources used by the IMR and full domain simulations..... | 196 |
| Table 5-4: Antenna input impedances at the frequencies of interest for different separations. | 196 |
| Table 5-5: Simulation parameters and computer resources used by the IMR and full domain simulations..... | 197 |
| Table 5-6: Antenna input impedances at the frequencies of interest. | 198 |

| | |
|---|-----|
| Table 5-7: Simulation parameters and computer resources used by the IMR and full domain simulations..... | 200 |
| Table 5-8: Antenna input impedances at the frequencies of interest for different separations. | 200 |
| Table 5-9: Simulation parameters and computer resources used by the IMR and full domain simulations..... | 201 |
| Table 5-10: Antenna input impedances at the frequencies of interest. | 202 |
| Table 5-11: Simulation parameters and computer resources used by the IMR and full domain simulations..... | 202 |
| Table B-1: The computer specifications. | 210 |

1 INTRODUCTION

Solution of large-scale electromagnetic scattering and radiation problems has been one of the major challenges of computational electromagnetics because the solution of such problems requires long computation time and large computer memory. One approach to this problem is to develop a time and memory efficient algorithms by dividing a large problem domain into smaller unconnected subregions, to solve each subregion separately, and to combine the solutions of subregions after introducing the effect of interactions between them to obtain solutions for the large domain. Solutions of the subregions using the frequency domain solvers has been the preferred approach as such solutions using time domain solvers require computationally expensive bookkeeping of time signals between subregions. In this contribution, we present an algorithm that makes it feasible to use the finite-difference time-domain (FDTD) method in the iterative multi-region (IMR) technique, a divide and conquer algorithm, to obtain solutions at a pre-specified number of frequencies.

The decomposition of a problem domain into smaller domains is known as the domain decomposition method (DDM) [1–28], which in general requires either common boundaries or overlapping regions between subregions. It is possible to solve each subregion with the same method such as finite element method (FEM) [3–16] or finite-difference frequency-domain (FDFD) method [17–23]. IMR is one of such methods that divides a problem space into smaller subregions. In the case of IMR, a problem space contains multiple objects with separations from each other, and each subregion contains one and more of the objects. The subregions do not need to have common boundaries or overlapping regions.

IMR, as originally introduced by Al Sharkawy et al. [19–22], uses the FDFD method to solve Maxwell equations in subregions to calculate the scattering from many objects. This technique requires the solution of the fields in the subregions a number of times instead of one solution of the complete computational domain at a single frequency. In this contribution, we adapt the use of the FDTD method instead of the FDFD method; as a consequence a problem can be solved at a number of frequencies instead of a single frequency in a single simulation. In the IMR technique, the scattered fields from subregions that lead to interactions between the subregions are evaluated in the frequency domain, thus a frequency-domain to time-domain transformation is needed to convert the scattered fields into excitation fields as time-limited waveforms in order to excite the FDTD problem spaces. A key contribution in this research is a time-limited waveform construction (TWC) algorithm for the iterative interactions between subregions. The TWC algorithm is used to construct time-limited waveforms which include the desired frequencies of solution with the required magnitudes and phases in their frequency spectrums.

The iterative procedure in [19–22] is similar to the procedure denoted as the iterative field bouncing (IFB) method and described briefly by [24]. In [25] and [26], the iterative method is used to calculate the scattered field from a large perfectly conducting cavity using integral equations and physical optics, respectively. The DDM using the FDTD method [27] and using the fast multi-pole method [28] was used to solve a two-dimensional sparse multi-cylinder scattering problem. Multiple-Region FDTD (MR/FDTD) proposed in [29] was introduced to solve a sparse modeling problem. In [27], [28], and [29], the interaction and coupling effects between the objects are not considered very much because the separation distances between the objects are much larger than the

largest dimension of one object which means that the coupling between the objects is small enough. Furthermore, some hybrid techniques based on combinations of the method of moments (MoM), FDFD, and FEM, proposed in [24], [30], and [31], have been used to calculate scattering from multiple objects achieving a time and memory efficient algorithms.

In this dissertation, the FDTD method is integrated into the IMR technique to obtain solutions at multiple frequencies in a single IMR simulation by using the TWC algorithm. This technique is based on decomposing a large-scale scattering problem into smaller separated subregions and each subregion is solved using the FDTD method independently. In each subregion, the scattered electromagnetic fields due to the same original incident plane wave are captured on the imaginary surface. Then fictitious electric and magnetic currents are calculated from the scattered fields over the imaginary surface in each subregion, using the surface equivalence principle [32] in the frequency domain at a finite number of frequencies. Radiated fields generated by these currents are imposed as the new excitation fields on the opposing subregions in a new iteration. Since the new excitation fields are in the frequency domain at a number of frequencies, these fields must be converted into time-limited waveforms which include the desired frequencies with the right magnitudes and phases in their frequency spectrum before exciting the FDTD problem spaces. This procedure between subregions is repeated iteratively until the difference between two successive steps is less than a convergence criterion value. The most prominent feature of this technique is to obtain solutions at multiple frequencies in a single IMR simulation by constructing time-limited waveforms to use in FDTD solutions.

The procedure of the presented technique is also used to analyze large-scale radiation problems which are difficult to handle using the conventional FDTD method. This procedure is based on dividing the original problem domain into multiple subregions: one of them is the source subregion including an antenna, and the others are the scatterer subregions including scatterer objects. First, the antenna is driven in isolation so that, in what will be called the 0th iteration, there is no incident field in the subregion containing the driven antenna, and the incident fields in all the other subregions consist of the field of the driven antenna in isolation. Then the solutions of the subregions are combined, after multiple interactions between subregions, to obtain the solutions for the original problem. This iterative procedure between subregions is repeated until the difference between two successive steps is less than a convergence criterion value.

Initially, the scattered field (SF) formulation [33] has been used to excite the FDTD domains. The SF formulation requires the computation of new excitation fields at all field points in the problem space. It has been realized that a considerable amount of computation time is spent for the calculation of the new excitation fields due to the fictitious currents. Therefore, total-field scattered-field (TF/SF) formulation [34] is used to speed up the calculation of the new excitation fields. Thus these fields are calculated on the TF/SF boundary rather than the entire computational domain in subregions. Then an interpolation process is applied to current points on the imaginary surface and field points on the TF/SF boundary in subregions. These two techniques provide remarkable reduction in the computation time of the new excitation fields.

Another contribution presented in this dissertation is the utilization of the IMR technique as a hybrid procedure which combines the desirable features of the MoM and

the FDTD method. Such a hybrid method has been extensively studied in [35–39] to simulate the interaction between a linear antenna and a scatterer object. In [35] and [36], the coupling between subregions is simulated by employing the equivalence principle on the boundary surface surrounding each subregion. In [37–39], the proposed hybrid method does not use the equivalence principle on the surface of a subregion which includes an antenna solved using the MoM. Their iterative approach of a hybrid method provides solution at a single frequency in a single simulation. In our work, however we integrate the MoM and the FDTD method into the IMR technique to obtain solutions at multiple frequencies using the TWC algorithm in a single IMR simulation. The idea of the proposed hybrid method based on the IMR technique is to divide an original problem domain into multiple unconnected subregions and use the more appropriate method in each domain. The interactions between subregions continue until the difference between two successive iterations is less than a convergence criterion value.

The IMR technique based on FDTD method requires solutions of the fields in the subregions a number of times instead of one solution of the original complete domain. This technique effectively reduces the size of the memory requirements. Furthermore, reduction in the computation time is also achieved if the separation between some subregions is large and/or coarser grids are used in some of the subregions, which may not be possible to use if only one domain is used for the solution of the problem. Another feature of the IMR technique is that it can provide solutions at multiple frequencies to large-scale radiation and scattering problems that are difficult or impossible to solve in a single domain due to the large size using the conventional FDTD method.

As a summary the main contribution of the dissertation is the integration of the FDTD method into the IMR technique by using the TWC algorithm to analyze large-scale scattering and radiation problems. Thus the solutions of the IMR technique at multiple frequencies can be obtained by exciting the FDTD problem space with constructed time-limited waveforms. The second contribution is the hybrid use of the MoM and FDTD method to obtain solutions at multiple frequencies using the TWC algorithm in a single IMR run. To prove the validity of the proposed procedures, some scattering and radiation problems are simulated and good agreements between the IMR solutions and the full domain solutions are achieved.

In Chapter 2, the integration of FDTD method into the IMR technique is presented to solve large-scale electromagnetic scattering and radiation problems by using the TWC algorithm. Chapter 3 and Chapter 4 present numerical results for scattering and radiation problems using the proposed technique, respectively. Chapter 5 presents the solution of the hybrid (MoM/FDTD) method integrated into the IMR technique. Chapter 6 concludes the dissertation.

2 IMR TECHNIQUE USING THE FDTD METHOD

In this chapter, we present the integration of the FDTD method into the iterative multi-region (IMR) technique. IMR is an iterative approach used to solve large-scale electromagnetic scattering and radiation problems. The idea of the IMR technique is based on dividing a large computation domain into smaller unconnected subregions and solving each subregion separately. Then the solutions of subregions are combined through an iterative procedure to obtain the solutions for the large domain. Since dividing the original problem into smaller separated sub-problems reduces the corresponding computational domain sizes and minimizes the complexity of the problem, a huge saving in memory requirements is achieved. Furthermore, the computational time reduction is achieved if the separation between the subregions is large and/or coarser grids are used in some of the subregions, which may not be possible to use if a single domain is used for the solution of the original large problem.

IMR is essentially a frequency domain procedure as it uses the frequency domain analysis methods such as FDFD, FEM or MoM to calculate scattered electromagnetic fields in subregions. A similar procedure that uses a time domain method for subregions field calculations can be developed. However, it would require computationally expensive bookkeeping of time signals between subregions and it would not be feasible. In this contribution we present an algorithm that allows to use the FDTD method, a time domain numerical technique, in the IMR technique to achieve solutions at a pre-specified number of frequencies.

The most prominent feature of this presented technique is a time-limited waveform construction (TWC) algorithm that is used to synthesize a time-limited waveform. The

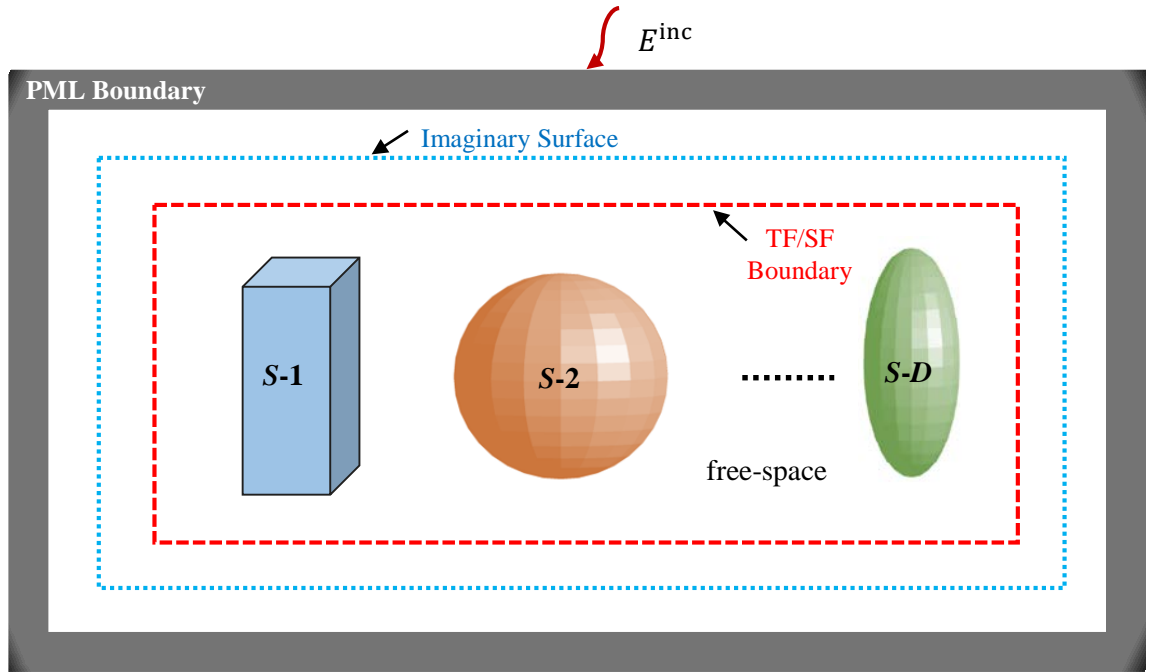
synthesized waveforms are used to excite the subregions as incident fields, thus enabling the use of a time domain method, i.e. the FDTD method in this contribution, to calculate the scattered fields in the subregions.

Once it is possible to use the FDTD method to solve subregions, a single run of FDTD solution is sufficient for each subregion to calculate the scattered fields at all frequencies of interest as opposed to running multiple FDFD or MoM solutions. Together with other benefits of the IMR procedure, the presented algorithm can lead to considerable reduction in the memory storage requirements and computation time especially when there is a larger distance between the subregions.

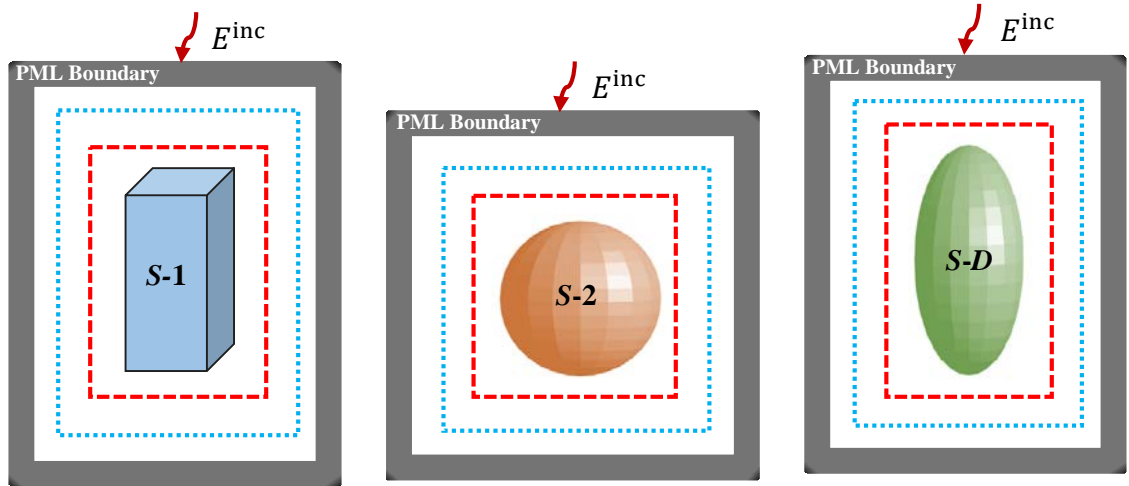
In this chapter, first, we present a summary of the IMR procedure as it utilizes the FDFD method. Next we introduce the integration of the FDTD method into the IMR technique for scattering and radiation problems. The details of the TWC algorithm and speeding up techniques are also presented here.

2.1 Iterative Procedure Using the FDFD method

The IMR technique was first presented as a frequency domain method where the FDFD method is employed to calculate scattered fields in the subregions of an original large scattering problem. In the procedure of the IMR technique, the original problem domain, as shown in Figure 2.1, is divided into several unconnected subregions, each subregion including a scatterer object. The subregion boundaries are terminated by absorbing boundaries to simulate an open space problem. In this contribution an absorbing boundary formulation known as perfectly matched layers (PML) [33] is used to terminate subregion boundaries as illustrated by solid lines in Figure 2.1.



(a)



(b)

Figure 2.1: Scattering from multiple objects: a) original problem and b) subregions.
(dotted line: imaginary surface and dashed line: TF/SF boundary)

The iterative procedure between D numbers of subregions is shown in Figure 2.2. The iterations consist of iteration # 0, iteration # 1, and as many repetitions of iteration # 1 as are necessary. The set of operations described in each iteration is performed D times, first for $d = 1$, then for $d = 2$, and so forth, up to $d = D$.

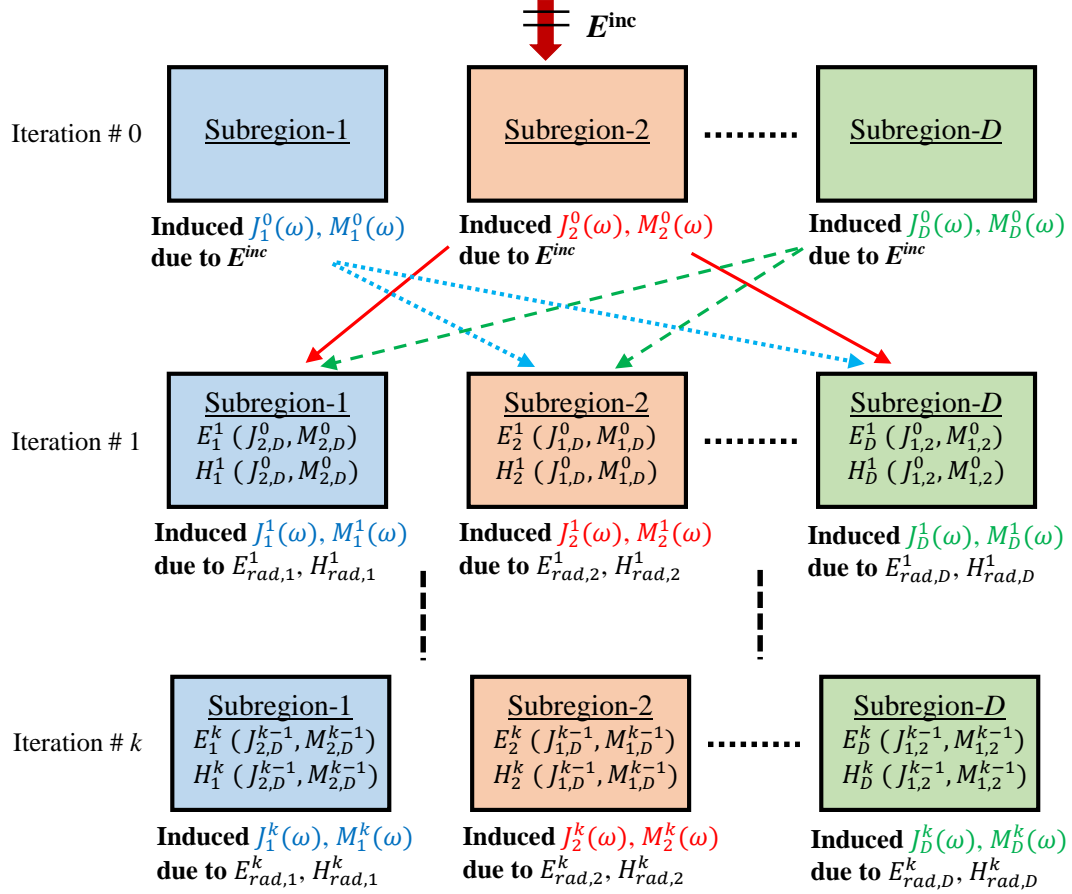


Figure 2.2: Iterative procedure between subregions.

In the iteration # 0, the scatterer in each subregion is excited by a same incident plane wave (E^{inc}). A method known as the total-field/scattered-field (TF/SF) formulation [34] is used to impose the incident plane wave on the problem space. The dashed lines indicate the TF/SF boundary in Figure 2.1. The TF/SF formulation divides the problem space into two regions. The electromagnetic fields inside the TF/SF boundary are total fields and the fields outside are scattered fields. The incident plane wave is imposed on the TF/SF boundary itself. The scattered fields (E_d^0, H_d^0) due to the incident plane wave are captured over the imaginary surface in subregion- d . In E and H , the superscript 0 indicates iteration # 0, the subscript d indicates the d^{th} subregion. Then fictitious electric and

magnetic currents (J_d^0, M_d^0) in (2.1), shown in Figure 2.3, due to the scattered fields are calculated on the imaginary surface in subregion- d , using the equivalence principle [32].

$$J_d^0(\omega) = \hat{n} \times H_d^0(\omega) \text{ and } M_d^0(\omega) = -\hat{n} \times E_d^0(\omega). \quad (2.1)$$

where \hat{n} is the unit normal vector that points outward from the surface. The existence of the fictitious currents of all subregions obtained in iteration # 0 is denied until iteration # 1 is started.

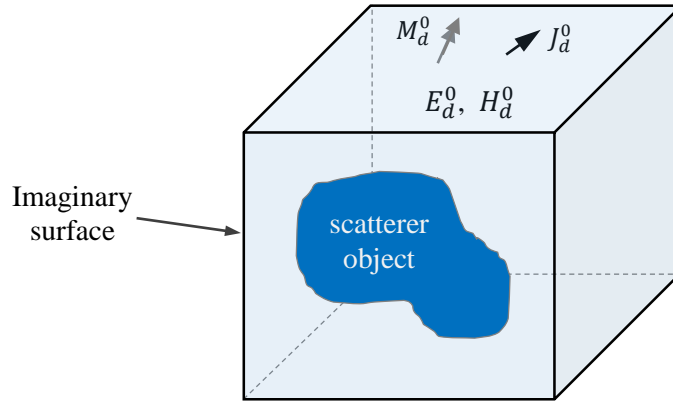


Figure 2.3: Imaginary surface in subregion- d .

At the beginning of the iteration # 1, radiated electromagnetic fields $(E_{rad,d}^1(\omega), H_{rad,d}^1(\omega))$ which are the sum of the fields generated by the fictitious currents in other subregions are calculated on each field point of the TF/SF boundary in subregion- d , using near-field to near-field (NF/NF) transformation [32]. Details of NF/NF transformation are provided in Appendix A.

$$E_{rad,d}^1(\omega) = \sum_{\substack{d'=1 \\ d' \neq d}}^D E_{d'} \left(J_{d'}^0(\omega), M_{d'}^0(\omega) \right), \quad (2.2a)$$

$$H_{rad,d}^1(\omega) = \sum_{\substack{d'=1 \\ d' \neq d}}^D H_{d'} \left(J_{d'}^0(\omega), M_{d'}^0(\omega) \right), \quad (2.2b)$$

where $E_{d'}$ and $H_{d'}$ are the electromagnetic fields radiated by the combination of the fictitious currents obtained on the imaginary surface in subregion- d' in iteration # 0. The

term for which $d = d'$ is omitted from the summation because the scatterer in subregion- d is inside the imaginary surface in subregion- d where $(J_d^0(\omega), M_d^0(\omega))$ radiates no field. Then these radiated fields in (2.2) are used as the new excitation fields for the subregion- d . The new excitation fields on the TF/SF boundary in subregion- d start a FDFD procedure whose solution on the imaginary surface in subregion- d is used to obtain the scattered electromagnetic fields. This cycle of iterations is processed until a convergence (stopping) criterion is achieved.

In the IMR technique using the FDFD method, all fields and fictitious currents are defined in the frequency domain at a single frequency. Here we propose to use FDTD method instead of the FDFD method for the solutions in the subregions. Still the fictitious currents on the imaginary surfaces can be obtained in the frequency domain and NF/NF transformation can be performed in the frequency domain to calculate the excitation fields. When the FDTD method is used instead of the FDFD method, the new excitation fields can be in the frequency domain at a number of frequencies instead of a single frequency.

2.2 Iterative Procedure Using the FDTD method

In this contribution, we adapt the use of the FDTD method to solve each subregion independently; as a consequence a problem can be solved at a number of frequencies instead of a single frequency. As in the IMR technique based on the FDFD method the excitation fields are calculated in the frequency domain, thus a frequency-domain to time-domain transformation is needed to convert the calculated excitation fields into time-limited waveforms in order to use these waveforms to excite the FDTD problem spaces. A key contribution in this research is a TWC mechanism for the iterative interactions between

subregions. Therefore, an algorithm is developed to construct time-limited waveforms. The TWC algorithm is presented in the next section. In this section, we discuss the integration of the FDTD method into IMR to solve large-scale scattering problems.

The scattering problem illustrated in Figure 2.1 is divided into D number of unconnected subregions. There is a scattering object in each subregion. The subregion boundaries are terminated by convolution perfectly matched layers (CPML) [33] indicated by solid lines in Figure 2.1. The iterative procedure between subregions, solved using the FDTD method, is shown in Figure 2.4. The iterations consist of iteration # 0 and iteration # k for $\{k=1, 2, \dots, K\}$ where K is an integer depending on how many iterations are necessary. In the rest of this chapter, fields in the time domain are indicated by lowercase letters, whereas fields in the frequency domain are indicated by capital letters.

At the beginning of the iteration # 0, the scatterer in each subregion, isolated from the scatterers in all other subregions, is illuminated by the same incident plane wave whose electric field, $\mathbf{e}^{\text{inc}}(\mathbf{r}, t)$, can be expressed as

$$\mathbf{e}^{\text{inc}}(\mathbf{r}, t) = (E_\theta \hat{\theta} + E_\phi \hat{\phi})g\left((t - t_0) - \frac{1}{c}(\hat{\mathbf{k}} \cdot \mathbf{r} - \mathbf{r}_0)\right), \quad (2.3)$$

where E_θ and E_ϕ are the components of the incident electric fields, t_0 and \mathbf{r}_0 are the time and spatial shift, g is a Gaussian waveform, c is the speed of light, $\hat{\mathbf{k}}$ is a unit vector that is constant and is in the direction of propagation, and \mathbf{r} is a position vector for a given point in the problem space.

In iteration # 0, the set of operations described in the remainder of this paragraph is performed D times, first for $d=1$, then for $d=2$, and so forth, up to $d=D$. The incident plane wave in (2.3) imposed on the TF/SF boundary in subregion- d starts a FDTD procedure whose solution on the imaginary surface is used to obtain the scattered fields.

The scattered electric and magnetic fields $((\mathbf{e}_{scat,d}^0)^n, (\mathbf{h}_{scat,d}^0)^n)$ at every point of the imaginary surface are captured at every time step of the FDTD time-marching loop.

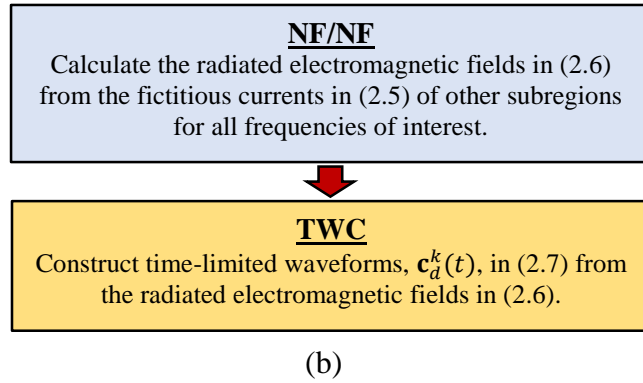
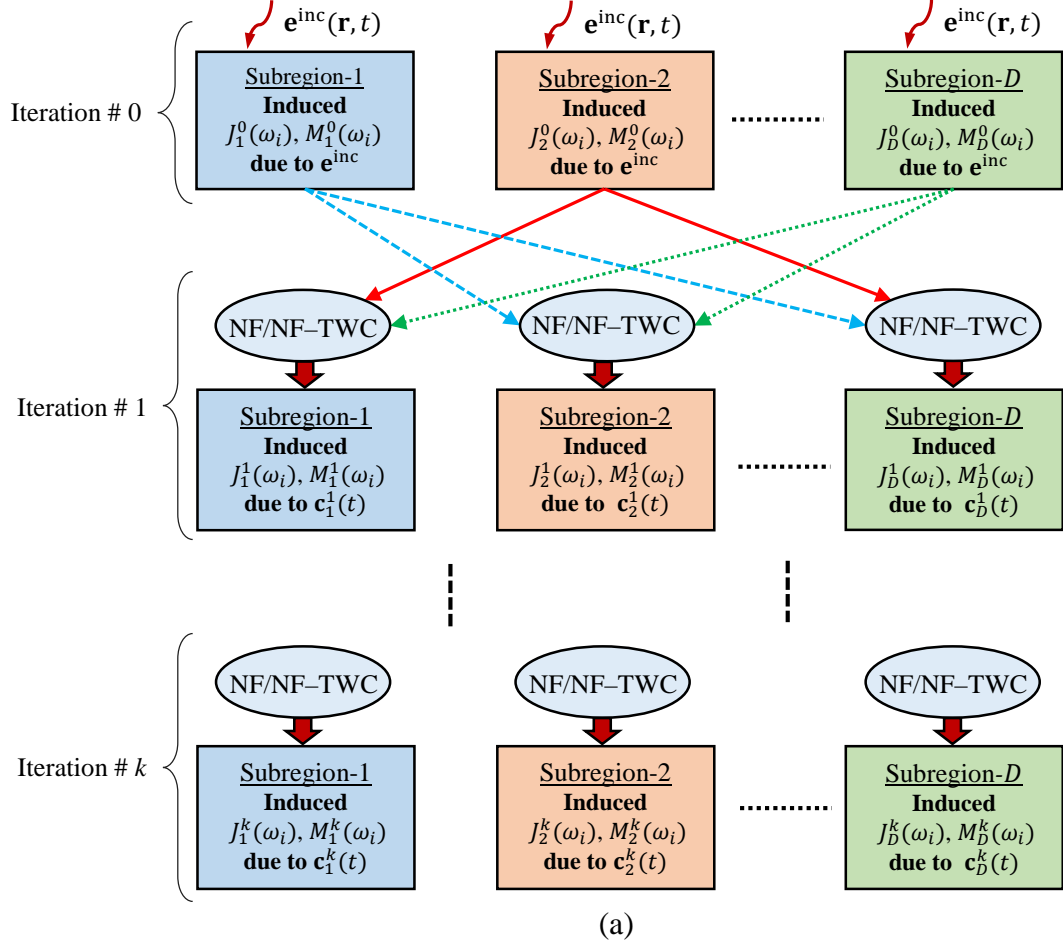


Figure 2.4: a) Iterative procedure between subregions and b) NF/NF-TWC algorithm.

In each \mathbf{e}_{scat} and \mathbf{h}_{scat} the superscript 0 indicates iteration # 0 and the subscript d indicates the d^{th} subregion. During each time step of the FDTD time-marching loop, the equivalence principle is used to obtain the fictitious electric and magnetic currents in (2.4) from the scattered electric and magnetic fields captured over the imaginary surface.

$$(\mathbf{j}_d^0)^n = \hat{\mathbf{n}} \times (\mathbf{h}_{scat,d}^0)^n \text{ and } (\mathbf{m}_d^0)^n = -\hat{\mathbf{n}} \times (\mathbf{e}_{scat,d}^0)^n, \quad (2.4)$$

where $\hat{\mathbf{n}}$ is the unit normal vector that points outward from the surface, n is the current time step, $(\mathbf{j}_d^0)^n$ and $(\mathbf{m}_d^0)^n$ are the fictitious currents calculated on the imaginary surface of the subregion- d in iteration # 0 at n^{th} time step. These current values in the time domain are then converted into currents in the frequency domain using the “on-the-fly” Numerical Fourier Transform (NFT) [33] while the FDTD time-marching loop is running such that

$$J_d^0(\omega_i) = J_d^0(\omega_i) + \Delta t (\mathbf{j}_d^0)^n e^{-j\omega_i n \Delta t}, \quad (2.5a)$$

$$M_d^0(\omega_i) = M_d^0(\omega_i) + \Delta t (\mathbf{m}_d^0)^n e^{-j\omega_i n \Delta t}, \quad (2.5b)$$

where ω_i is one of the frequencies of interest, Δt is the duration of a time step, and $J_d^0(\omega_i)$ and $M_d^0(\omega_i)$ are the fictitious currents obtained in the frequency domain at the frequency ω_i . At the start of the first time step, $J_d^0(\omega_i) = M_d^0(\omega_i) = 0$ in (2.5). For each frequency of interest, the NFT in (2.5) is performed for all frequencies of interest. The existence of all the fictitious currents obtained in iteration # 0 is denied until iteration # 1 is started.

In iteration # 1, the set of operations described in the remainder of this paragraph is performed D times, first for $d=1$, then for $d=2$, and so forth, up to $d=D$. At the beginning of the iteration # 1, radiated electromagnetic fields $(E_{rad,d}^1(\omega_i), H_{rad,d}^1(\omega_i))$ in (2.6) which are the sum of the radiated fields generated by the fictitious currents in other subregions are calculated on each field point of the TF/SF boundary in subregion- d , using the NF/NF

transformation presented in Appendix A. For each frequency of interest, the NF/NF transformation is performed with the corresponding frequency value.

$$E_{rad,d}^1(\omega_i) = \sum_{\substack{d'=1 \\ d' \neq d}}^D E_{d'} \left(J_{d'}^0(\omega_i), M_{d'}^0(\omega_i) \right), \quad (2.6a)$$

$$H_{rad,d}^1(\omega_i) = \sum_{\substack{d'=1 \\ d' \neq d}}^D H_{d'} \left(J_{d'}^0(\omega_i), M_{d'}^0(\omega_i) \right), \quad (2.6b)$$

where $E_{d'}$ and $H_{d'}$ are the electromagnetic fields radiated by the combination of the fictitious electric and magnetic currents obtained on the imaginary surface in subregion- d' in iteration # 0. The term for which $d = d'$ is omitted from the summation because the scatterer in subregion- d is inside the imaginary surface in subregion- d where $(J_d^0(\omega_i), M_d^0(\omega_i))$ radiates no field. Then these radiated fields in (2.6) are used as the new excitation fields for the subregion- d . Since the new excitation fields are in the frequency domain at a number of frequencies and cannot be used to start a FDTD procedure in subregions, these fields must be converted into time-limited waveforms, $\mathbf{c}_d^1(t)$ in (2.7), before exciting the subregion- d . Therefore, TWC algorithm is used to construct time-limited waveforms from the new excitation fields.

$$\mathbf{c}_d^1(t) = \text{TWC} \left\{ \sum_{i=1}^N (E_{rad,d}^1(\omega_i) \delta(\omega - \omega_i), H_{rad,d}^1(\omega_i) \delta(\omega - \omega_i)) \right\}, \quad (2.7)$$

where N is the number of frequencies of interest and δ is the Dirac delta function. Then the constructed time-limited waveforms in (2.7) imposed on the TF/SF boundary in subregion- d start a FDTD procedure whose solution on the imaginary surface in subregion- d is used to obtain the scattered electromagnetic fields. The scattered electric and magnetic fields $((\mathbf{e}_{scat,d}^1)^n, (\mathbf{h}_{scat,d}^1)^n)$ at every point of the imaginary surface in subregion- d are captured at every time step of the FDTD time-marching loop. Finally in iteration # 1, during

each time step of the FDTD time-marching loop, the fictitious electric and magnetic currents are calculated from the scattered fields on the imaginary surface as

$$(\mathbf{j}_d^1)^n = \hat{\mathbf{n}} \times (\mathbf{h}_{scat,d}^1)^n \text{ and } (\mathbf{m}_d^1)^n = -\hat{\mathbf{n}} \times (\mathbf{e}_{scat,d}^1)^n. \quad (2.8)$$

These time domain current values are then used in “on-the-fly” NFT such that

$$J_d^1(\omega_i) = J_d^1(\omega_i) + \Delta t (\mathbf{j}_d^1)^n e^{-j\omega_i n \Delta t}, \quad (2.9a)$$

$$M_d^1(\omega_i) = M_d^1(\omega_i) + \Delta t (\mathbf{m}_d^1)^n e^{-j\omega_i n \Delta t}. \quad (2.9b)$$

The NFT in (2.9) is performed for each frequency of interest. The existence of all the fictitious currents obtained in iteration # 0 is denied until the first repetition of iteration # 1 is started.

Iteration # 1 is repeated $K-1$ times until a convergence (stopping) criterion is achieved. The iterations are terminated when the Euclidean norm of the difference in the fictitious electric and magnetic currents from one iteration to the next iteration is small over the imaginary surface in each subregion at each frequency of interest.

In order to check the convergence of the IMR solutions, the Euclidean norm $(\varepsilon_{J_{x_k}}^d)$ of the difference between the k^{th} and $(k-1)^{\text{th}}$ iterations in the x -component of the fictitious electric current $(J_{x_k}^d(\omega_i))$ over the imaginary surface of the subregion- d is defined as follows;

$$\varepsilon_{J_{x_k}}^d = \max_{i=1,2,\dots,N} \left| \frac{\|J_{x_k}^d(\omega_i) - J_{x_{(k-1)}}^d(\omega_i)\|}{\|J_{x_{(k-1)}}^d(\omega_i)\|} \right| \times 100 \%, \quad (2.10)$$

where N is the number of desired frequencies, and d is the subregion number. In this expression, $\|\cdot\|$ refers to the l^2 -norm and also known as the Euclidean norm [40]. The average of $\varepsilon_{J_{x_k}}^d$ in (2.10) over all subregions is given by

$$\varepsilon_{J_{x_k}} = \text{average}(\varepsilon_{J_{x_k}}^d), \quad d = 1, 2, \dots, D. \quad (2.11)$$

Similarly, the Euclidean norm of difference for other J and M currents $(\varepsilon_{J_{y_k}}, \varepsilon_{J_{z_k}}, \varepsilon_{M_{x_k}}, \varepsilon_{M_{y_k}}, \varepsilon_{M_{z_k}})$ are calculated from (2.10) and (2.11). The average norm of difference of the fictitious currents is the convergence ε_k for the k^{th} iteration and defined as follows;

$$\varepsilon_k = \text{average}(\varepsilon_{J_{x_k}}, \varepsilon_{J_{y_k}}, \varepsilon_{J_{z_k}}, \varepsilon_{M_{x_k}}, \varepsilon_{M_{y_k}}, \varepsilon_{M_{z_k}}). \quad (2.12)$$

Based on the numerical experiments, 5 % is found sufficient to indicate that convergence ε_k is achieved since RCS values at desired frequencies do not change significantly for smaller values.

Once the convergence (ε_k) in (2.12) reaches the convergence criterion value, the IMR iterations are completed and the total fictitious currents coming from all iterations are calculated in (2.13) for each subregion.

$$J_d(\omega_i) = \sum_{k=0}^{K-1} J_d^k(\omega_i), \text{ and } M_d(\omega_i) = \sum_{k=0}^{K-1} M_d^k(\omega_i), \quad (2.13)$$

where $J_d(\omega_i)$ and $M_d(\omega_i)$ are the total fictitious currents at frequency ω_i in subregion- d , and K is the total number of iterations. The far-field terms ($L_\theta^d(\omega_i)$, $L_\phi^d(\omega_i)$, $N_\theta^d(\omega_i)$, and $N_\phi^d(\omega_i)$) from the total fictitious currents in (2.13) are calculated for subregion- d , using the near-field to far-field transformation [33]. Then the total far-field terms ($L_\theta(\omega_i)$, $L_\phi(\omega_i)$, $N_\theta(\omega_i)$, and $N_\phi(\omega_i)$) in (2.14) are the sum of the far-field terms from all subregions.

$$L_\theta(\omega_i) = \sum_{d=1}^D L_\theta^d(\omega_i) \text{ and } L_\phi(\omega_i) = \sum_{d=1}^D L_\phi^d(\omega_i). \quad (2.14a)$$

$$N_\theta(\omega_i) = \sum_{d=1}^D N_\theta^d(\omega_i) \text{ and } N_\phi(\omega_i) = \sum_{d=1}^D N_\phi^d(\omega_i). \quad (2.14b)$$

At the end of the algorithm, these total far-field terms in (2.14) are used to obtain the components of the bistatic radar cross-section (RCS_θ and RCS_ϕ) which are expressed at each frequency of interest in the following form;

$$RCS_\theta(\omega_i) = \frac{k_i^2}{8\pi\eta_0 P_{inc}(\omega_i)} |L_\phi(\omega_i) + \eta_0 N_\theta(\omega_i)|^2, \quad (2.15a)$$

$$RCS_\phi(\omega_i) = \frac{k_i^2}{8\pi\eta_0 P_{inc}(\omega_i)} |L_\theta(\omega_i) - \eta_0 N_\phi(\omega_i)|^2, \quad (2.15b)$$

where η_0 is the intrinsic impedance of the free space, $k_i = \omega_i \sqrt{\mu_0 \epsilon_0}$ is the propagation constant in free space, and $P_{inc}(\omega_i)$ is the power per unit area carried by the incident plane wave. The $P_{inc}(\omega_i)$ can be calculated as

$$P_{inc}(\omega_i) = \frac{1}{2\eta_0} |E^{inc}(\omega_i)|^2, \quad (2.16)$$

where $E^{inc}(\omega_i)$ is the NFT of the incident electric field waveform (\mathbf{e}^{inc}) of (2.3) at frequency ω_i for which the RCS is sought.

To prove the convergence of the solutions for the problem, a normalized average error is calculated at each iteration to provide more information related to the convergence of the full domain solution. Once the number of iterations used within the IMR technique increases, the error decreases and the solution of the IMR technique converges to that of the full domain. The level of the final error depends on the simulated problem. The normalized average error at each iteration is defined as

$$Error(\omega_i) = average \left(\frac{|RCS^{IMR}(\omega_i) - RCS^{FD}(\omega_i)|}{\max(|RCS^{FD}(\omega_i)|)} \right) \times 100 \%, \quad FD: \text{Full Domain}. \quad (2.17)$$

Since a single run of the IMR technique using the FDTD method provides solutions at multiple frequencies, numerical results at multiple frequencies are presented to prove the validity of the IMR technique based on the FDTD method in Chapter 3.

2.3 Time-Limited Waveform Construction (TWC) Algorithm

As discussed before, when proceeding to a new IMR iteration, radiated electromagnetic fields in (2.6) are calculated at every field point on the TF/SF boundary of each subregion due to the fictitious currents calculated in the previous iteration on the imaginary surface of other subregions. These fields are considered as the new excitation fields for subregion- d and there are N number of field components for each field point in the frequency domain, where N is the number of frequencies in consideration. These excitation field components need to be combined and transformed into the time domain to excite the FDTD problem. Here we propose an algorithm to construct time-limited waveform, i.e. $\mathbf{c}_d^1(t)$ in (2.7), which includes the required magnitudes and phases of time-harmonic signals of the solution in its frequency spectrum. Then $\mathbf{c}_d^1(t)$ is used to excite the FDTD problem space during the current iteration of IMR technique. In this section, the following operations are performed for all subregions $\{d=1, 2, \dots, D\}$ and in all iterations except iteration # 0.

The constructed time-limited waveform, $\mathbf{c}_d^1(t)$, is a Gaussian waveform that is modulated by a series of cosine waveforms. Each of the cosine terms in the series is related to one of the desired solution frequencies. The constructed time-limited waveform is then expressed as

$$\mathbf{c}_d^1(t) = g(t) \times \sum_{i=1}^N (B_i)_d^1 \cos(\omega_i t + (\theta_i)_d^1), \quad (2.18)$$

where $g(t)$ is a Gaussian waveform, ω_i is the desired frequency, N is the pre-specified number of frequencies, and $(B_i)_d^1$ and $(\theta_i)_d^1$ are the unknown coefficients and phases of the cosine waveform in subregion- d , respectively. The unknown coefficients and phases of the cosine waveforms, i.e. $(B_i)_d^1$ and $(\theta_i)_d^1$, are to be determined using the known

magnitudes and phases of the radiated electromagnetic fields in (2.6) at the desired solution frequencies.

The Gaussian waveform, $g(t)$, and its Fourier transform, $G(\omega)$, are given respectively as follows:

$$g(t) = e^{-(t-t_0)^2/\tau^2}, \quad (2.19)$$

$$G(\omega) = \tau\sqrt{\pi}e^{-(\tau\omega)^2/4}e^{-j\omega t_0}, \quad (2.20)$$

where τ is a parameter that determines the width of the Gaussian waveform, and t_0 is the time at which $g(t)$ is maximum.

The Fourier transform of the constructed time-limited waveform, $C_d^1(\omega)$, which equals to radiated electromagnetic fields in (2.6) can be expressed as

$$C_d^1(\omega) = \left(\sum_{i=1}^N (E_{rad,d}^1(\omega_i)\delta(\omega - \omega_i), H_{rad,d}^1(\omega_i)\delta(\omega - \omega_i)) \right). \quad (2.21)$$

The Fourier transform of the constructed time-limited waveform, $C_d^1(\omega)$, can also be expressed as the Fourier transform of a Gaussian waveform modulated by a series of cosine waveforms in (2.18).

$$\begin{aligned} C_d^1(\omega) &= \mathcal{F}\{\mathbf{c}_d^1(t)\} = \mathcal{F}[g(t) \times \sum_{i=1}^N (B_i)_d^1 \cos(\omega_i t + (\theta_i)_d^1)] \\ &= 0.5 \left(\sum_{i=1}^N (B_i)_d^1 \left[G(\omega - \omega_i) e^{j(\theta_i)_d^1} + G(\omega + \omega_i) e^{-j(\theta_i)_d^1} \right] \right). \end{aligned} \quad (2.22)$$

The time-limited waveform, $\mathbf{c}_d^1(t)$, is constructed from knowledge of the magnitude and phase of radiated electromagnetic fields in (2.6) at each of $\omega_1, \omega_2, \dots, \omega_N$ and $-\omega_1, -\omega_2, \dots, -\omega_N$. From this knowledge, a linear set of equations is constructed using (2.22). This linear set of equations is then solved for the unknowns $(B_i)_d^1$ and $(\theta_i)_d^1$ in (2.18).

Setting $\omega = \omega_m$ in (2.22) and, in the resulting equation, taking $C_d^1(\omega_m)$ to be $C_{d,m}^1 e^{j\phi_{d,m}^1}$, where $C_d^1(\omega_m)$ is a known complex number, we obtain

$$C_{d,m}^1 e^{j\phi_{d,m}^1} = 0.5 \left(\sum_{i=1}^N (B_i)_d^1 \left[G(\omega_m - \omega_i) e^{j(\theta_i)_d^1} + G(\omega_m + \omega_i) e^{-j(\theta_i)_d^1} \right] \right). \quad (2.23)$$

We also obtain

$$C_{d,m}^1 e^{-j\phi_{d,m}^1} = 0.5 \left(\sum_{i=1}^N (B_i)_d^1 \left[G(-\omega_m - \omega_i) e^{j(\theta_i)_d^1} + G(-\omega_m + \omega_i) e^{-j(\theta_i)_d^1} \right] \right). \quad (2.24)$$

Taking $\{m=1, 2, \dots, N\}$ in (2.23) and (2.24), we obtain a set of $2N$ linear equations in the $2N$ complex unknowns $(B_1)_d^1 e^{j(\theta_1)_d^1}, (B_2)_d^1 e^{j(\theta_2)_d^1}, \dots, (B_N)_d^1 e^{j(\theta_N)_d^1}$ and $(B_1)_d^1 e^{-j(\theta_1)_d^1}, (B_2)_d^1 e^{-j(\theta_2)_d^1}, \dots, (B_N)_d^1 e^{-j(\theta_N)_d^1}$ which are assumed to be independent of each other.

This set of $2N$ linear equations can then be solved for the $2N$ complex unknowns.

Once the coefficients and phases of the cosine waveforms in (2.22) are known, the constructed time-limited waveform can be expressed as

$$\mathbf{c}_d^1(t) = e^{\left(-\frac{(t-t_0)^2}{\tau^2}\right)} \times \left[(B_1)_d^1 \cos(\omega_1 t + (\theta_1)_d^1) + (B_2)_d^1 \cos(\omega_2 t + (\theta_2)_d^1) + \dots + (B_N)_d^1 \cos(\omega_N t + (\theta_N)_d^1) \right]. \quad (2.25)$$

As an example, let's construct a time-limited waveform which includes the two desired frequencies (ω_1 and ω_2) in its frequency spectrum. The time-limited waveform which includes two desired frequencies can be written as a function of frequency as

$$\begin{aligned} C_d^1(\omega) &= 0.5 \times \left(\sum_{i=1}^2 (B_i)_d^1 \left[G(\omega - \omega_i) e^{j(\theta_i)_d^1} + G(\omega + \omega_i) e^{-j(\theta_i)_d^1} \right] \right), \\ &= \frac{(B_1)_d^1}{2} \times \left[G(\omega - \omega_1) e^{j(\theta_1)_d^1} + G(\omega + \omega_1) e^{-j(\theta_1)_d^1} \right] \\ &\quad + \frac{(B_2)_d^1}{2} \times \left[G(\omega - \omega_2) e^{j(\theta_2)_d^1} + G(\omega + \omega_2) e^{-j(\theta_2)_d^1} \right]. \end{aligned} \quad (2.26)$$

Then, evaluating ω at $\omega_1, \omega_2, -\omega_1$, and $-\omega_2$ in (2.26), one can obtain the following four equations;

$$\begin{aligned} C_d^1(\omega = \omega_1) &= C_{d,1}^1 e^{j\phi_{d,1}^1} = \frac{(B_1)_d^1}{2} \left[G(0) e^{j(\theta_1)_d^1} + G(2\omega_1) e^{-j(\theta_1)_d^1} \right] \\ &\quad + \frac{(B_2)_d^1}{2} \left[G(\omega_1 - \omega_2) e^{j(\theta_2)_d^1} + G(\omega_1 + \omega_2) e^{-j(\theta_2)_d^1} \right], \end{aligned} \quad (2.27a)$$

$$C_d^1(\omega = \omega_2) = C_{d,2}^1 e^{j\phi_{d,2}^1} = \frac{(B_1)_d^1}{2} \left[G(\omega_2 - \omega_1) e^{j(\theta_1)_d^1} + G(\omega_2 + \omega_1) e^{-j(\theta_1)_d^1} \right] \\ + \frac{(B_2)_d^1}{2} \left[G(0) e^{j(\theta_2)_d^1} + G(2\omega_2) e^{-j(\theta_2)_d^1} \right], \quad (2.27b)$$

$$C_d^1(\omega = -\omega_1) = C_{d,1}^1 e^{-j\phi_{d,1}^1} = \frac{(B_1)_d^1}{2} \left[G(-2\omega_1) e^{j(\theta_1)_d^1} + G(0) e^{-j(\theta_1)_d^1} \right] \\ + \frac{(B_2)_d^1}{2} \left[G(-\omega_1 - \omega_2) e^{j(\theta_2)_d^1} + G(-\omega_1 + \omega_2) e^{-j(\theta_2)_d^1} \right], \quad (2.27c)$$

$$C_d^1(\omega = -\omega_2) = C_{d,2}^1 e^{-j\phi_{d,2}^1} = \frac{(B_1)_d^1}{2} \left[G(-\omega_2 - \omega_1) e^{j(\theta_1)_d^1} + G(-\omega_2 + \omega_1) e^{-j(\theta_1)_d^1} \right] \\ + \frac{(B_2)_d^1}{2} \left[G(-2\omega_2) e^{j(\theta_2)_d^1} + G(0) e^{-j(\theta_2)_d^1} \right], \quad (2.27d)$$

where $C_{d,1}^1$, $C_{d,2}^1$, and $\phi_{d,1}^1$, $\phi_{d,2}^1$ are the magnitudes and phases of $C_d^1(\omega)$ at ω_1 and ω_2 frequencies, respectively, and Gaussian waveform, $G(\omega)$, at the corresponding frequencies is calculated in (2.20). This set of four linear equations (2.27) can be expressed in a matrix form as

$$\begin{bmatrix} C_{d,1}^1 e^{j\phi_{d,1}^1} \\ C_{d,2}^1 e^{j\phi_{d,2}^1} \\ C_{d,1}^1 e^{-j\phi_{d,1}^1} \\ C_{d,2}^1 e^{-j\phi_{d,2}^1} \end{bmatrix} = 0.5 \begin{bmatrix} G(0) & G(\omega_1 - \omega_2) & G(2\omega_1) & G(\omega_1 + \omega_2) \\ G(\omega_2 - \omega_1) & G(0) & G(\omega_2 + \omega_1) & G(2\omega_2) \\ G(-2\omega_1) & G(-\omega_1 - \omega_2) & G(0) & G(-\omega_1 + \omega_2) \\ G(-\omega_2 - \omega_1) & G(-2\omega_2) & G(-\omega_2 + \omega_1) & G(0) \end{bmatrix} \begin{bmatrix} (B_1)_d^1 e^{j(\theta_1)_d^1} \\ (B_2)_d^1 e^{j(\theta_2)_d^1} \\ (B_1)_d^1 e^{-j(\theta_1)_d^1} \\ (B_2)_d^1 e^{-j(\theta_2)_d^1} \end{bmatrix}. \quad (2.28)$$

Solution of (2.28) yields the coefficients and phases, $(B_1)_d^1$, $(B_2)_d^1$, $(\theta_1)_d^1$, and $(\theta_2)_d^1$, of the cosine waveforms. Then the constructed time-limited waveform is expressed as

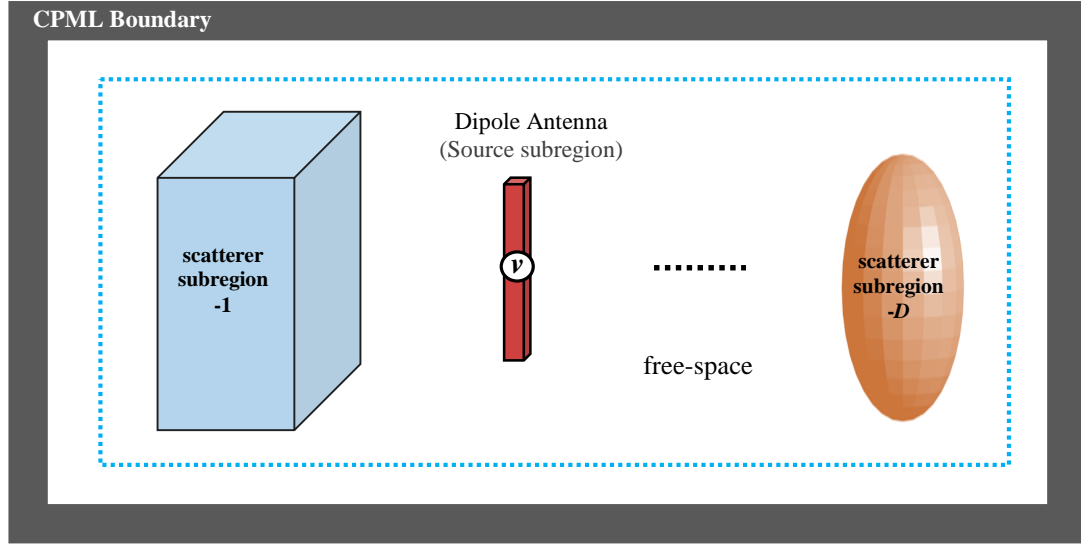
$$\mathbf{c}_d^1(t) = e^{-(t-t_o)^2/\tau^2} \times [(B_1)_d^1 \cos(\omega_1 t + (\theta_1)_d^1) + (B_2)_d^1 \cos(\omega_2 t + (\theta_2)_d^1)]. \quad (2.29)$$

The presented approach can be extended to construct time-limited waveforms which include the components with the required magnitudes and phases theoretically at any number of frequencies. Then these waveforms are used to excite the FDTD problem spaces to obtain solutions at the frequencies of interest.

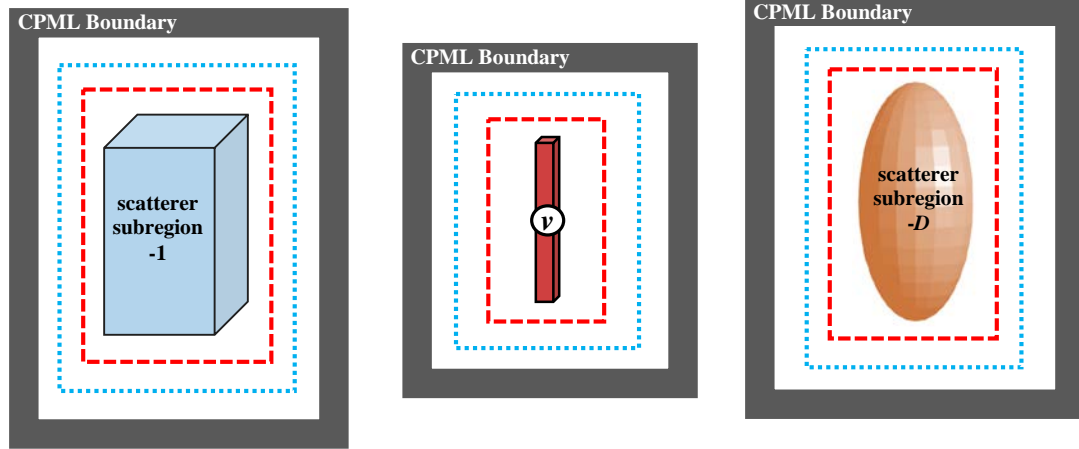
2.4 IMR Procedure for Radiation Problems

In Section 2.2 we show the integration of FDTD method into the IMR technique for scattering problems. In this section we extend this approach for radiation problems. In this case the radiation problem domain is divided into multiple subregions: one of them is the source subregion including an antenna, and the others are the scatterer subregions including scatterer objects. First, the antenna is driven in isolation so that, in what will be called the 0th iteration, there is no incident field in the subregion containing the driven antenna, and the incident fields in all the other subregions consist of the field of the driven antenna in isolation. Then the solutions of the subregions are combined, after multiple interactions between the subregions, to obtain the solutions at all frequencies of interest for the original problem.

For the sake of demonstration, the radiation problem illustrated in Figure 2.5a is divided into unconnected subregions: a source subregion and scatterer subregions, where each scatterer subregion contains a scatterer object, as shown in Figure 2.5b. The subregion boundaries are terminated by CPML indicated by solid lines in Figure 2.5. The dashed and dotted lines indicate the TF/SF boundary and imaginary surface in Figure 2.5, respectively. The iterative procedure between subregions of a radiation problem, shown in Figure 2.6, is similar to the iterative procedure between subregions of a scattering problem, shown in Figure 2.4, but the only difference is that the antenna in the source subregion is excited by the near zone source excitation. Radiated fields from the antenna are considered as the excitation fields for the other subregions including scatterer objects. The iterative procedure between subregions consists of iteration # 0, iteration # 1, and as many repetitions of iteration # 1 as are necessary.



(a)



(b)

Figure 2.5: Radiation from multiple objects: a) original problem and b) source and scatterer subregions. (dotted line: imaginary surface and dashed line: TF/SF boundary)

At the beginning of the iteration # 0, first, the source subregion is simulated by the near zone source excitation. The scattered electromagnetic fields are captured at every point of the imaginary surface at every time step of the FDTD time-marching loop. Then the fictitious currents in (2.4) are calculated from the scattered fields over the imaginary surface in the source subregion. The fictitious currents in the time domain are transformed to the frequency domain data in (2.5) at the frequencies of interest, using the NFT. The

radiated electromagnetic fields in (2.6) due to these currents are calculated on the TF/SF boundaries of the scatterer subregions, using the NF/NF transformation. These radiated fields are considered as the excitation fields for the scatterer subregions. Since the NF/NF transformation is carried out in the frequency domain for each frequency of interest, the excitation fields are in the frequency domain. In order to excite the FDTD problem space, these fields are converted into time-limited waveforms, $\mathbf{c}(t)$, by using the TWC algorithm. Then the constructed time-limited waveforms in (2.7) from the radiated fields imposed on the TF/SF boundary of the scatterer subregions start a FDTD procedure whose solution on the imaginary surface is used to obtain the fictitious currents in the frequency domain from the calculated scattered electromagnetic fields. The existence of all the fictitious currents obtained in iteration # 0 is denied until iteration # 1 is started.

At the beginning of iteration # 1, radiated fields due to the fictitious currents generated by two scatterer subregions in iteration # 0 are considered as the excitation fields for the source subregion after converting these fields into time-limited waveforms by using the TWC algorithm, but now the dipole antenna in the source subregion is inactive because it behaves like a scatterer. Therefore, a resistor which is equal to internal impedance of the voltage source is placed at the terminal of the antenna. Then fictitious currents calculated in the source subregion and those calculated in the scatterer subregions obtained in iteration # 0 are used to calculate the radiated fields on the field points of the TF/SF boundary in the scatterer subregions, using the NF/NF transformation. The time-limited waveforms from these fields are imposed on the TF/SF boundary of the source subregion to start the FDTD simulation. After iteration # 1 is done, the procedure for the subsequent iterations is the same.

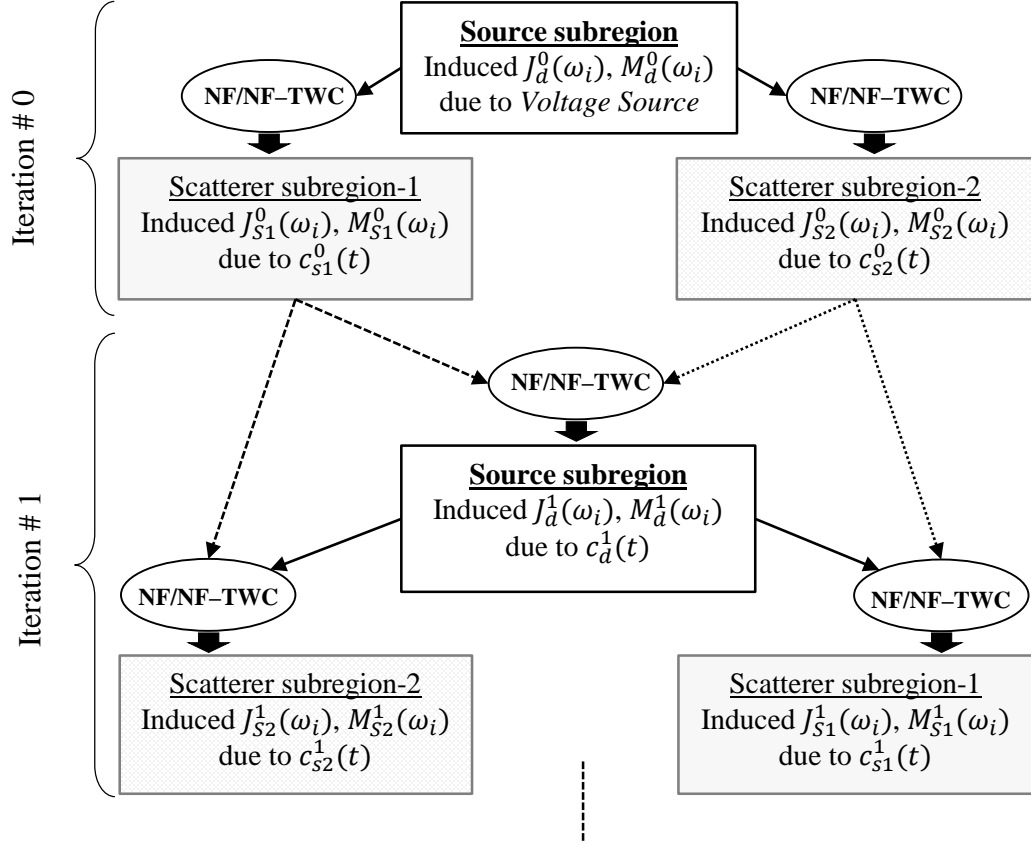


Figure 2.6: Iterative procedure between source subregion and scatterer subregions.

This cycle of iterations is processed until a convergence (stopping) criterion is achieved. Once the convergence (ε_k) in (2.12) reaches the convergence criterion value, the IMR iterations are completed and the total far-field terms, $L_\theta(\omega_i)$, $L_\phi(\omega_i)$, $N_\theta(\omega_i)$, and $N_\phi(\omega_i)$, are calculated in (2.14) at all frequencies of interest. At the end of the algorithm, these total far-field terms are used to obtain the components of the radiation patterns [33] (Gain_θ and Gain_ϕ) at all frequencies of interest expressed as

$$\text{Gain}_\theta(\omega_i) = \frac{k_i^2}{8\pi\eta_0 P_{\text{del}}(\omega_i)} |L_\phi(\omega_i) + \eta_0 N_\theta(\omega_i)|^2, \quad (2.30a)$$

$$\text{Gain}_\phi(\omega_i) = \frac{k_i^2}{8\pi\eta_0 P_{\text{del}}(\omega_i)} |L_\theta(\omega_i) - \eta_0 N_\phi(\omega_i)|^2, \quad (2.30b)$$

where $P_{\text{del}}(\omega_i)$ is delivered power to an antenna determined by the product of the sample voltage and current provided from the voltage source and can be expressed as

$$P_{\text{del}}(\omega_i) = \frac{1}{2} \text{Re}\{V_{\text{total}}(\omega_i)I_{\text{total}}^*(\omega_i)\}, \quad (2.31)$$

where the asterisk ‘*’ denotes the complex conjugate, and

$$V_{\text{total}}(\omega_i) = \sum_k V_s^k(\omega_i), \quad I_{\text{total}}(\omega_i) = \sum_k I_s^k(\omega_i). \quad (2.32)$$

In (2.32), $V_s^k(\omega_i)$ and $I_s^k(\omega_i)$ represent the Fourier transform values of the source voltage and current at the k^{th} iteration. After each iteration, the total delivered power is calculated according to the total source voltage and current. Once the convergence criterion is achieved, the radiation patterns in (2.30) are calculated.

To prove the convergence of the solutions for the problems, a normalized average error is calculated to provide more information related to the convergence of the full domain solution. The normalized average error is defined at each iteration as

$$\text{Error}(\omega_i) = \text{average} \left(\frac{|\text{Gain}^{\text{IMR}}(\omega_i) - \text{Gain}^{\text{FD}}(\omega_i)|}{\max(|\text{Gain}^{\text{FD}}(\omega_i)|)} \right) \times 100\%. \quad \text{FD: Full Domain.} \quad (2.33)$$

The numerical results at multiple frequencies are presented to prove the validity of the IMR technique based on the FDTD method in Chapter 4.

2.5 Speeding up Techniques

It has been realized that a considerable amount of the computation time is spent for the calculation of the excitation fields of the subregions. Therefore, two approaches are proposed in this work to improve the timing issue: TF/SF formulation, and interpolation process at current points on the imaginary surface and field points on the TF/SF boundary.

These two speeding up techniques provide remarkable reduction in the computation time of the excitation fields. These improvements are discussed in this section.

2.5.1 Total-Field Scattered-Field (TF/SF) Formulation

Initially, we have used the scattered field (SF) formulation [33] to excite the FDTD problem domains. Since the SF formulation requires the computation of the excitation fields at all field points in the problem space, a considerable amount of computation time is spent for the calculation of these fields. Therefore, the TF/SF formulation [34] is used to speed up the calculation of them. They are calculated on the TF/SF boundary rather than the entire computational domain in the subregions.

2.5.2 Interpolation Process

An interpolation process can be simply described as an averaging process. The interpolation process has been applied to the current points on the imaginary surface and the field points on the TF/SF boundary in each subregion. This process provides 90 % reduction in the computation time of the excitation fields.

In the interpolation process at the current points on the imaginary surface, the average of four neighboring original current points is considered as a new current point for the calculation of the excitation fields. In Figure 2.7, the small dots on the imaginary surface are the original current points, whereas the big dots on the surface are the new current points.

In the interpolation process at the field points on the TF/SF boundary, radiated fields in all directions (x , y , and z) are calculated at the odd field points, whereas each of fields at the even field points is simply an average of fields on two successive odd field

points. Figure 2.8 describes the interpolation process at the field points, for the x direction, which is to be applied also for the y and z directions on the TF/SF boundary. In Figure 2.8, the red dots on the boundary are the odd field points where the fields are actually calculated based on the fictitious currents generated from other subregions, whereas the blue squares on the boundary show the even field points where each field is the average of the fields on two successive odd field points.

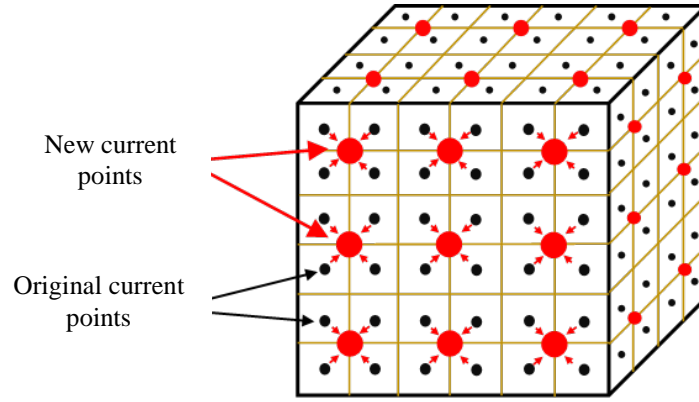


Figure 2.7: Configuration for the averaging process of current points on the imaginary surface.

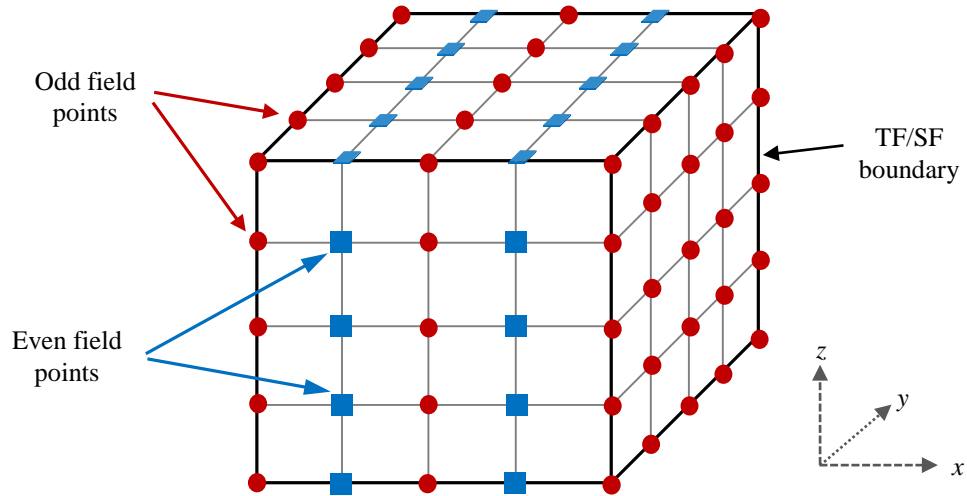


Figure 2.8: Configuration for the averaging process of field points along the x direction on the TF/SF boundary.

3 NUMERICAL RESULTS FOR SCATTERING PROBLEMS

In this chapter, numerical results of scattering problems are provided to prove the validity of the FDTD method integrated into the IMR technique. The problems are simulated to obtain solutions at a number of frequencies. In all simulations, the incident plane waves are both θ and ϕ polarized Gaussian waves with arbitrary incident angles (θ^i and ϕ^i). The incident electric field (\mathbf{e}^{inc}) [33] can be expressed as

$$\mathbf{e}^{\text{inc}} = (E_\theta \hat{\theta} + E_\phi \hat{\phi}) g_w, \quad (3.1)$$

where g_w is a Gaussian waveform function, E_θ and E_ϕ are the magnitudes of the incident electric field components, and indicating the polarization types. The incident plane waves are both θ and ϕ polarized by assigning $E_\theta=1$ and $E_\phi=1$.

FDTD problem spaces are terminated by eight CPML layers with CPML parameters [33] of CPML_order: 3, CPML_sigma_factor: 1.5, CPML_kappa: 7, CPML_alpha_min: 0, and CPML_alpha_max: 0.05. In addition to the eight CPML layers, ten air buffer layers are introduced between the inner CPML boundary and the object. The specifications of the computer used for the simulations are given in Appendix B.

An algorithm is developed to stop the FDTD time-marching loop and define the necessary number of time steps for the full domain and IMR simulations. In this algorithm, the excitation fields are applied to a problem space until the magnitudes of the scattered electric fields at certain points in the computation domain reach to values less than a threshold value. In our analysis, the threshold is defined as 5×10^{-4} (Volts/meter). Thus the FDTD time-marching loop is stopped when the scattered fields reach below the threshold.

3.1 Electromagnetic Scattering from Two Objects-1

The geometry of the first problem illustrated in Figure 3.1 is excited by a ϕ and θ polarized plane wave with $\theta^{\text{inc}}=90^\circ$ and $\phi^{\text{inc}}=0^\circ$ to obtain bistatic RCS for the xy , xz , and yz plane cuts at 200 MHz, 225 MHz, 250 MHz, 275 MHz and 300 MHz. The separation between the dielectric ellipsoid and sphere is 0.5 m. The semi-axes of the dielectric ellipsoid are 0.2 m, 0.2 m, and 1 m along the x , y , and z axes, respectively. The radius of the dielectric sphere is 0.4 m. The relative permittivity of the dielectric ellipsoid is 2.2, whereas that of the dielectric sphere is 3. The relative permeability of dielectric objects is 1. The problem space is composed of cells with size 0.02 m in the x , y , and z directions for the full domain simulation. As for the IMR simulation, a cell size 0.02 m is used in the subregion containing the ellipsoid, whereas a cell size 0.04 m is used in the subregion containing the sphere. One of the main features of the IMR technique is the flexibility. It provides for choosing different cell sizes in each subregion. Figure 3.2 shows the convergence of the IMR iteration calculated by (2.12). It can be seen that the IMR algorithm reaches the convergence criterion ($\epsilon_k < 5\%$) after iteration # 2. Figures 3.3-3.8 show the bistatic RCS_θ and RCS_ϕ for the xy , xz , and yz plane cuts at 200 MHz, 225 MHz, 250 MHz, 275 MHz and 300 MHz. To prove the convergence of the full domain and IMR technique results, the normalized average errors for RCS_θ and RCS_ϕ in the three plane cuts are calculated using (2.17) and shown in Figures 3.9-3.10. Simulation parameters and computer resources used are summarized in Table 3-1 for the full domain solution and the IMR solution. Comparison shows a considerable reduction in the memory storage requirements and computation time.

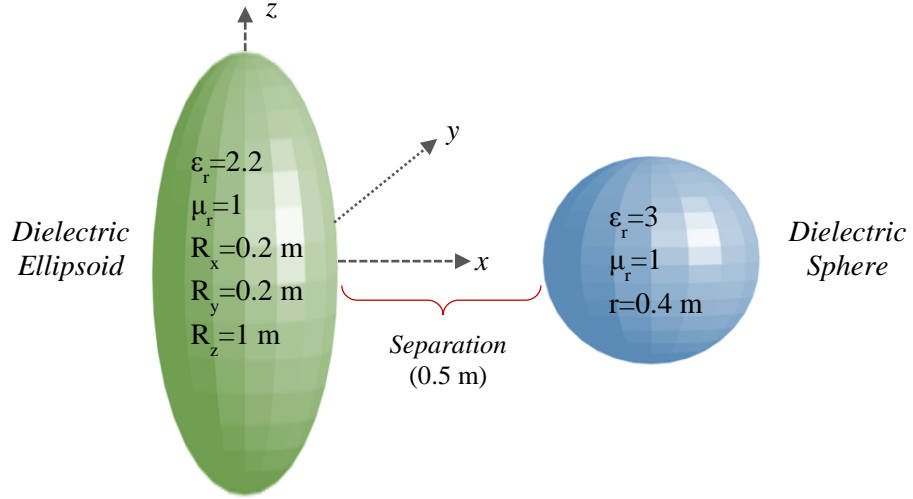


Figure 3.1: Geometry of the first problem.

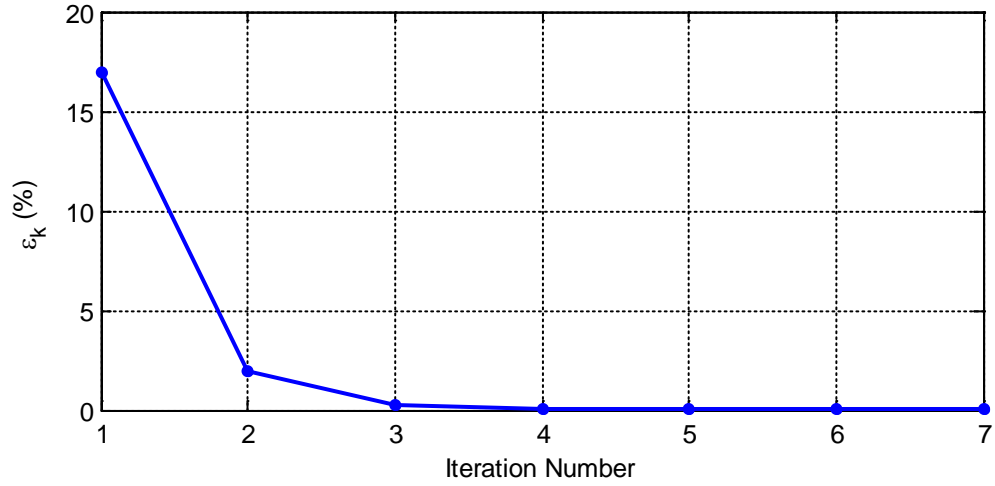
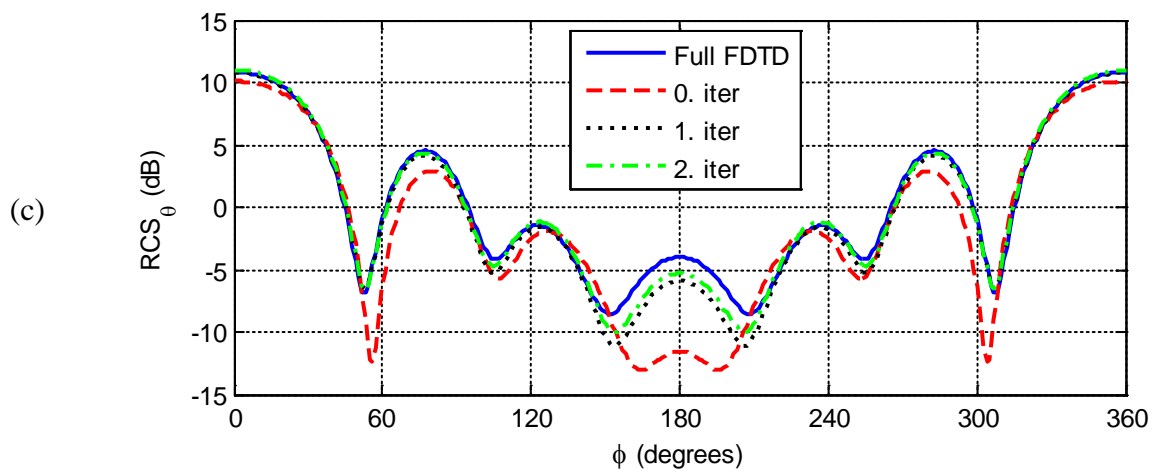
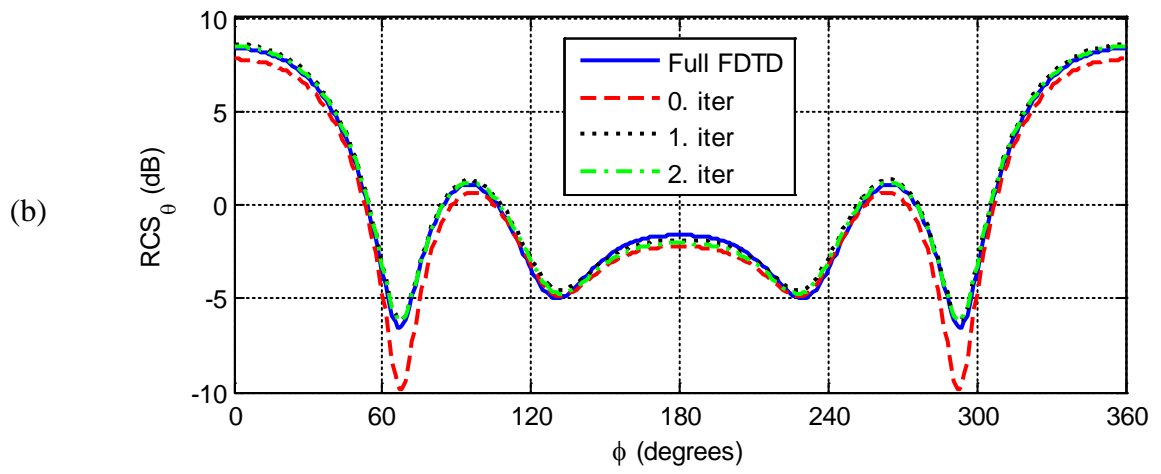
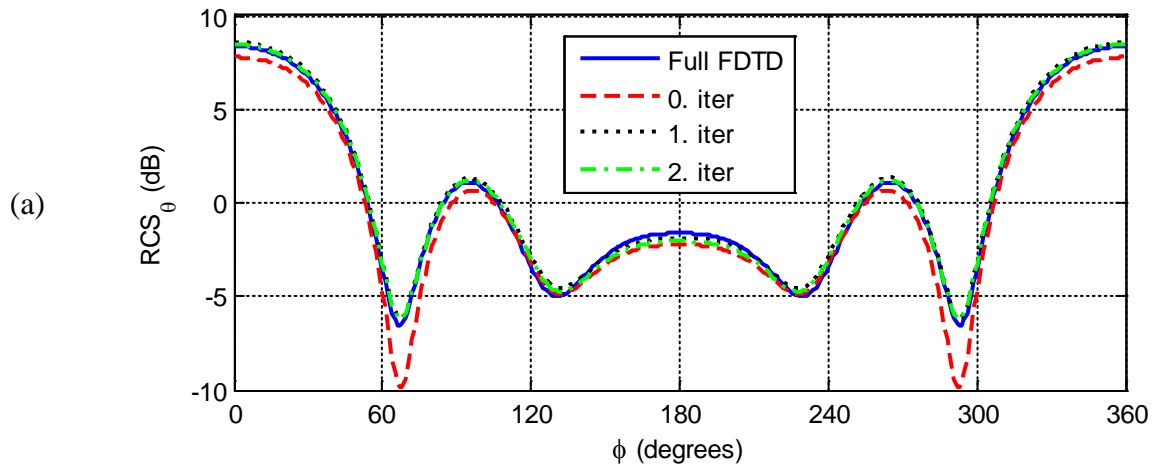


Figure 3.2: Convergence (ε_k) between iteration steps for the first problem.

Table 3-1: Simulation parameters and computer resources used by the IMR and full domain simulations.

| | Number of Domains | Total Number of Cells | Computation Time (min.) | Iteration Number | Memory (MB) |
|------------------|-------------------|-----------------------|-------------------------|------------------|-------------|
| Full FDTD | — | 1,250,656 | 39 | — | 926 |
| IMR-FDTD | 2 | 602,112 | 25 | 2 | 425 |



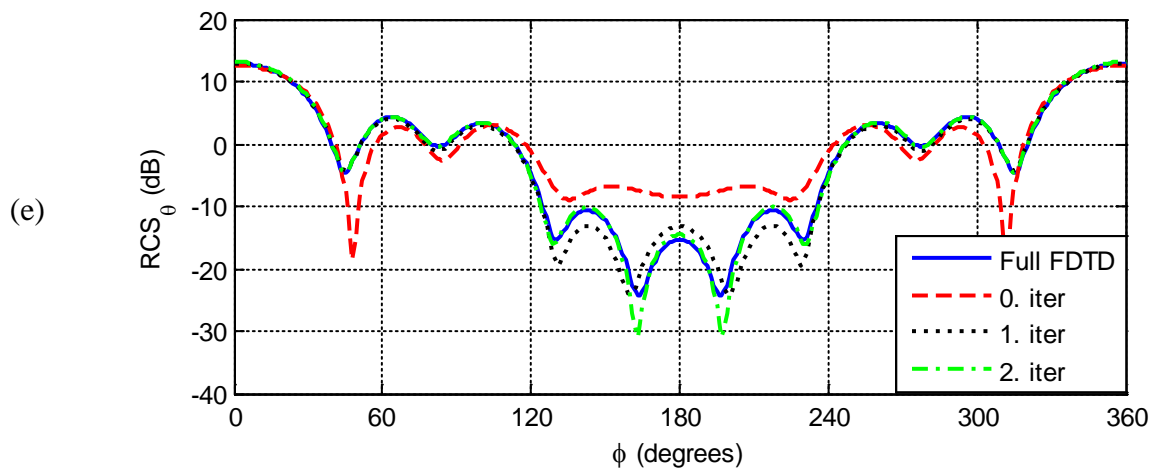
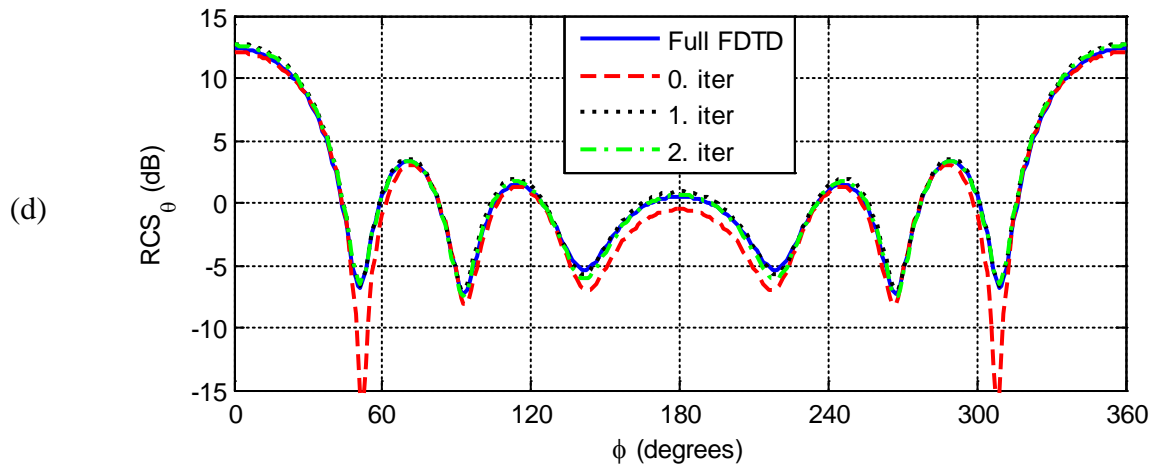
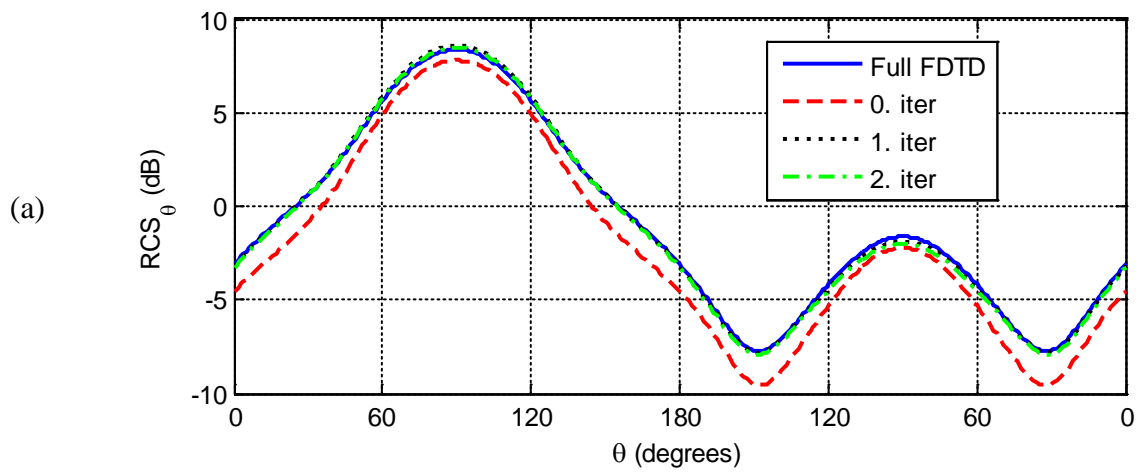
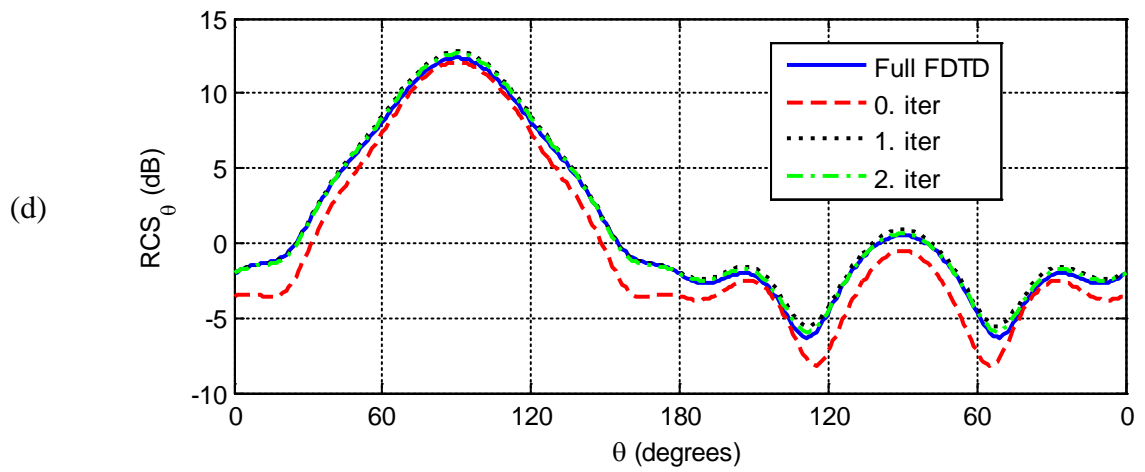
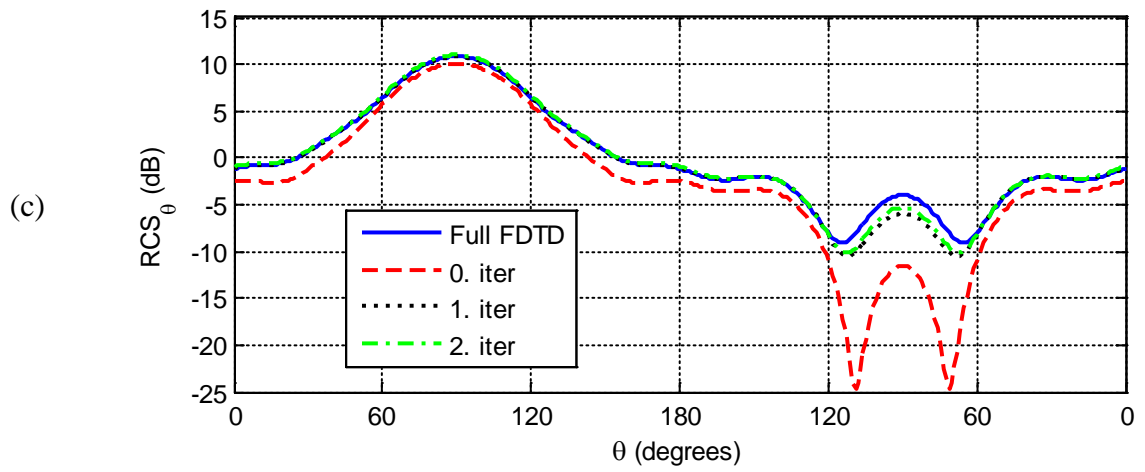
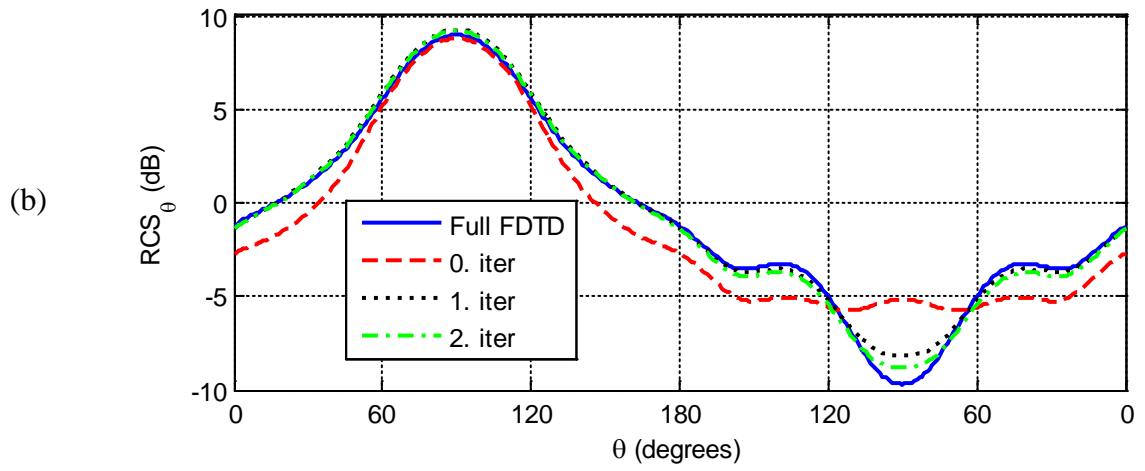


Figure 3.3: Bistatic RCS_θ for xy -plane cuts at frequencies: a) 200 MHz, b) 225 MHz, c) 250 MHz, d) 275 MHz, and e) 300 MHz.





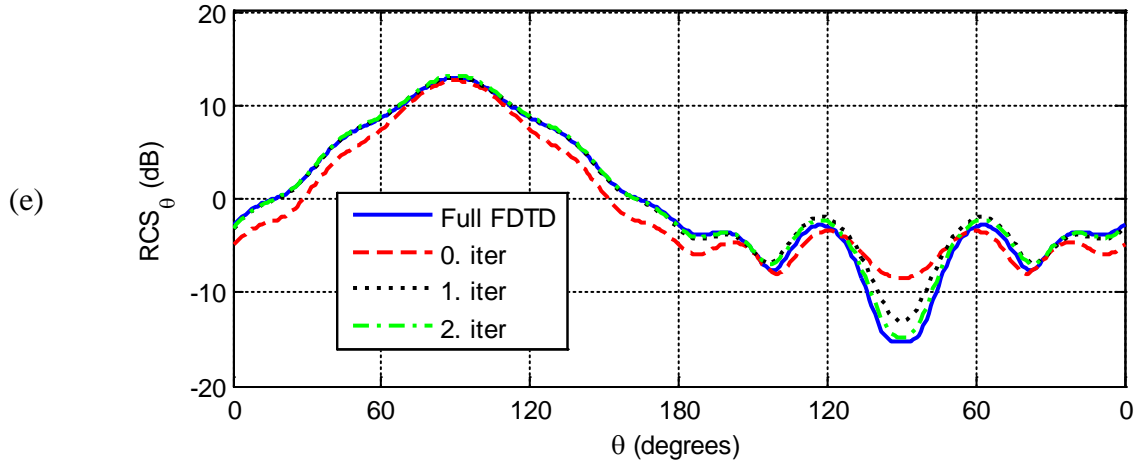
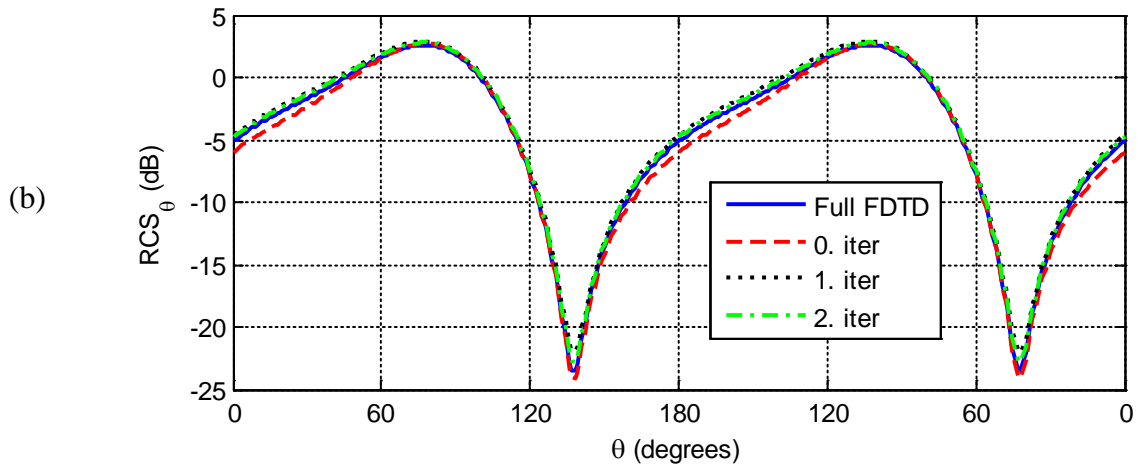
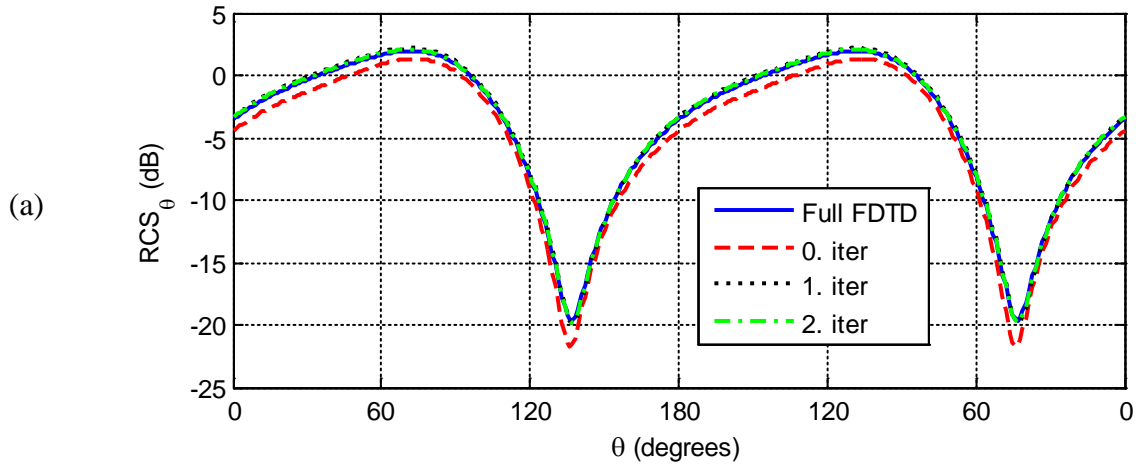


Figure 3.4: Bistatic RCS_θ for xz-plane cuts at frequencies: a) 200 MHz, b) 225 MHz, c) 250 MHz, d) 275 MHz, and e) 300 MHz.



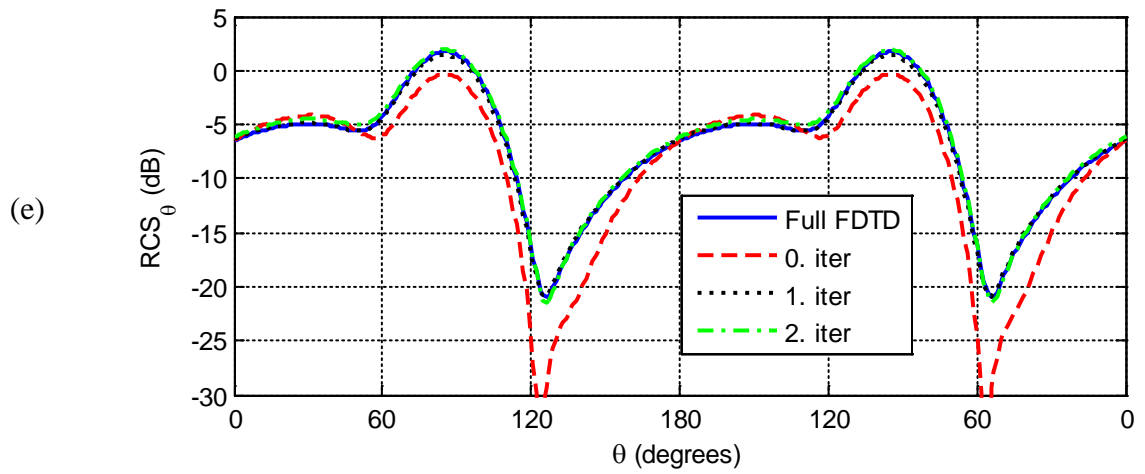
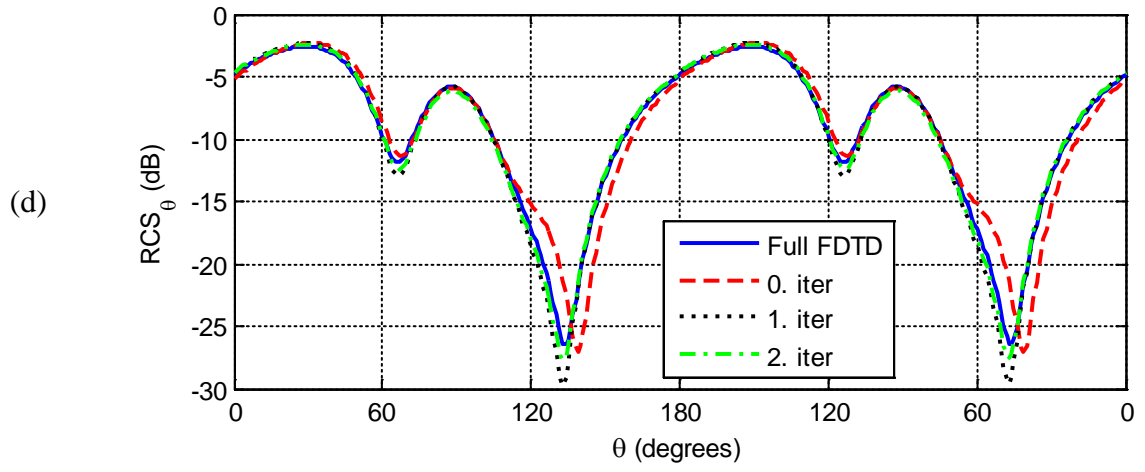
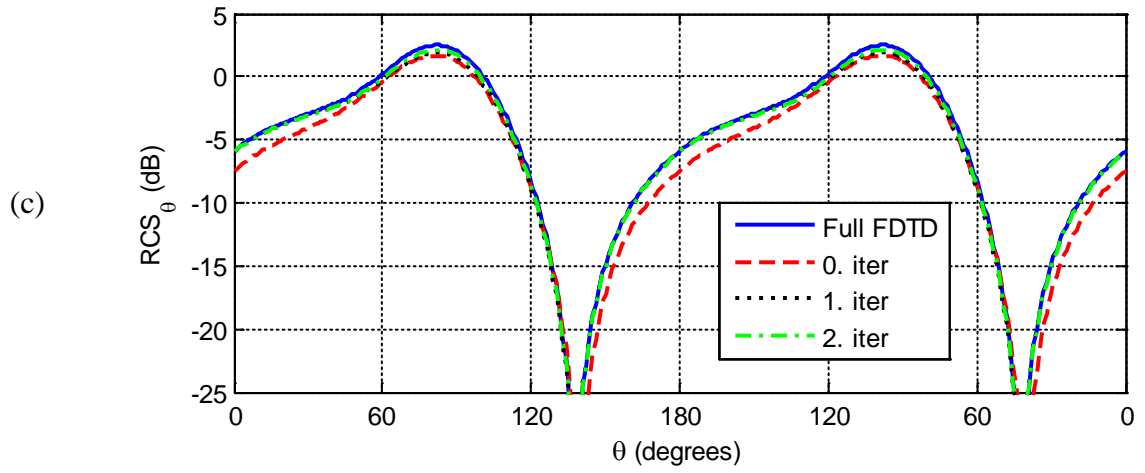
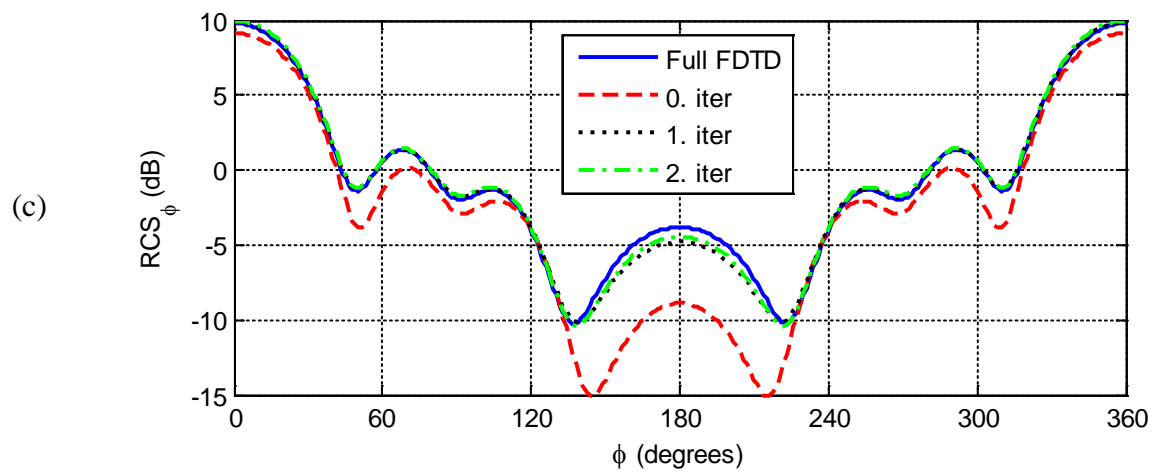
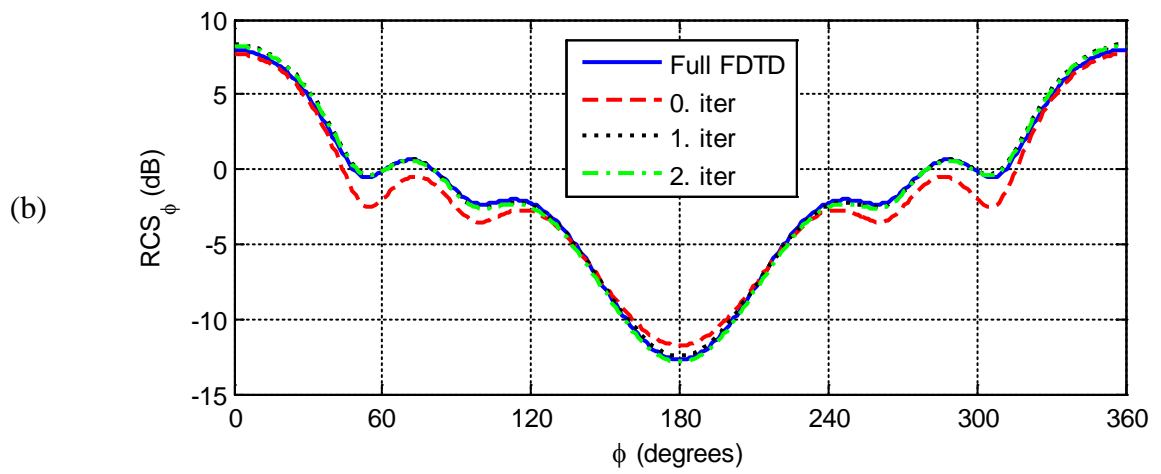
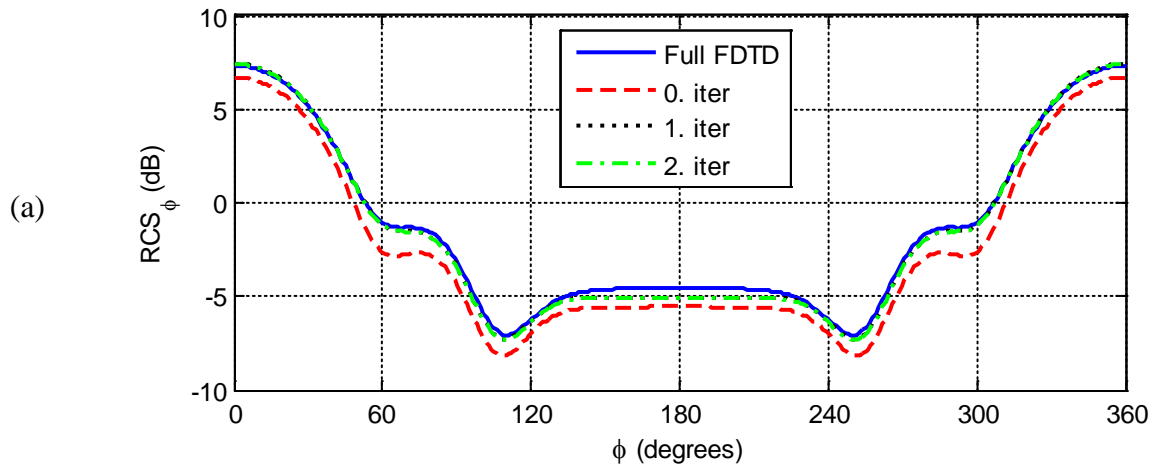


Figure 3.5: Bistatic RCS_{θ} for yz -plane cuts at frequencies: a) 200 MHz, b) 225 MHz, c) 250 MHz, d) 275 MHz, and e) 300 MHz.



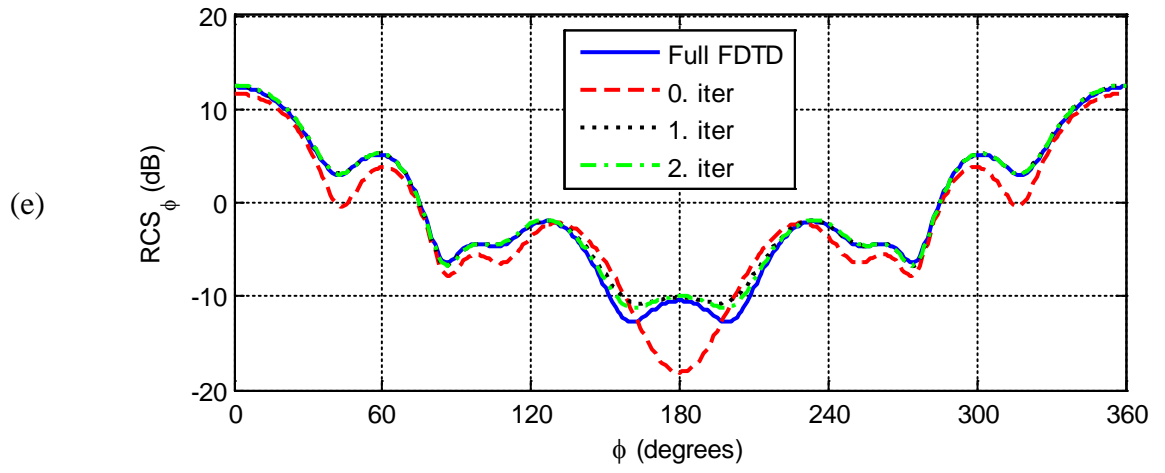
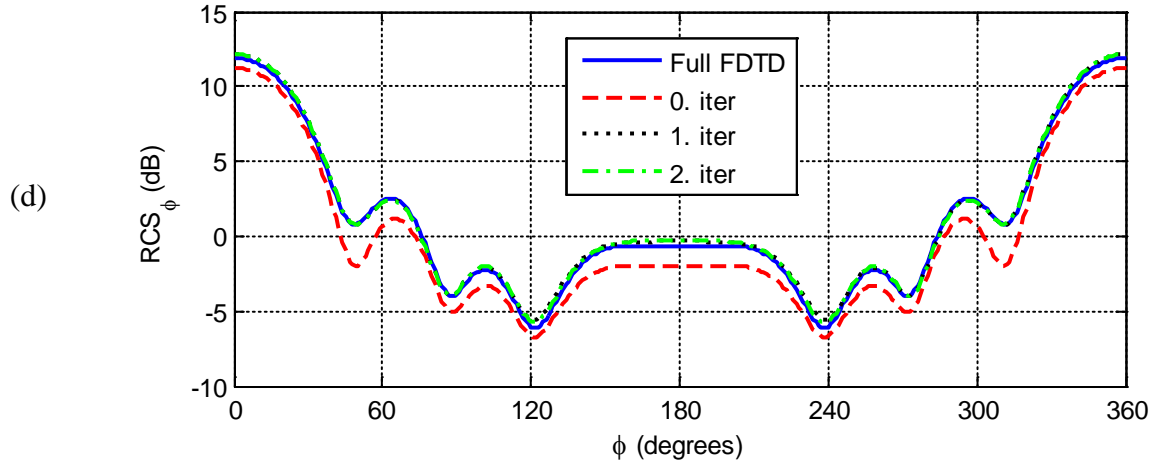
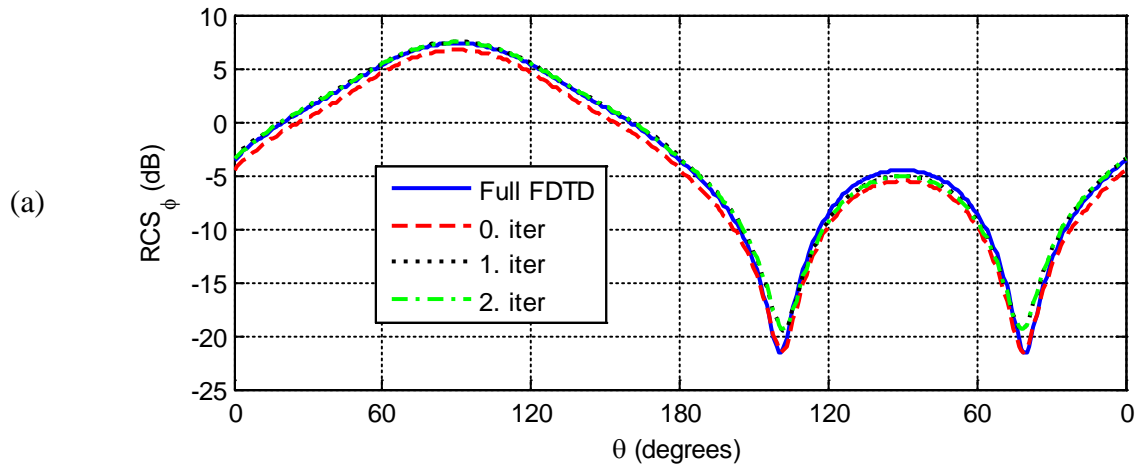
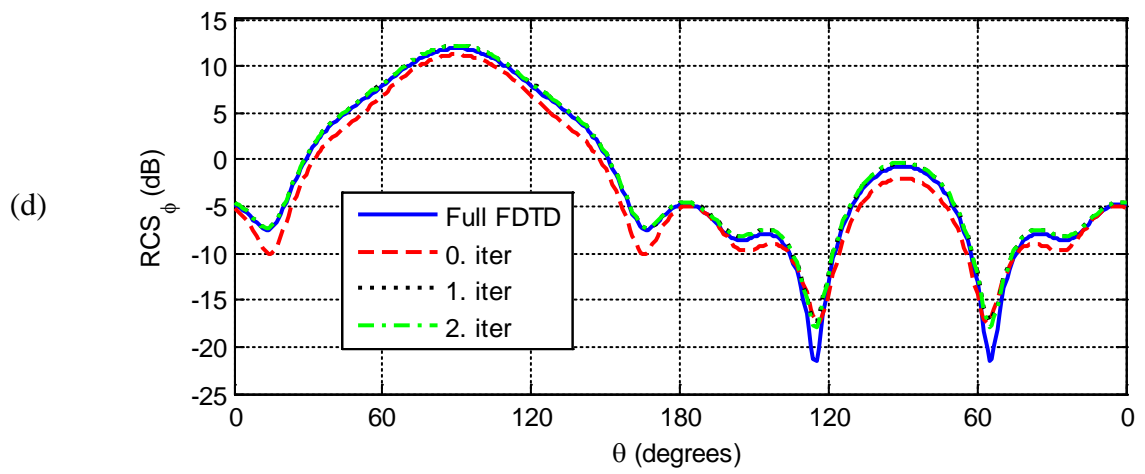
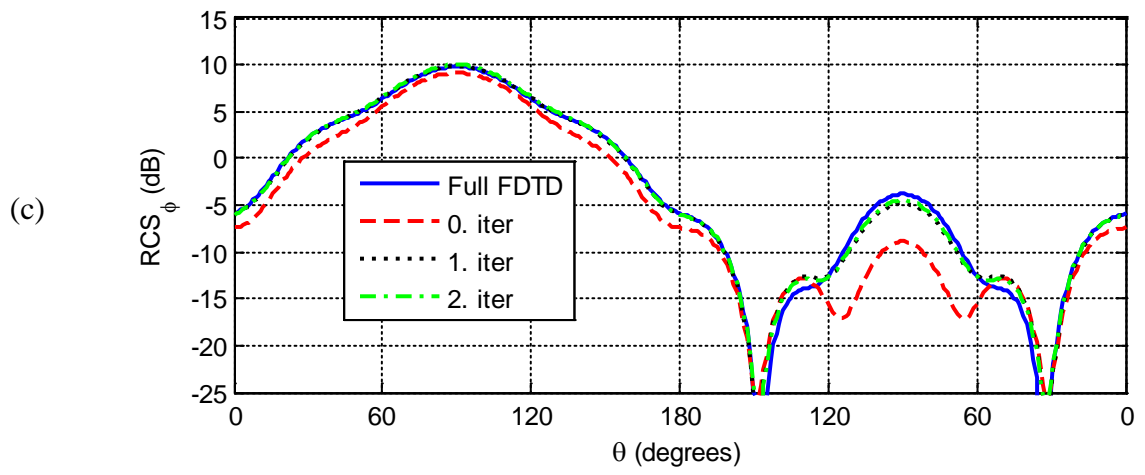
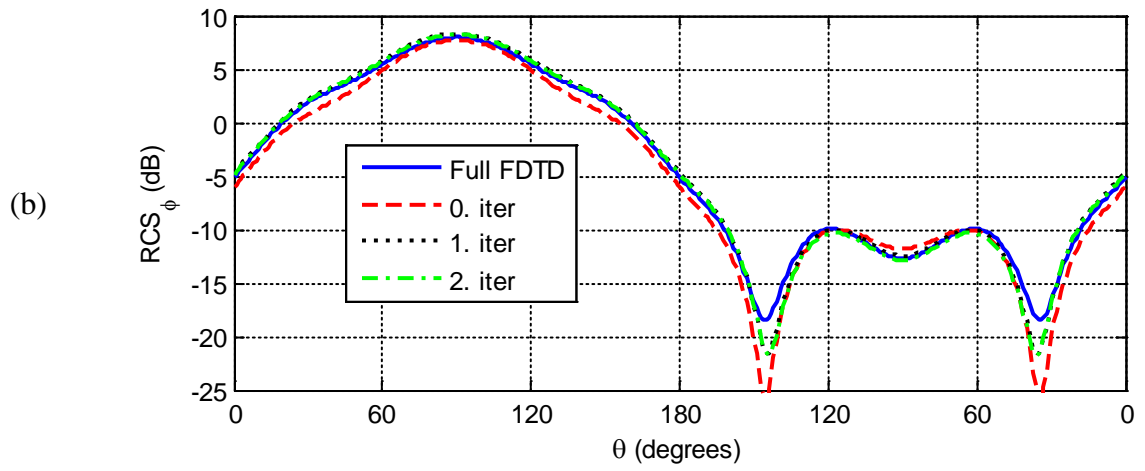


Figure 3.6: Bistatic RCS_φ for xy -plane cuts at frequencies: a) 200 MHz, b) 225 MHz, c) 250 MHz, d) 275 MHz, and e) 300 MHz.





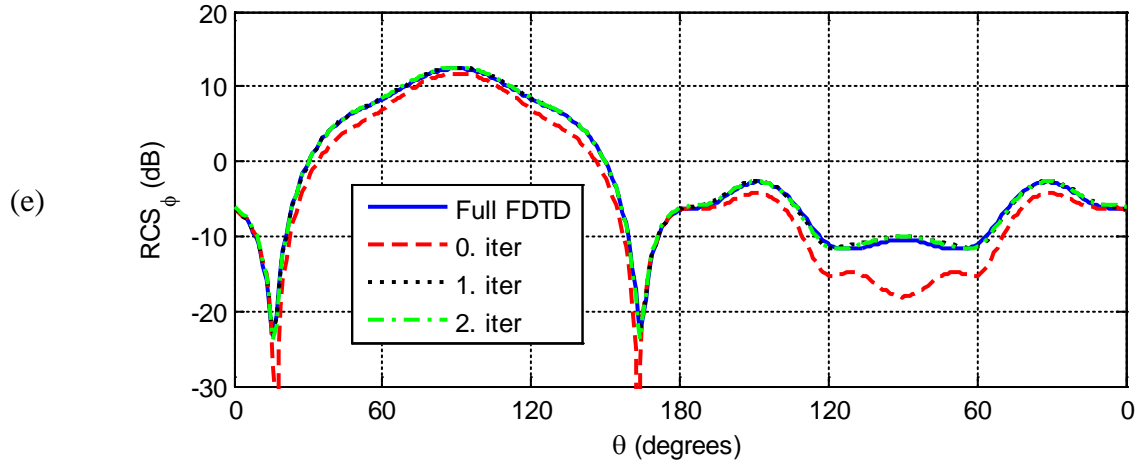
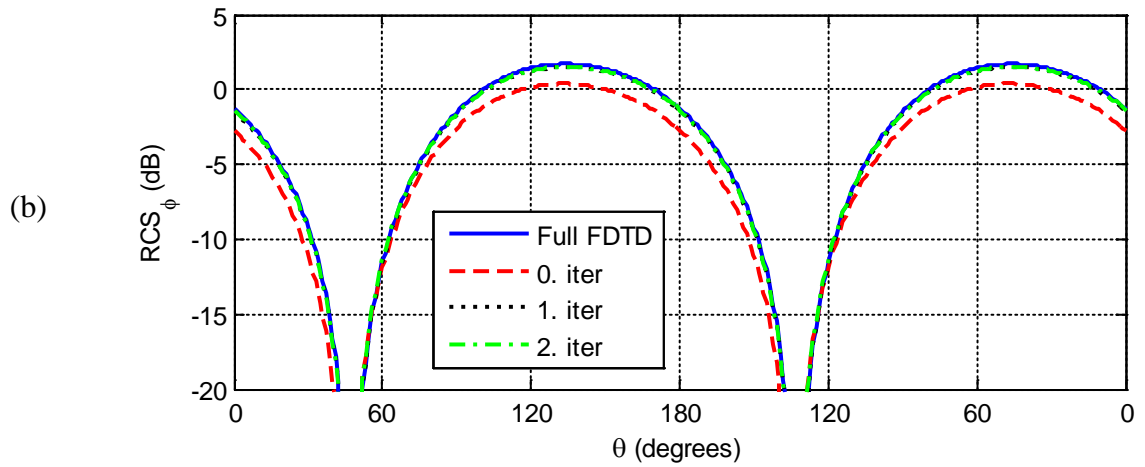
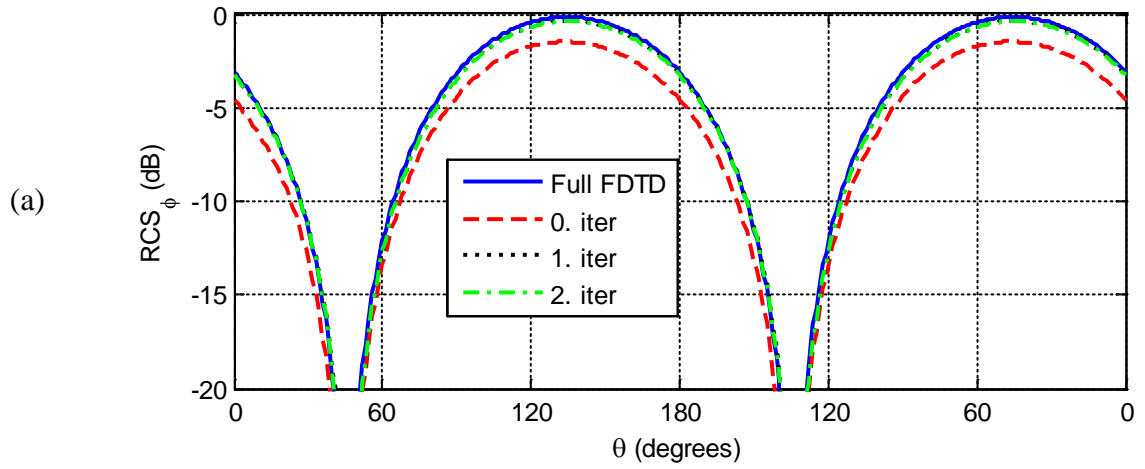


Figure 3.7: Bistatic RCS_{ϕ} for xz -plane cuts at frequencies: a) 200 MHz, b) 225 MHz, c) 250 MHz, d) 275 MHz, and e) 300 MHz.



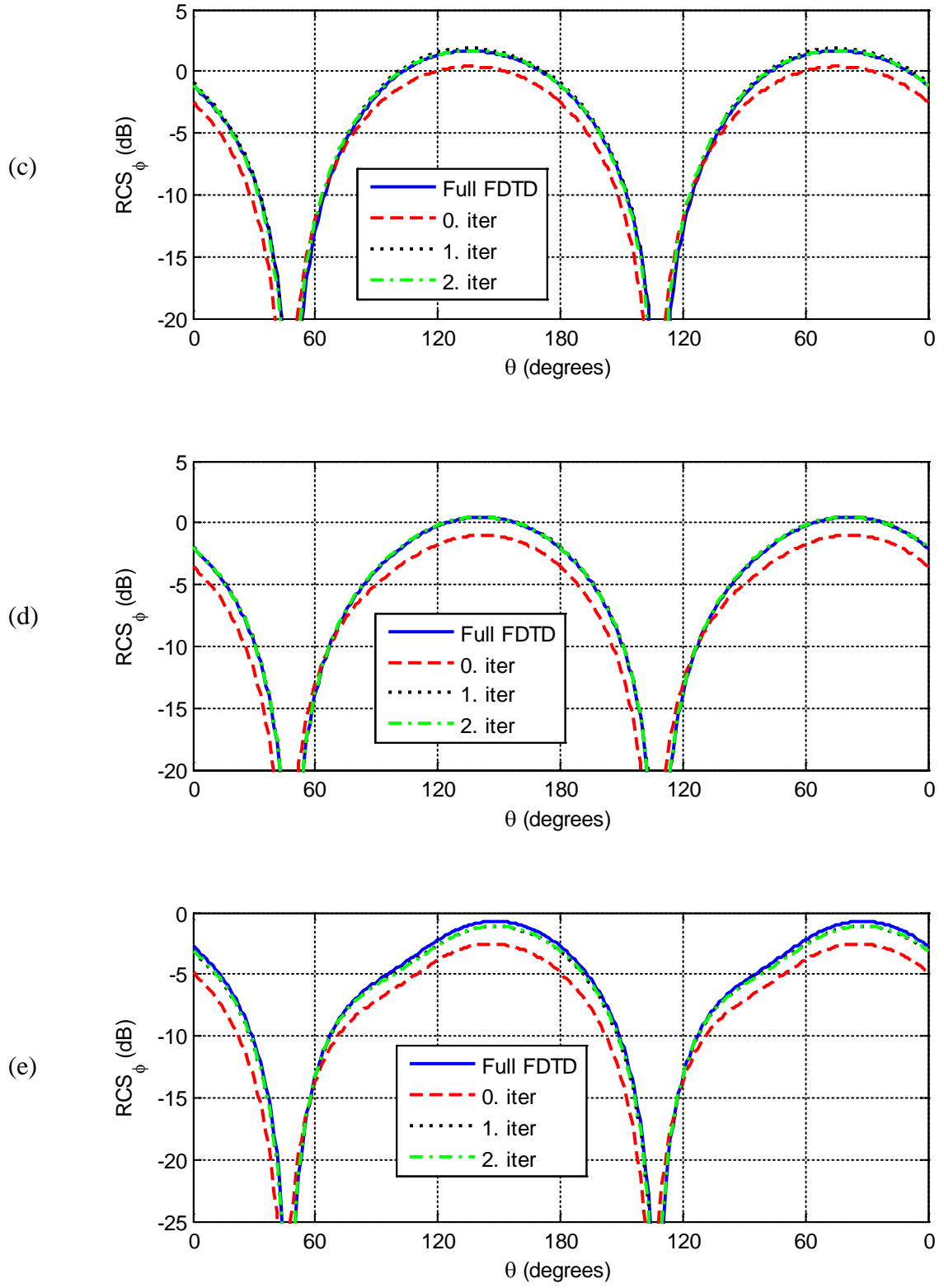


Figure 3.8: Bistatic RCS_ϕ for yz-plane cuts at frequencies: a) 200 MHz, b) 225 MHz, c) 250 MHz, d) 275 MHz, and e) 300 MHz.

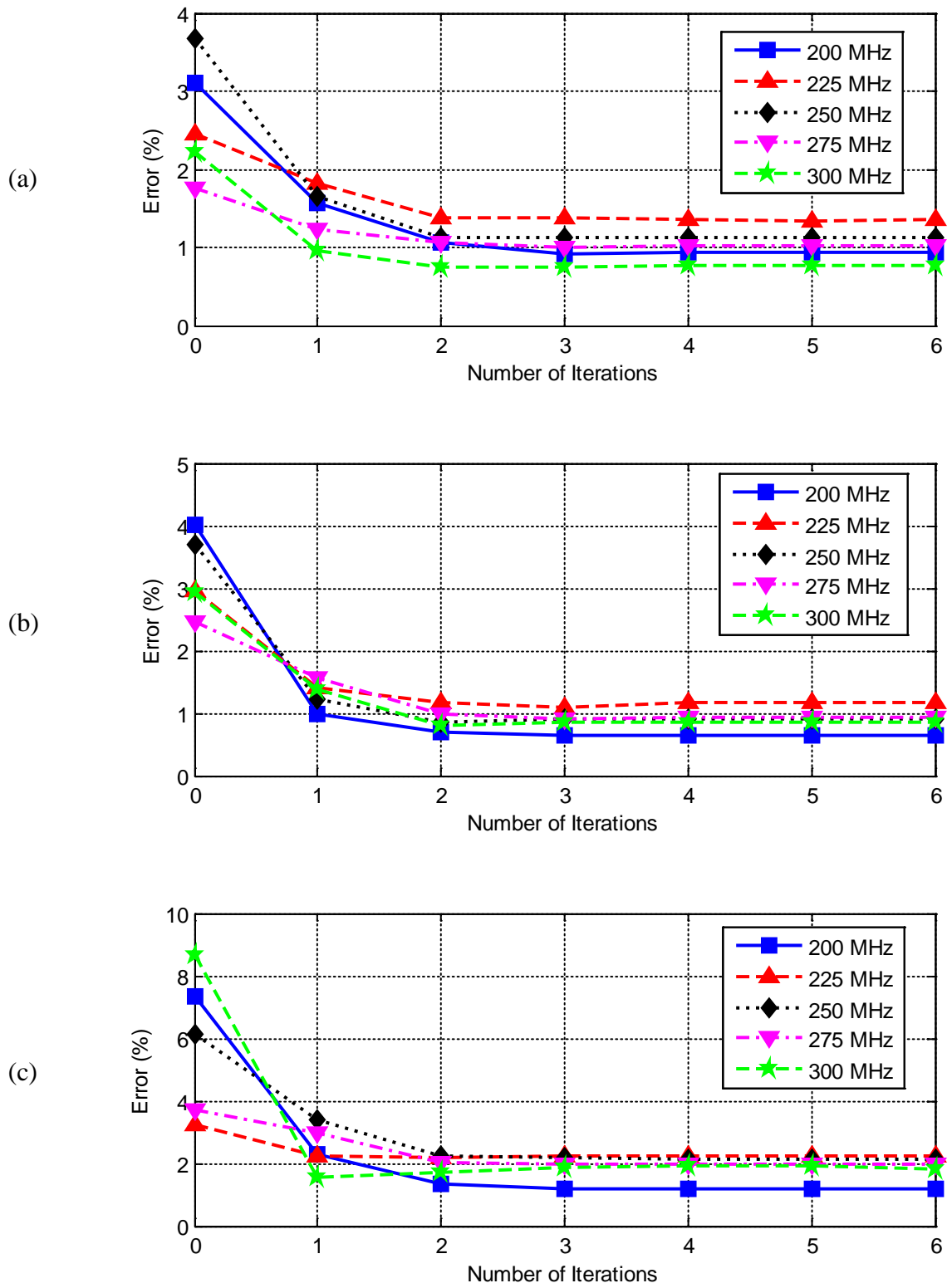


Figure 3.9: Normalized average errors for RCS_0 in the three plane cuts: a) xy -plane, b) xz -plane, and c) yz -plane.

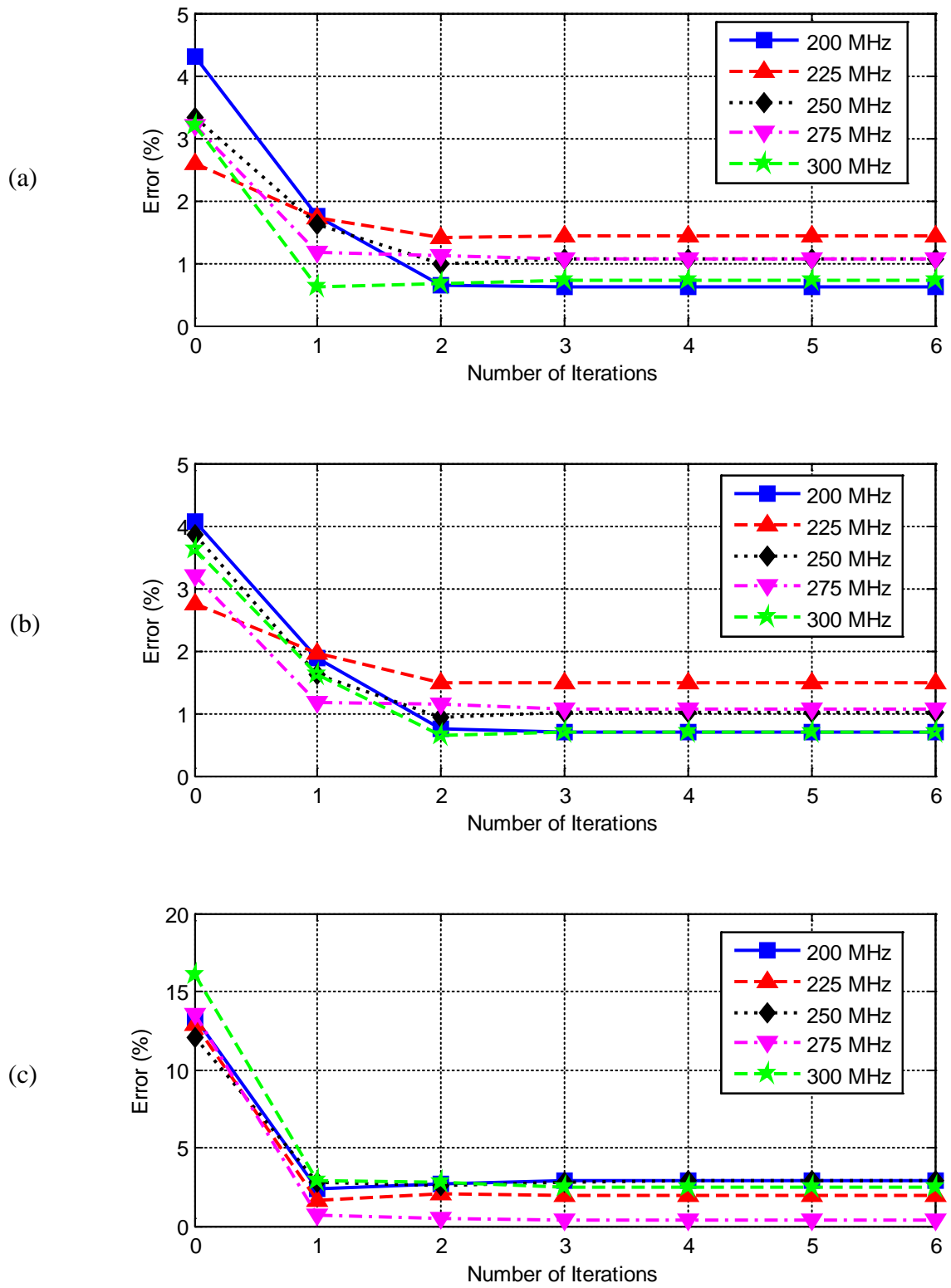


Figure 3.10: Normalized average errors for RCS_{ϕ} in the three plane cuts: a) xy -plane, b) xz -plane, and c) yz -plane.

3.2 Electromagnetic Scattering from Two Objects-2

The geometry of the second problem illustrated in Figure 3.11 is excited by a ϕ and θ polarized plane wave with $\theta^{\text{inc}}=90^\circ$ and $\phi^{\text{inc}}=90^\circ$ to obtain RCS at 200, 225, 250, 275, and 300 MHz. The separation between the dielectric ellipsoid and conducting rod is 0.5 m. The semi-axes of the dielectric ellipsoid are 0.6 m, 0.4 m, and 0.4 m along the x , y , and z axes, respectively. The relative permittivity and permeability of the dielectric ellipsoid are 3 and 1, respectively. The dimensions of the conducting rod are 0.4 m, 0.4 m, and 2 m along the x , y , and z directions, respectively. The problem space is composed of cells with size 0.02 m in the x , y , and z directions for the full domain simulation. As for the IMR simulation, a cell size 0.02 m is used in the subregion of the rod, whereas a cell size 0.04 m is used in the subregion of the ellipsoid. It can be seen from Figure 3.12 that the IMR technique results converge to the full domain results after iteration # 2. Figures 3.13-3.18 show the bistatic RCS_θ and RCS_ϕ for the xy , xz , and yz plane cuts at each frequency. Good agreement between the IMR solution and the full domain solution is achieved. To prove the convergence of the full domain and IMR technique results, the normalized average errors for RCS_θ and RCS_ϕ in the three plane cuts are shown in Figures 3.19-3.20. Simulation parameters and computer resources used are summarized in Table 3-2 for the full domain solution and the IMR solution. Results show a considerable reduction in the memory storage requirements, but there is no significant change in the computation time. The computation time would be less and the memory gain would be more for problems that have large separation between the objects.

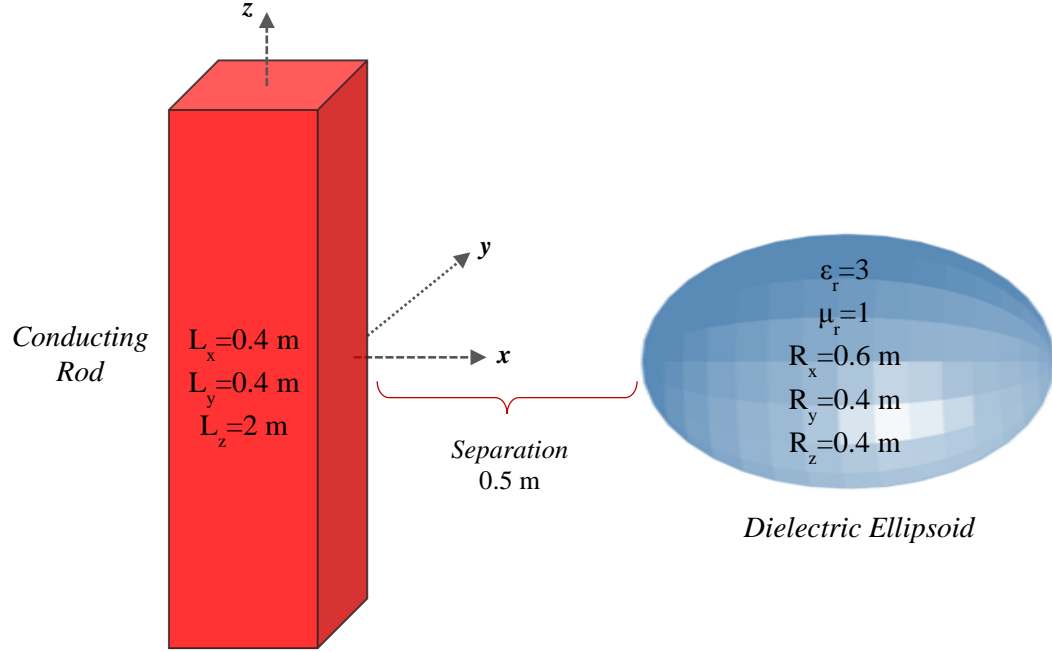


Figure 3.11: Geometry of the second problem.

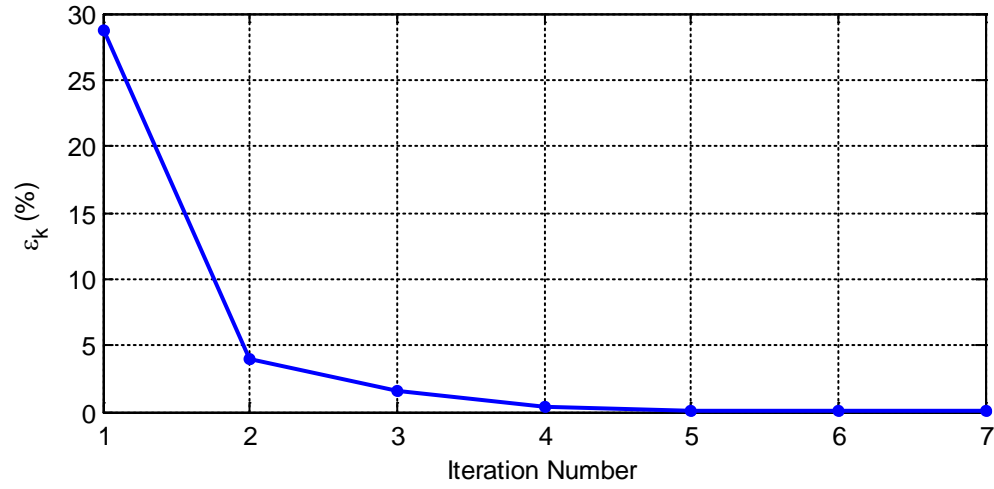
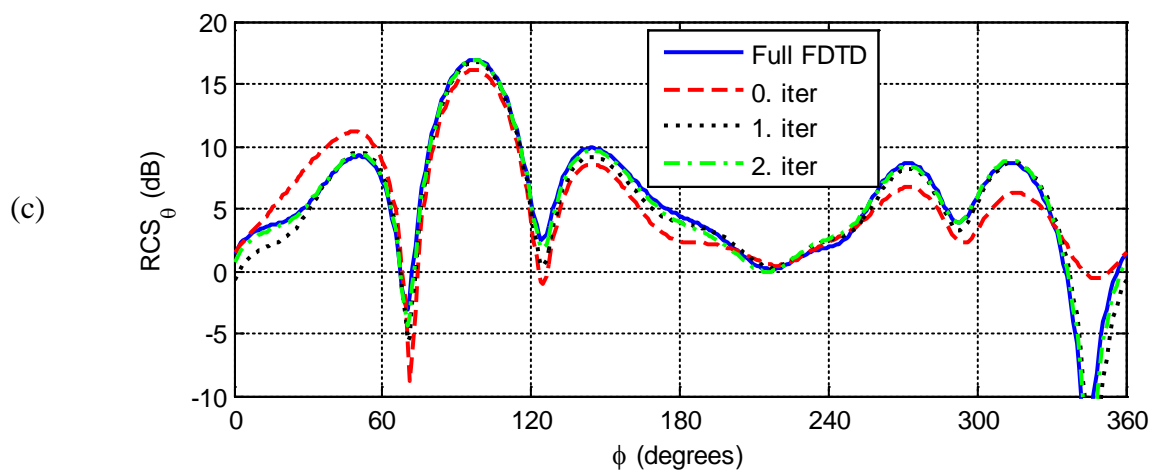
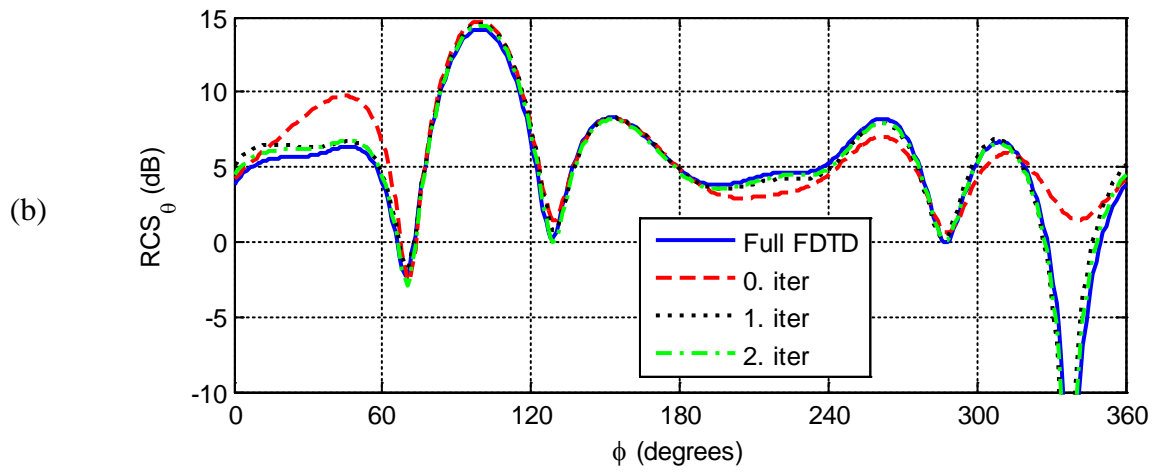
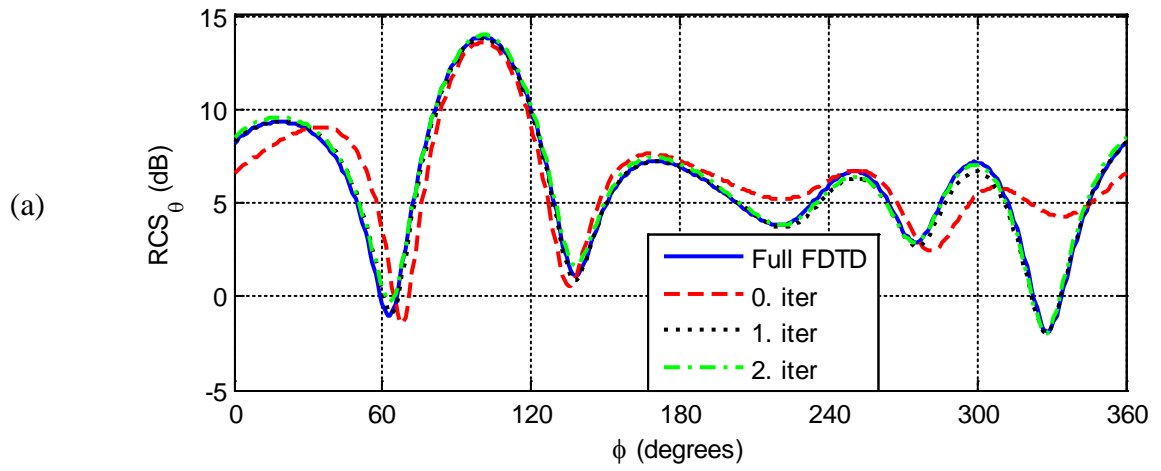


Figure 3.12: Convergence (ϵ_k) between iteration steps for the second problem.

Table 3-2: Simulation parameters and computer resources used by the IMR and full domain simulation.

| | Number of Domains | Total Number of Cells | Computation Time (min.) | Iteration Number | Memory (MB) |
|------------------|-------------------|-----------------------|-------------------------|------------------|-------------|
| Full FDTD | — | 1,457,376 | 39 | — | 995 |
| IMR-FDTD | 2 | 633,472 | 42 | 2 | 420 |



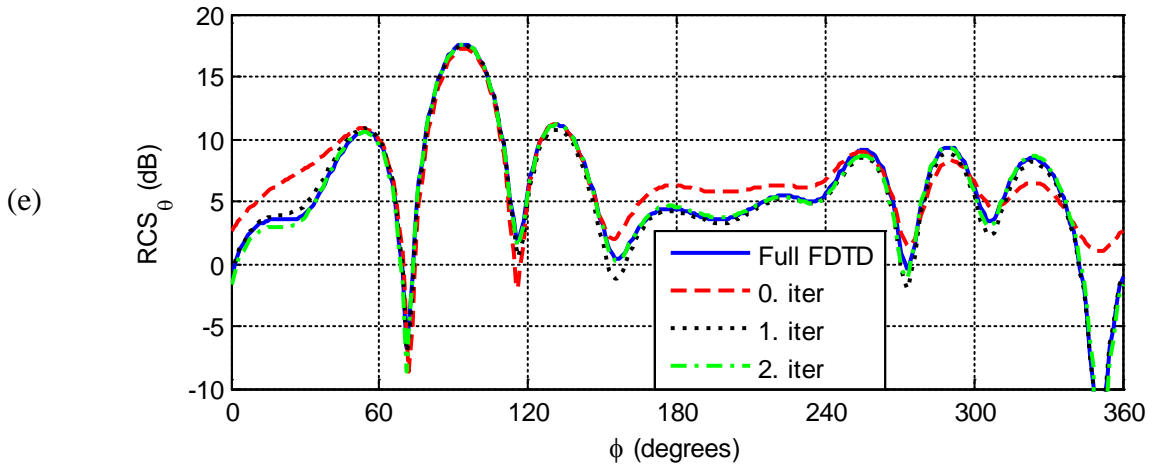
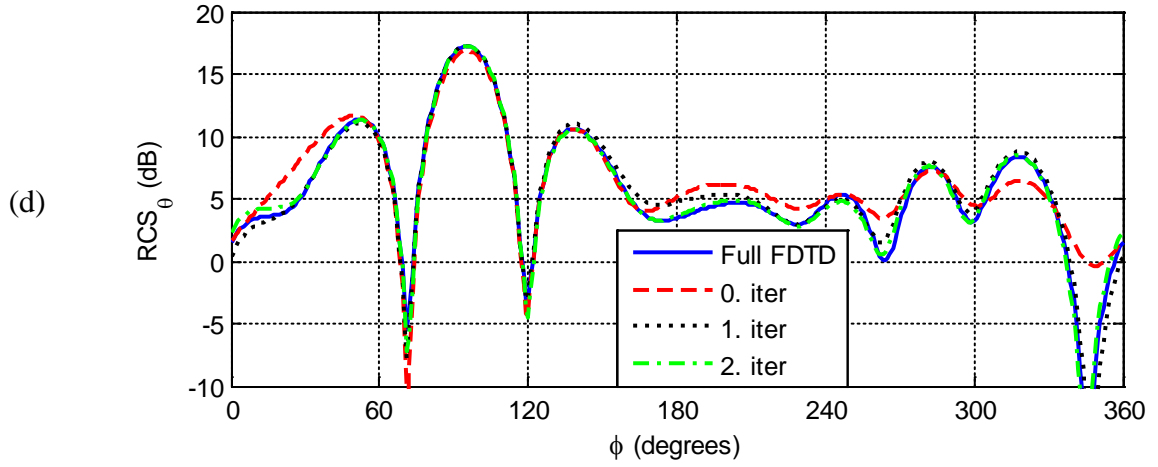
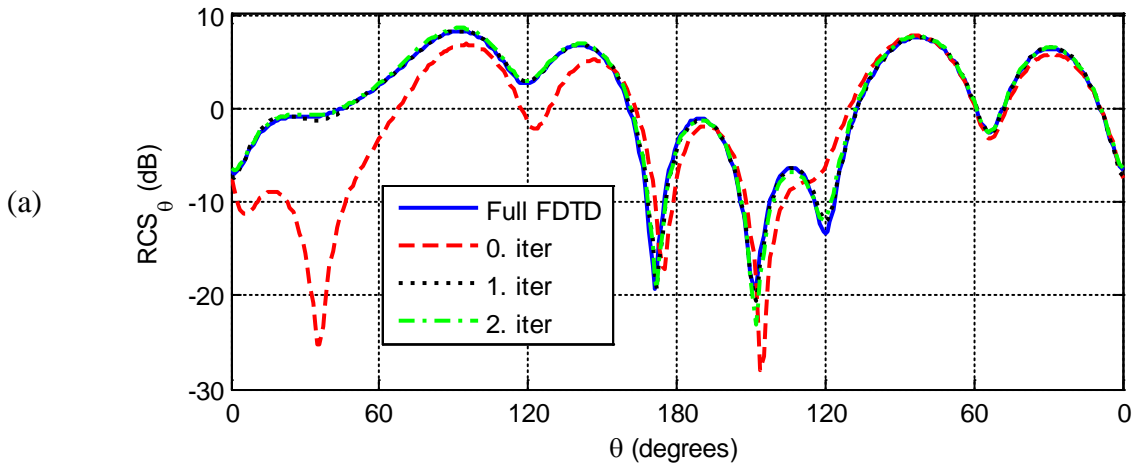
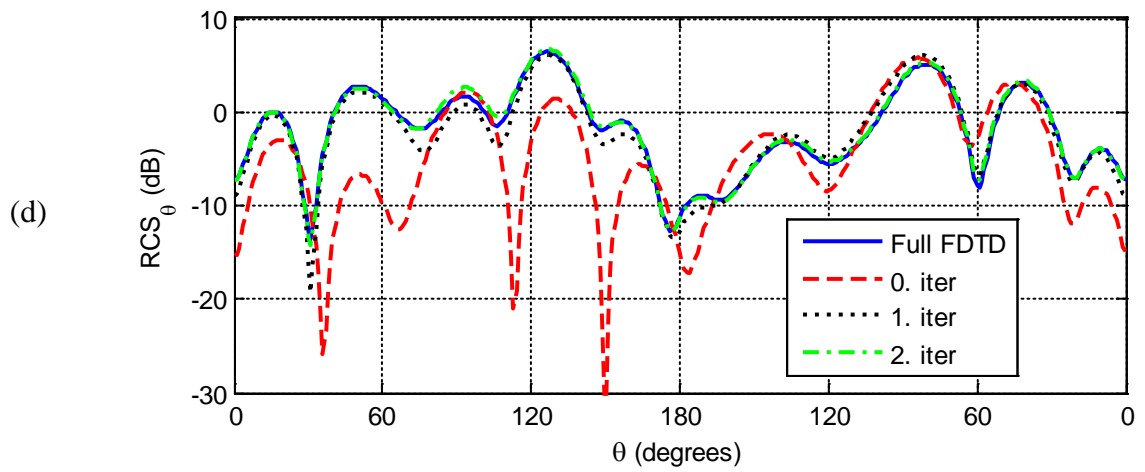
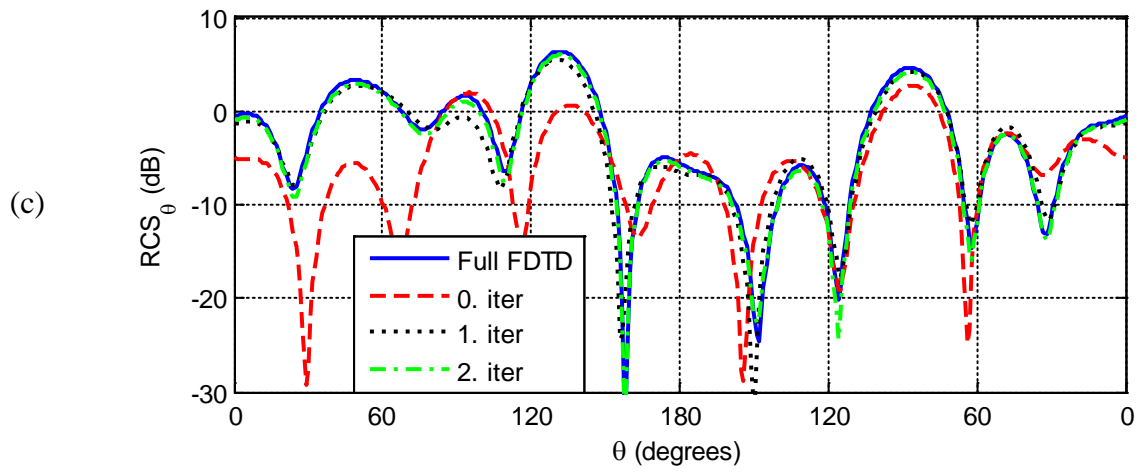
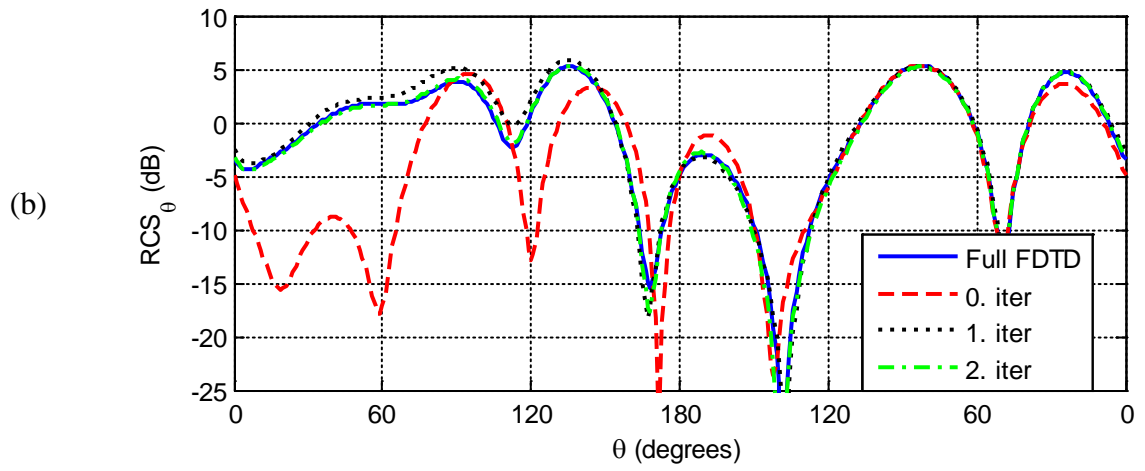


Figure 3.13: Bistatic RCS_θ for *xy*-plane cuts at frequencies: a) 200 MHz, b) 225 MHz, c) 250 MHz, d) 275 MHz, and e) 300 MHz.





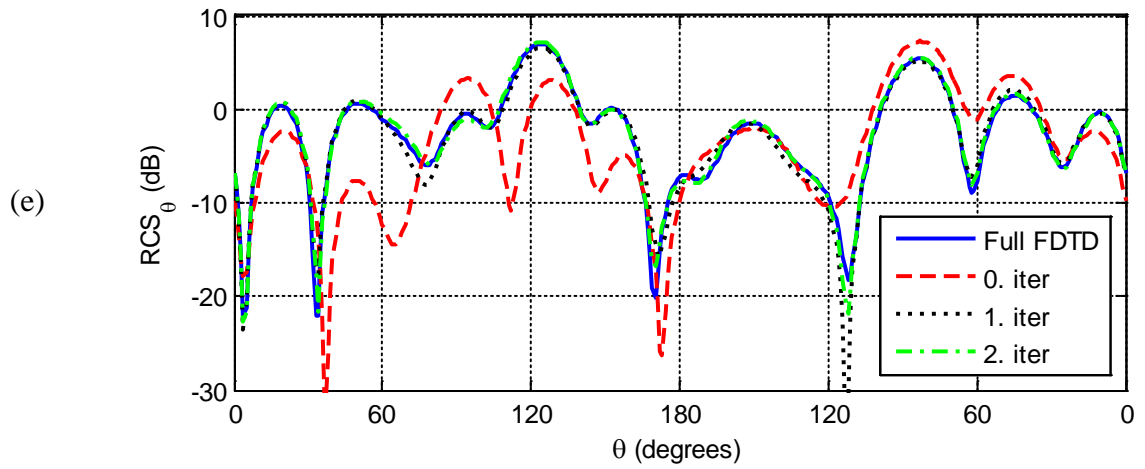
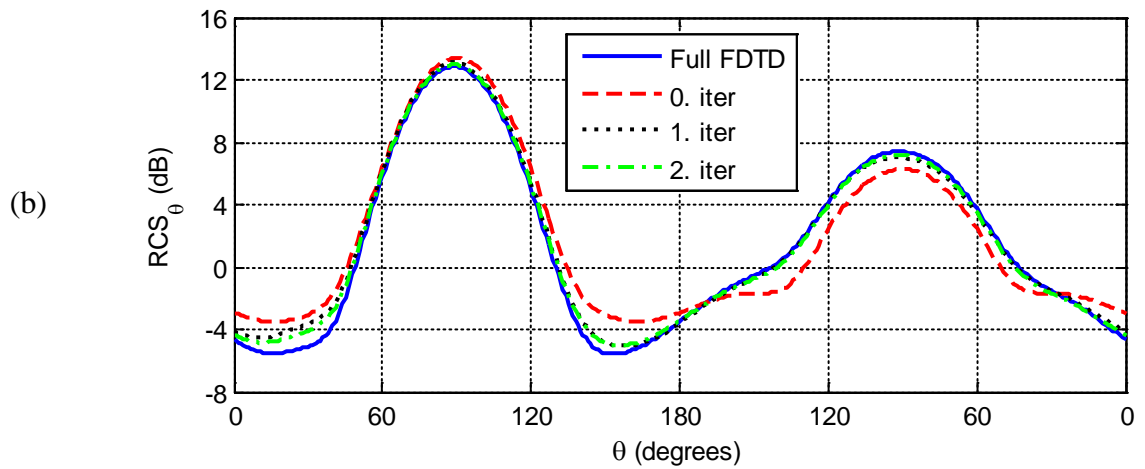
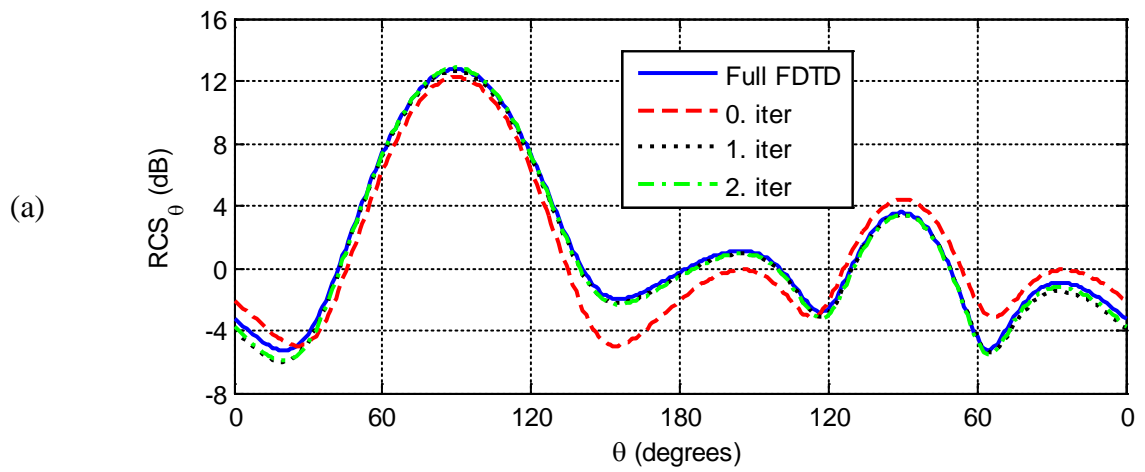


Figure 3.14: Bistatic RCS_{θ} for xz -plane cuts at frequencies: a) 200 MHz, b) 225 MHz, c) 250 MHz, d) 275 MHz, and e) 300 MHz.



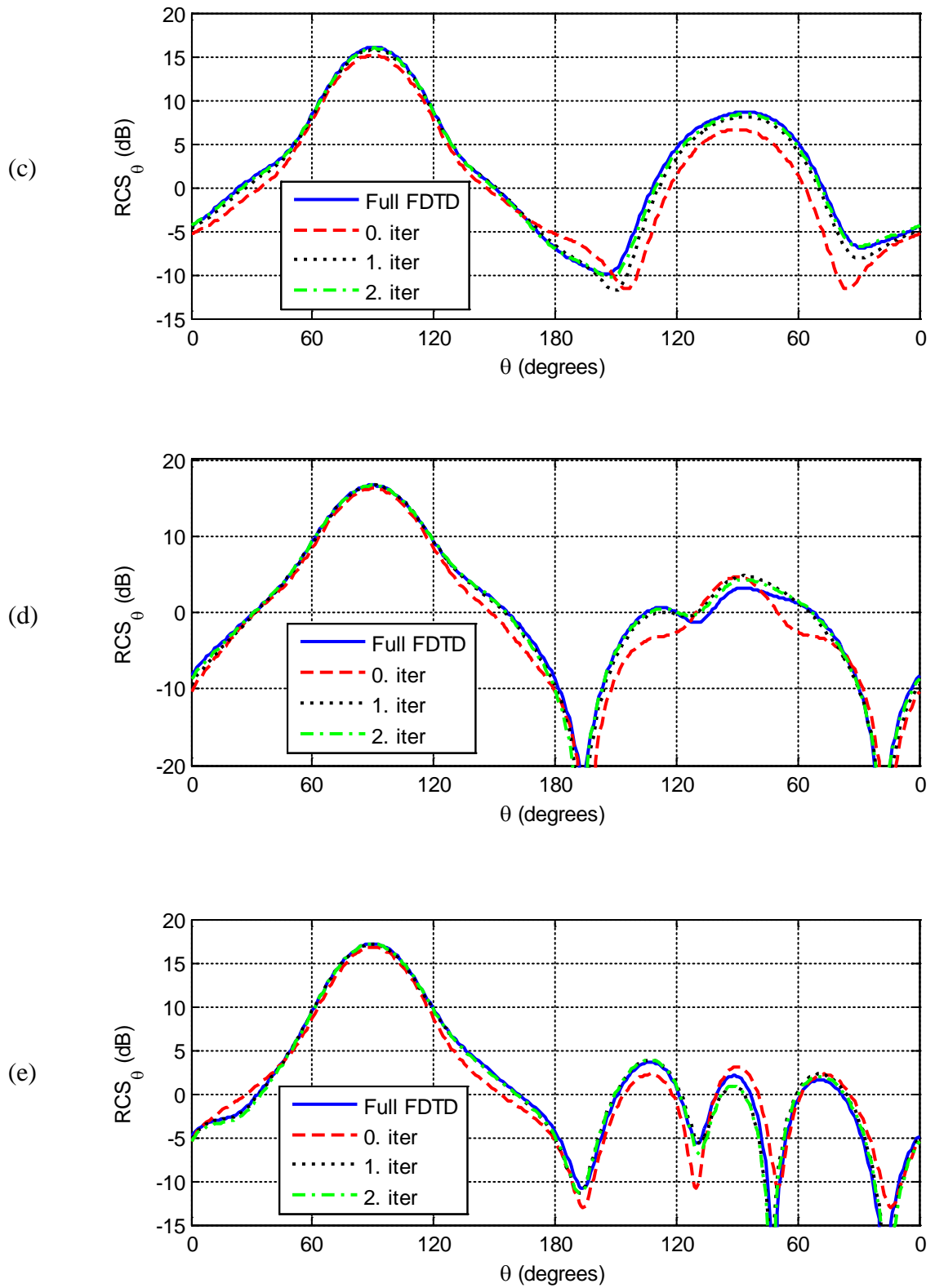
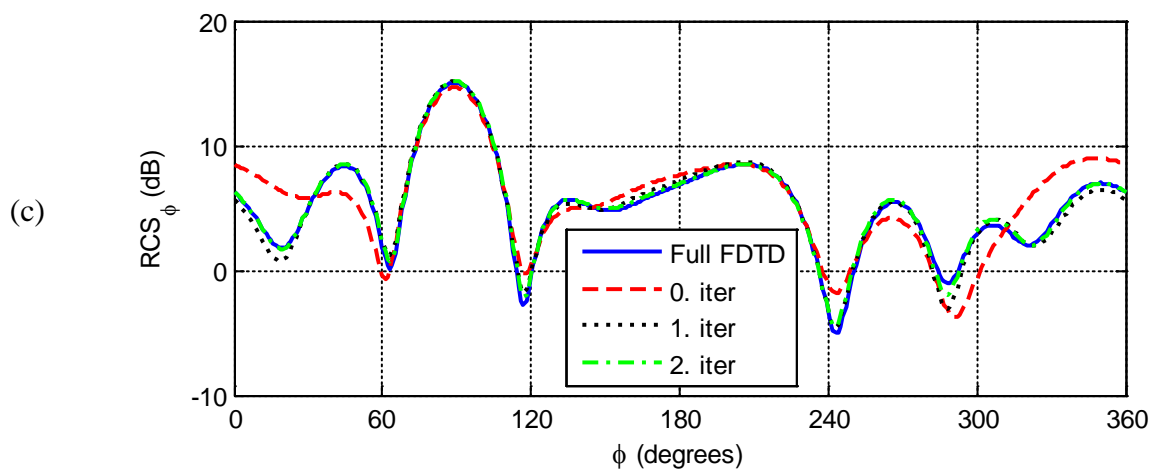
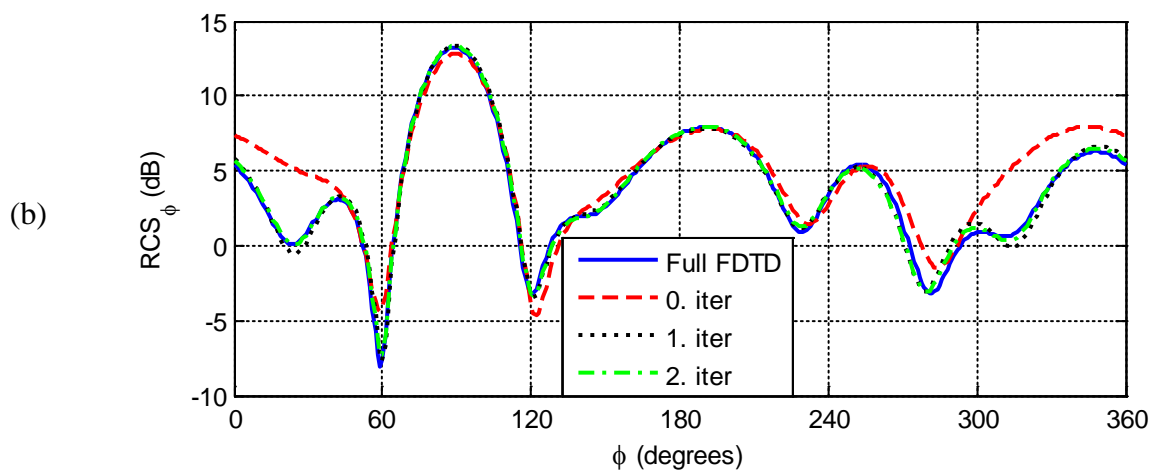
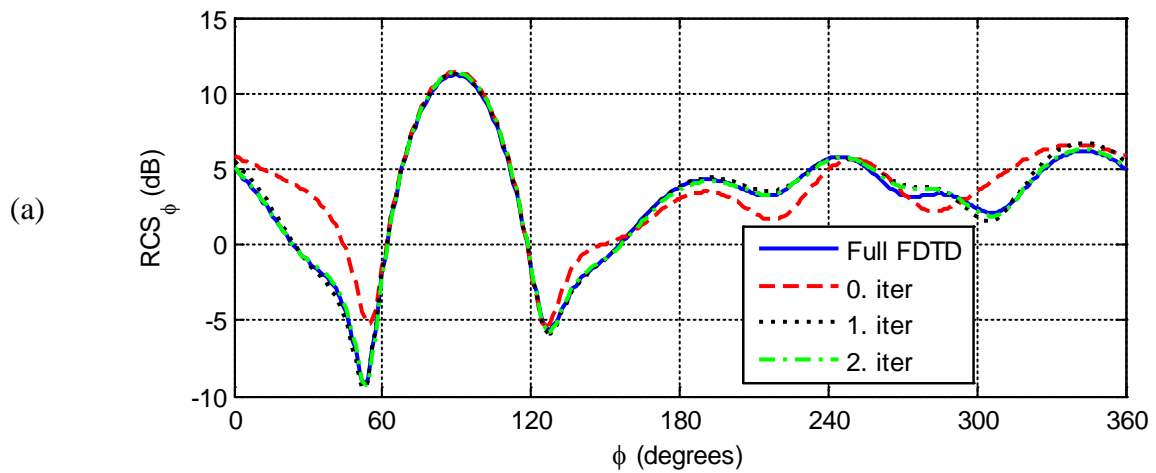


Figure 3.15: Bistatic RCS_{θ} for yz -plane cuts at frequencies: a) 200 MHz, b) 225 MHz, c) 250 MHz, d) 275 MHz, and e) 300 MHz.



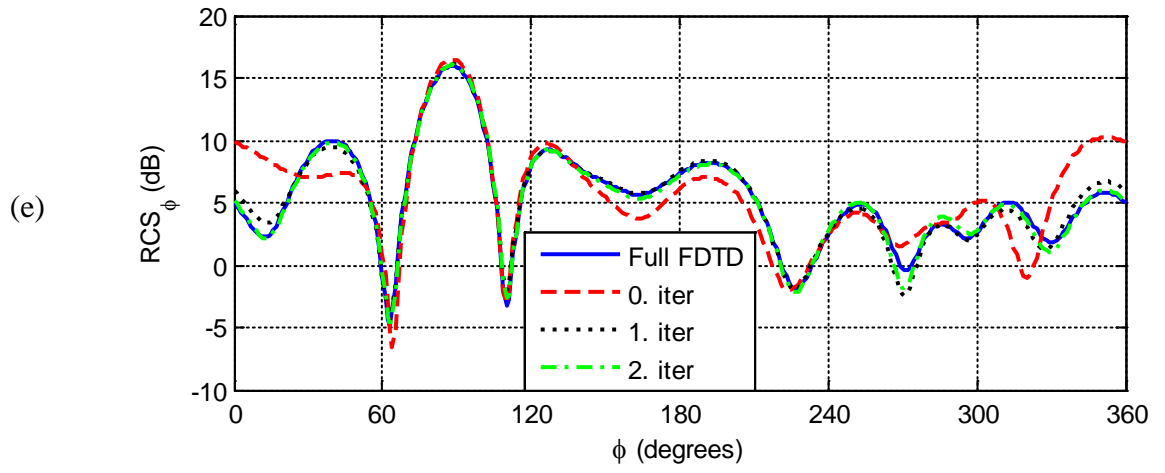
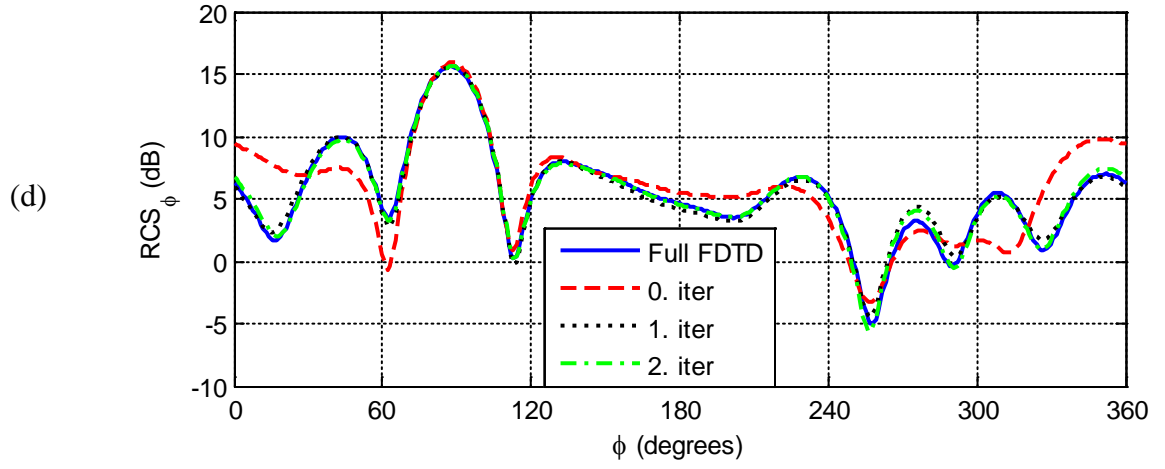
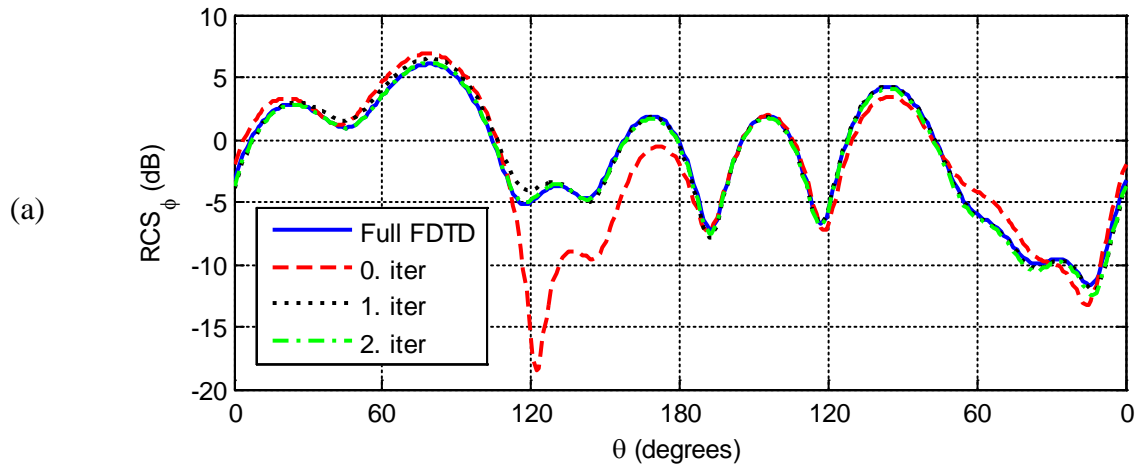
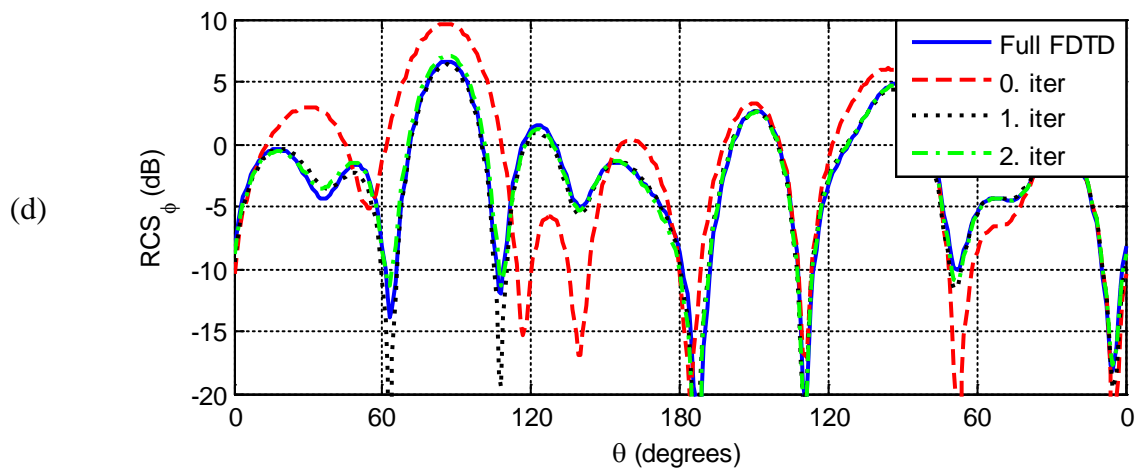
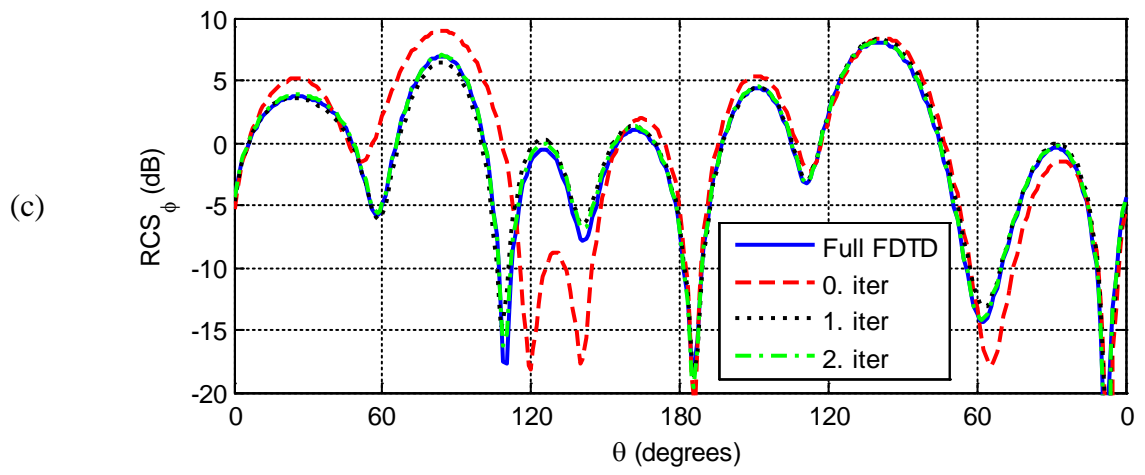
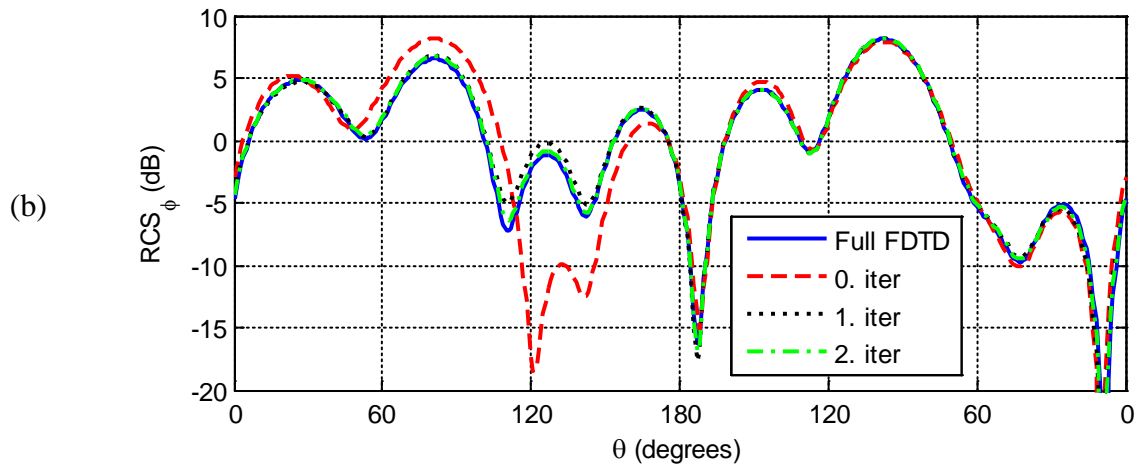


Figure 3.16: Bistatic RCS_{ϕ} for xy -plane cuts at frequencies: a) 200 MHz, b) 225 MHz, c) 250 MHz, d) 275 MHz, and e) 300 MHz.





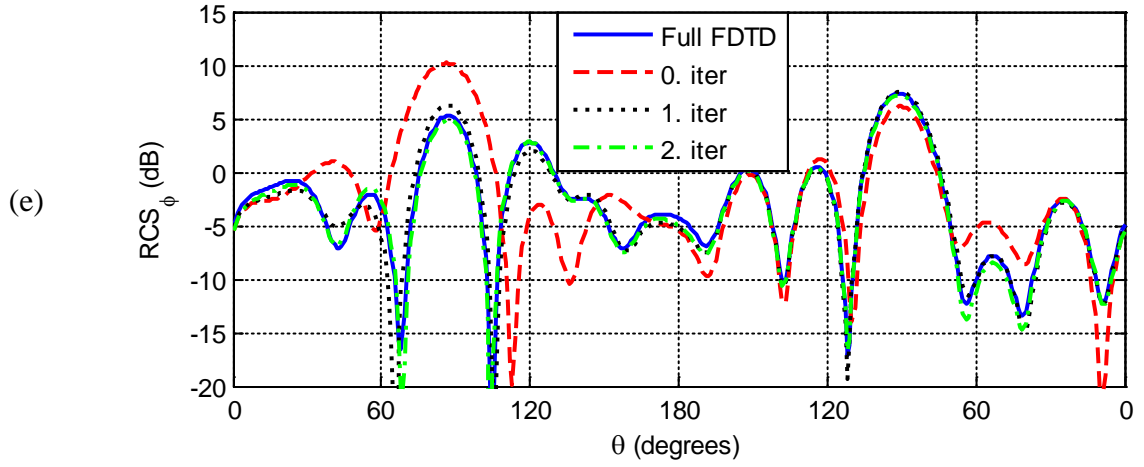
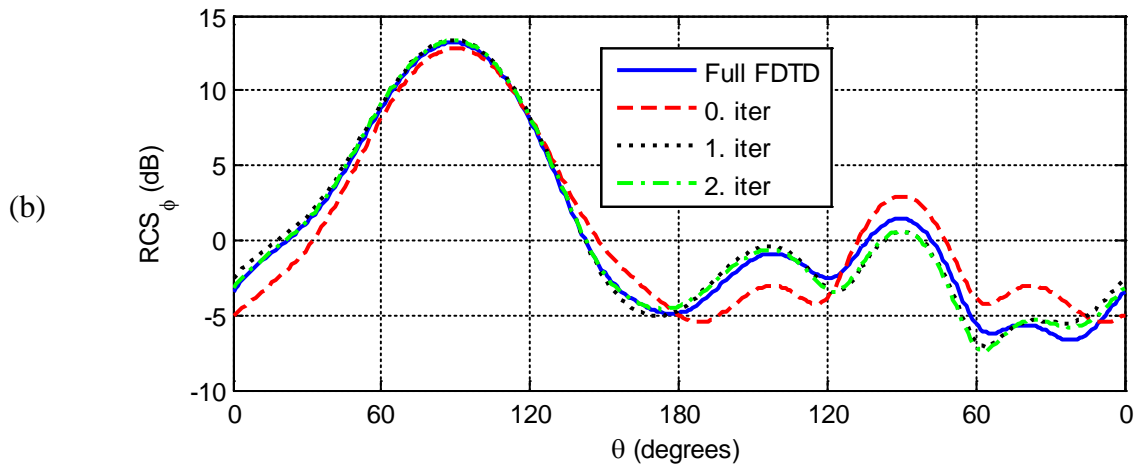
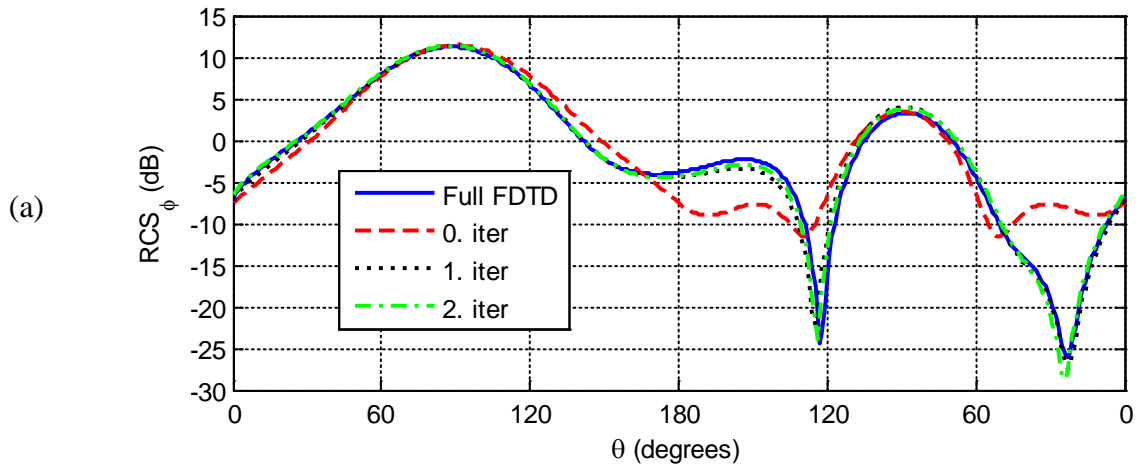


Figure 3.17: Bistatic RCS_φ for xz -plane cuts at frequencies: a) 200 MHz, b) 225 MHz, c) 250 MHz, d) 275 MHz, and e) 300 MHz.



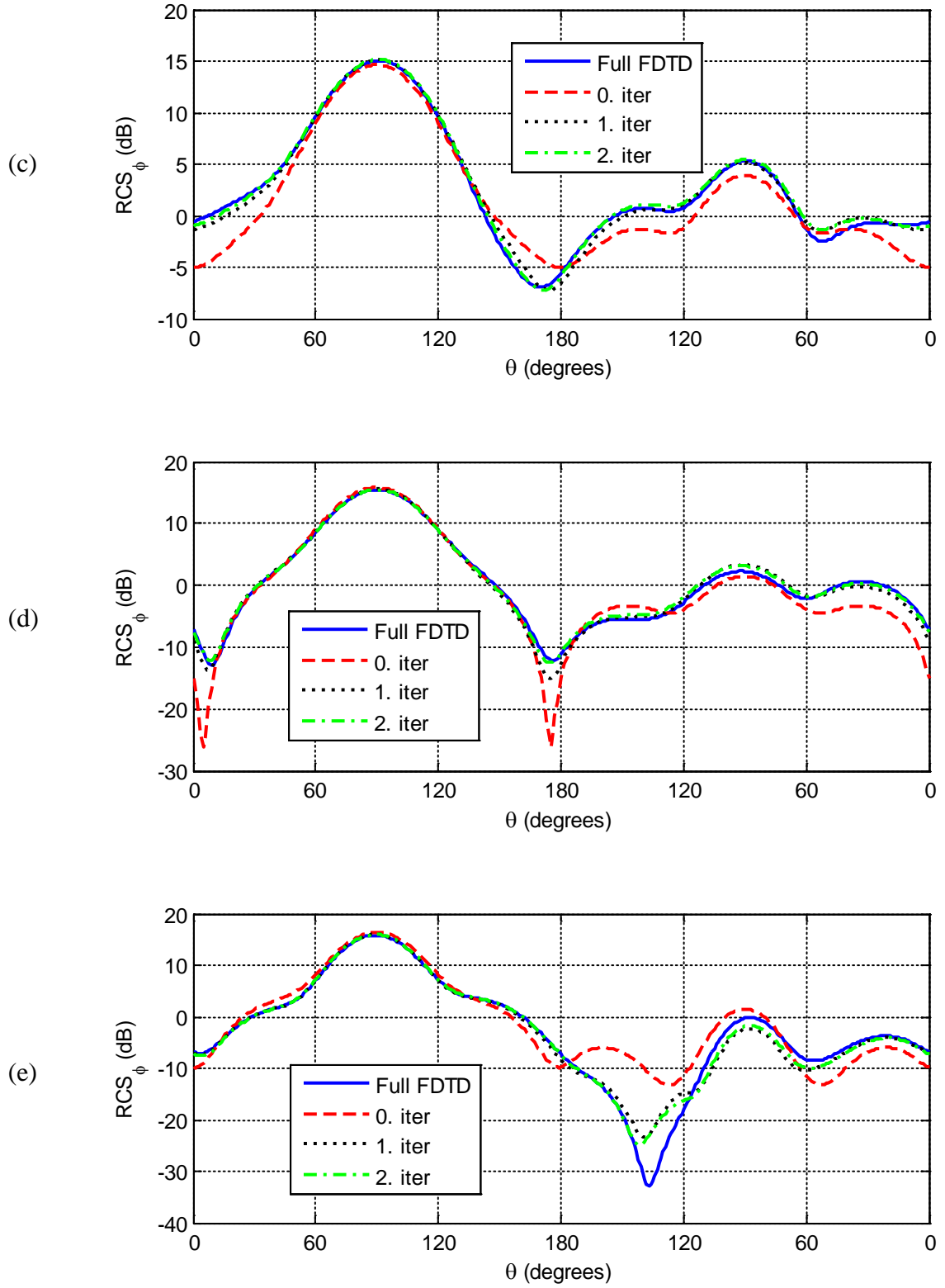


Figure 3.18: Bistatic RCS_ϕ for yz-plane cuts at frequencies: a) 200 MHz, b) 225 MHz, c) 250 MHz, d) 275 MHz, and e) 300 MHz.

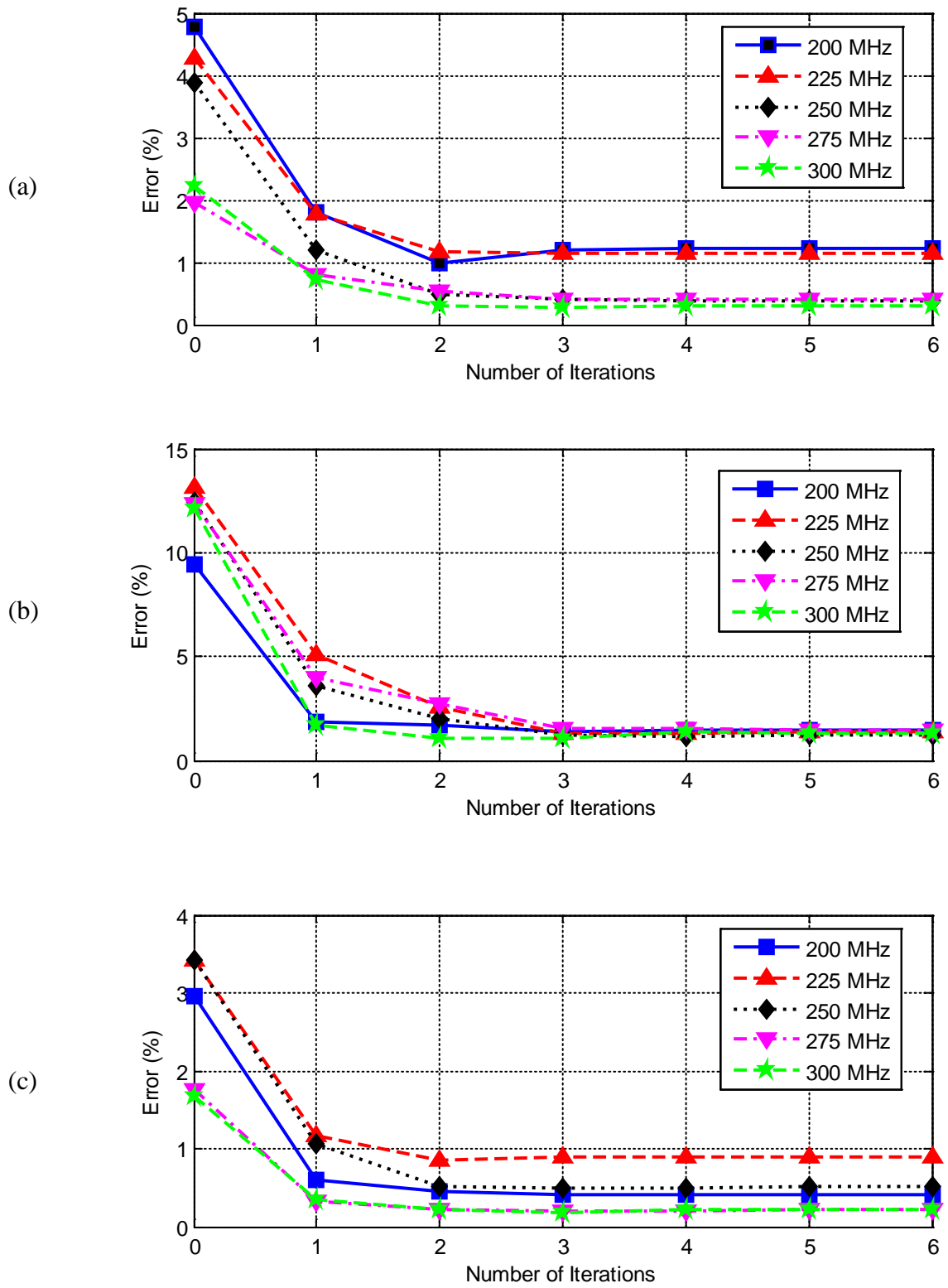


Figure 3.19: Normalized average errors for RCS_0 in the three plane cuts: a) xy -plane, b) xz -plane, and c) yz -plane.

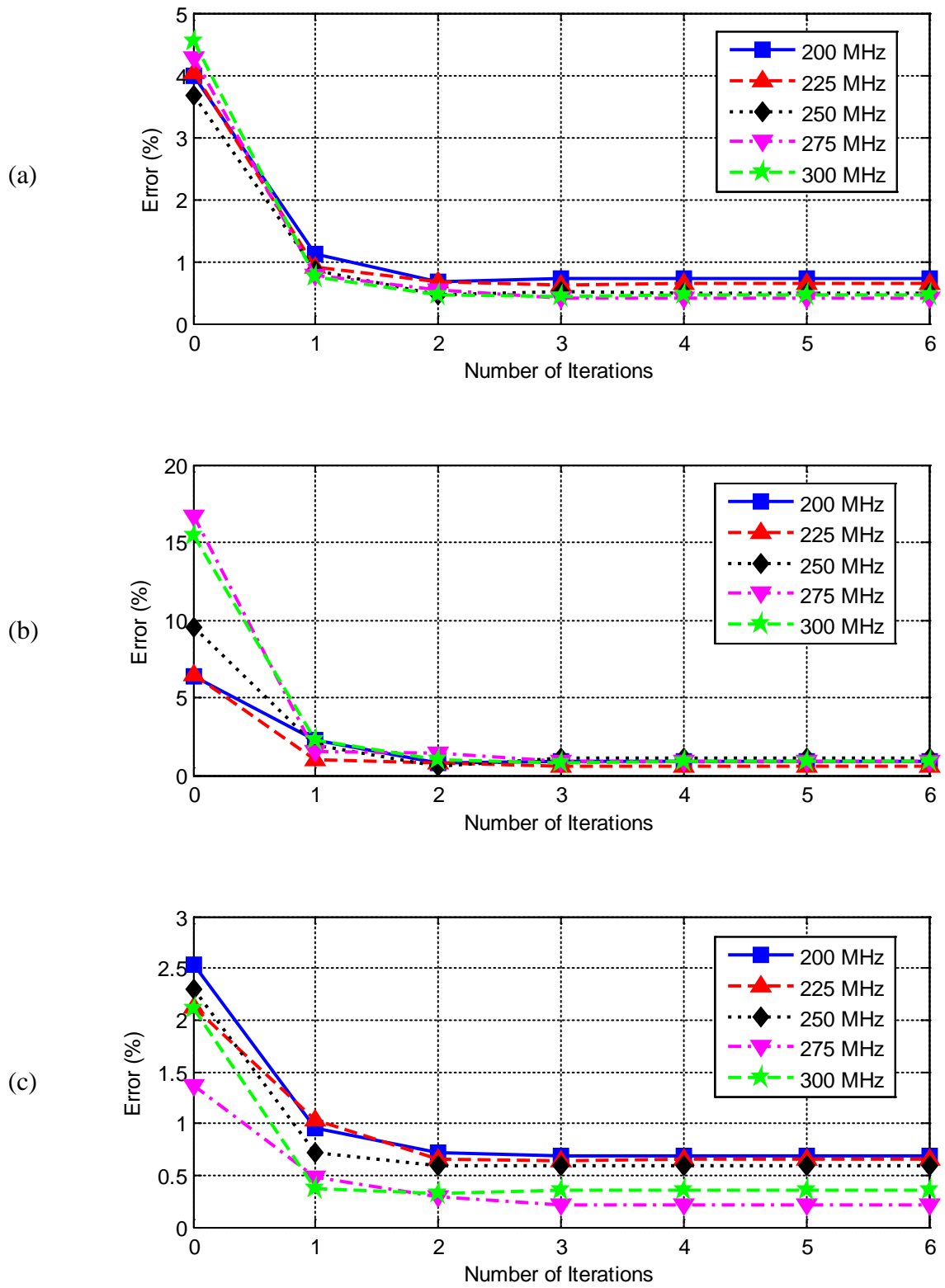


Figure 3.20: Normalized average errors for RCS_ϕ in the three plane cuts: a) xy -plane, b) xz -plane, and c) yz -plane.

3.3 Electromagnetic Scattering from Three Objects-1

The geometry of the third problem illustrated in Figure 3.21 is analyzed to prove the validity of the proposed technique for more than two scatterer objects where more interaction processes are required between them. Two identical dielectric spheres and a conducting ellipsoid are placed along the x -axis with 0.5 m separation. The radius of the dielectric spheres is 0.4 m. The relative permittivity and permeability of the dielectric spheres are 3 and 1, respectively. The semi-axes of the conducting ellipsoid are 0.2 m, 0.2 m, and 1 m along the x , y , and z axes, respectively. This problem space is excited by a θ and ϕ polarized plane wave with $\theta^{\text{inc}}=90^\circ$ and $\phi^{\text{inc}}=90^\circ$. The problem space is composed of cells with size 0.02 m in the x , y , and z directions for the full domain simulation. As for the IMR simulation, a cell size 0.02 m is used in ellipsoid subregion, whereas a cell size 0.04 m is used in other subregions. It can be seen from Figure 3.22 that the IMR algorithm reaches the convergence criterion after iteration # 2. Figures 3.23-3.28 show the bistatic RCS_θ and RCS_ϕ for the xy , xz , and yz plane cuts at 200, 225, 250, 275, and 300 MHz. To prove the convergence of the full domain and IMR technique results, the normalized average errors RCS_θ and RCS_ϕ in the three plane cuts are shown in Figures 3.29-3.30. Simulation parameters and computer resources used are summarized in Table 3-3 for the full domain solution and the IMR solution. Results show a considerable reduction in the memory storage requirements and computation time.

Table 3-3: Simulation parameters and computer resources used by the IMR and full domain simulation.

| | Number of Domains | Total Number of Cells | Computation Time (min.) | Iteration Number | Memory (MB) |
|------------------|-------------------|-----------------------|-------------------------|------------------|-------------|
| Full FDTD | — | 1,922,496 | 58 | — | 1,190 |
| IMR-FDTD | 3 | 777,728 | 51 | 2 | 400 |

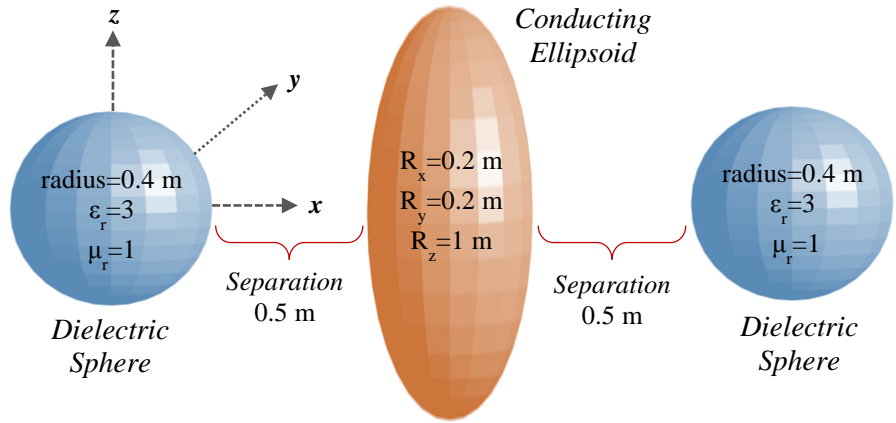


Figure 3.21: Geometry of the third problem.

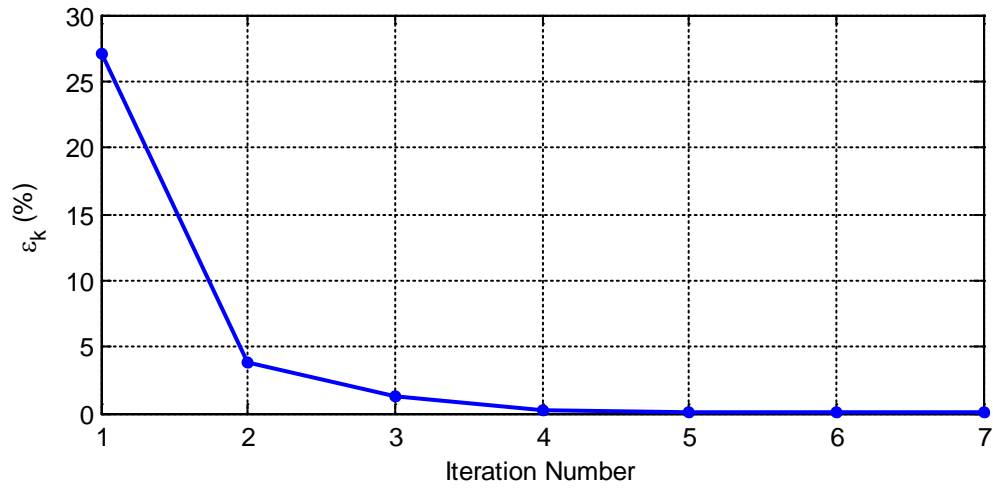
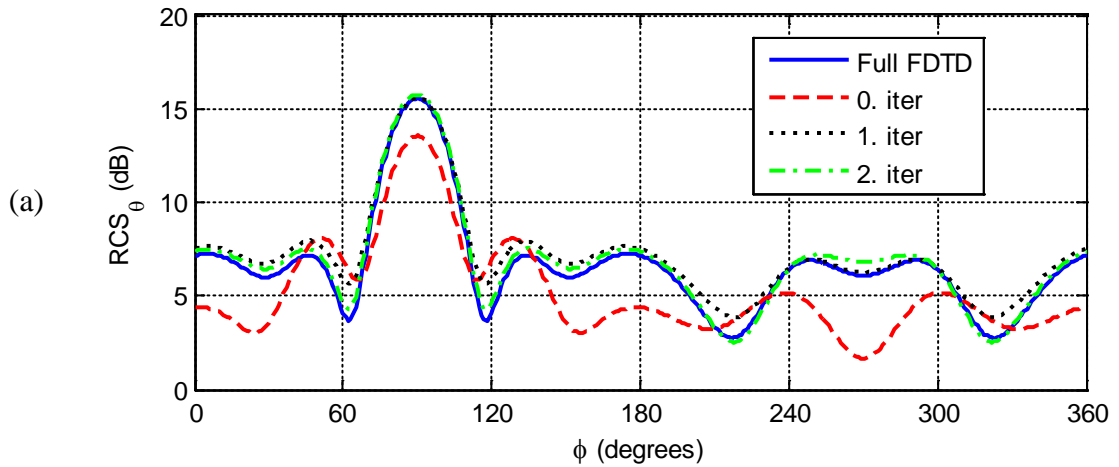
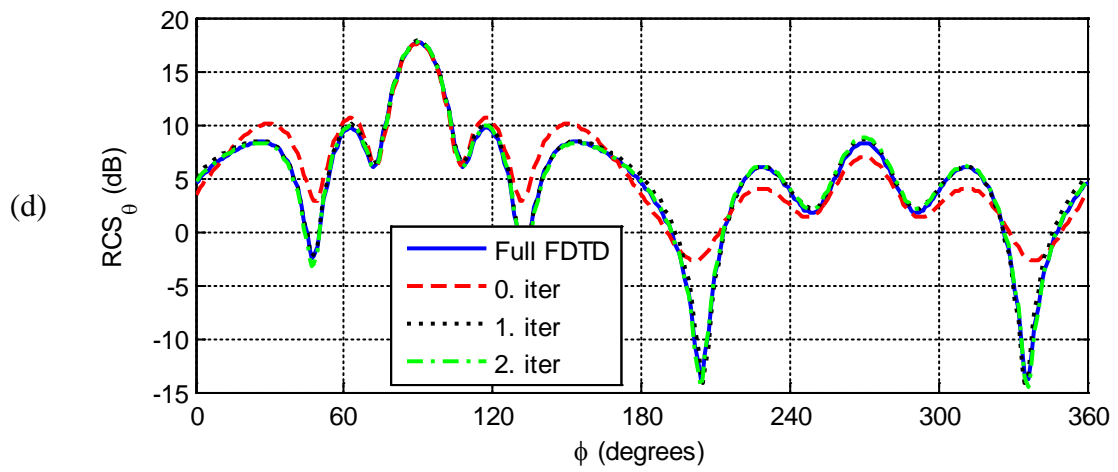
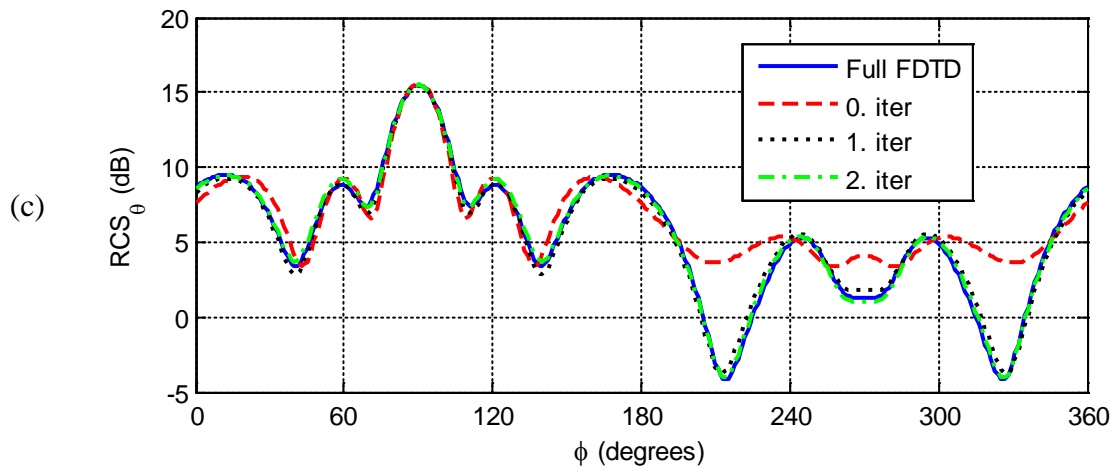
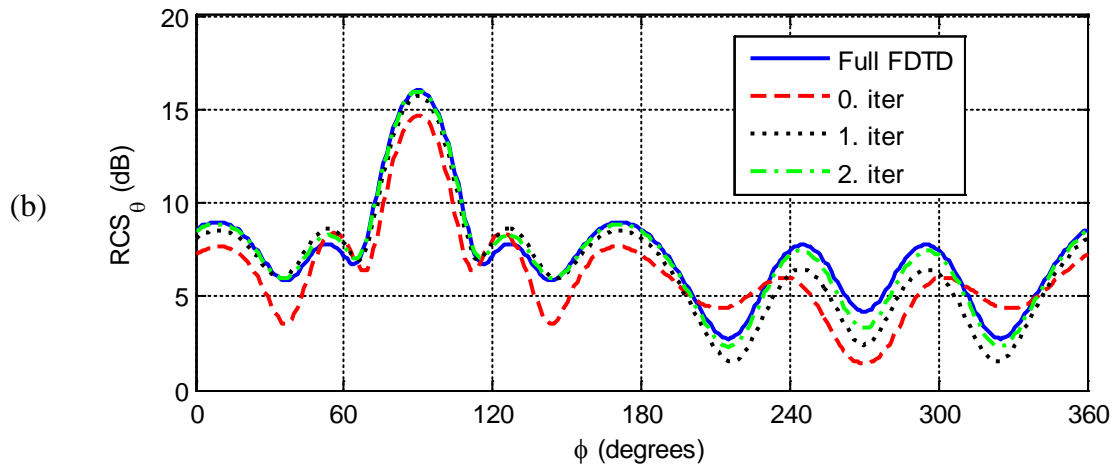


Figure 3.22: Convergence (ϵ_k) between iteration steps for the third problem.





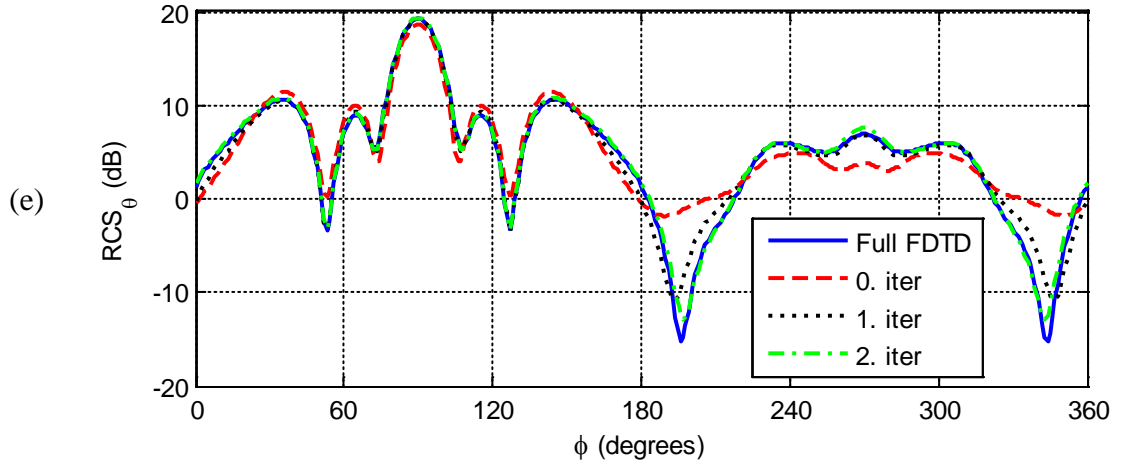
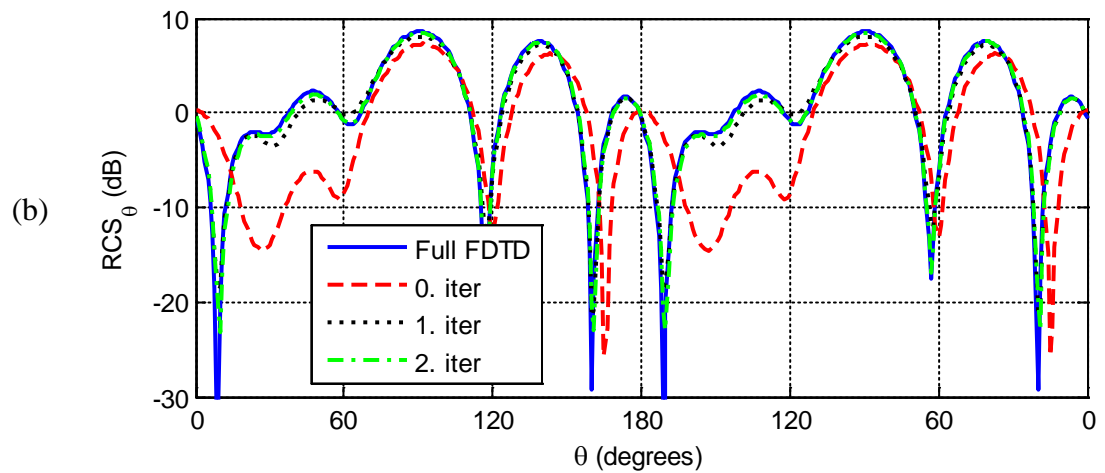
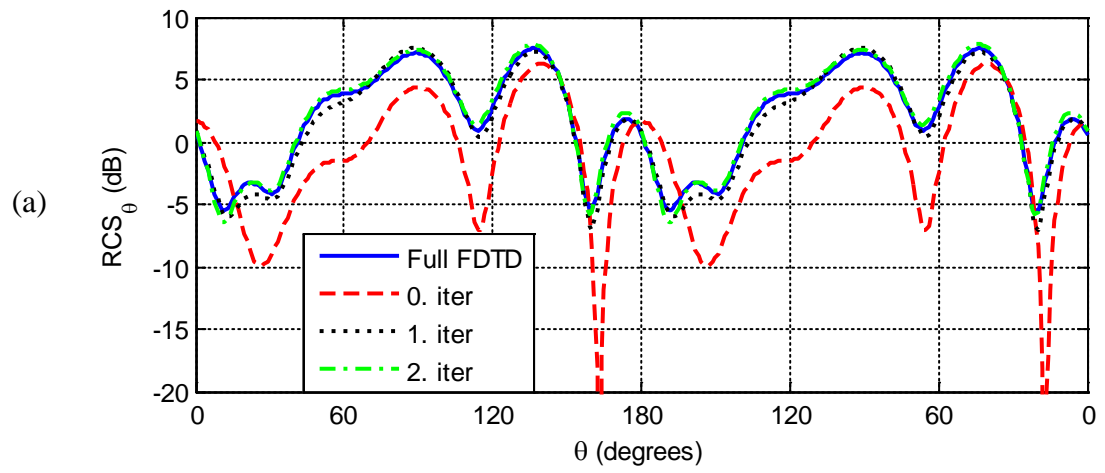


Figure 3.23: Bistatic RCS_θ for xy -plane cuts at frequencies: a) 200 MHz, b) 225 MHz, c) 250 MHz, d) 275 MHz, and e) 300 MHz.



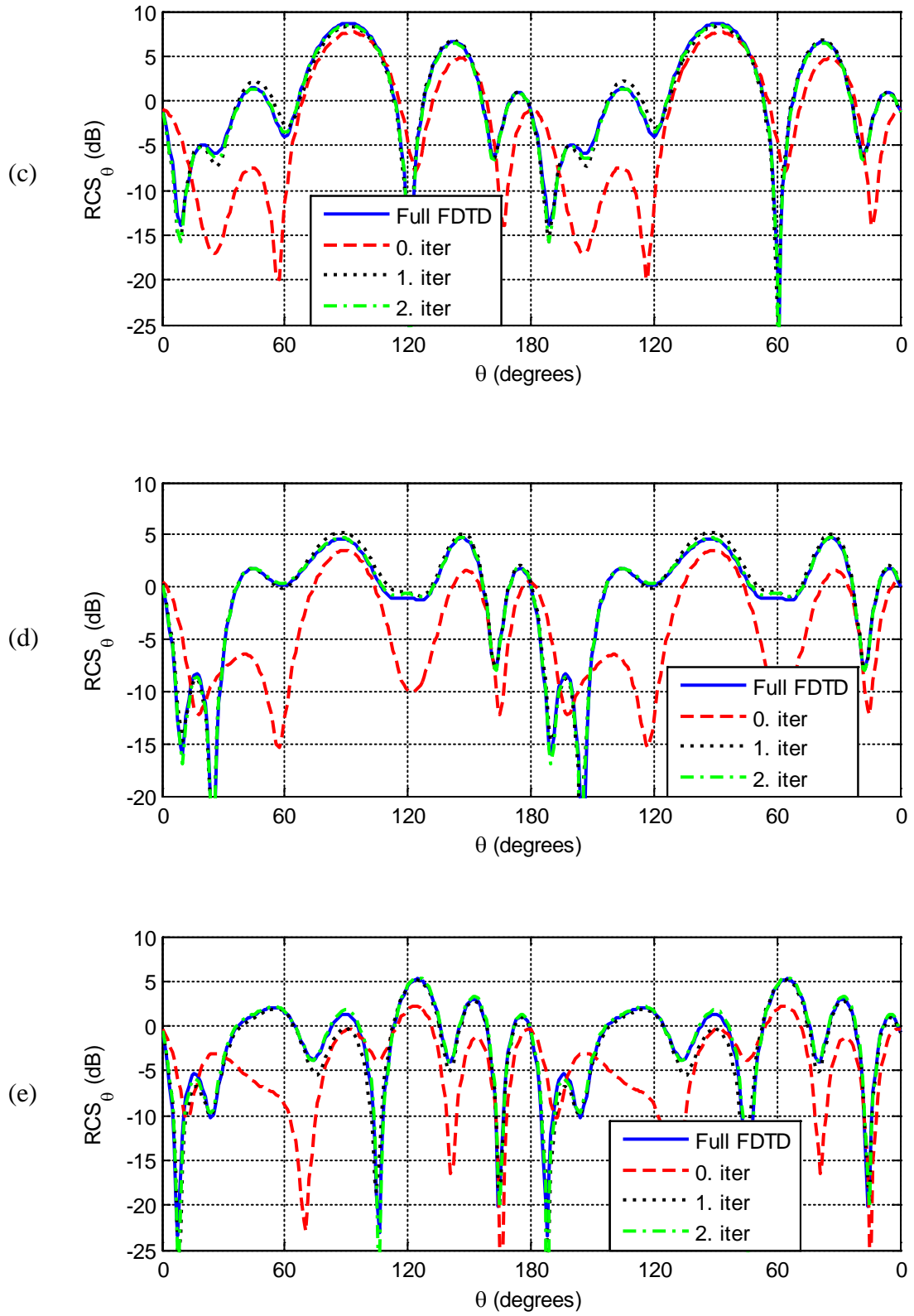
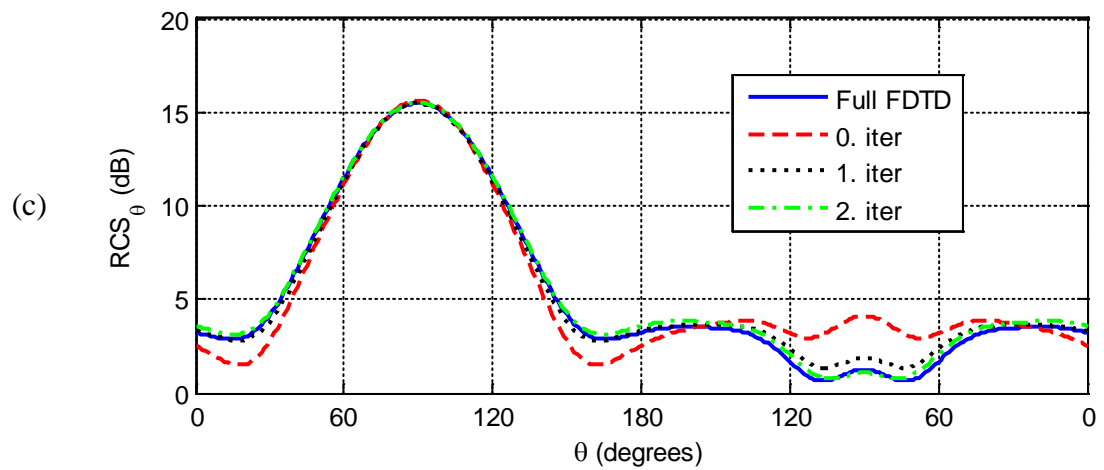
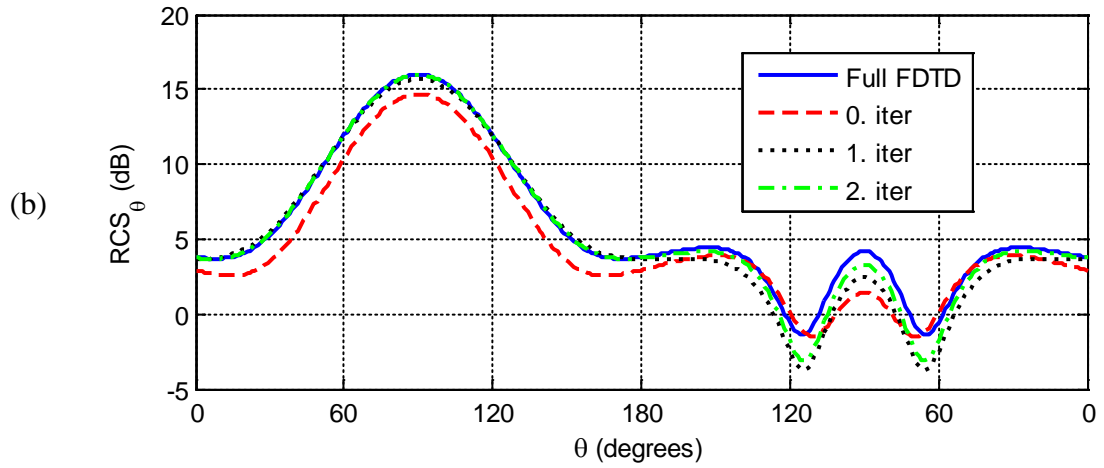
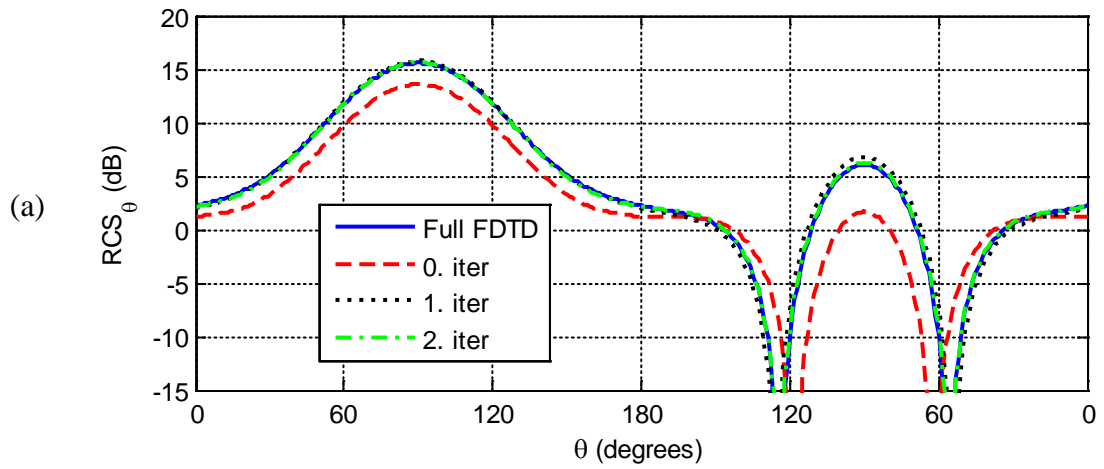


Figure 3.24: Bistatic RCS_θ for xz -plane cuts at frequencies: a) 200 MHz, b) 225 MHz, c) 250 MHz, d) 275 MHz, and e) 300 MHz.



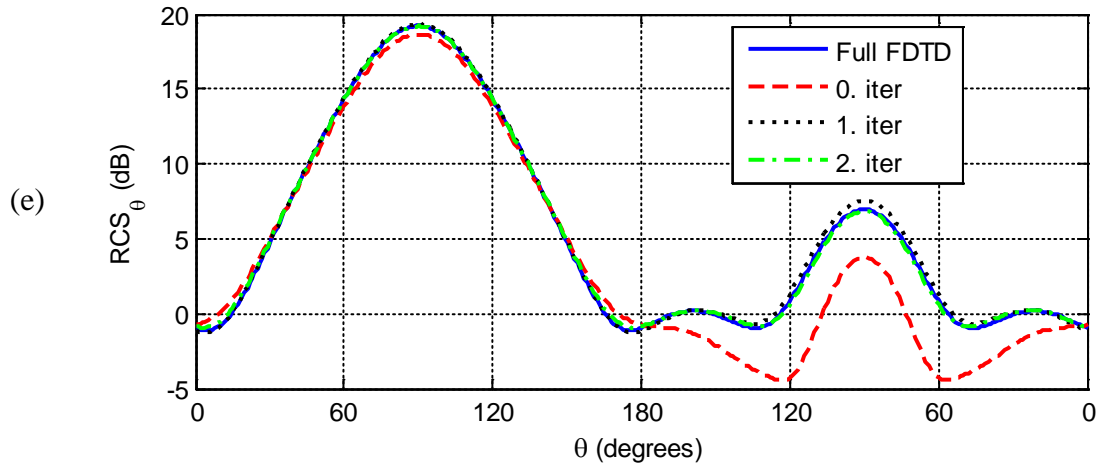
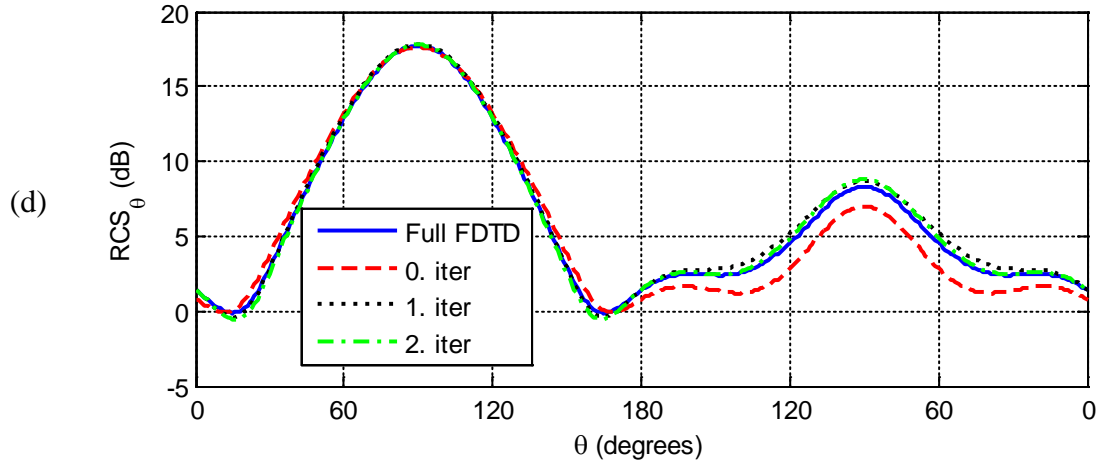
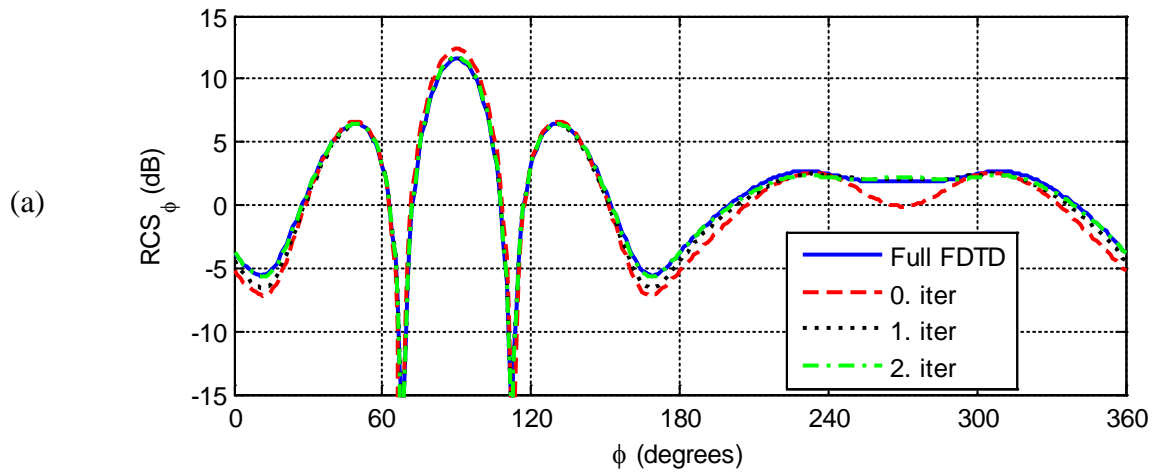
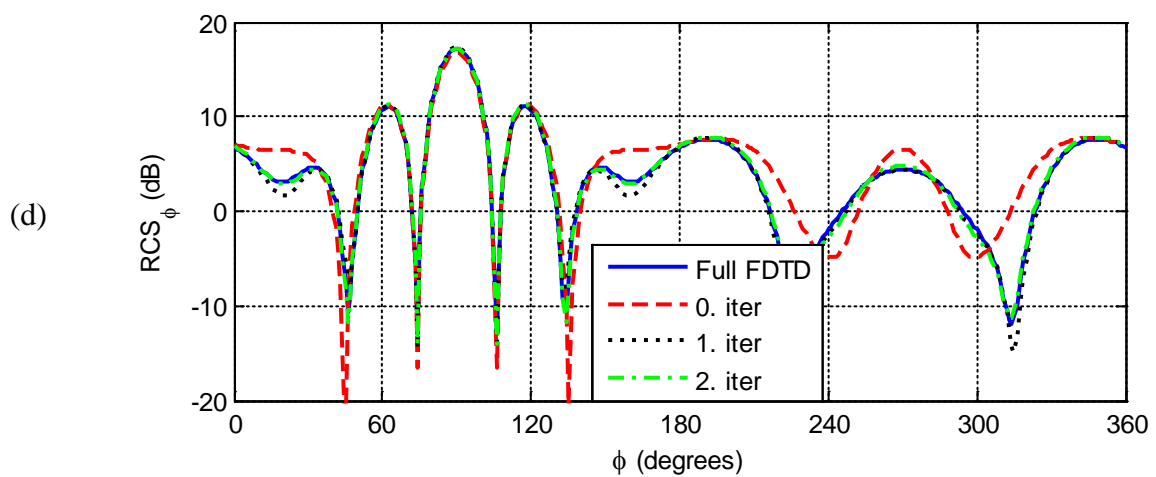
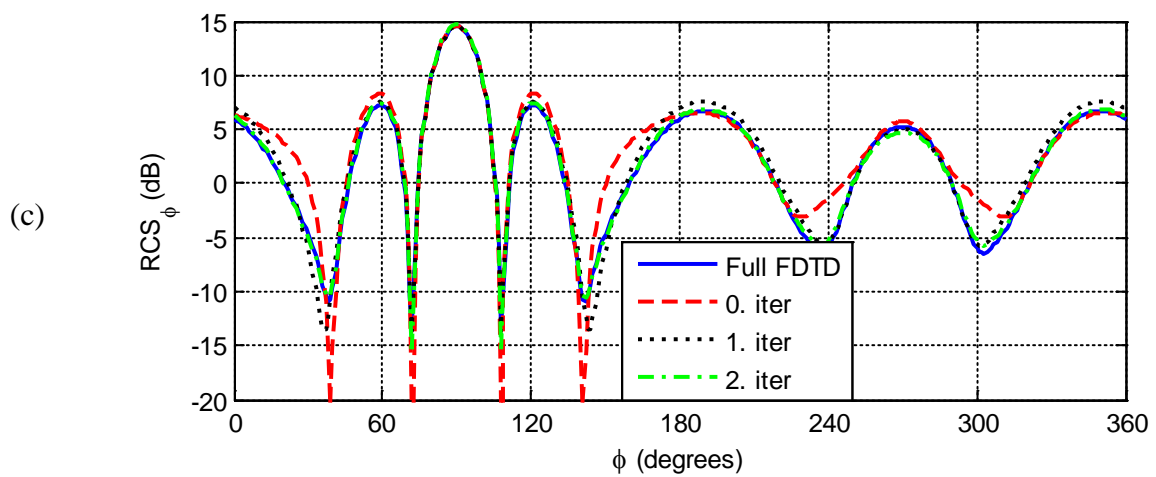
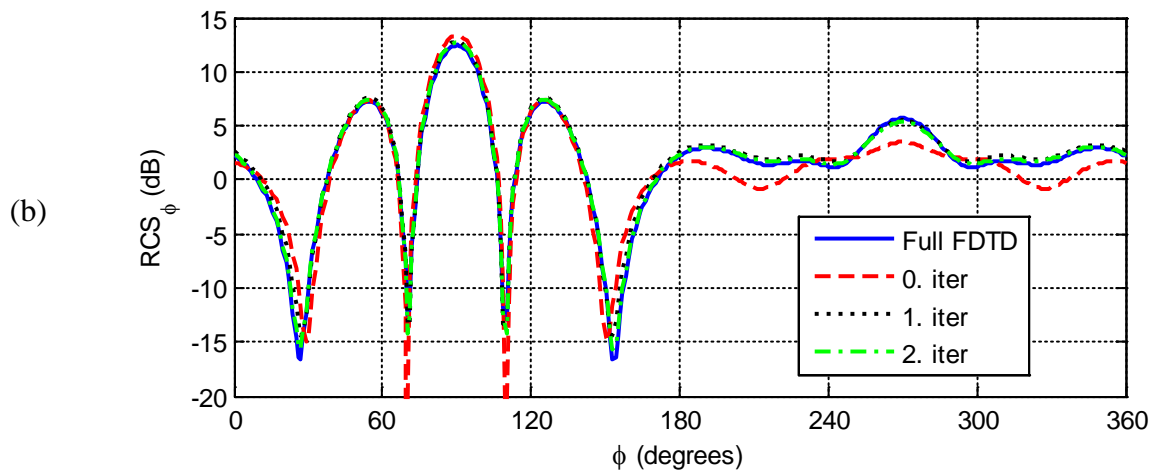


Figure 3.25: Bistatic RCS_θ for yz-plane cuts at frequencies: a) 200 MHz, b) 225 MHz, c) 250 MHz, d) 275 MHz, and e) 300 MHz.





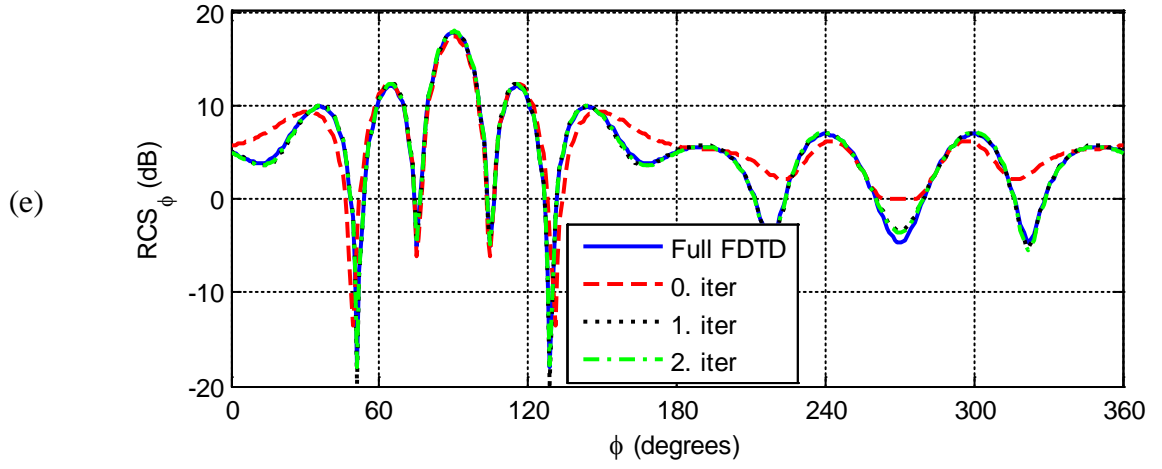
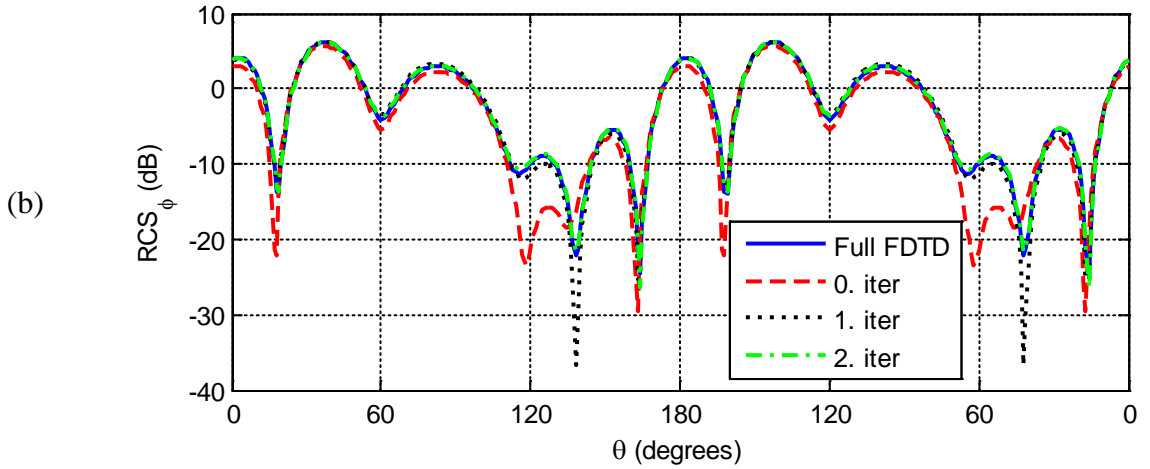
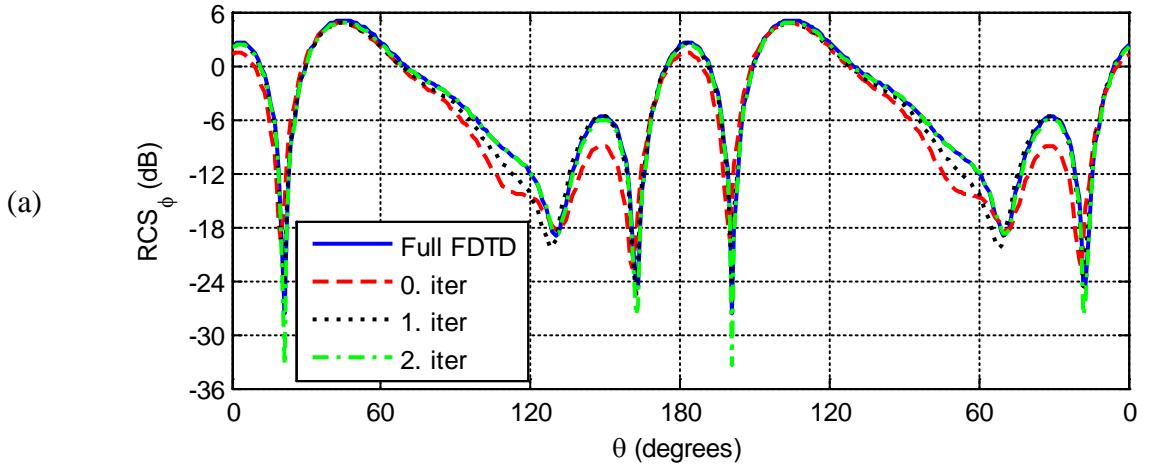


Figure 3.26: Bistatic RCS_φ for xy -plane cuts at frequencies: a) 200 MHz, b) 225 MHz, c) 250 MHz, d) 275 MHz, and e) 300 MHz.



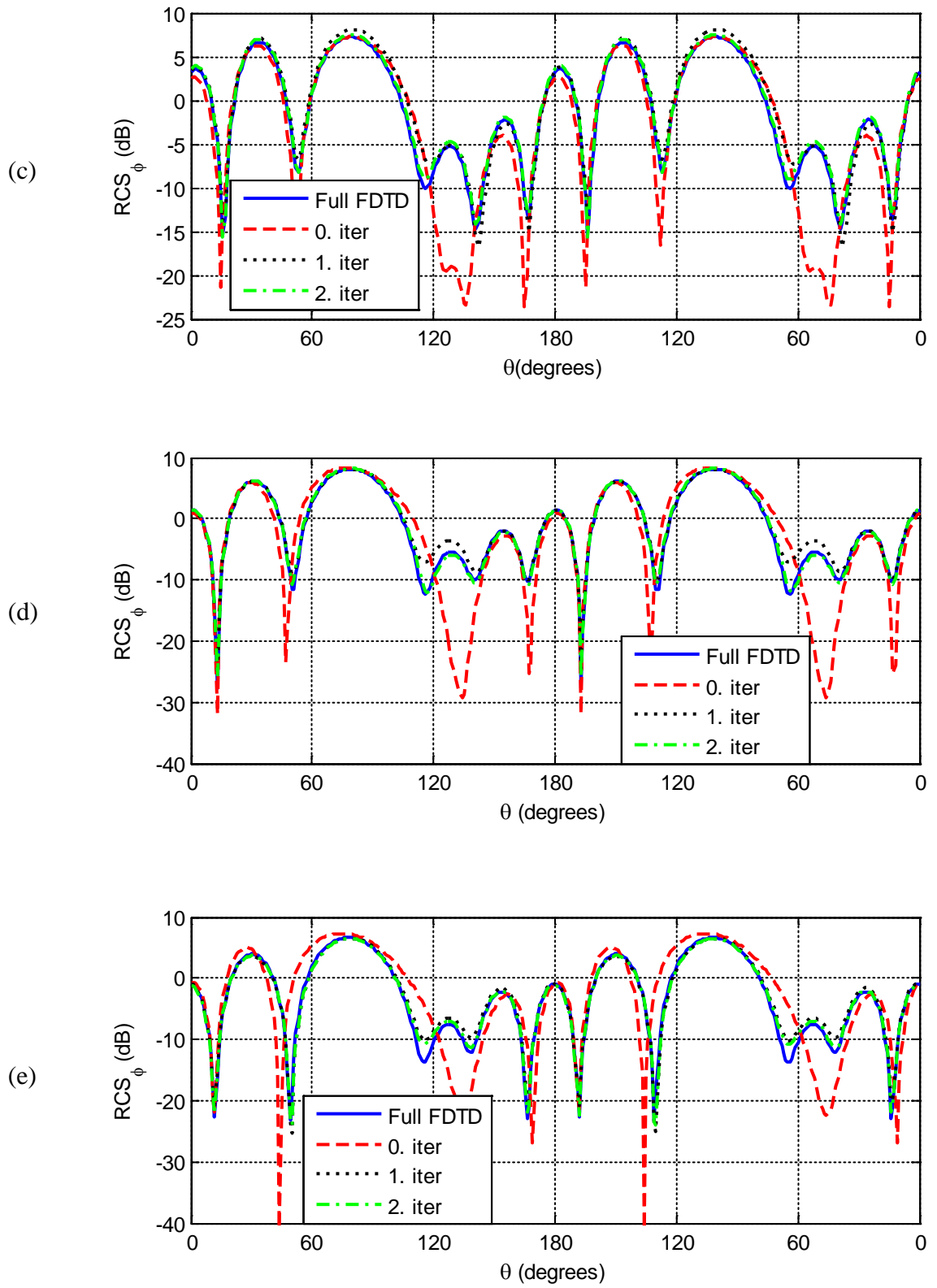
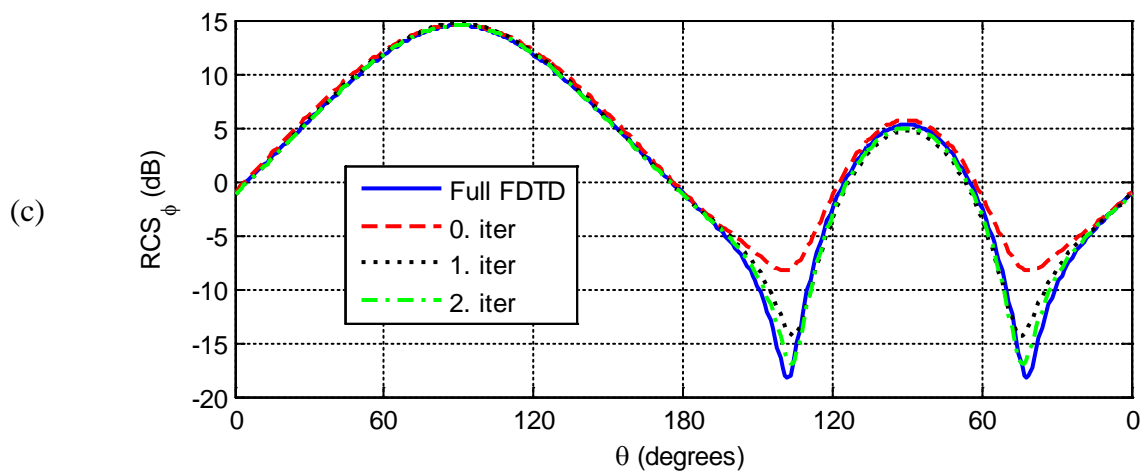
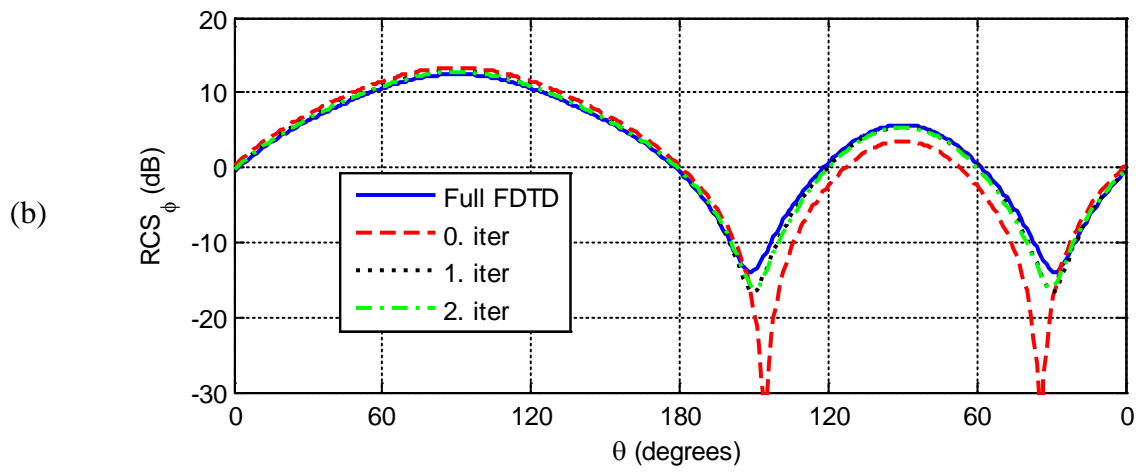
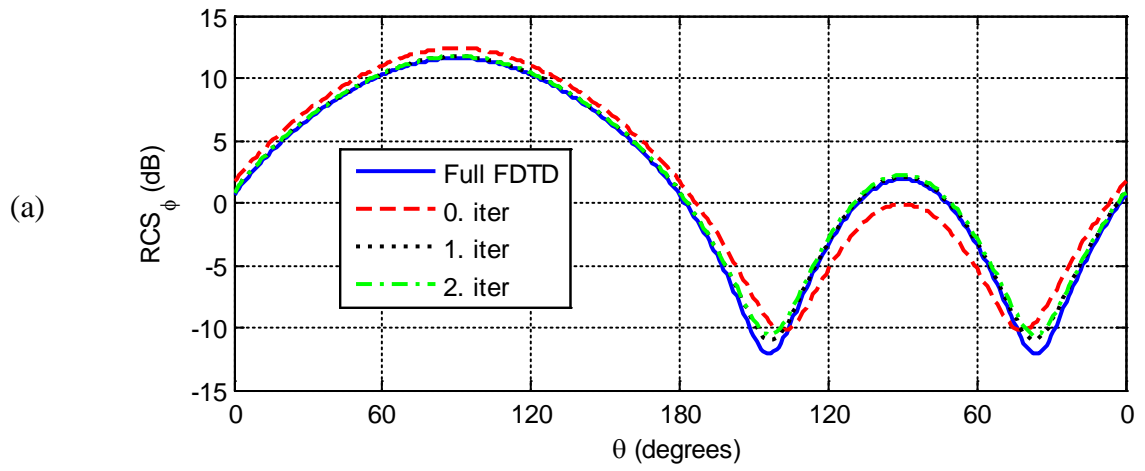


Figure 3.27: Bistatic RCS_ϕ for xz -plane cuts at frequencies: a) 200 MHz, b) 225 MHz, c) 250 MHz, d) 275 MHz, and e) 300 MHz.



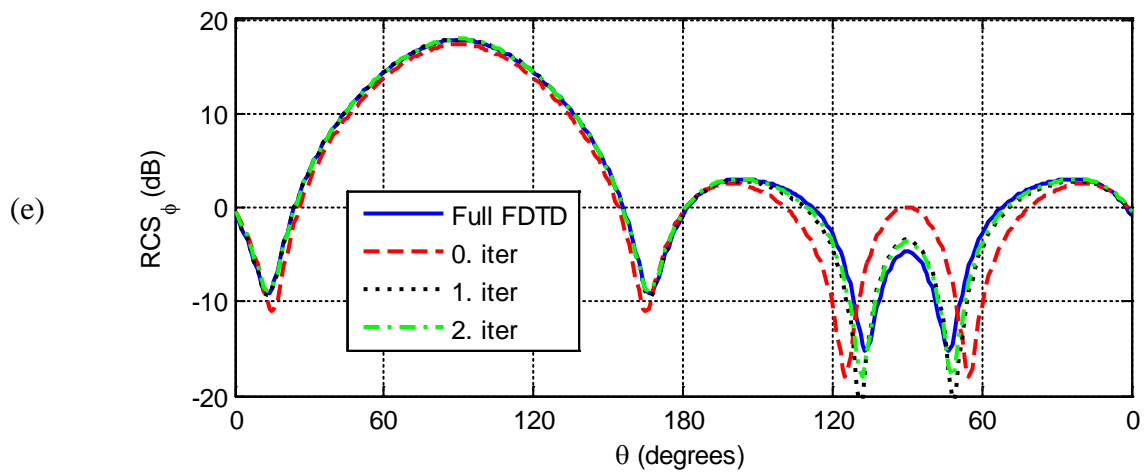
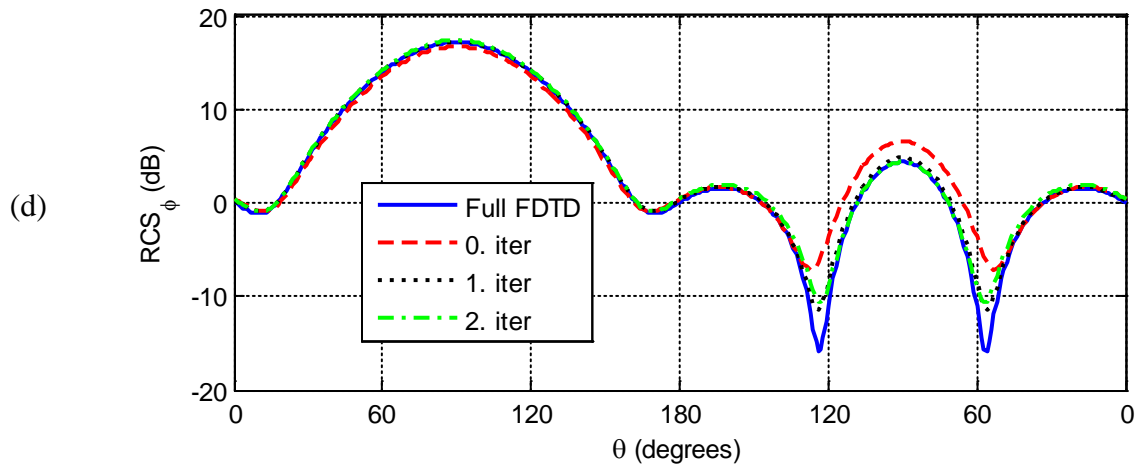
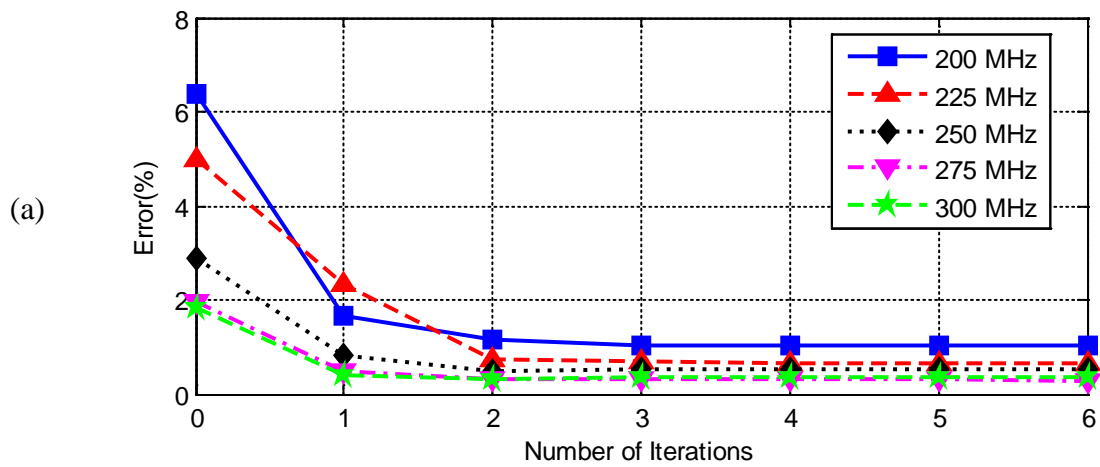


Figure 3.28: Bistatic RCS_{ϕ} for yz -plane cuts at frequencies: a) 200 MHz, b) 225 MHz, c) 250 MHz, d) 275 MHz, and e) 300 MHz.



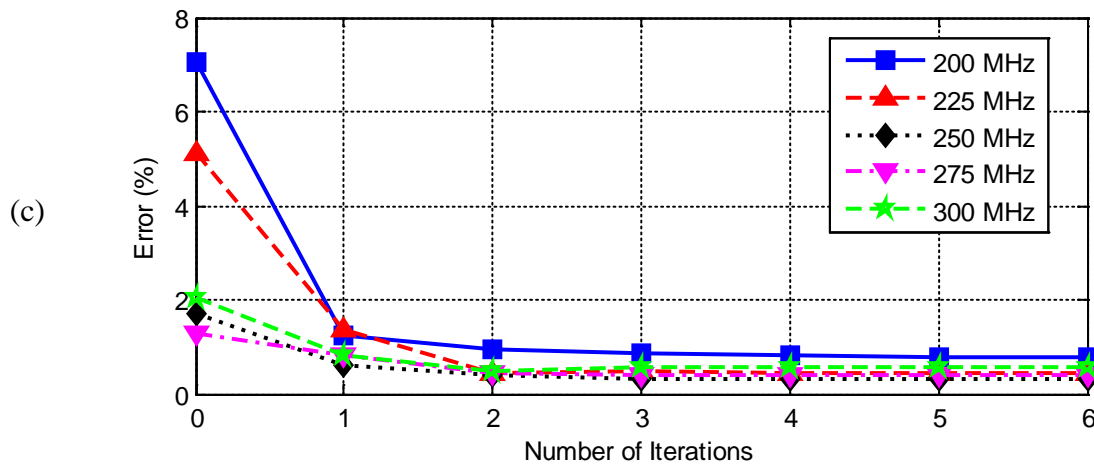
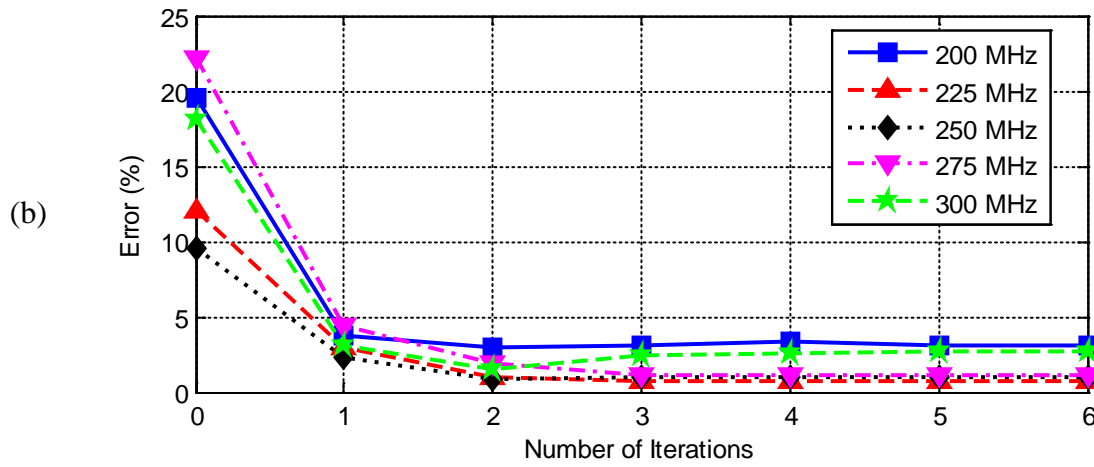
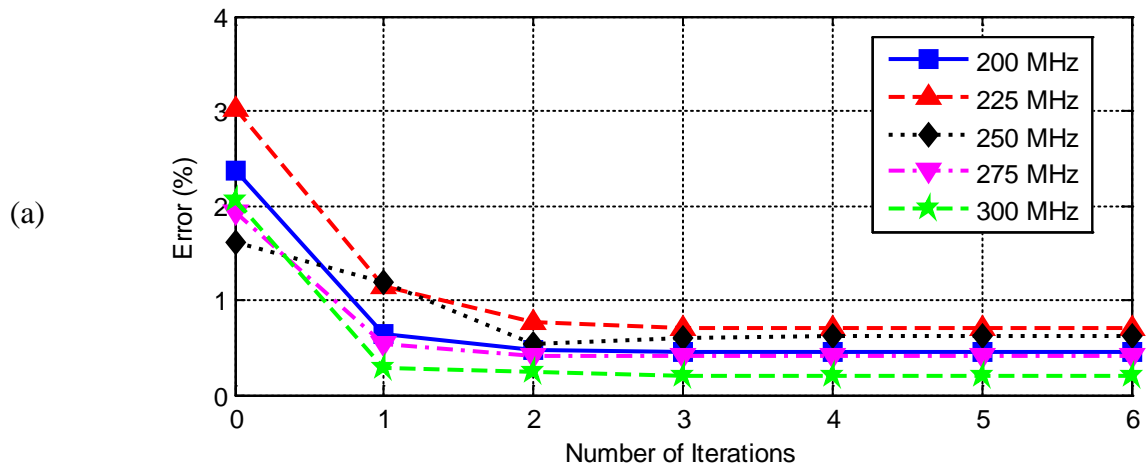


Figure 3.29: Normalized average errors for RCS_θ in the three plane cuts: a) xy -plane, b) xz -plane, and c) yz -plane.



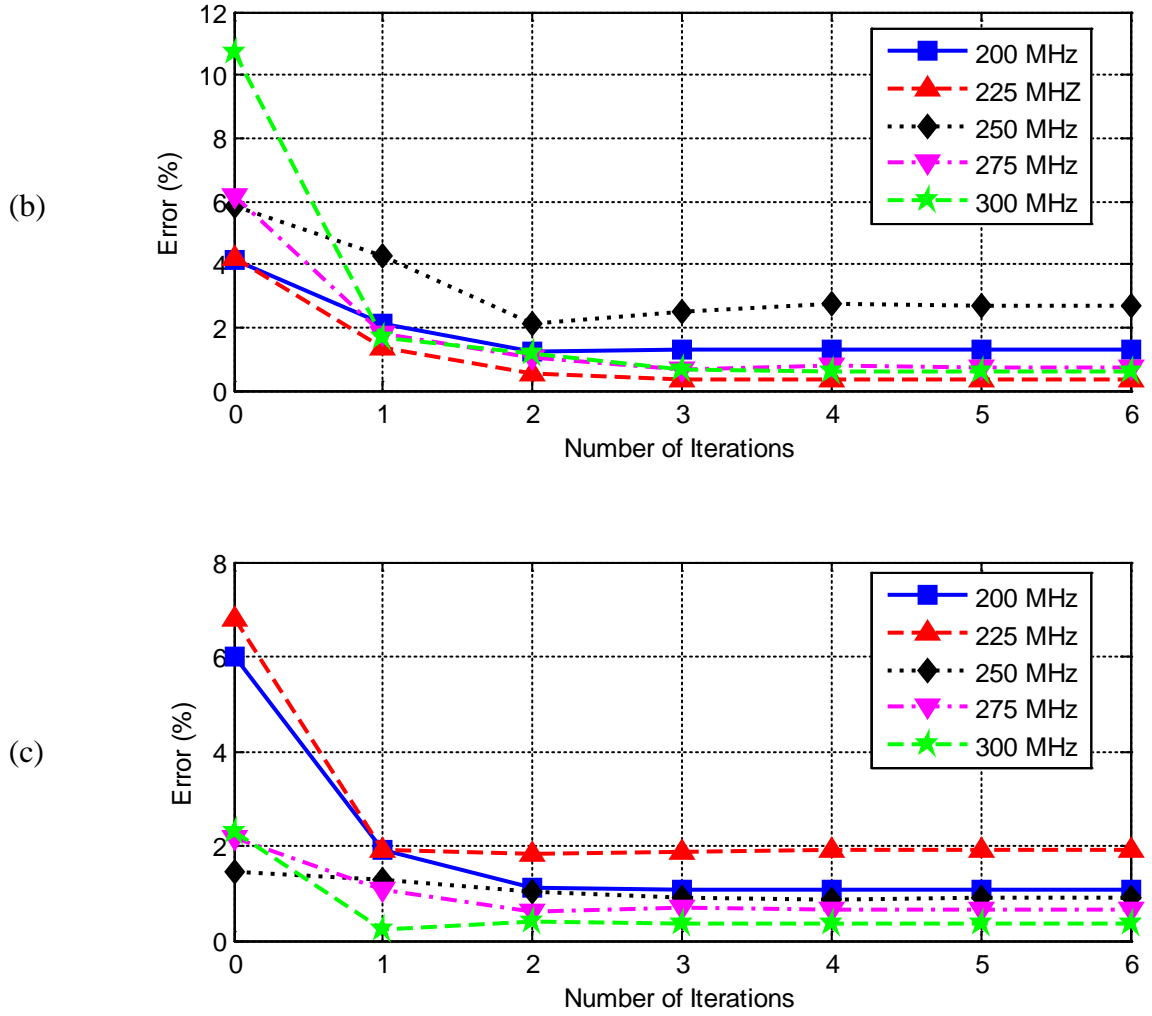


Figure 3.30: Normalized average errors for RCS_ϕ in the three plane cuts: a) xy -plane, b) xz -plane, and c) yz -plane.

3.4 Electromagnetic Scattering from Three Objects-2

The same geometry of third problem illustrated in Figure 3.21 is simulated as the fourth problem, but instead of using a conducting ellipsoid, a dielectric ellipsoid with the relative permittivity of 2.2 is used for a θ and ϕ polarized excitation with $\theta^{\text{inc}}=90^\circ$ and $\phi^{\text{inc}}=90^\circ$. It can be seen from Figure 3.31 that the IMR algorithm reaches the convergence criterion after iteration # 2. Figures 3.32-3.37 show the bistatic RCS_θ and

RCS_ϕ for the xy , xz , and yz plane cuts at 200 MHz, 225 MHz, 250 MHz, 275 MHz, and 300 MHz. A good agreement is achieved between the results generated using the IMR technique with those generated using the full domain simulation. To prove the convergence of the full domain and IMR technique results, the normalized average errors for RCS_θ and RCS_ϕ in the three plane cuts are shown in Figures 3.38-3.39. Simulation parameters and computer resources used are summarized in Table 3-4 for the full domain solution and the IMR solution.

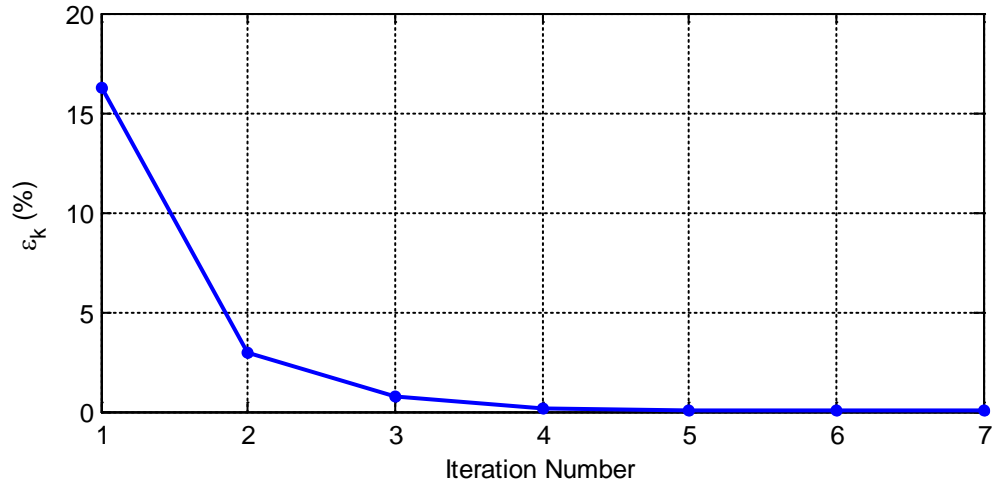
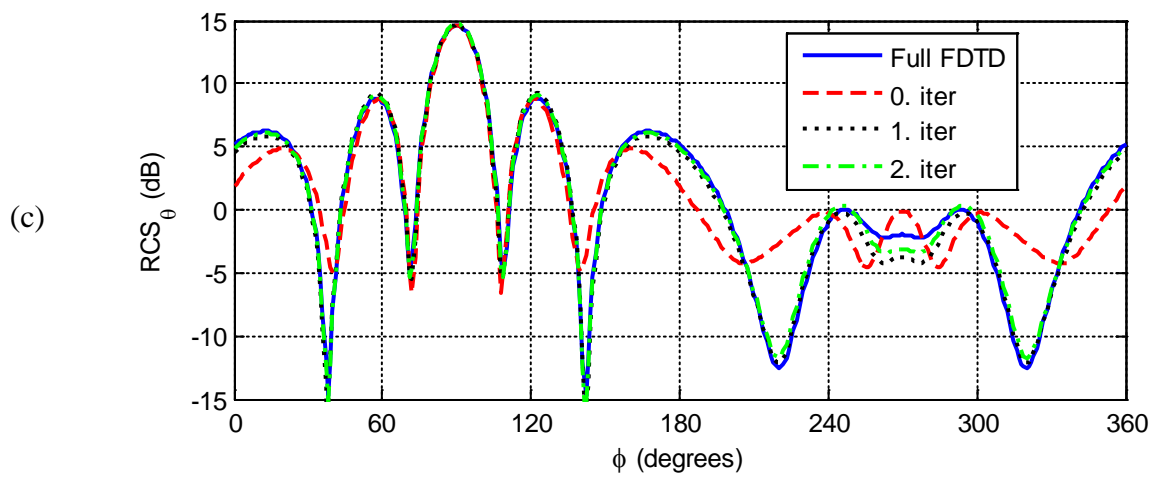
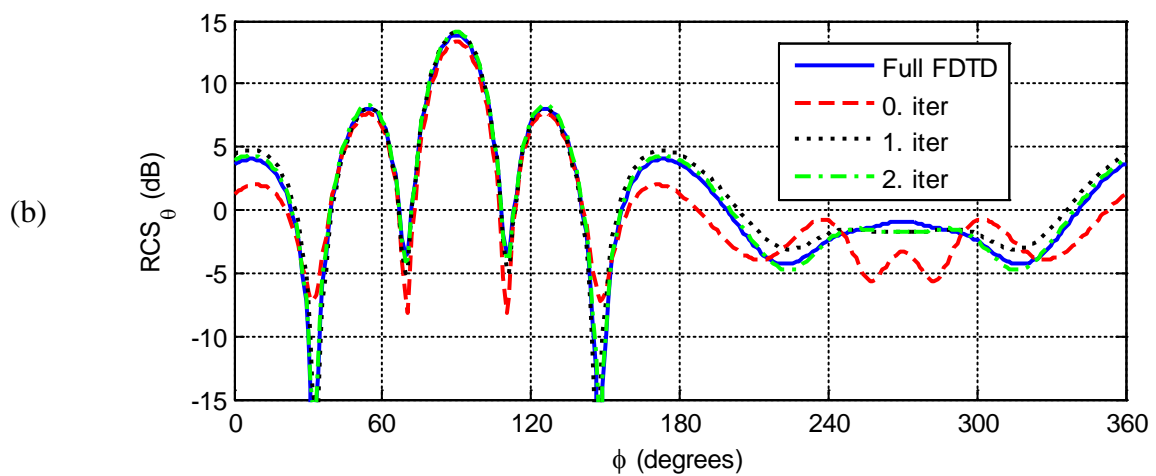
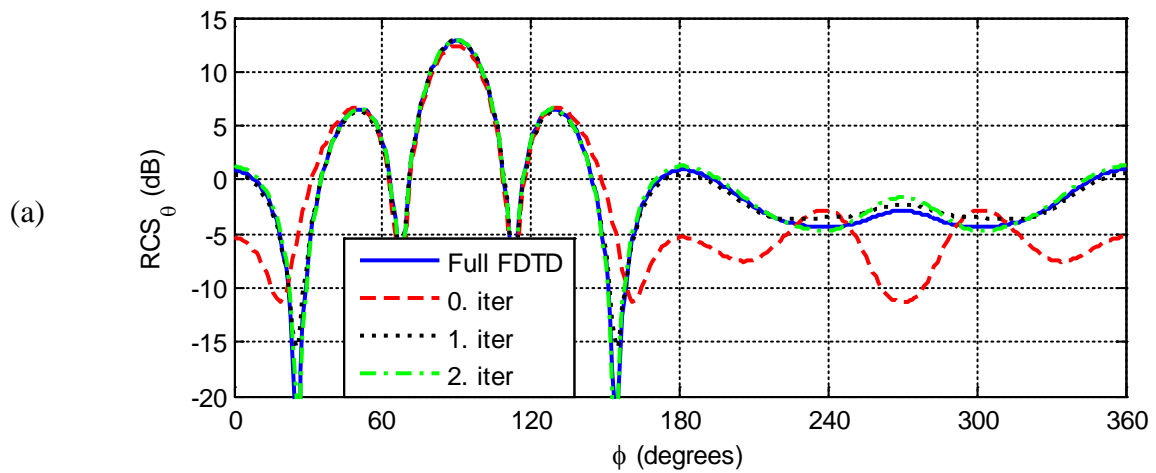


Figure 3.31: Convergence (ϵ_k) between iteration steps for the fourth problem.

Table 3-4: Simulation parameters and computer resources used by the IMR and full domain simulation.

| | Number of Domains | Total Number of Cells | Computation Time (min.) | Iteration Number | Memory (MB) |
|------------------|-------------------|-----------------------|-------------------------|------------------|-------------|
| Full FDTD | — | 1,922,496 | 53 | — | 1,220 |
| IMR-FDTD | 3 | 777,728 | 48 | 2 | 407 |



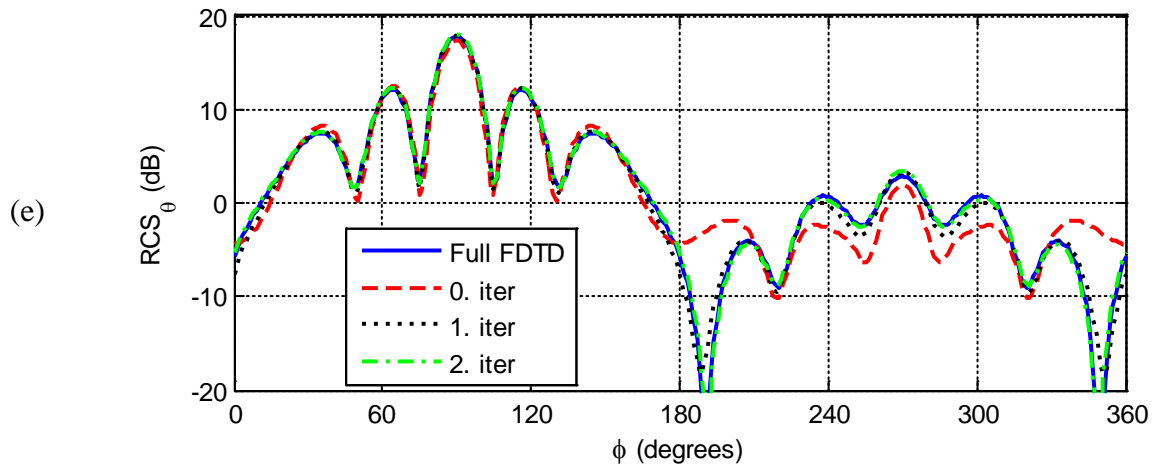
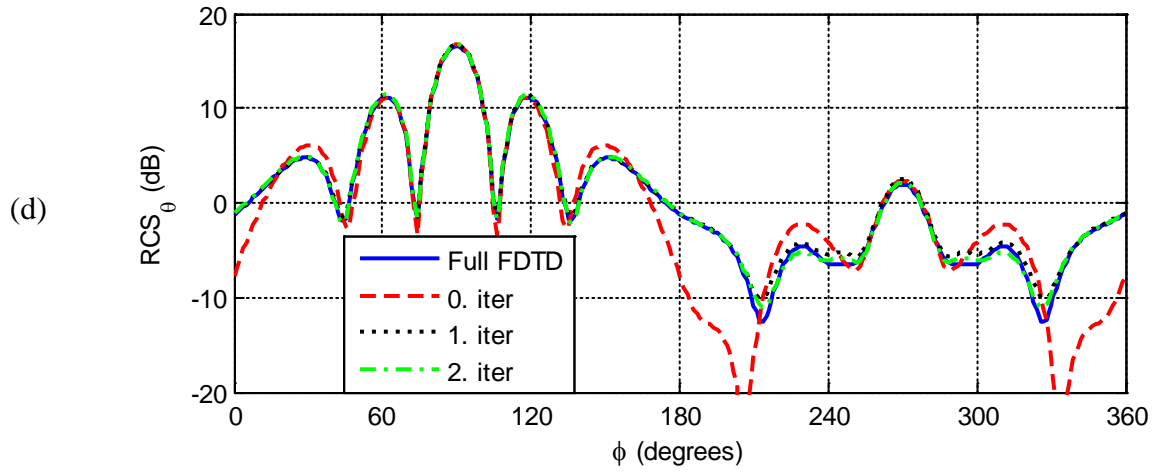
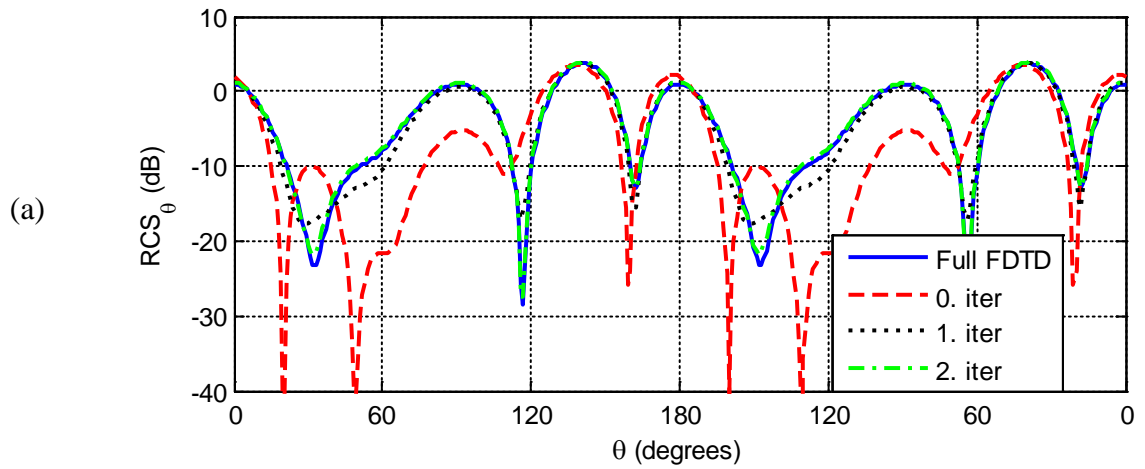
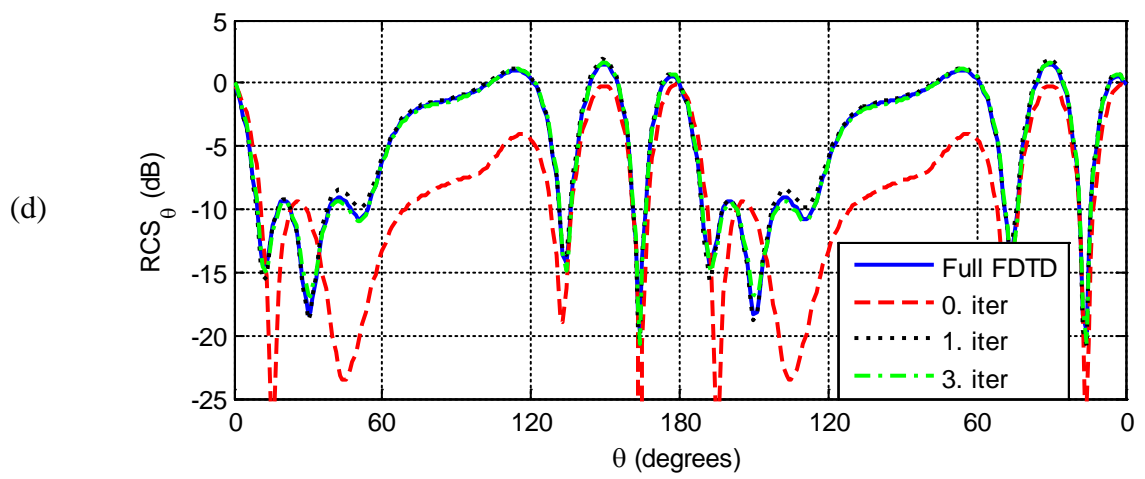
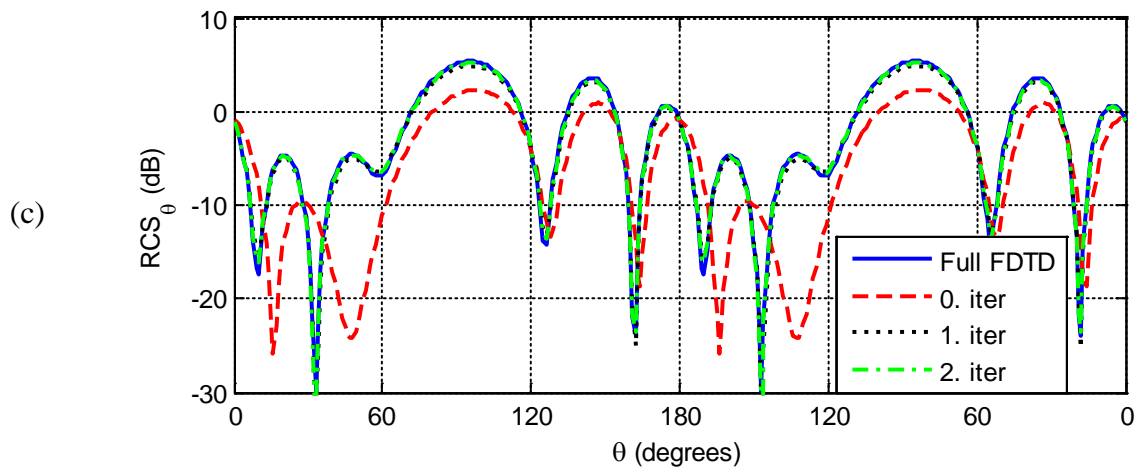
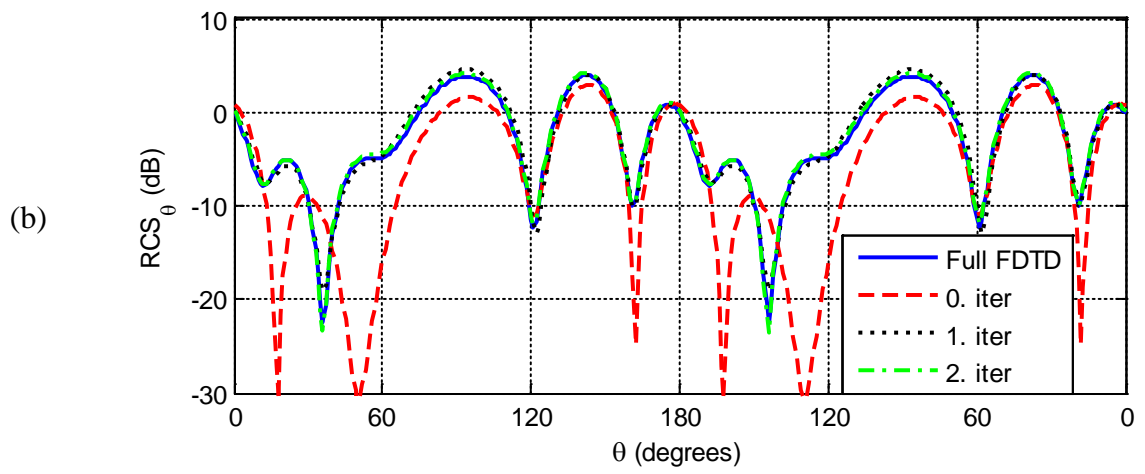


Figure 3.32: Bistatic RCS_θ for *xy*-plane cut at frequencies: a) 200 MHz, b) 225 MHz, c) 250 MHz, d) 275 MHz, and e) 300 MHz.





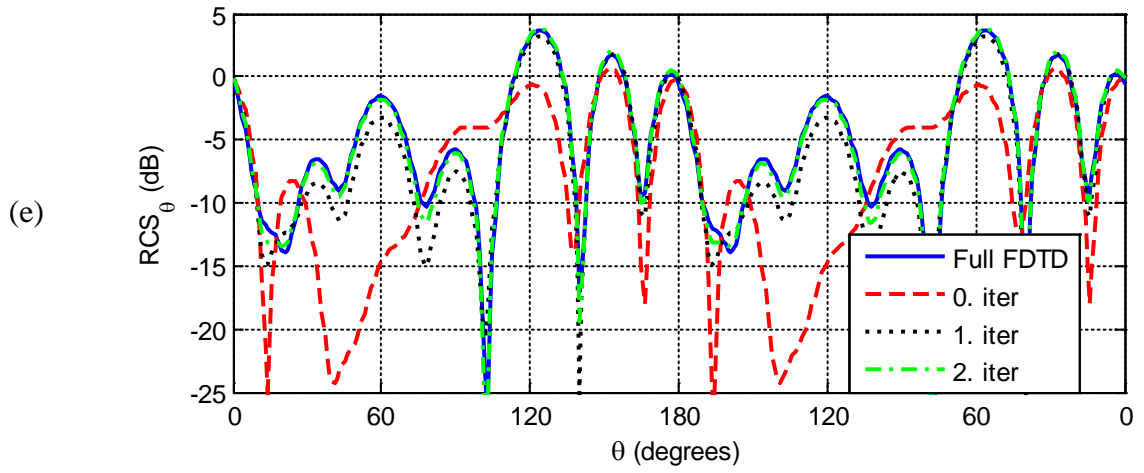
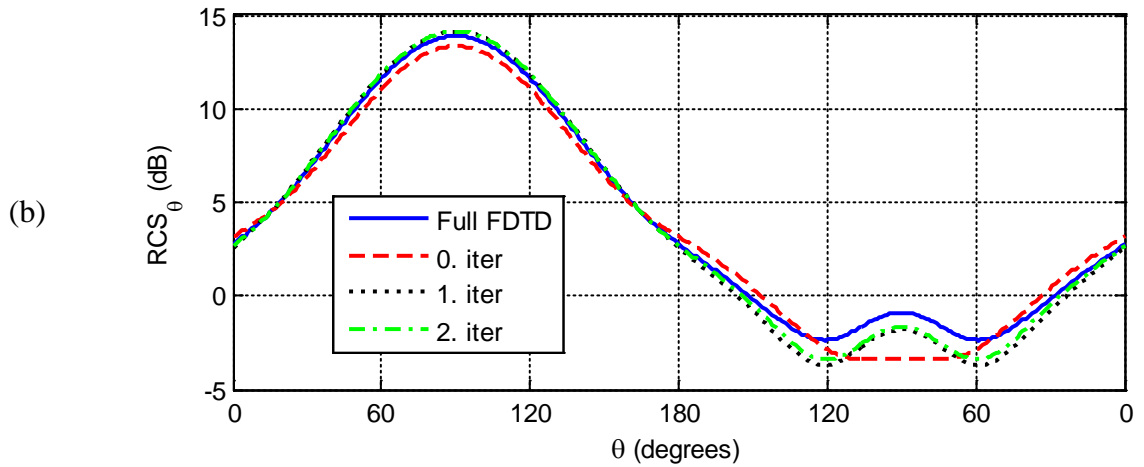
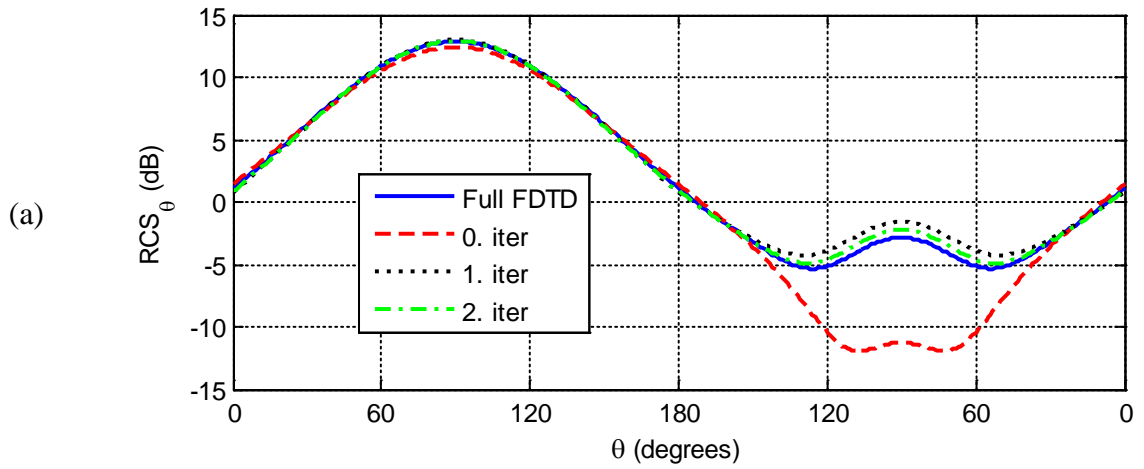


Figure 3.33: Bistatic RCS_{θ} for xz -plane cut at frequencies: a) 200 MHz, b) 225 MHz, c) 250 MHz, d) 275 MHz, and e) 300 MHz.



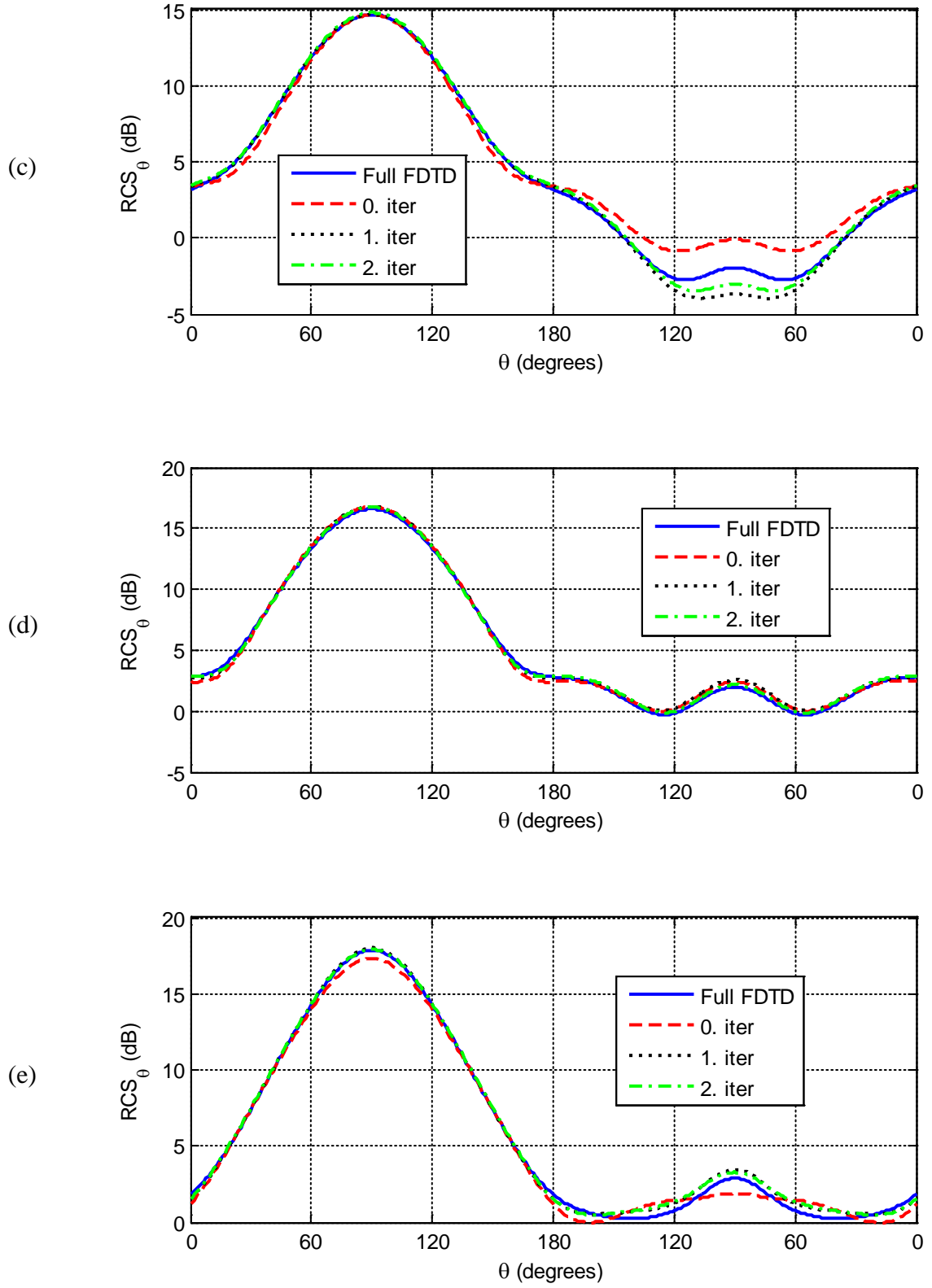
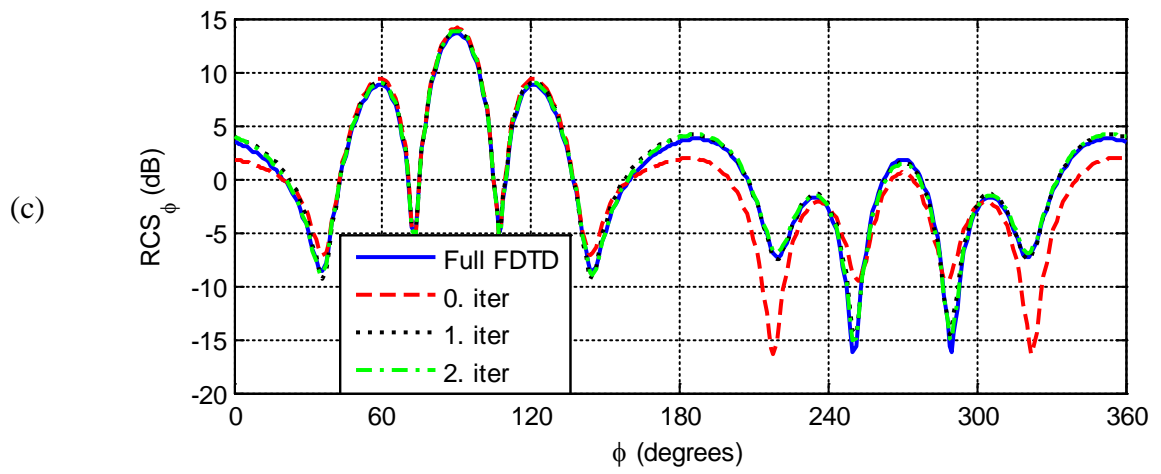
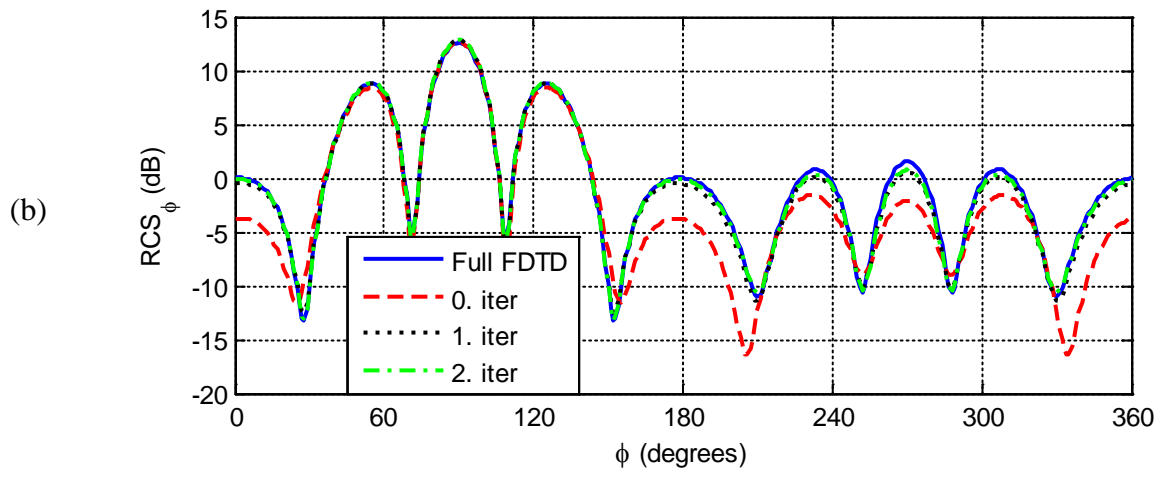
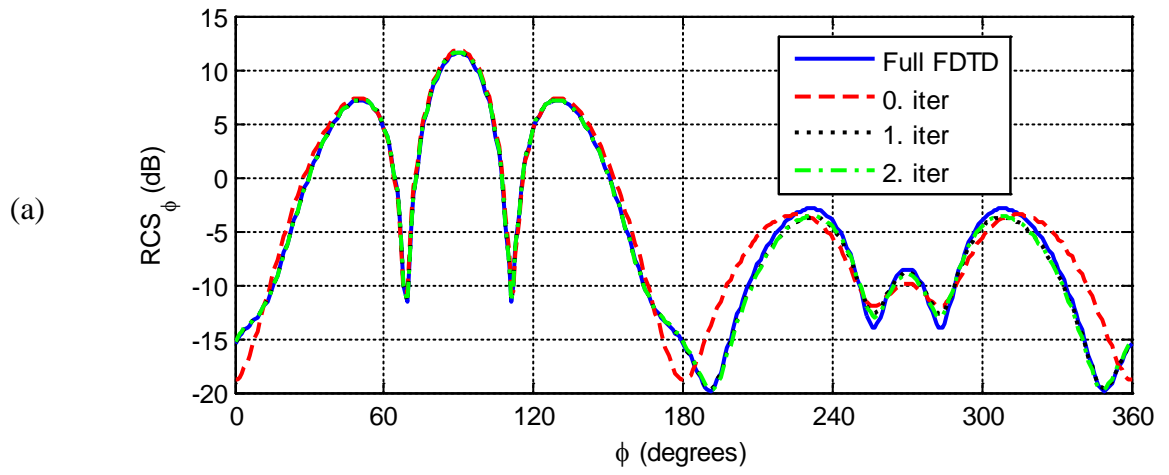


Figure 3.34: Bistatic RCS_θ for yz -plane cut at frequencies: a) 200 MHz, b) 225 MHz, c) 250 MHz, d) 275 MHz, and e) 300 MHz.



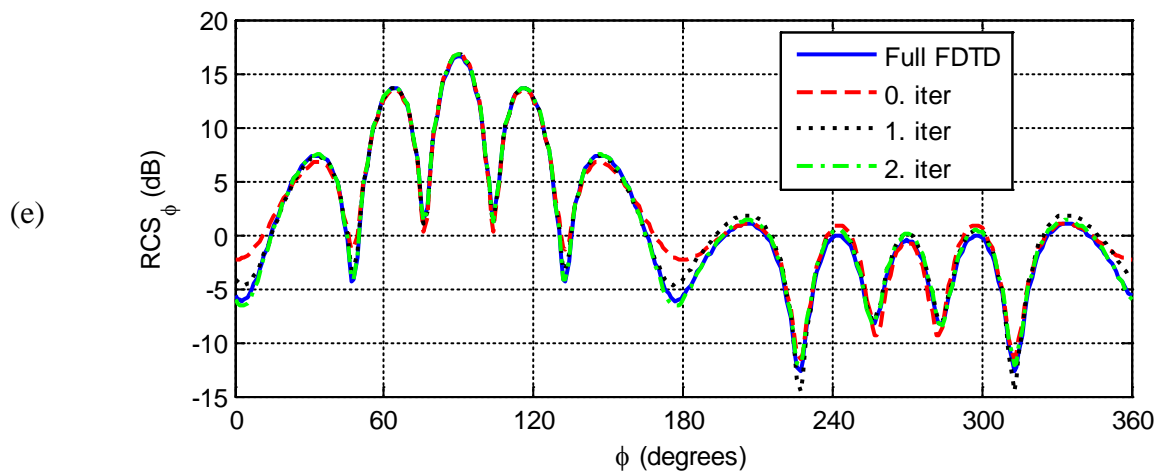
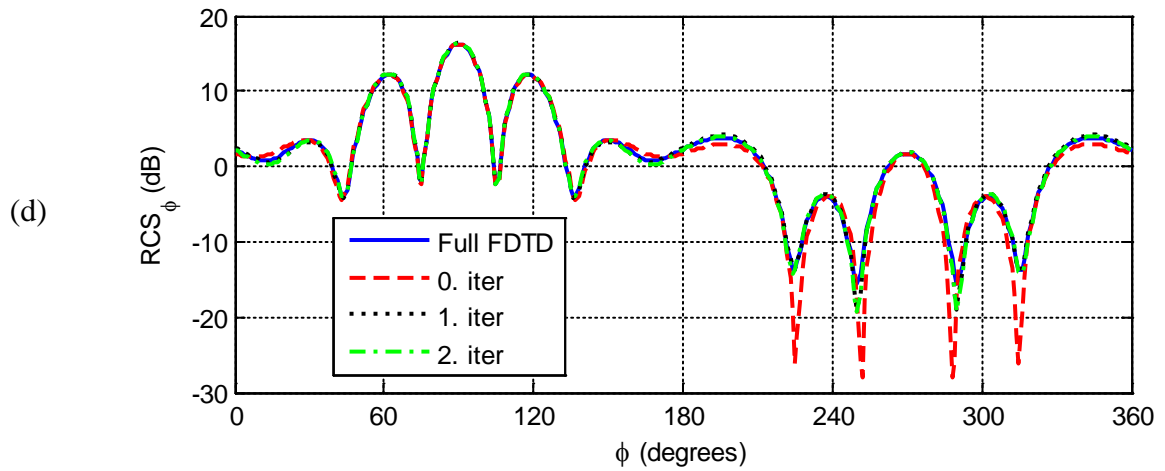
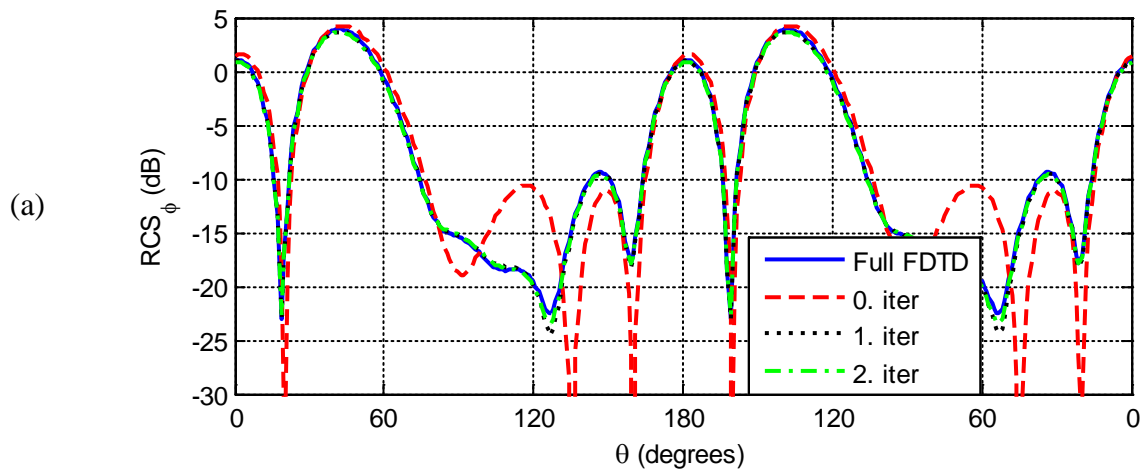
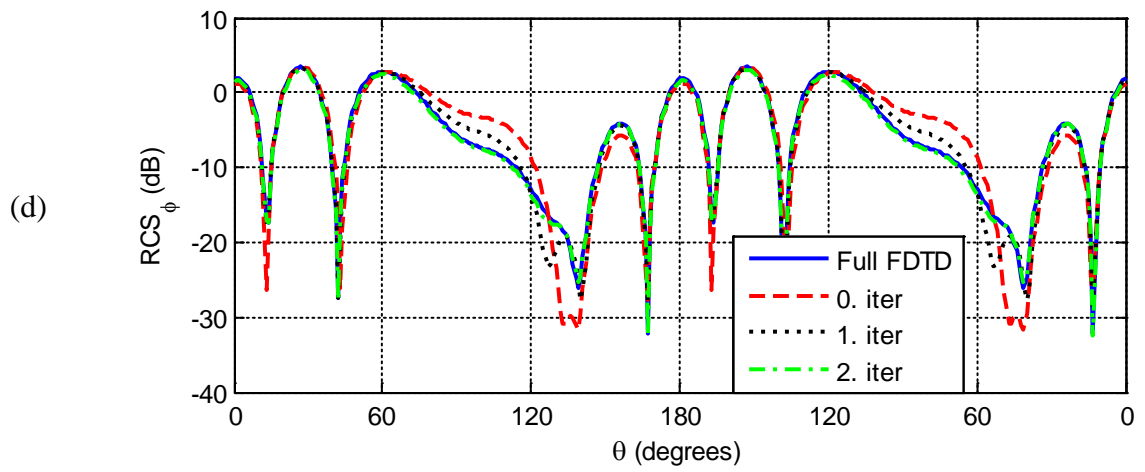
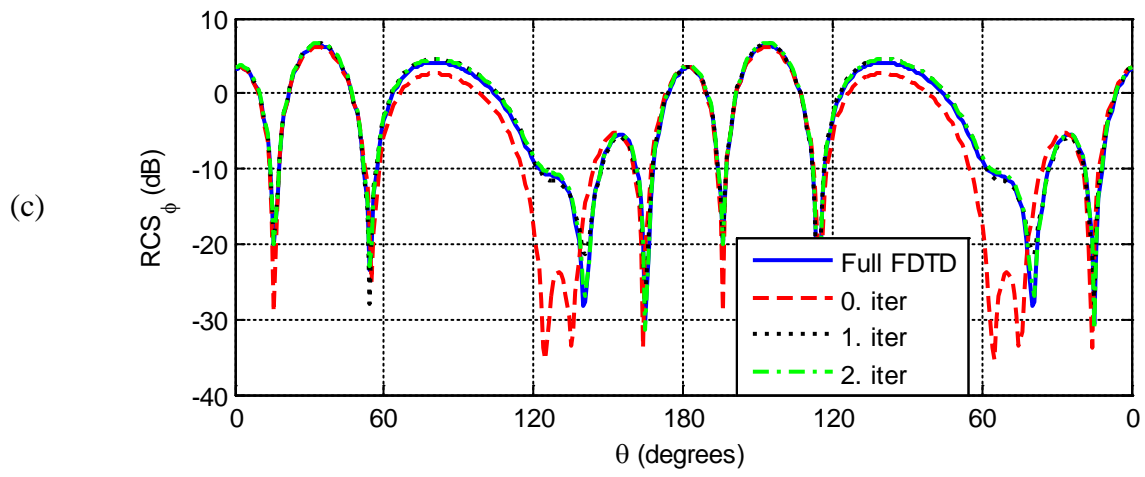
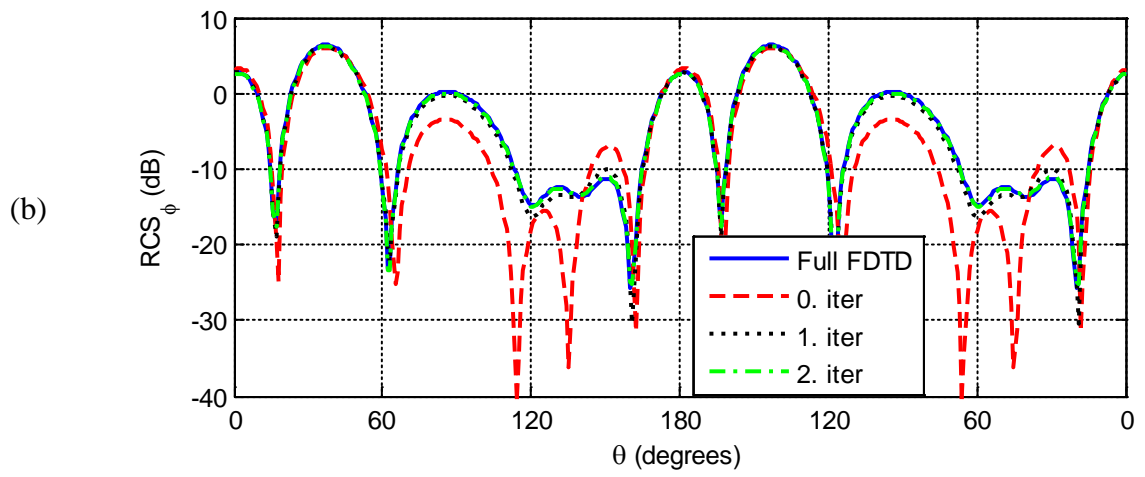


Figure 3.35: Bistatic RCS_φ for xy-plane cut at frequencies: a) 200 MHz, b) 225 MHz, c) 250 MHz, d) 275 MHz, and e) 300 MHz.





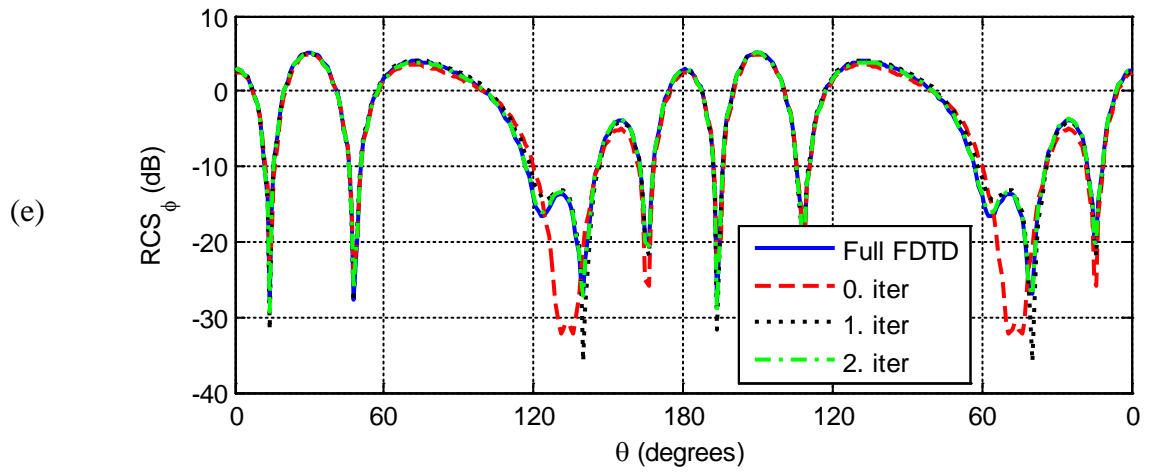
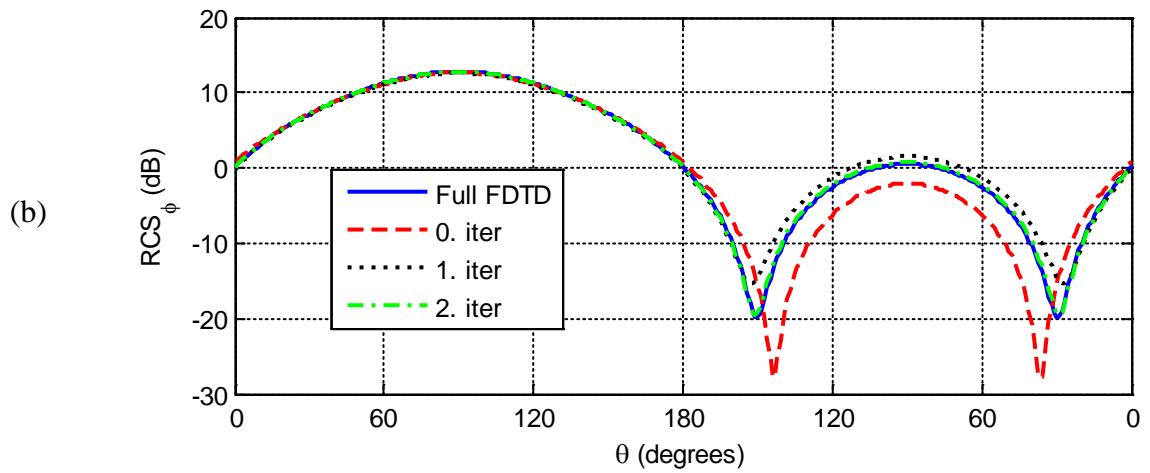
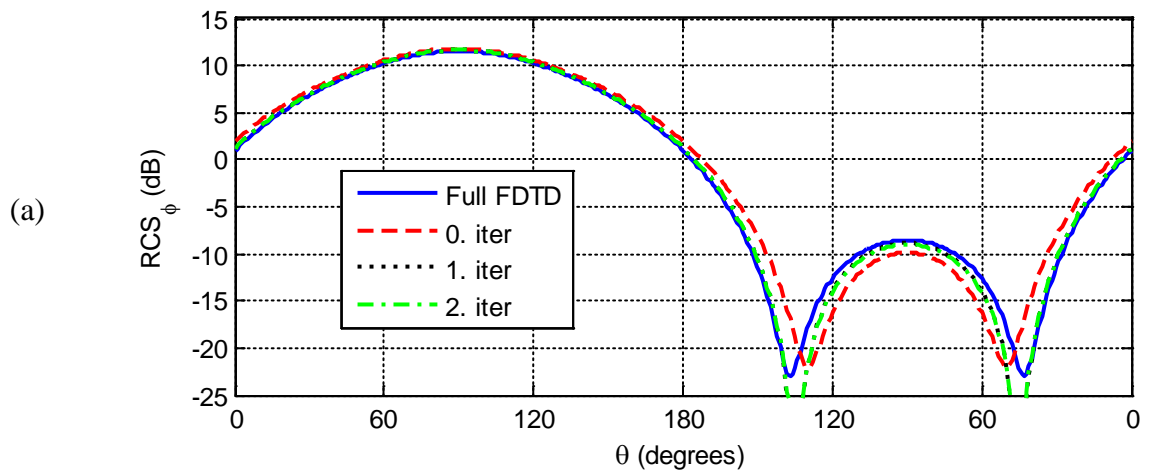


Figure 3.36: Bistatic RCS_ϕ for xz -plane cut at frequencies: a) 200 MHz, b) 225 MHz, c) 250 MHz, d) 275 MHz, and e) 300 MHz.



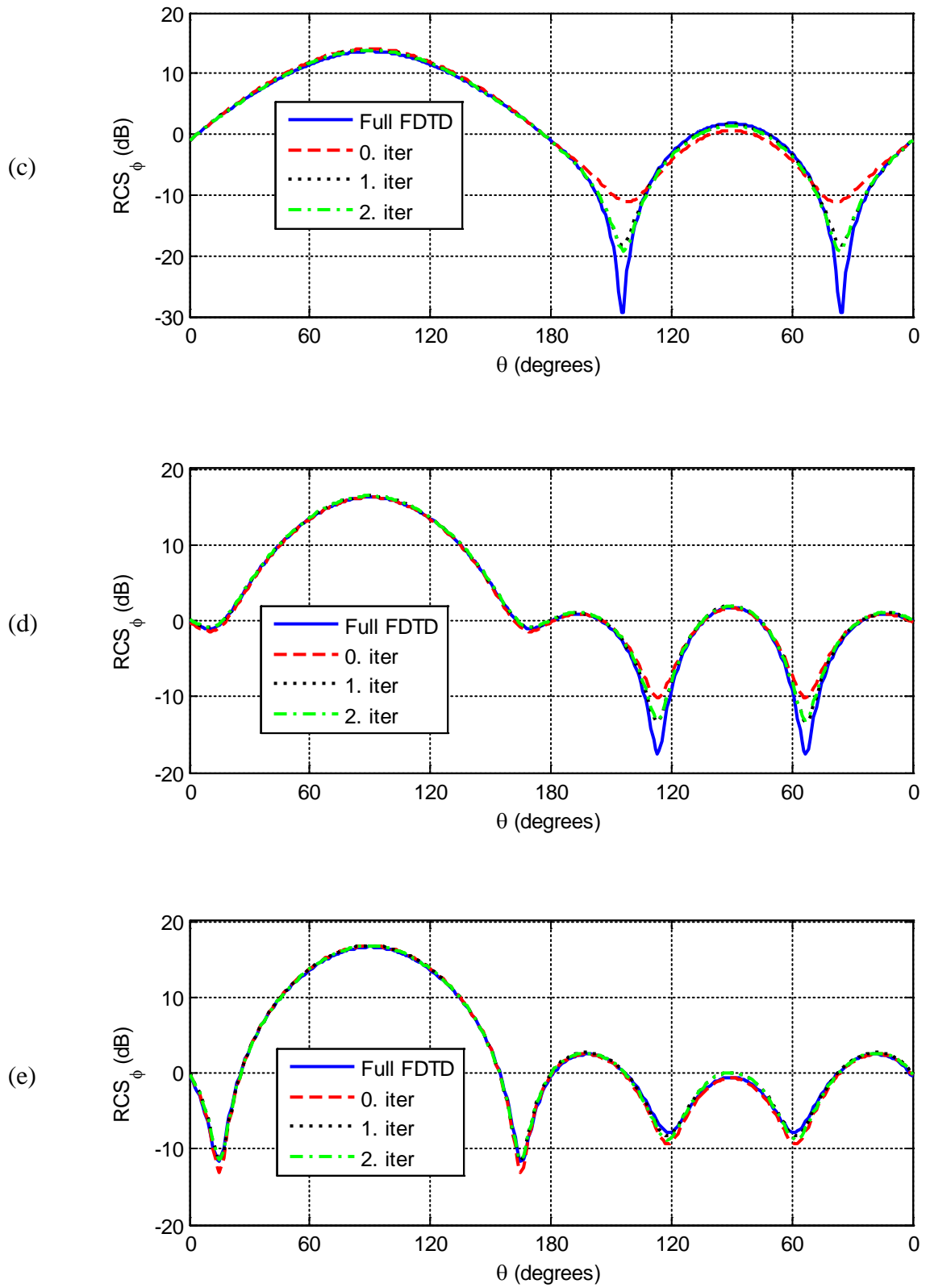


Figure 3.37: Bistatic RCS_ϕ for yz-plane cut at frequencies: a) 200 MHz, b) 225 MHz, c) 250 MHz, d) 275 MHz, and e) 300 MHz.

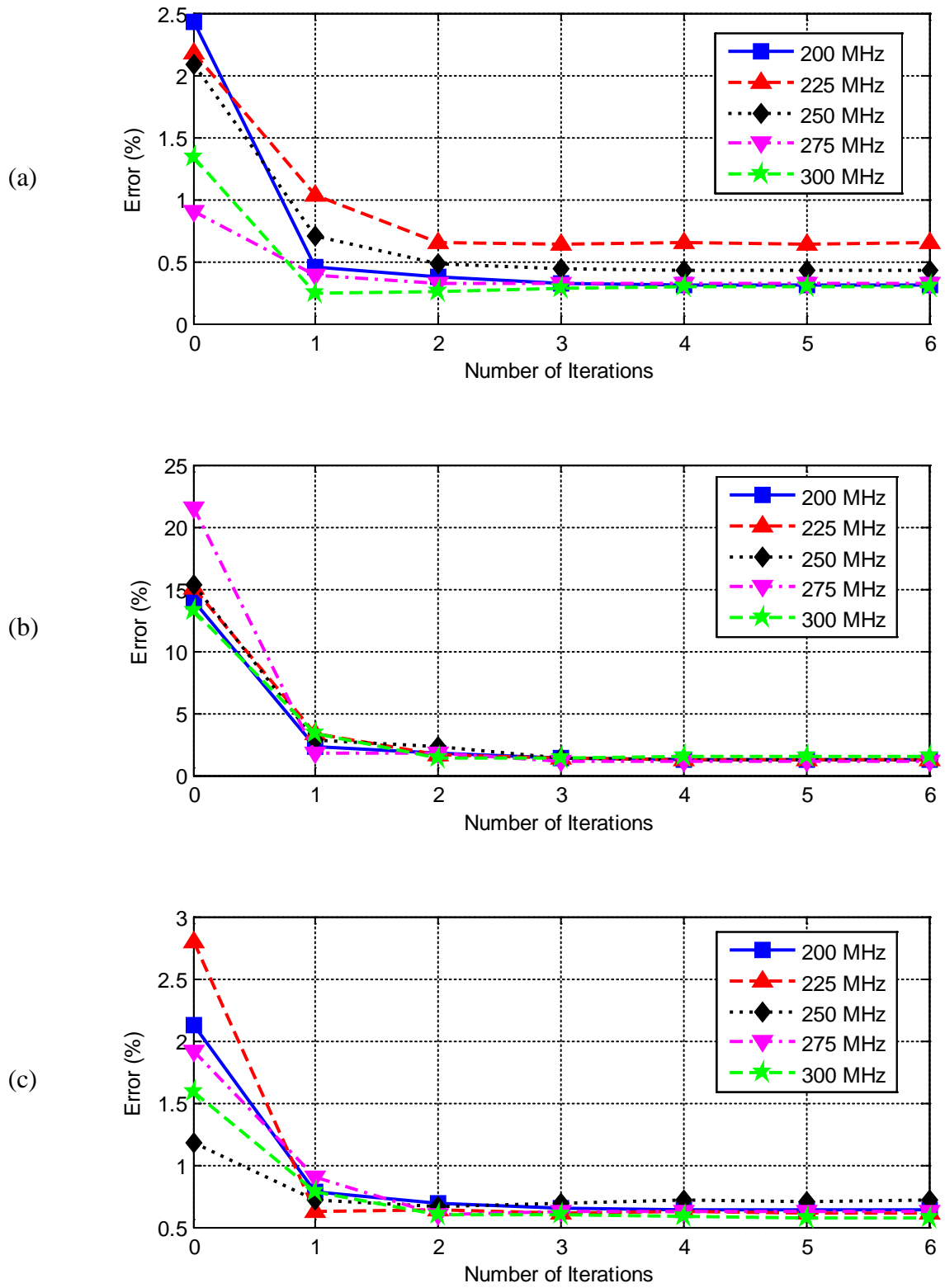


Figure 3.38: Normalized average errors for RCS_θ in the three plane cuts: a) xy -plane, b) xz -plane, and c) yz -plane.

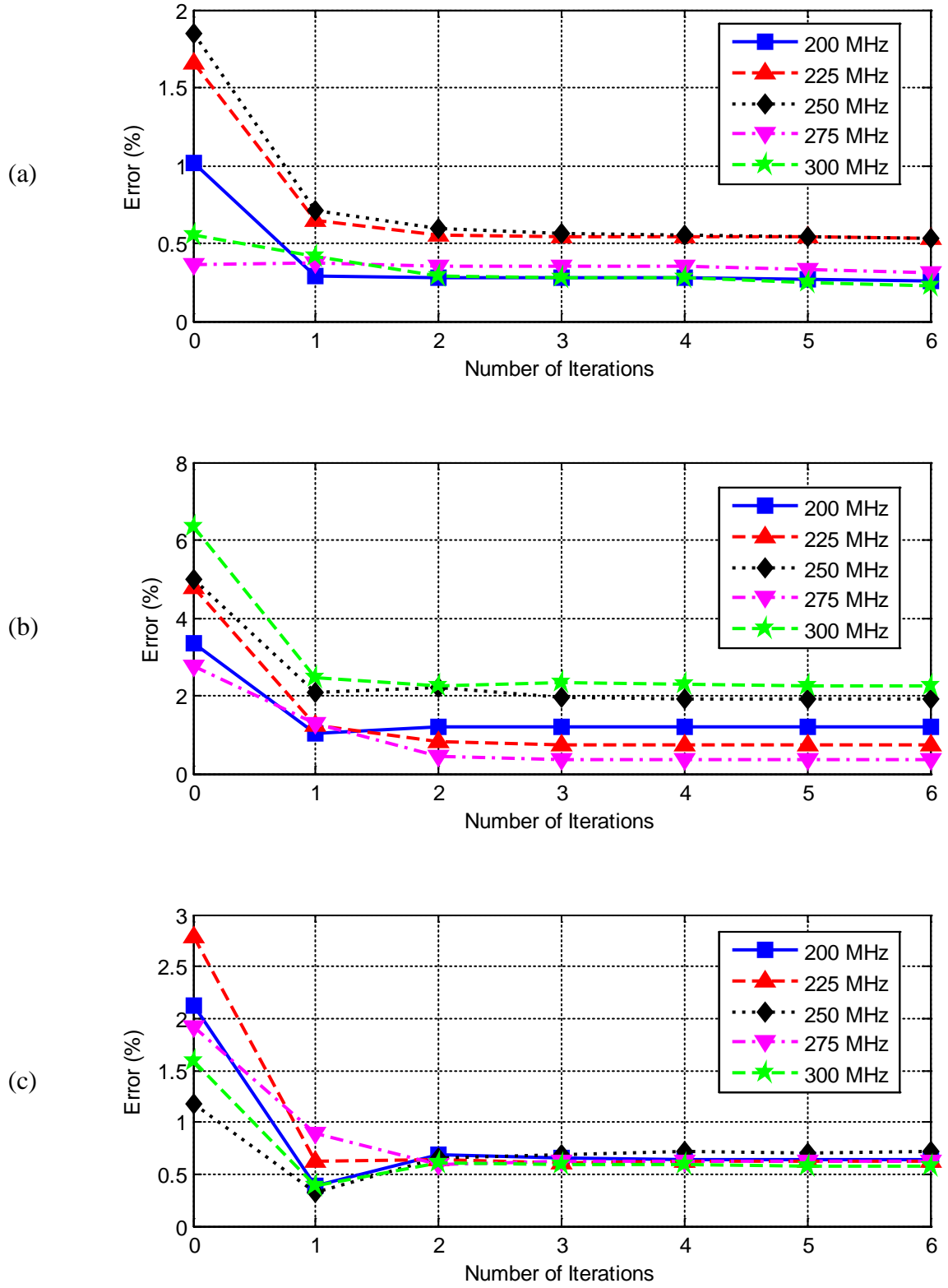


Figure 3.39: Normalized average errors for RCS_ϕ in the three plane cuts: a) xy -plane, b) xz -plane, and c) yz -plane.

3.5 Electromagnetic Scattering from Four Objects

The geometry of the fifth problem illustrated in Figure 3.40 is analyzed to prove the validity of the proposed technique for four scatterer objects where more interaction processes are required between them. Two identical dielectric spheres with the relative permittivity of 3 are placed along the x -axis with 1.2 m separation and two identical conducting ellipsoids are placed along the y -axis with 1.2 m separation. The radius of the dielectric spheres is 0.4 m. The semi-axes of the conducting ellipsoids are 0.2 m, 0.2 m, and 1 m along the x , y , and z axes, respectively. This problem space is excited by a θ and ϕ polarized plane wave with $\theta^{\text{inc}}=90^\circ$ and $\phi^{\text{inc}}=0^\circ$. The problem space is composed of cells with size 0.02 m in the x , y , and z directions for the full domain simulation. As for the IMR simulation, a cell size 0.02 m is used in ellipsoid subregions, whereas a cell size 0.04 m is used in sphere subregions. It can be seen from Figure 3.41 that the IMR algorithm reaches the convergence criterion after iteration # 3. Figures 3.42-3.47 show the bistatic RCS_θ and RCS_ϕ for the three plane cuts at 200 MHz, 225 MHz, 250 MHz, 275 MHz and 300 MHz. To prove the convergence of the full domain and IMR technique results, the normalized average errors for RCS_θ and RCS_ϕ in the three plane cuts are shown in Figures 3.48-3.49. Simulation parameters and computer resources used are summarized in Table 3-5. Results in the table show a considerable reduction in the memory storage requirements, but the computation time of the IMR algorithm is more than that of the full domain solution because the objects are close to each other. The computation time would be less and the memory gain would be more for problems that have large separation between the objects.

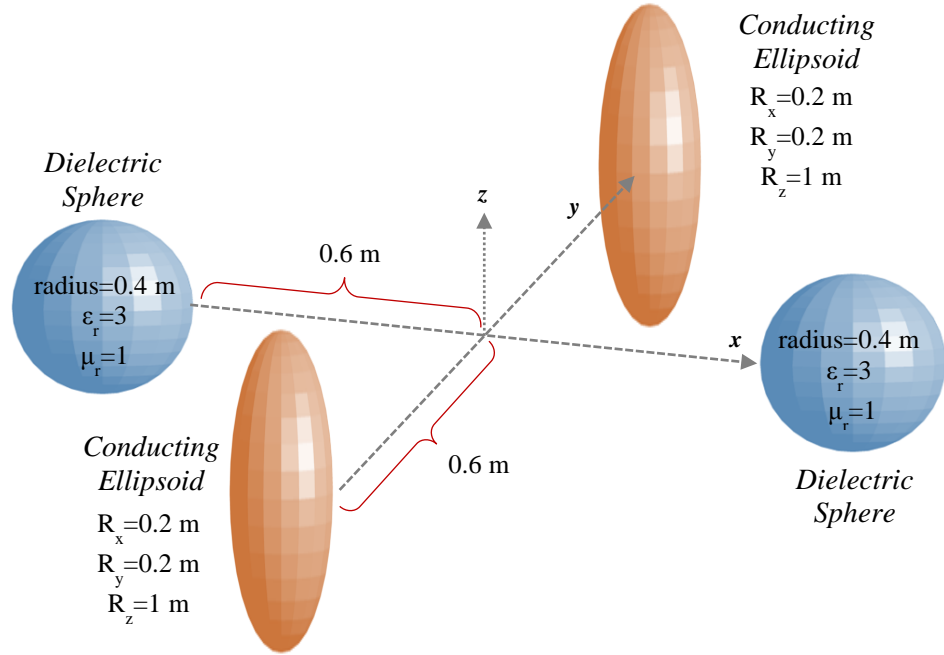


Figure 3.40: Geometry of the fifth problem.

Table 3-5: Simulation parameters and computer resources used by the IMR and full domain simulation.

| | Number of Domains | Total Number of Cells | Computation Time (min.) | Iteration Number | Memory (MB) |
|------------------|-------------------|-----------------------|-------------------------|------------------|-------------|
| Full FDTD | — | 3,345,556 | 132 | — | 1,780 |
| IMR-FDTD | 4 | 1,078,784 | 164 | 3 | 425 |

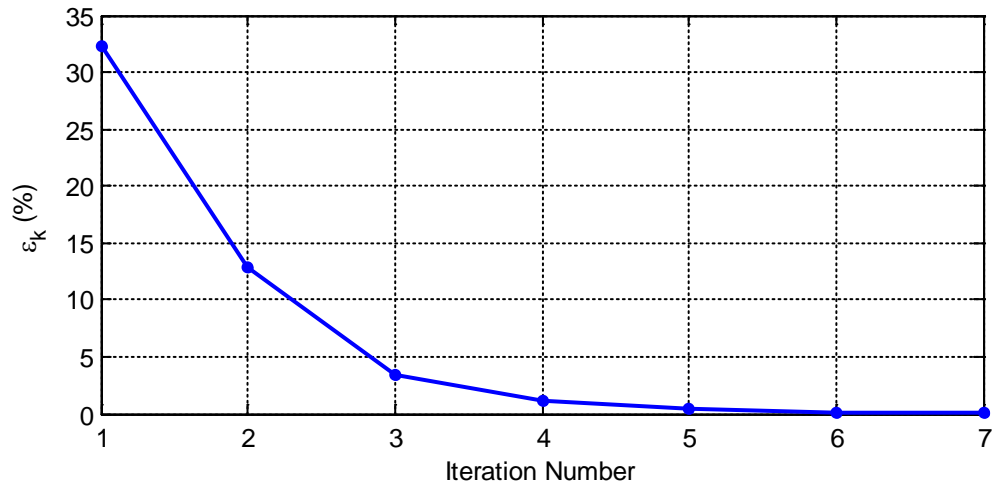
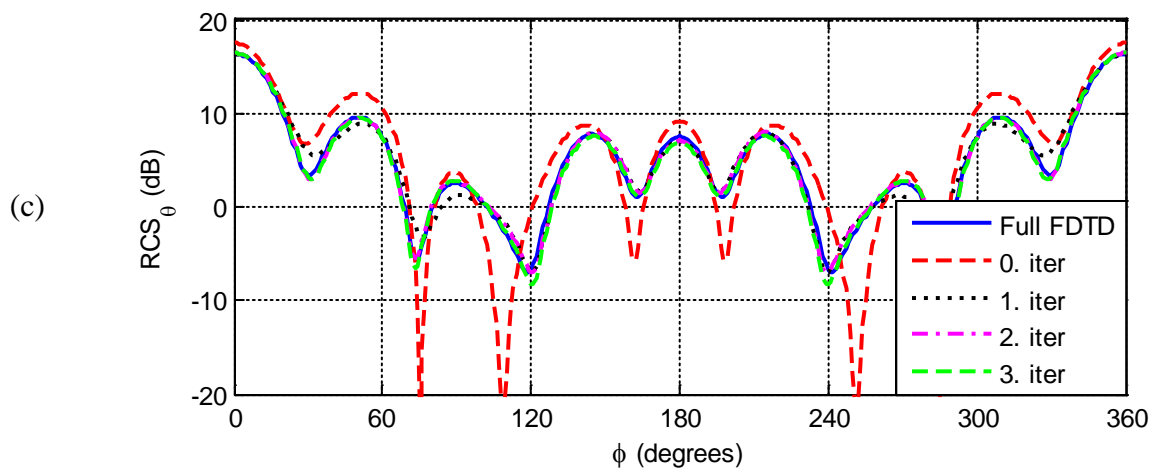
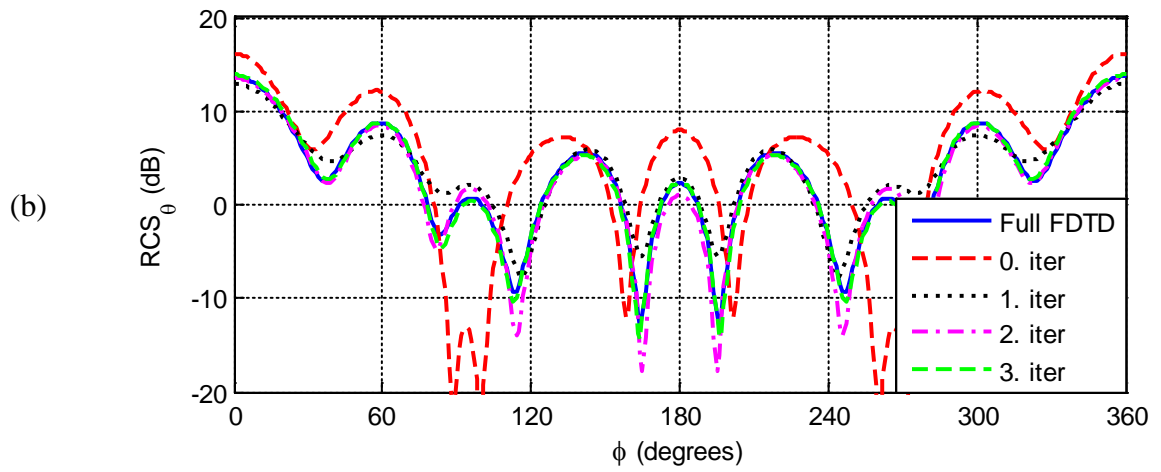
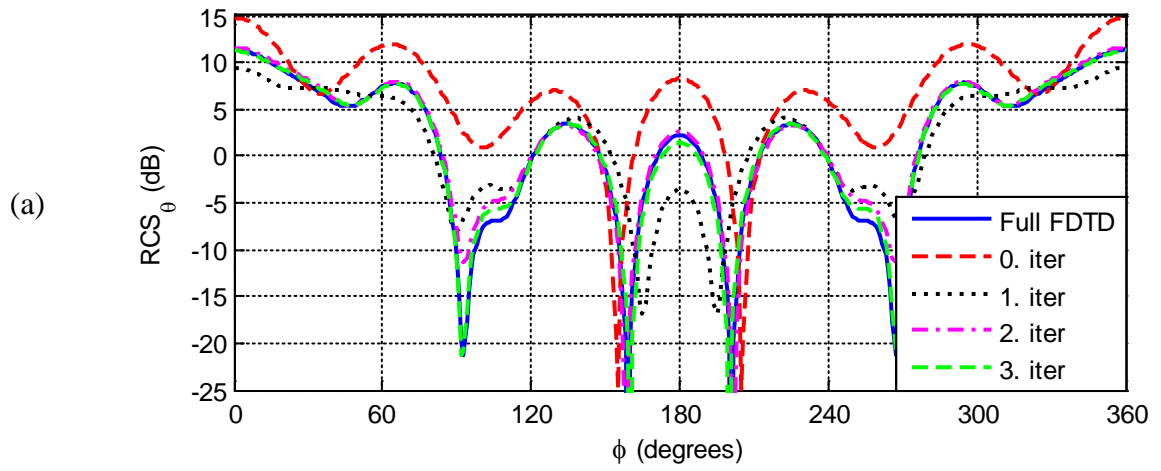


Figure 3.41: Convergence (ε_k) between iteration steps for the fifth problem.



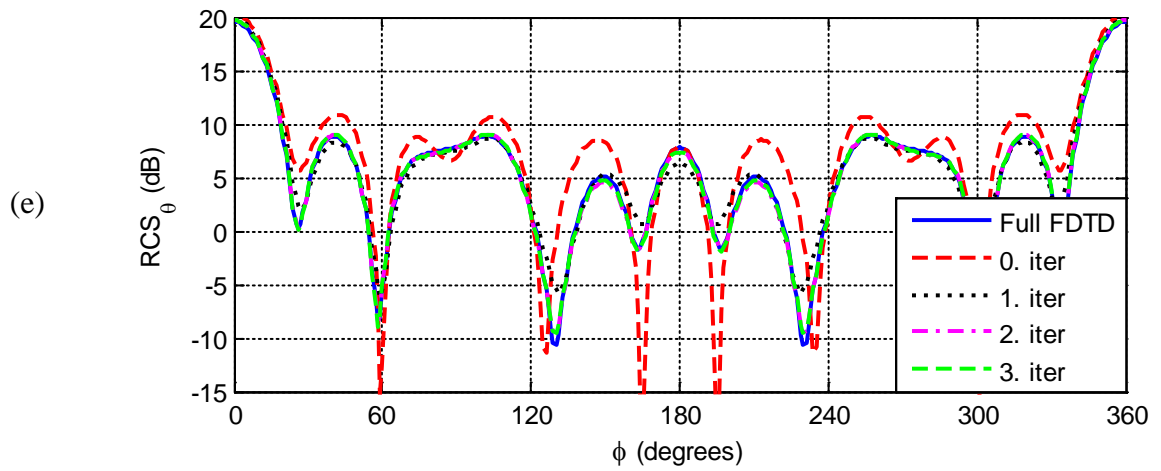
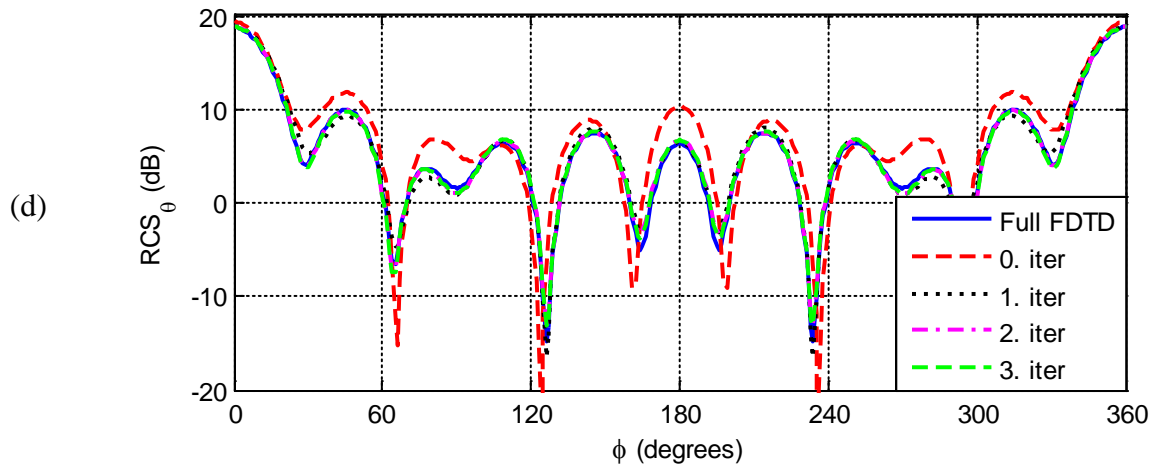
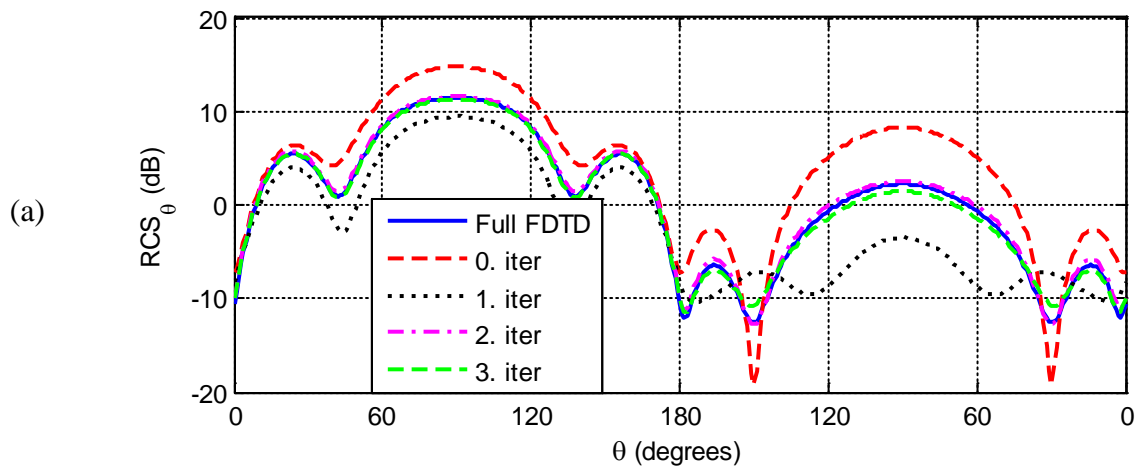
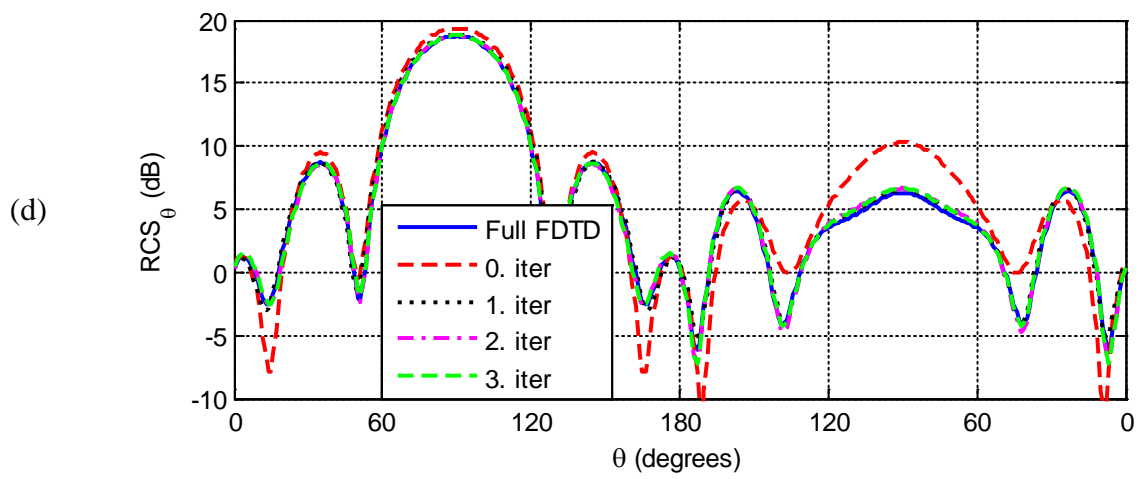
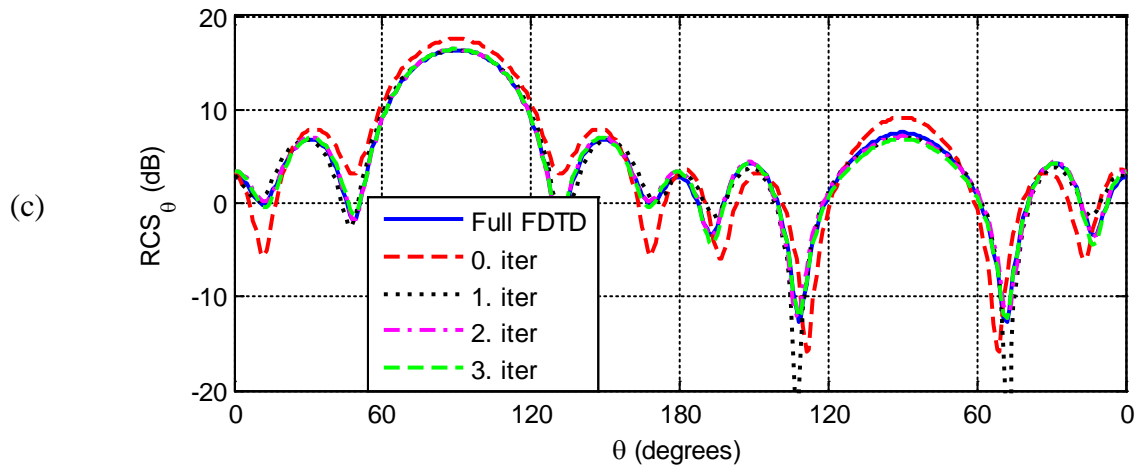
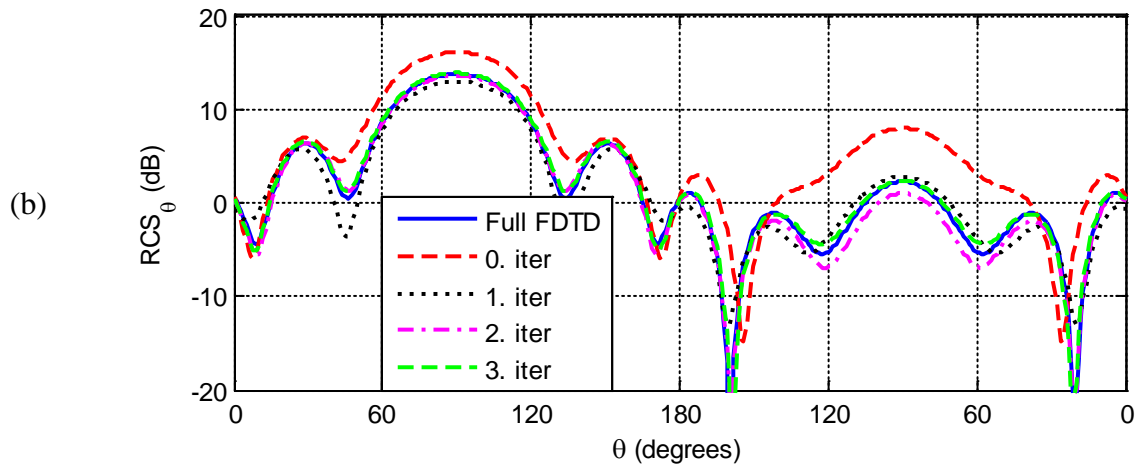


Figure 3.42: Bistatic RCS_{θ} for xy -plane cut at frequencies: a) 200 MHz, b) 225 MHz, c) 250 MHz, d) 275 MHz, and e) 300 MHz.





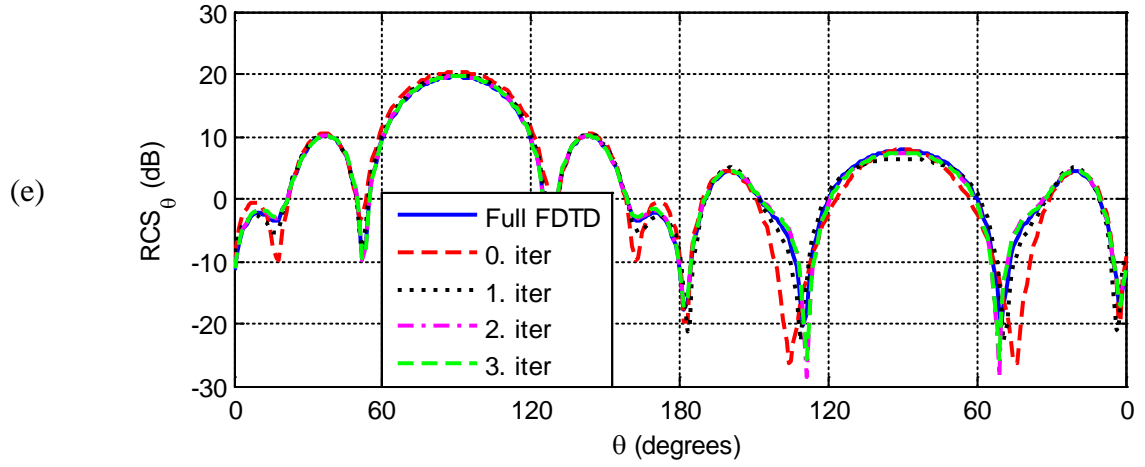
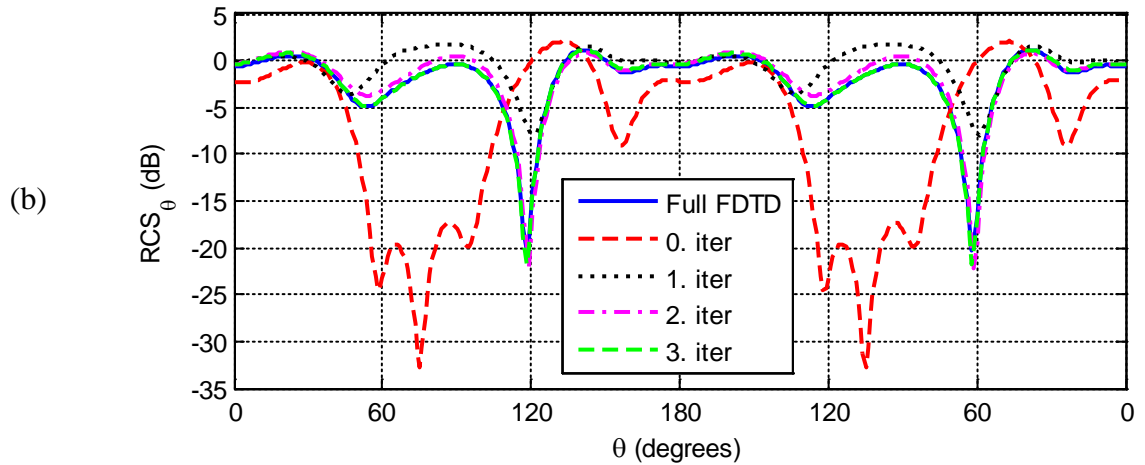
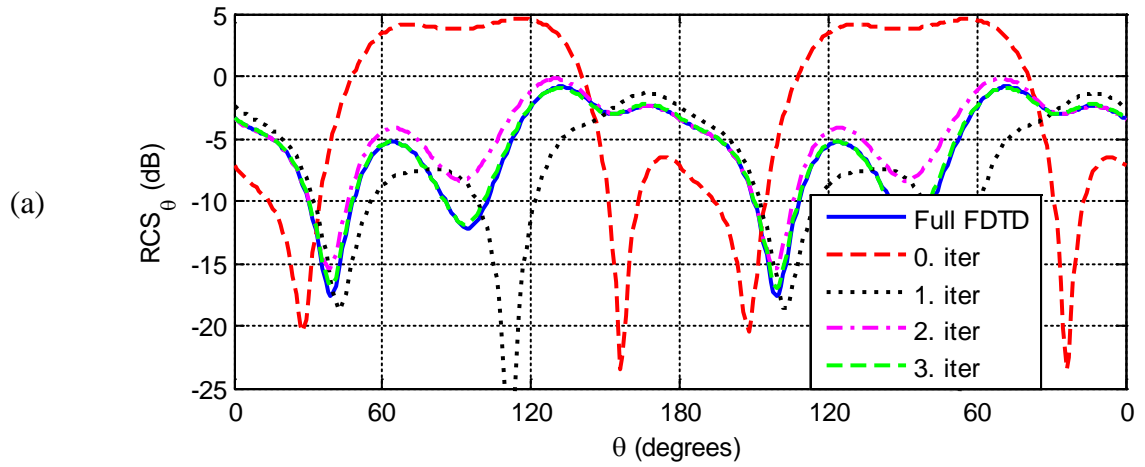


Figure 3.43: Bistatic RCS_θ for xz -plane cut at frequencies: a) 200 MHz, b) 225 MHz, c) 250 MHz, d) 275 MHz, and e) 300 MHz.



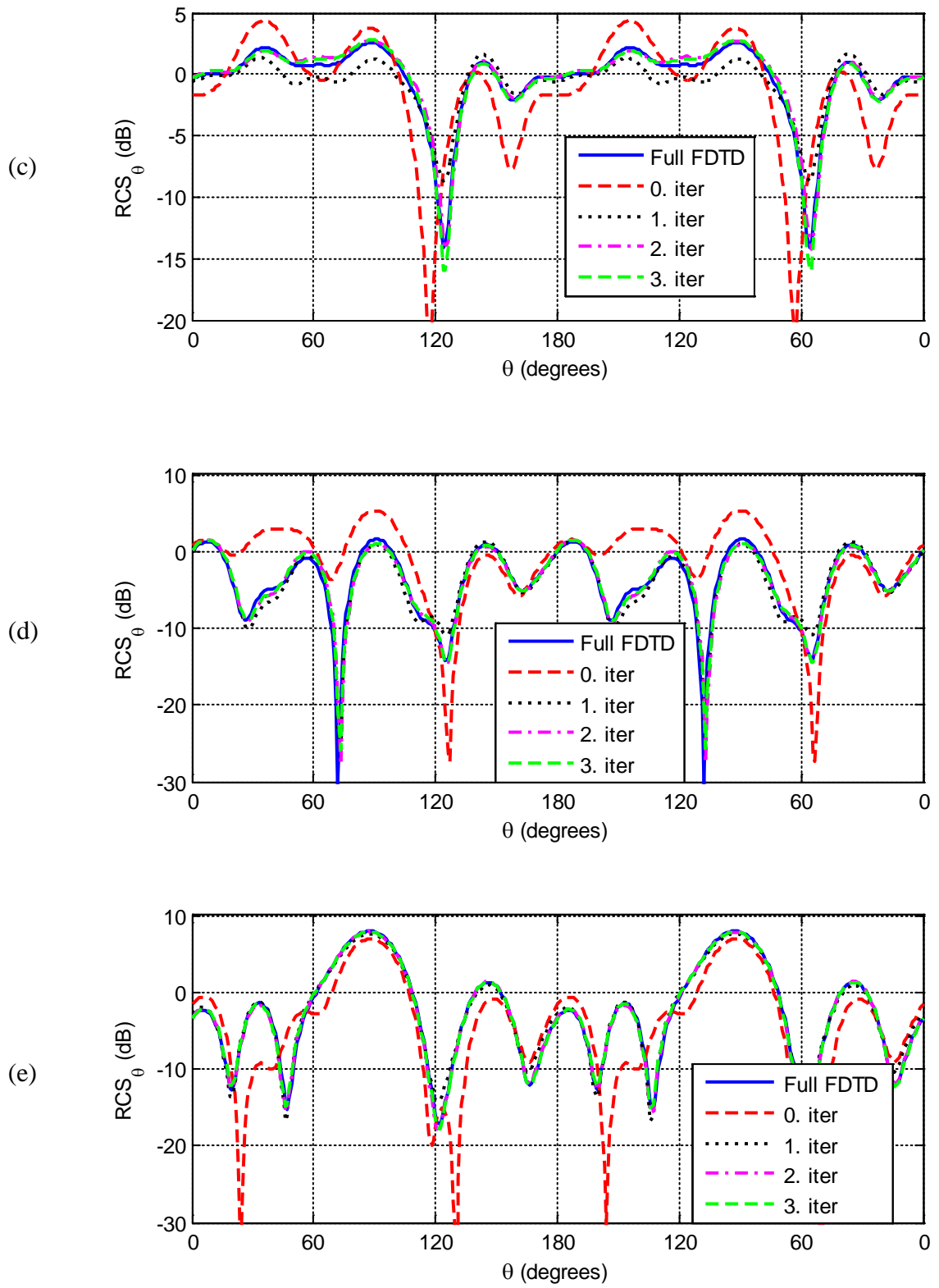
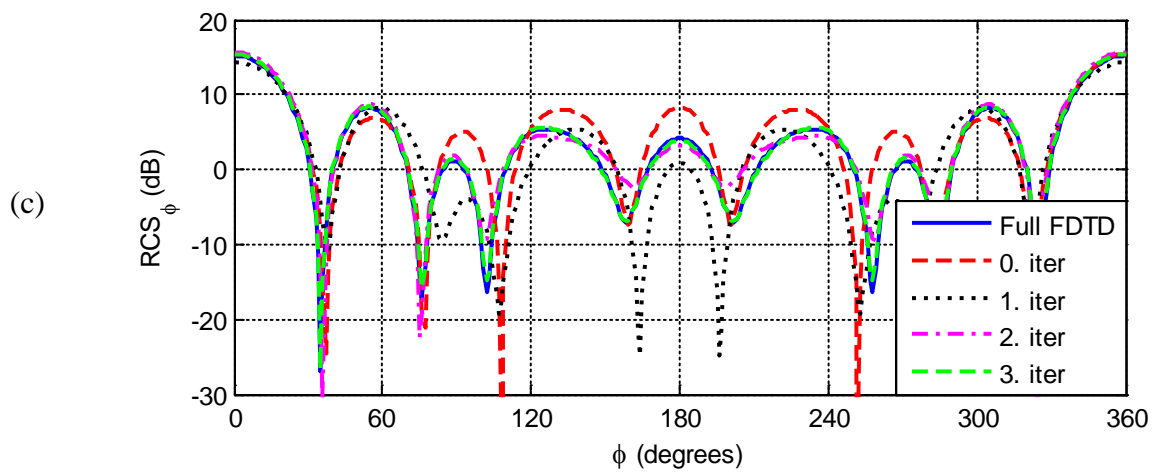
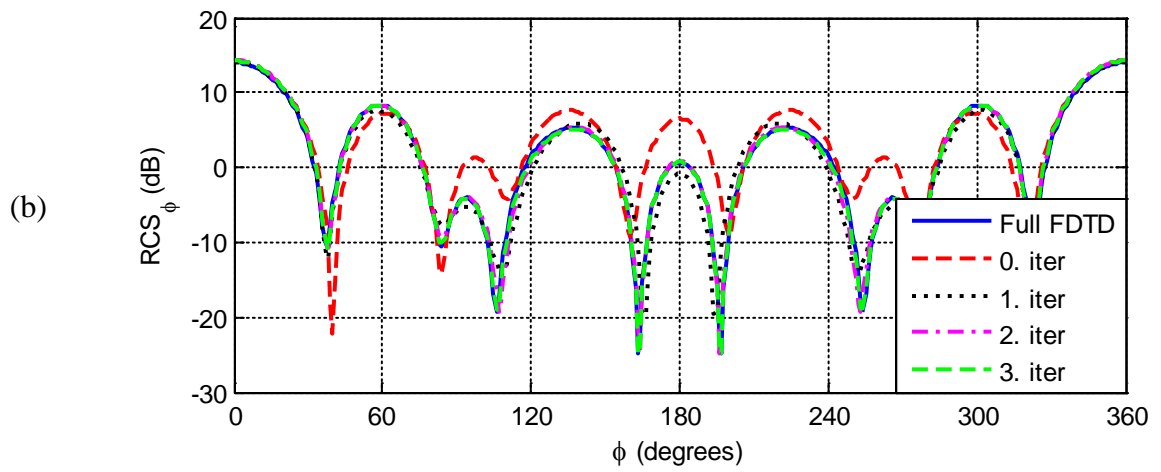
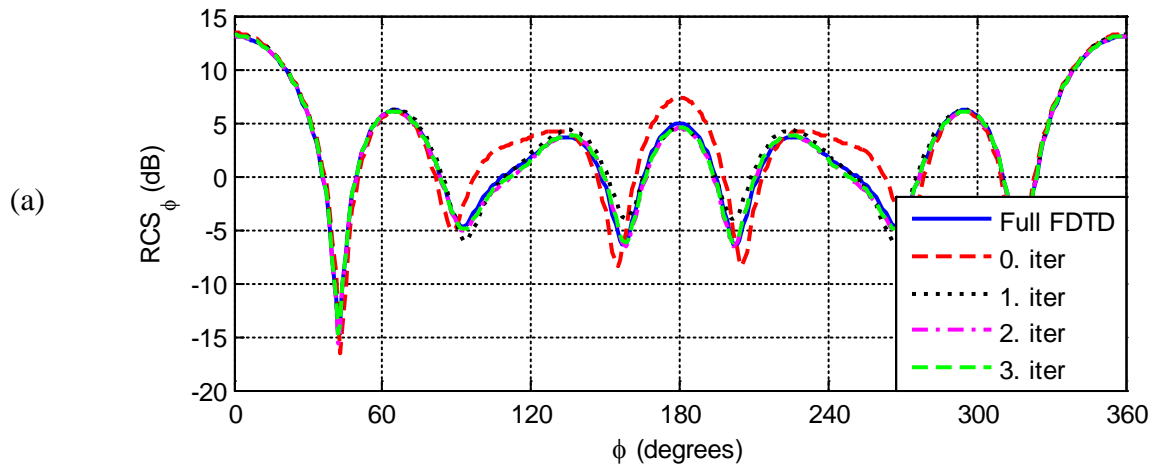


Figure 3.44: Bistatic RCS_θ for yz -plane cut at frequencies: a) 200 MHz, b) 225 MHz, c) 250 MHz, d) 275 MHz, and e) 300 MHz.



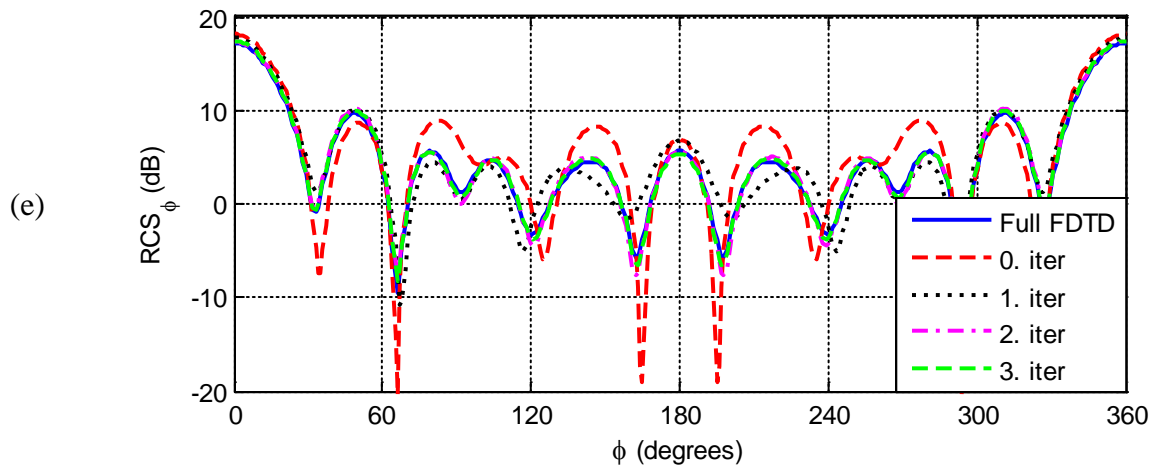
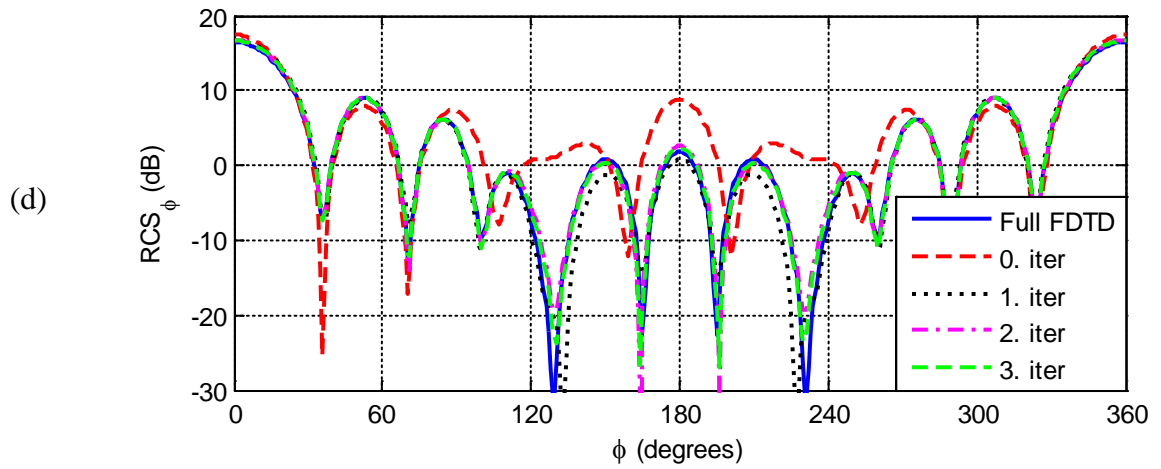
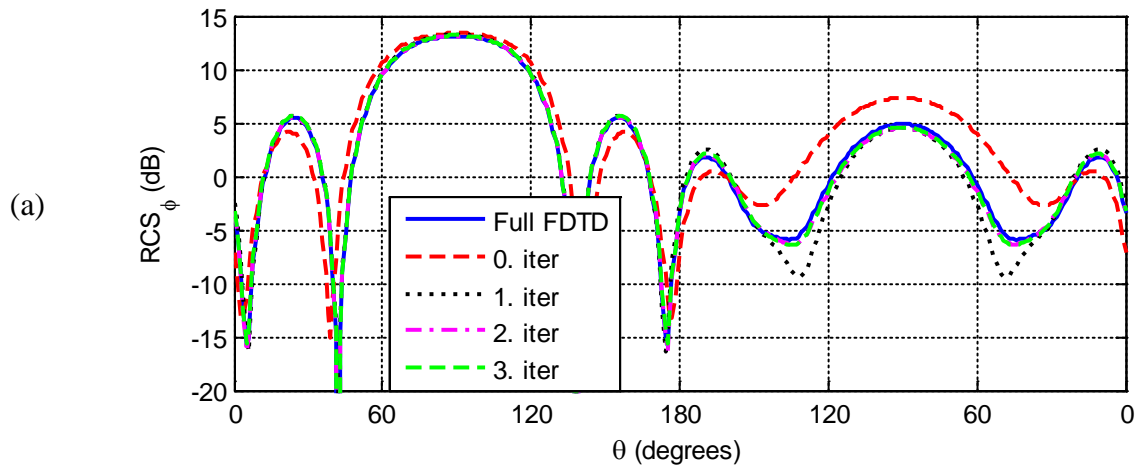
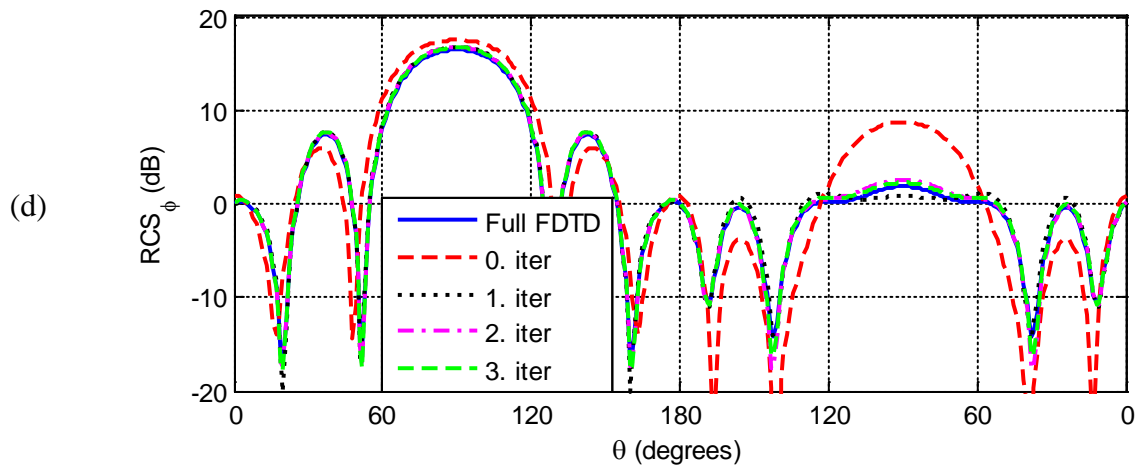
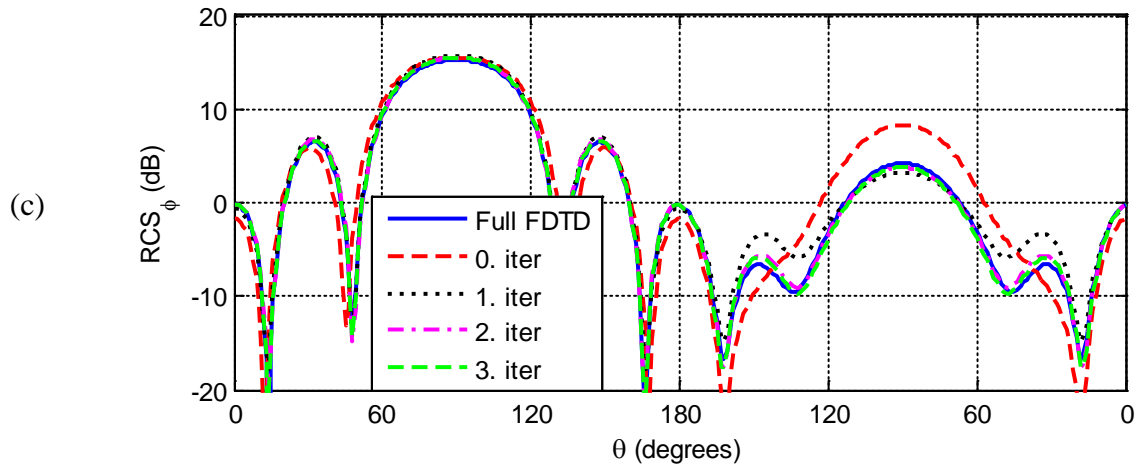
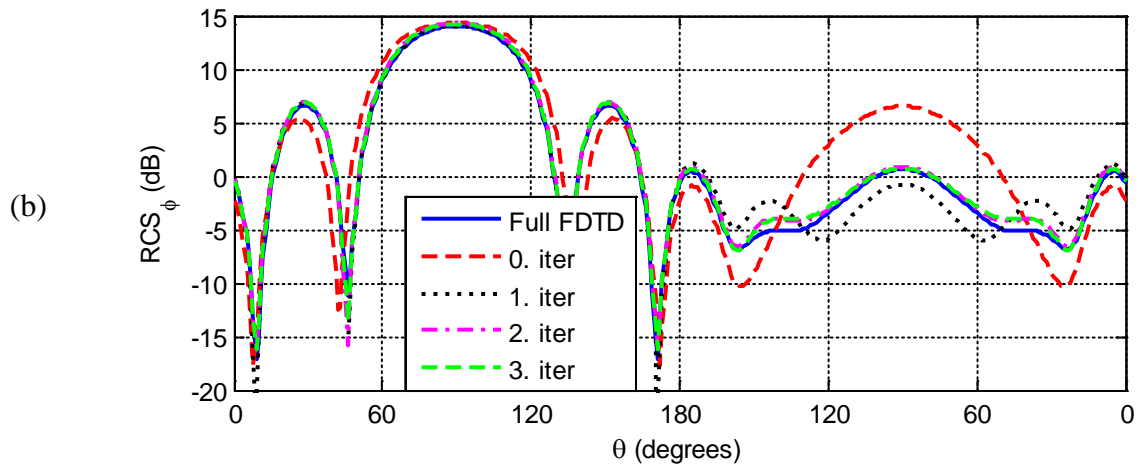


Figure 3.45: Bistatic RCS_φ for xy-plane cut at frequencies: a) 200 MHz, b) 225 MHz, c) 250 MHz, d) 275 MHz, and e) 300 MHz.





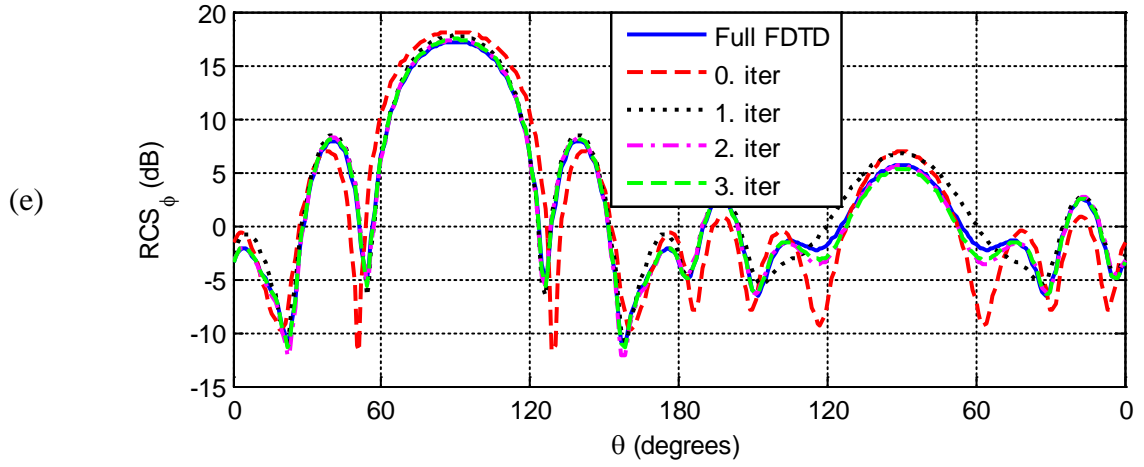
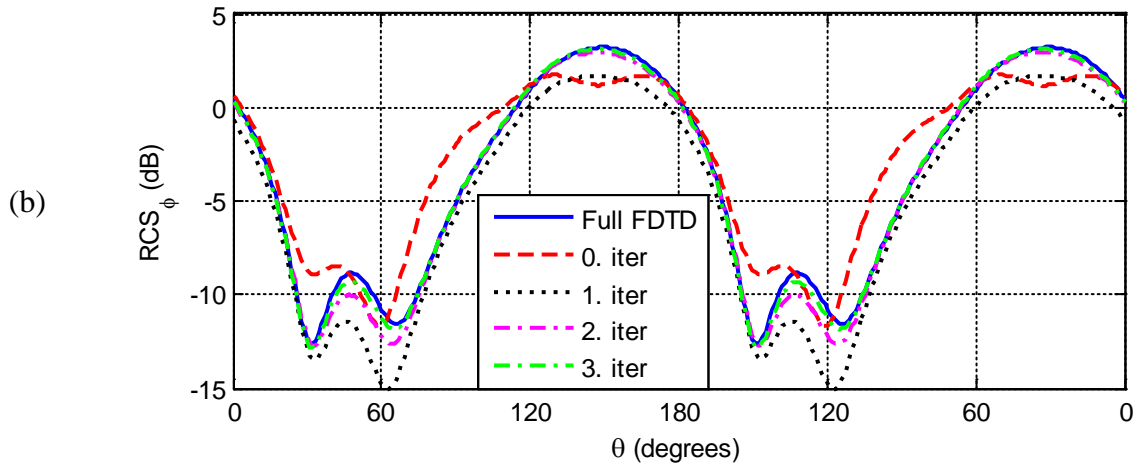
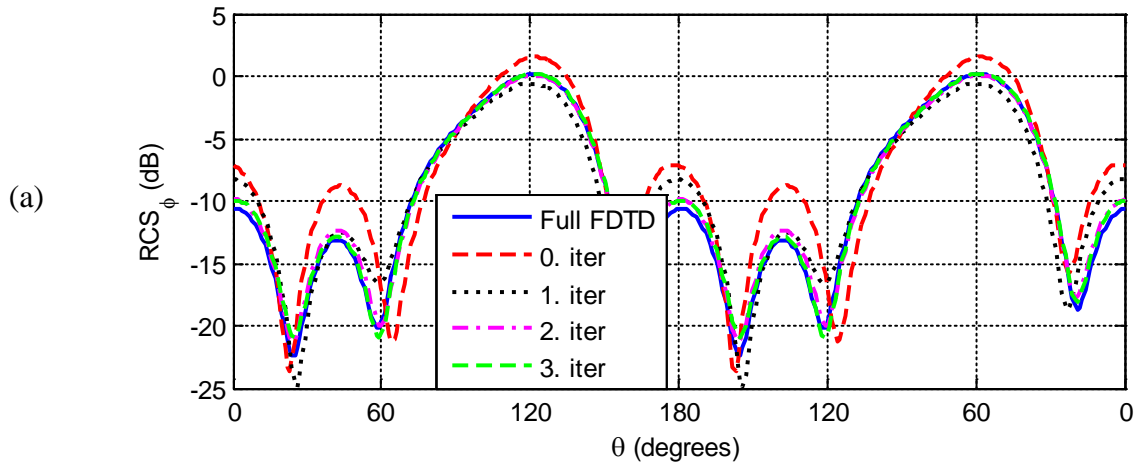


Figure 3.46: Bistatic RCS_ϕ for xz -plane cut at frequencies: a) 200 MHz, b) 225 MHz, c) 250 MHz, d) 275 MHz, and e) 300 MHz.



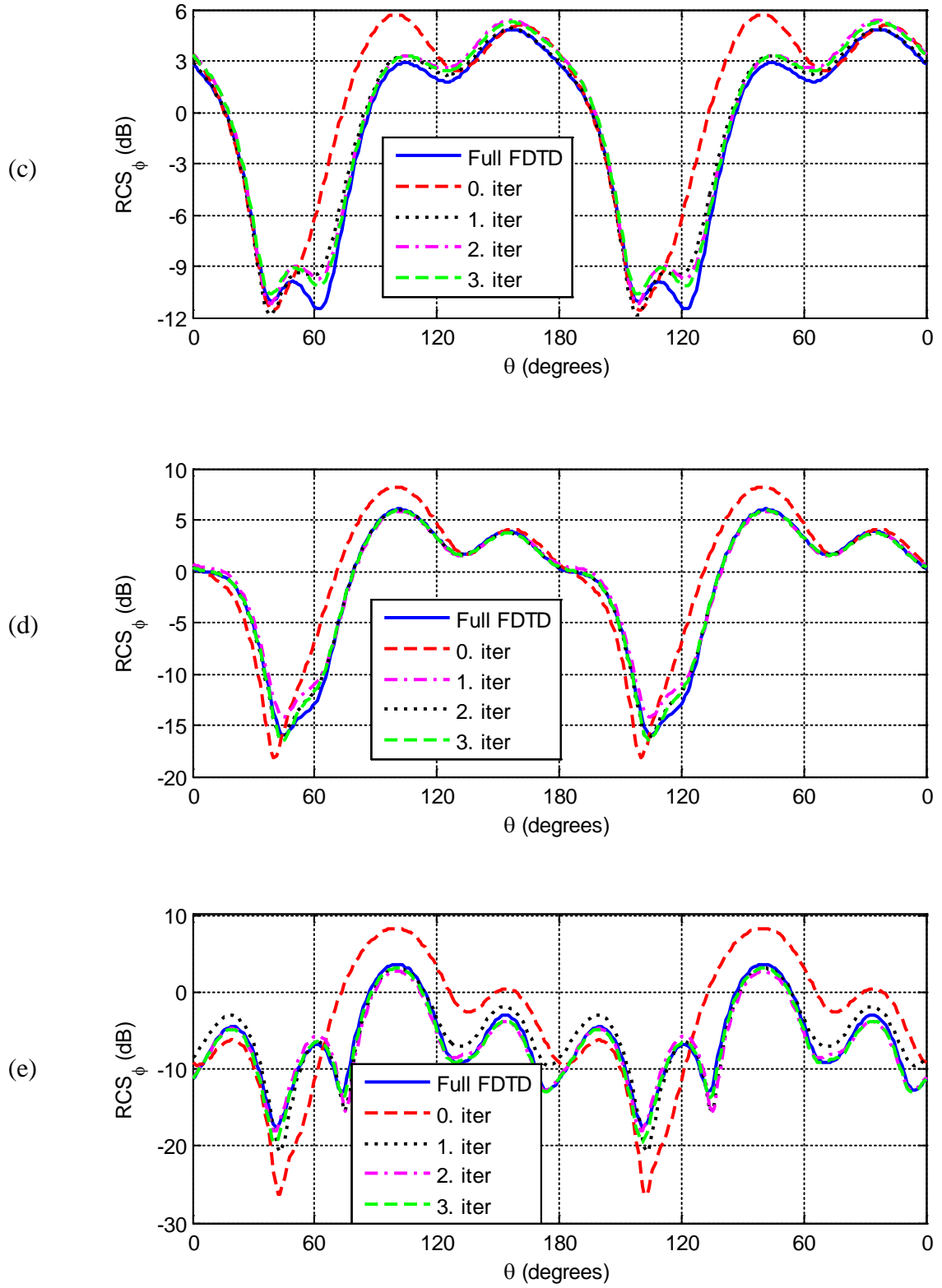


Figure 3.47: Bistatic RCS_ϕ for yz -plane cut at frequencies: a) 200 MHz, b) 225 MHz, c) 250 MHz, d) 275 MHz, and e) 300 MHz.

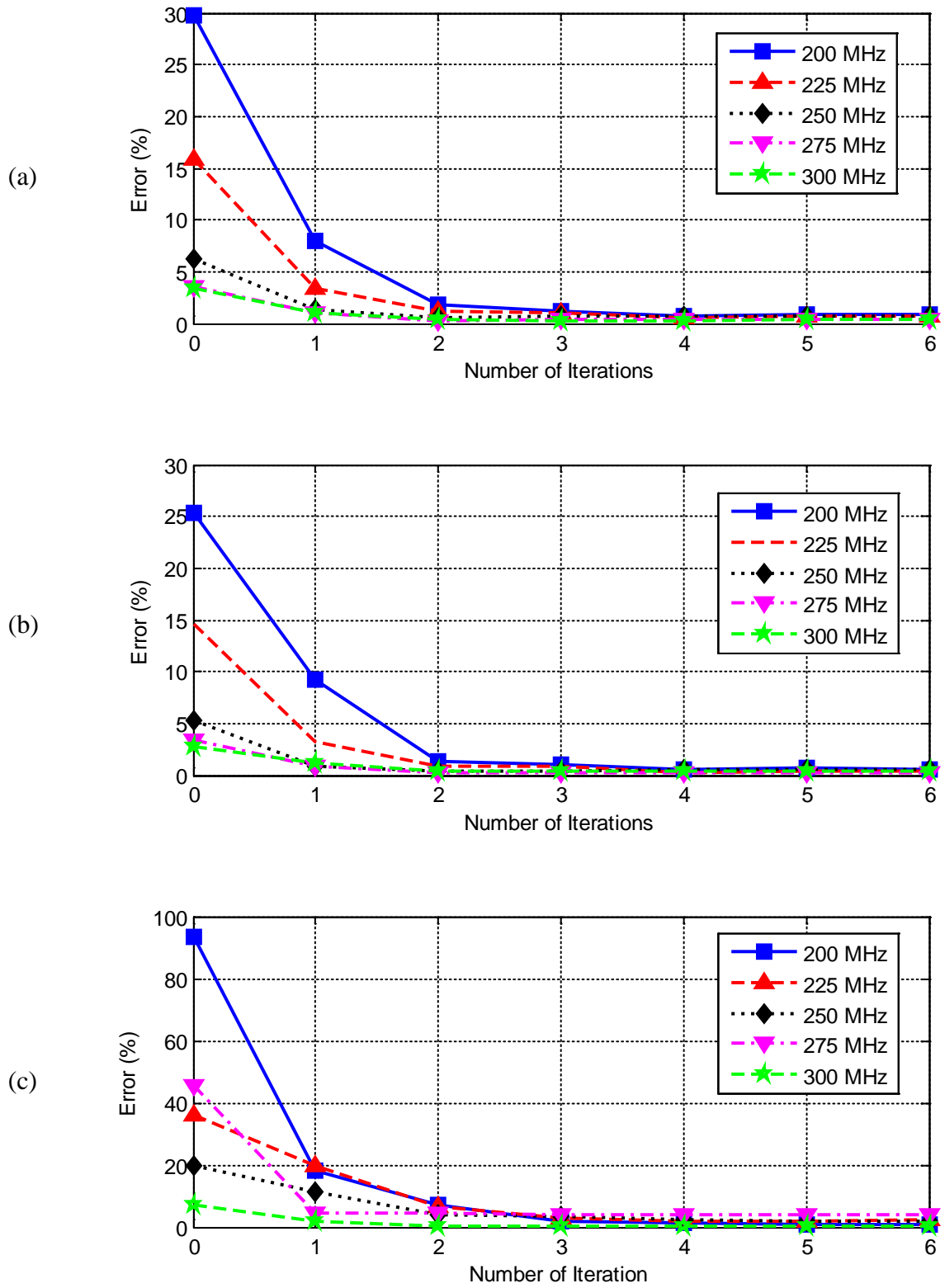


Figure 3.48: Normalized average errors for RCS_{θ} in the three plane cuts: a) xy -plane, b) xz -plane, and c) yz -plane.

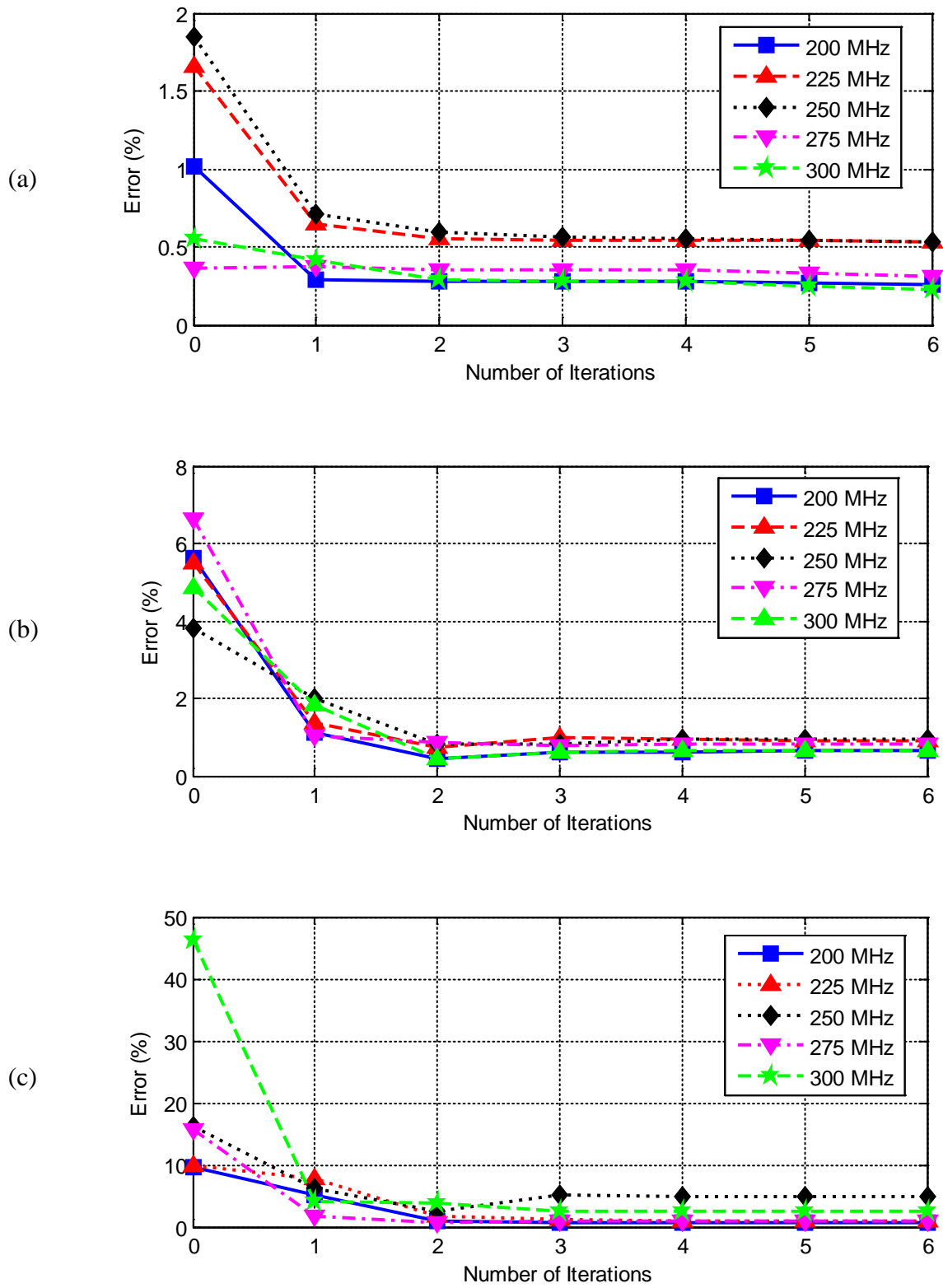


Figure 3.49: Normalized average errors for RCS_ϕ in the three plane cuts: a) xy -plane, b) xz -plane, and c) yz -plane.

4 NUMERICAL RESULTS FOR RADIATION PROBLEMS

In this chapter, numerical results of radiation problems including an antenna and scatterer objects are analyzed to prove the validity of the FDTD method integrated into the IMR technique. In all simulations, the problems include a 0.5 m dipole antenna. First, the dipole antenna is driven in isolation so that, in what will be called the 0th iteration, there is no incident field in the subregion containing the driven antenna, and the incident fields in all the other subregions consist of the field of the driven antenna in isolation. The driven antenna is active for the simulation of original problem and that of the IMR algorithm in iteration # 0, whereas the driven antenna is inactive in the IMR algorithm for other iterations. The active and inactive dipole antenna shown in Figure 4.1 are configured as two rectangular rods with square base of side length equal to 31.25 mm. The thickness of the dipole is four cells in both x and y direction. A voltage source with 50 Ω internal impedance and 1 Volt (V) magnitude is placed along four cells between the rods. A cell size of 7.8125 mm is used for the antenna.

The antenna is simulated alone using the FDTD method to determine the frequency bands in which it radiates well. The frequencies 230 MHz, 240 MHz, 250 MHz, 260 MHz, and 270 MHz are found to be in the band of operation. Figure 4.2 shows the magnitude of the reflection coefficient of the dipole antenna.

For all of the examples presented in this chapter the FDTD problem spaces are terminated by eight CPML layers with the CPML parameters [33] *CPML_order*: 3, *CPML_sigma_factor*: 1.5, *CPML_kappa*: 7, *CPML_alpha_min*: 0, and

CPML_α_{max}: 0.05. In addition to the eight CPML layers, ten air buffer layers are introduced between the inner CPML boundary and the objects inside the problem spaces. A cell size of 7.8125 mm is used for the full domain simulations and the subregion containing the antenna in the IMR simulations, whereas a cell size of 15.625 mm is used for the scatterer subregions in the IMR simulations. The specifications of the computer used for the simulations are given in Appendix B.

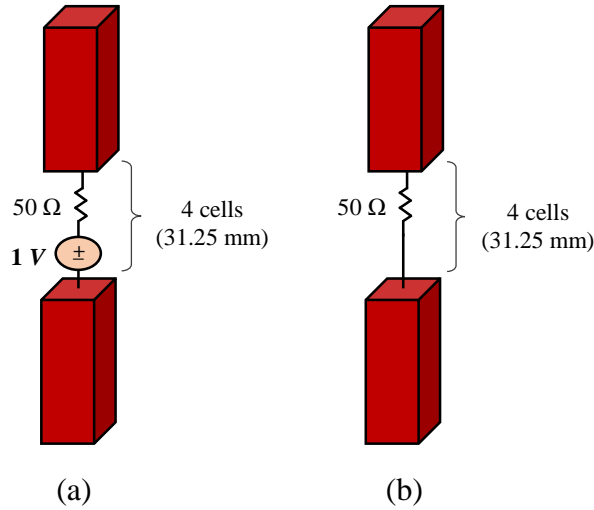


Figure 4.1: a) Configuration of the 0.5 m active dipole antenna and b) Configuration of the 0.5 m inactive dipole antenna.

An algorithm is developed to stop the FDTD time-marching loop and define the necessary number of time steps for the full domain and IMR simulations. In this algorithm, the excitation fields are applied to a problem space until the magnitudes of the scattered electric fields at certain points in the computation domain reach to values less than a threshold value. In our analysis, the threshold is defined as 5×10^{-4} (Volts/meter). Thus the FDTD time-marching loop is stopped when the scattered fields reach below the threshold.

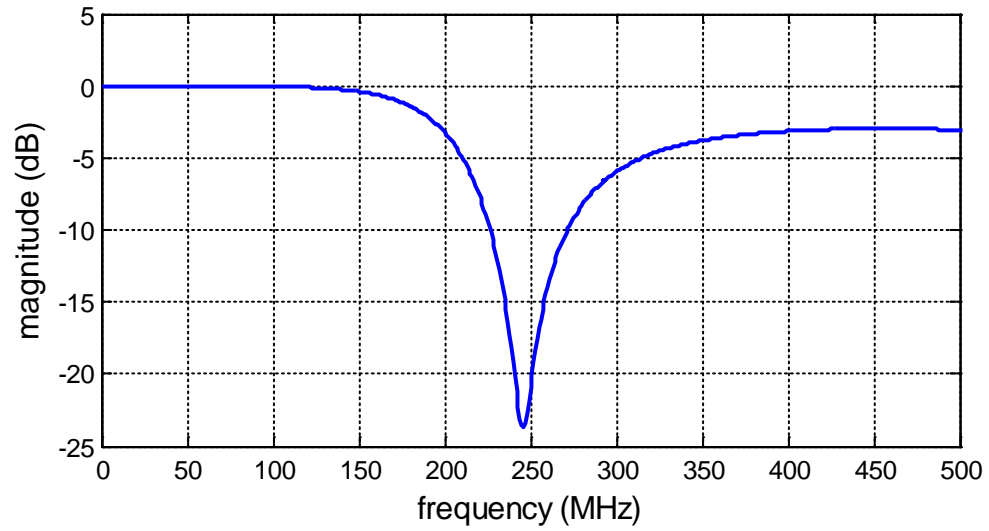


Figure 4.2: Magnitude of the reflection coefficient of a single 0.5 m dipole antenna.

4.1 Radiation from a Dipole Antenna in the Presence of an Object

The geometry of the first problem, as illustrated in Figure 4.3, consists of two objects; a 0.5 m dipole antenna placed a distance of 0.2 m away from a conducting L-shaped box along the x direction. The dimensions of the conducting L-shaped box are given in Figure 4.3. Figure 4.4 shows the convergence of the IMR iteration calculated by (2.12). It can be seen that the IMR algorithm reaches the convergence criterion ($\epsilon_k < 5\%$) after iteration # 2. Figures 4.5-4.7 show the radiation patterns (Gain_θ) of the configuration for the three plane cuts, i.e xy , xz , and yz planes, respectively. Figures 4.8-4.10 show the radiation patterns (Gain_ϕ) of the problem for the three plane cuts. The radiation patterns show a good agreement between the results generated using the IMR technique with those generated using the full domain simulation after iteration # 2. To prove the convergence of the IMR and the full domain results at the frequencies of interest, the normalized average

errors for Gain_θ and Gain_ϕ in the three plane cuts at each frequency of interest are calculated using (2.33) and shown in Figures 4.11-4.12, respectively. Simulation parameters and computer resources are summarized in Table 4-1. Results in the table show a considerable reduction in the memory storage requirements, but the computation time of the IMR algorithm is more than that of the full domain solution because the objects are close to each other. The computation time would be less and the memory gain would be more for problems that have large separation between the objects.

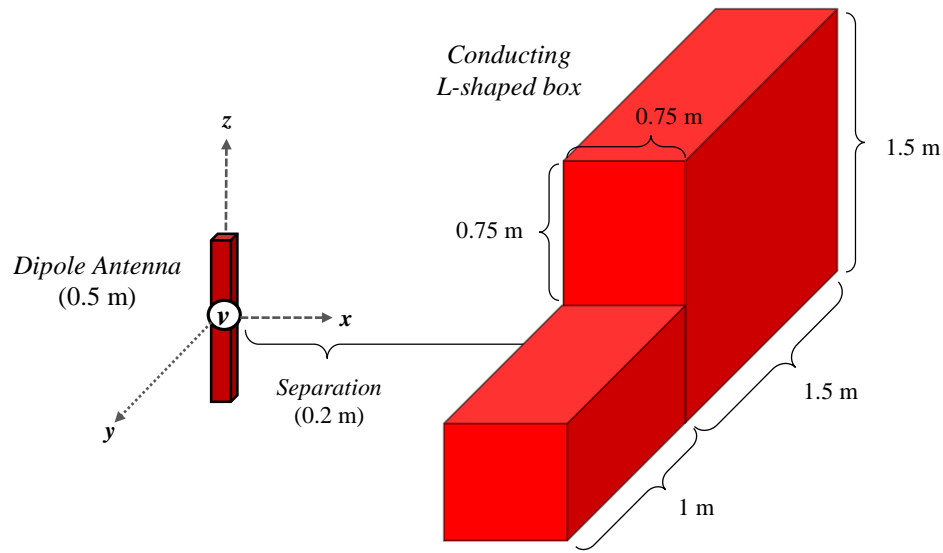


Figure 4.3: Geometry of the first problem.

Table 4-1: Simulation parameters and computer resources used by the IMR and full domain simulations.

| | Number of Domains | Total Number of Cells | Computation Time (min.) | Iteration Number | Memory (MB) |
|------------------|-------------------|-----------------------|-------------------------|------------------|-------------|
| Full FDTD | — | 10,389,504 | 143 | — | 3,850 |
| IMR-FDTD | 2 | 1,919,296 | 171 | 2 | 700 |

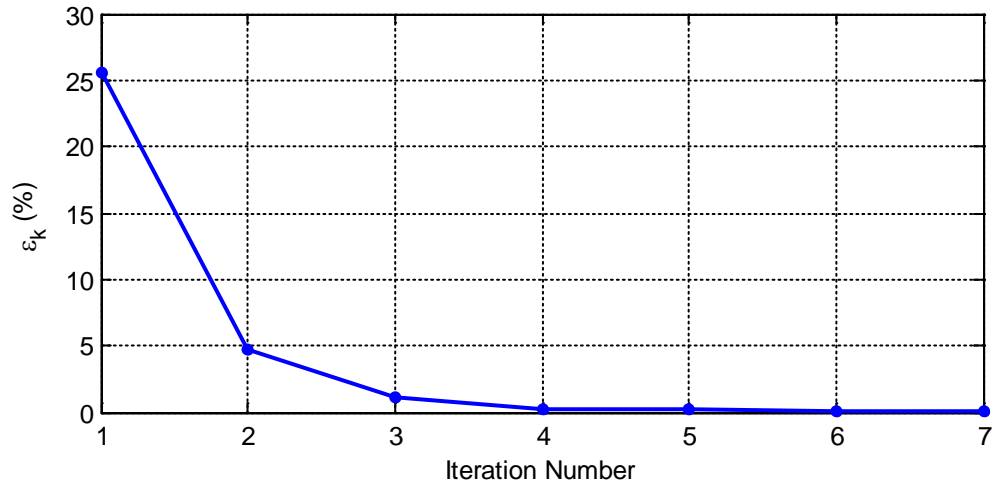
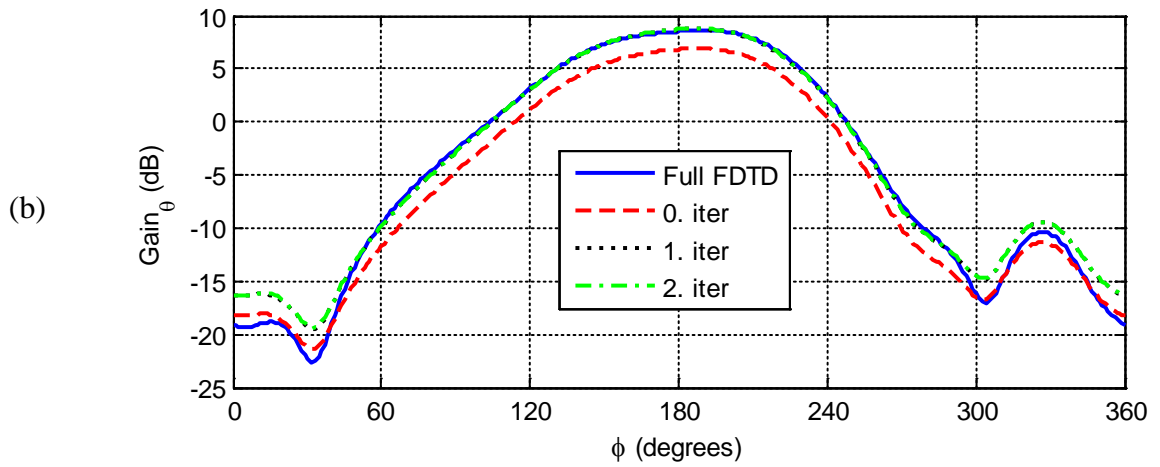
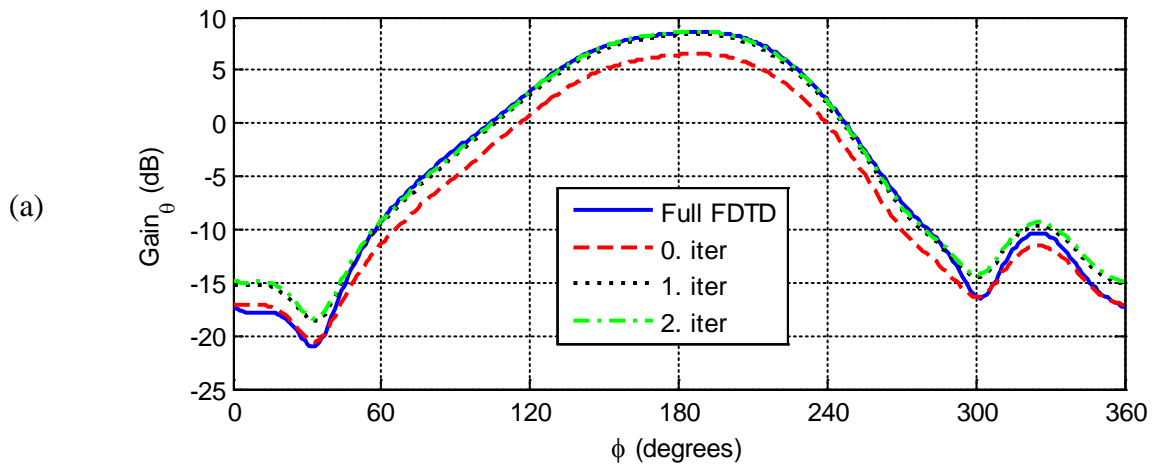


Figure 4.4: Convergence (ε_k) between iteration steps for the first problem.



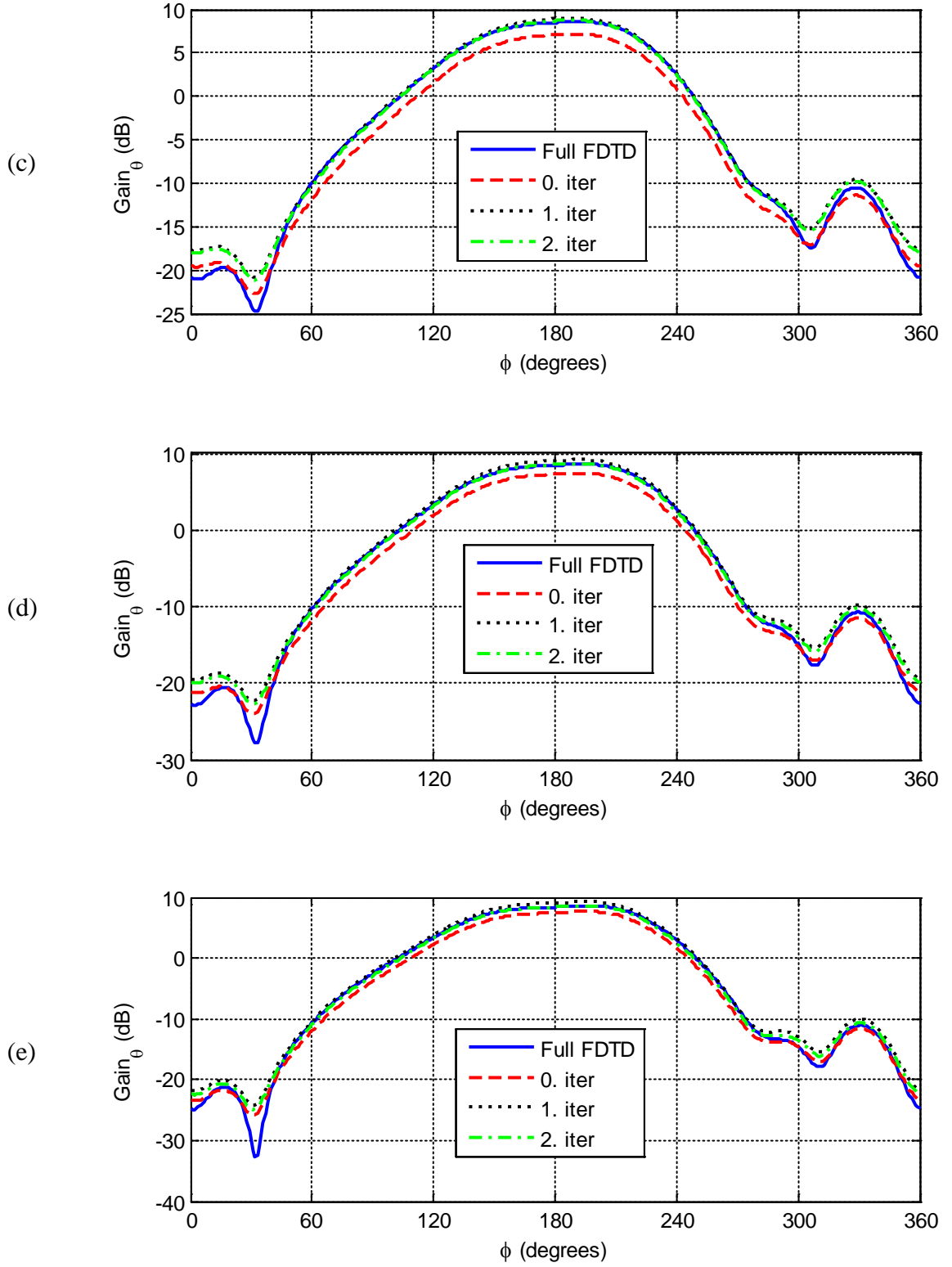
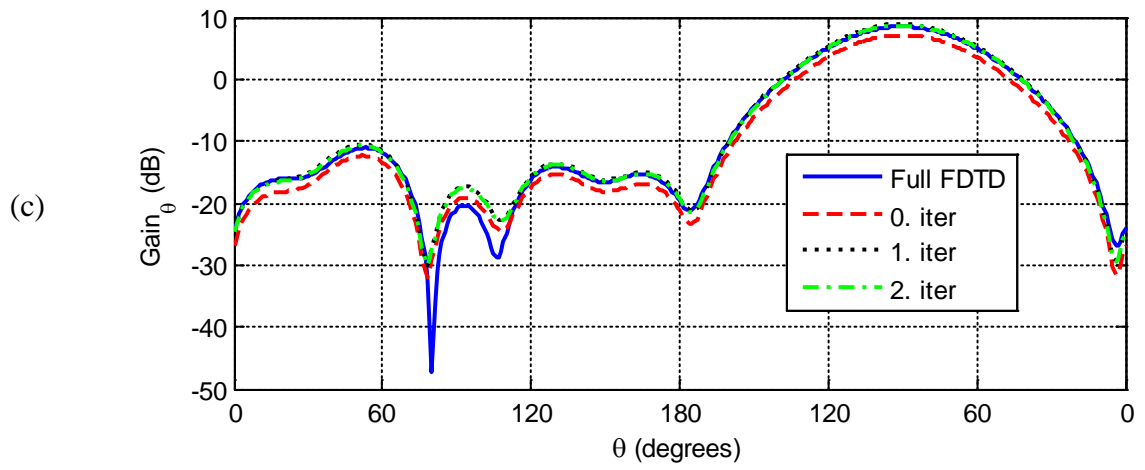
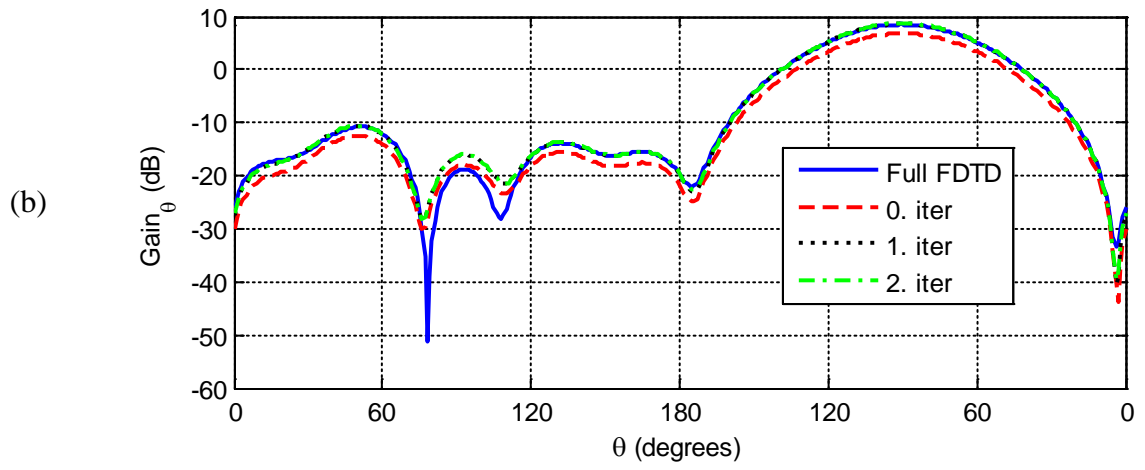
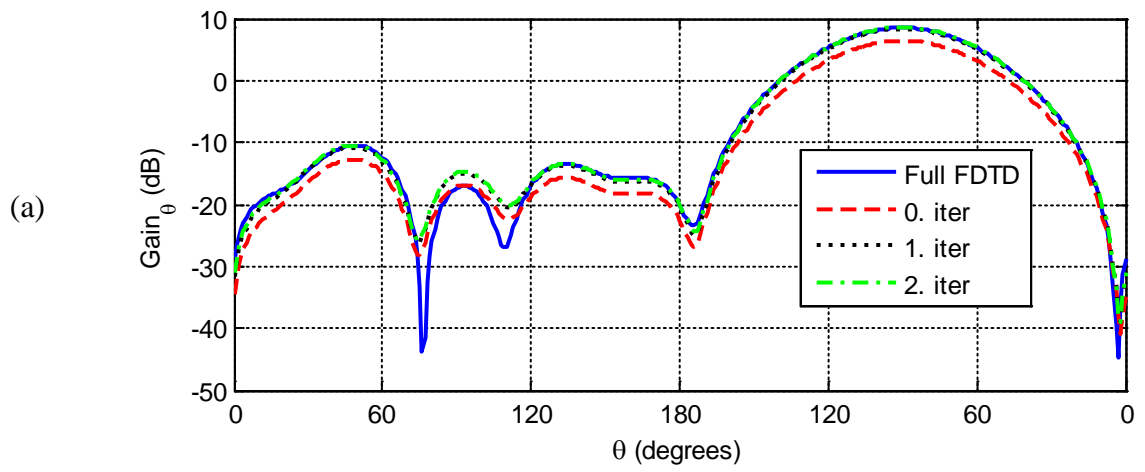


Figure 4.5: Radiation pattern (Gain_θ) for xy-plane cut at frequencies: a) 230 MHz, b) 240 MHz, c) 250 MHz, d) 260 MHz, and e) 270 MHz.



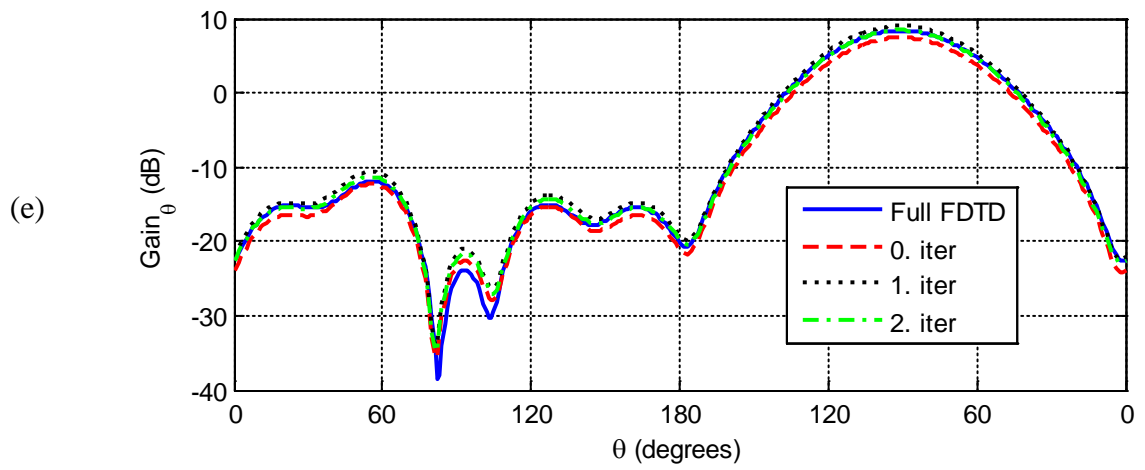
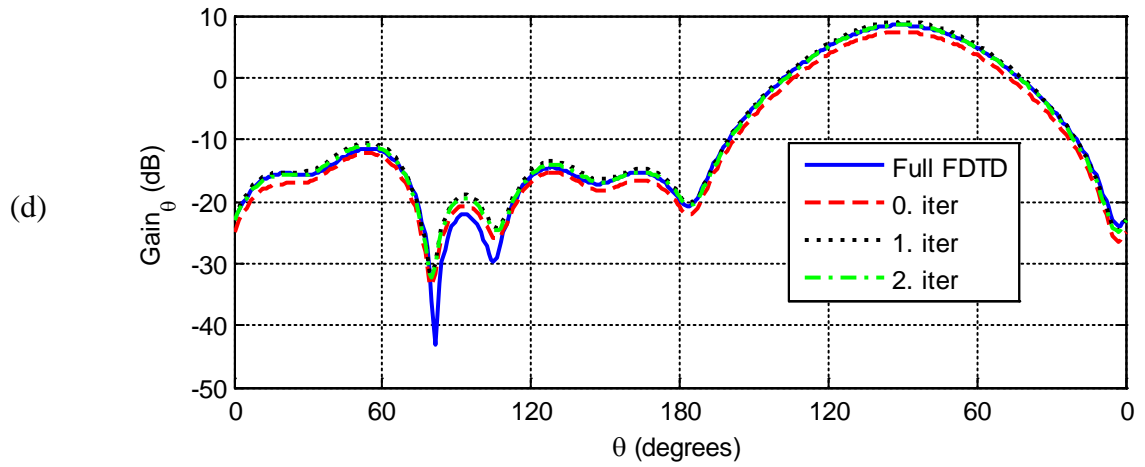
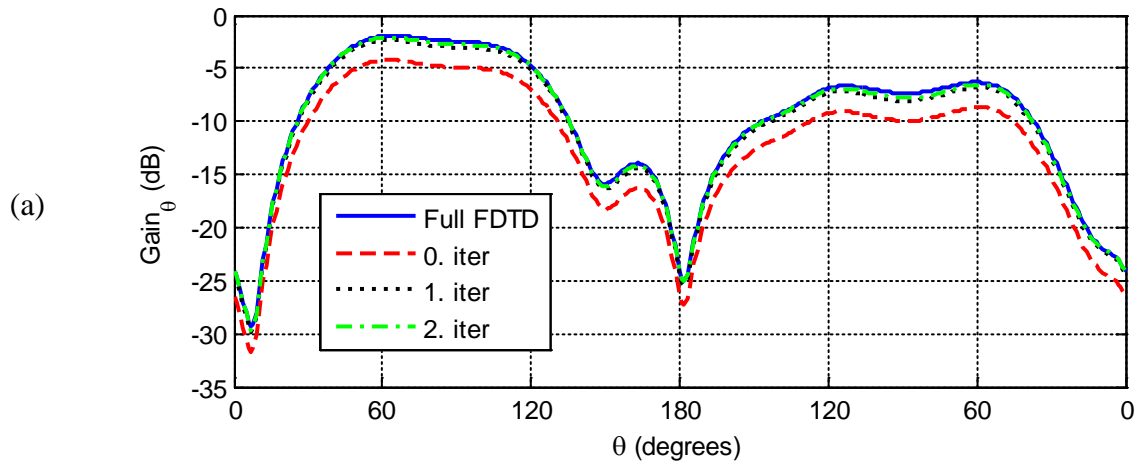
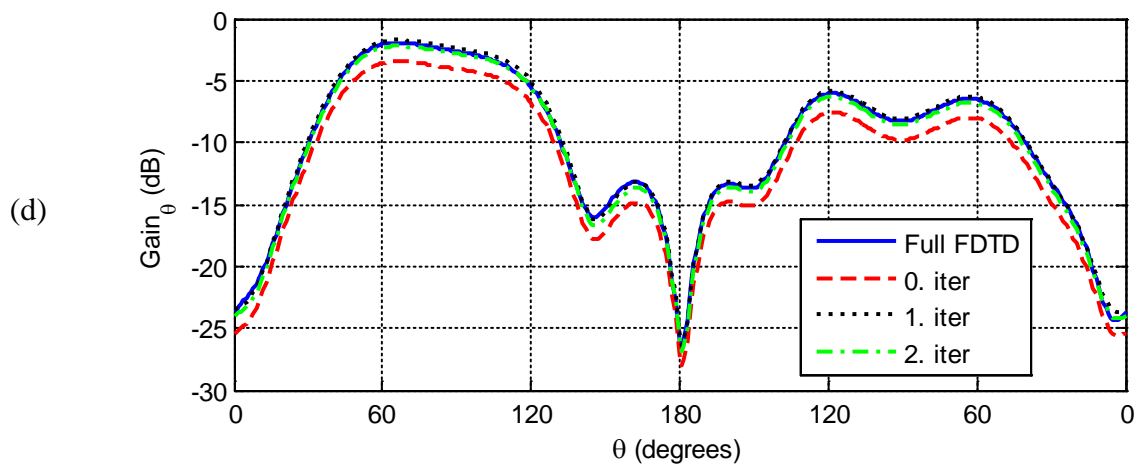
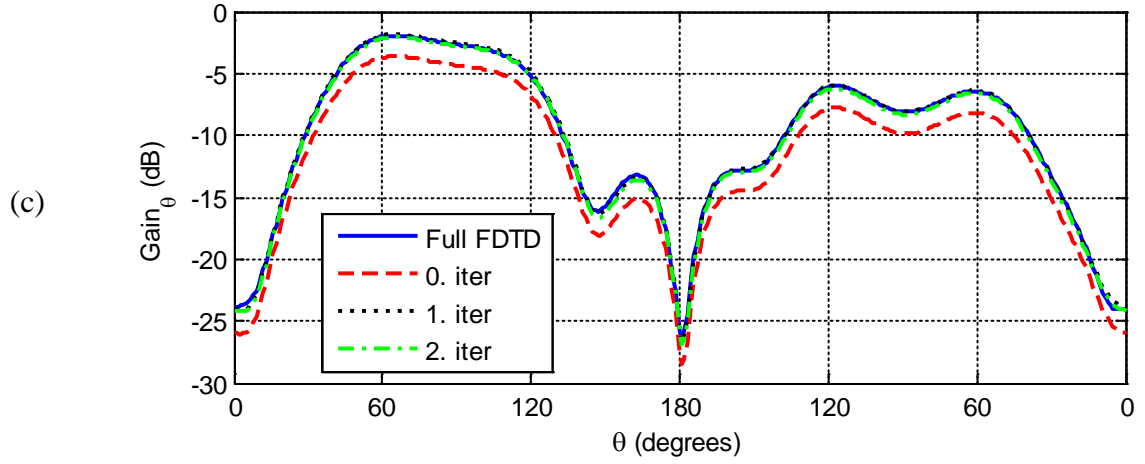
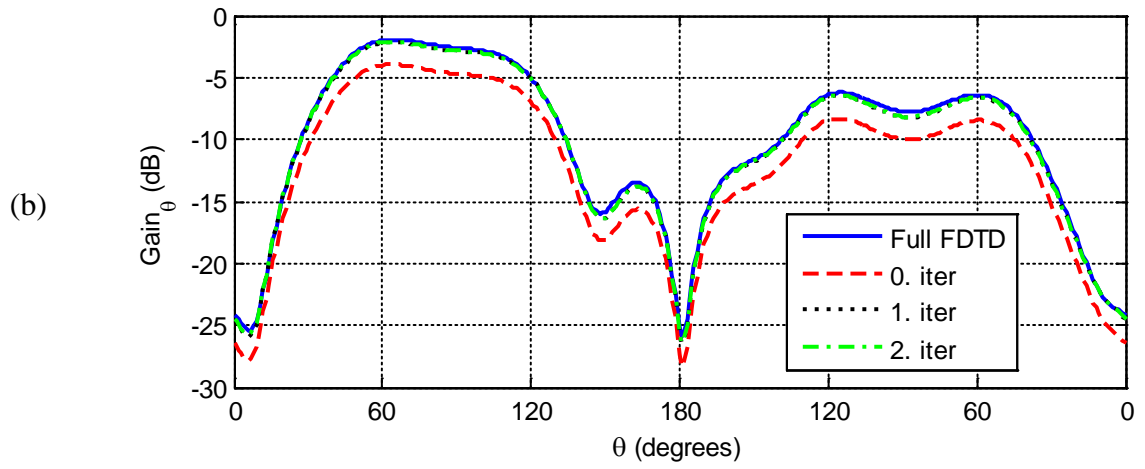


Figure 4.6: Radiation pattern (Gain_θ) for xz -plane cut at frequencies: a) 230 MHz, b) 240 MHz, c) 250 MHz, d) 260 MHz, and e) 270 MHz.





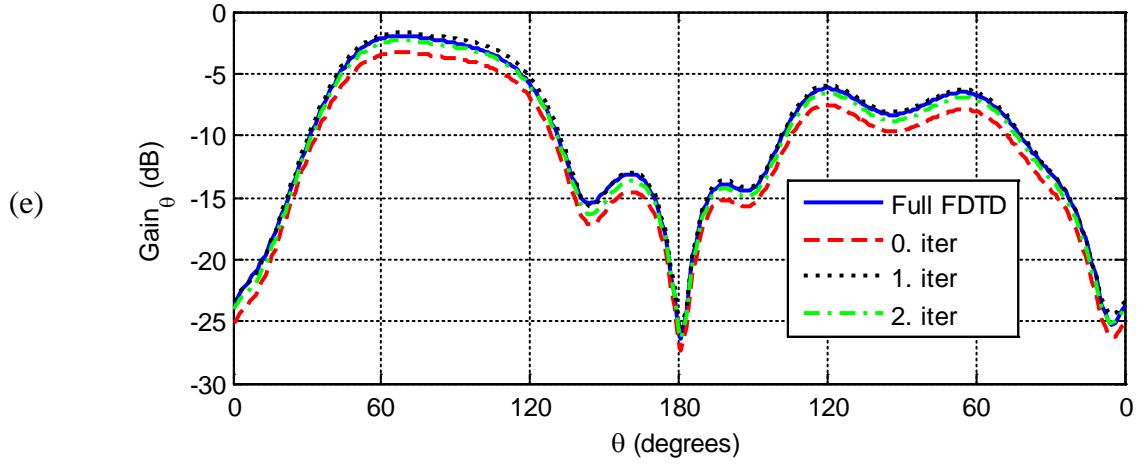
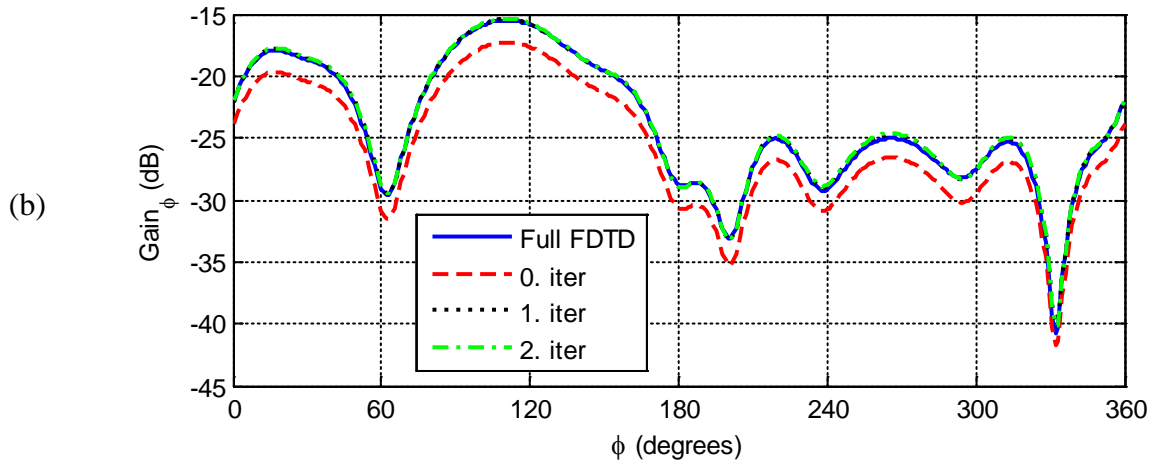
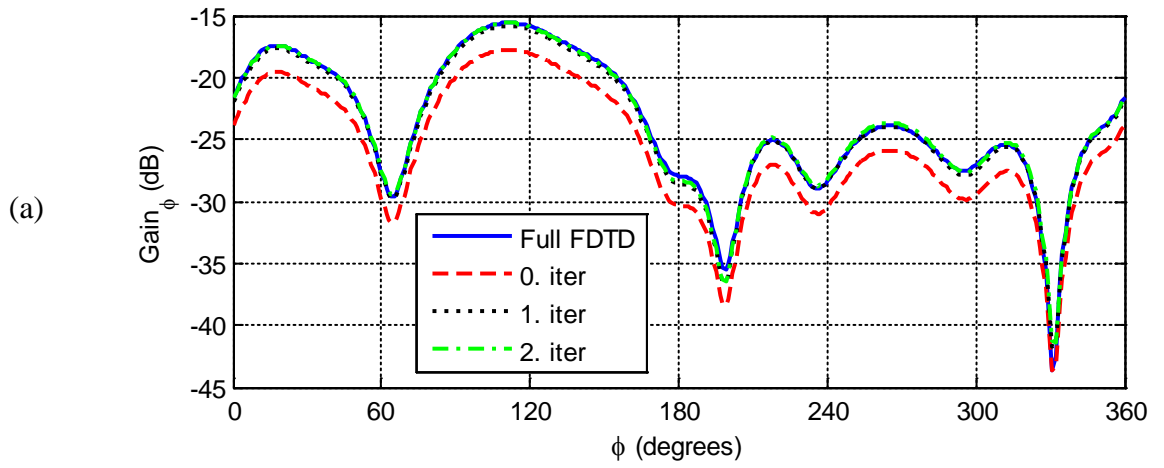


Figure 4.7: Radiation pattern (Gain_θ) for yz-plane cut at frequencies: a) 230 MHz, b) 240 MHz, c) 250 MHz, d) 260 MHz, and e) 270 MHz.



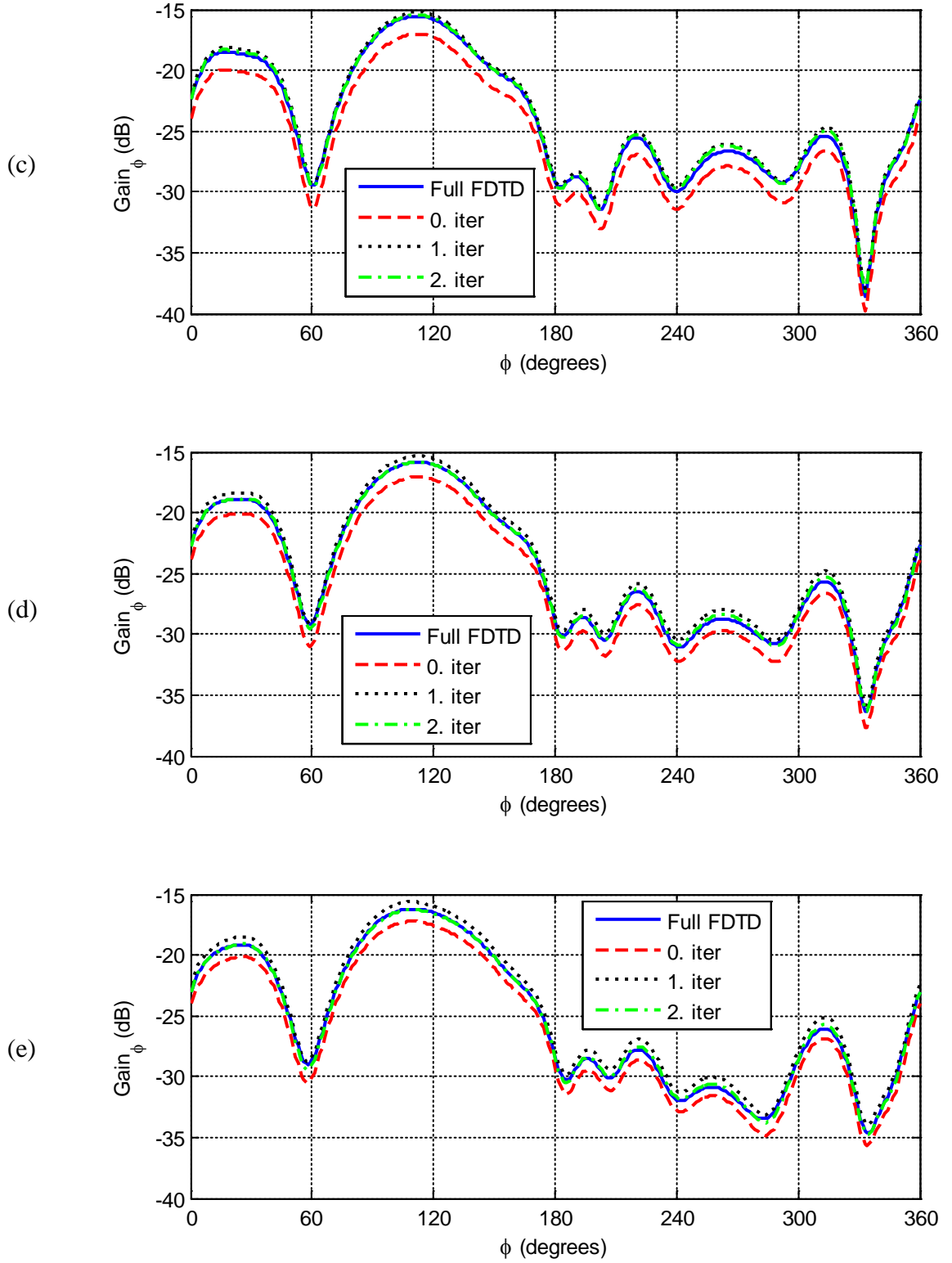
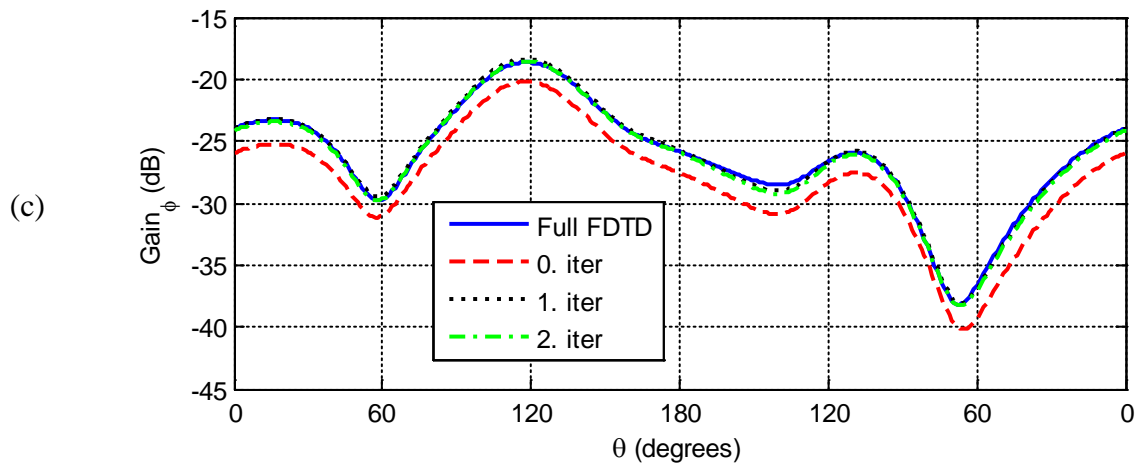
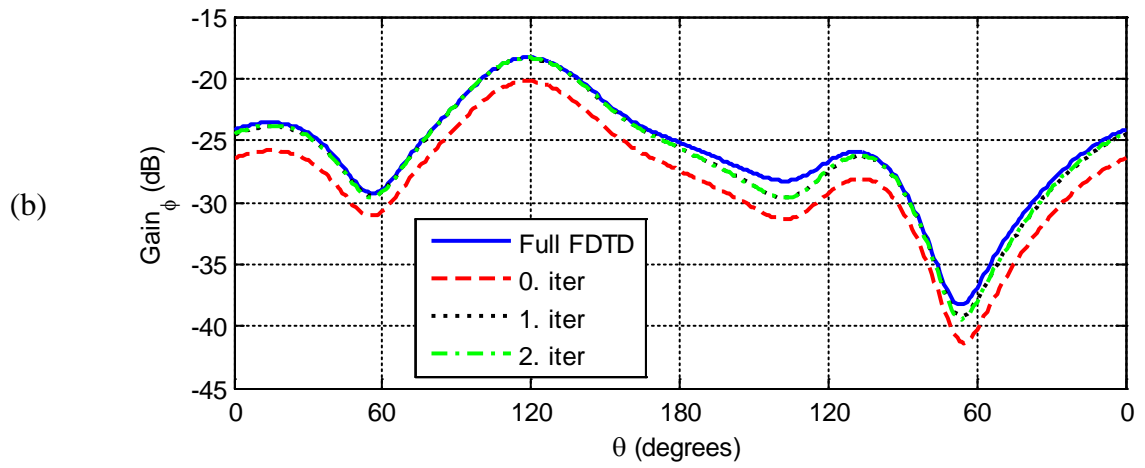
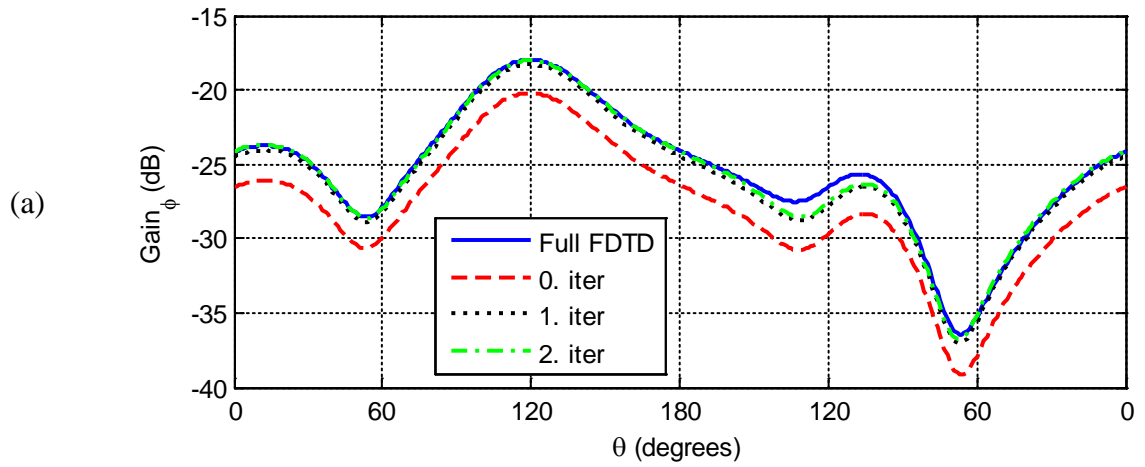


Figure 4.8: Radiation pattern (Gain_φ) for xy -plane cut at frequencies: a) 230 MHz, b) 240 MHz, c) 250 MHz, d) 260 MHz, and e) 270 MHz.



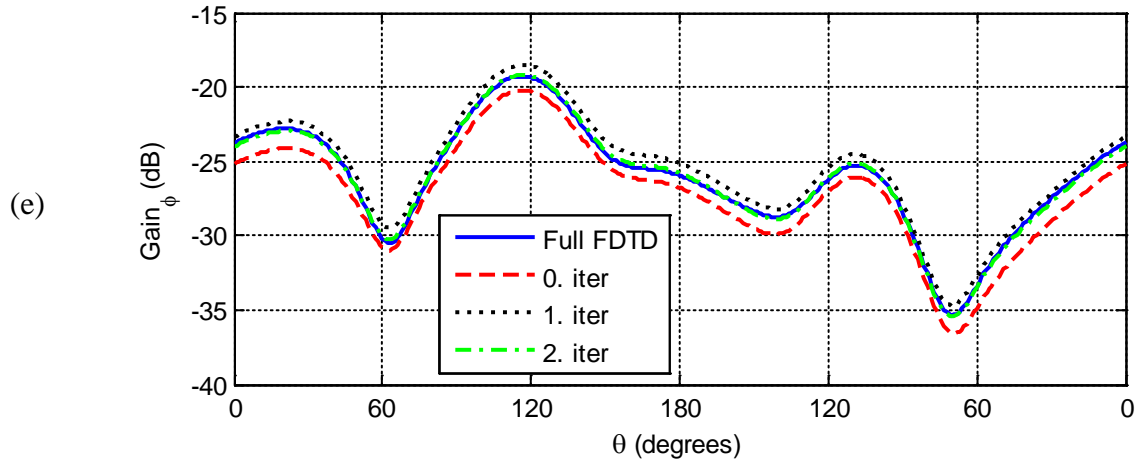
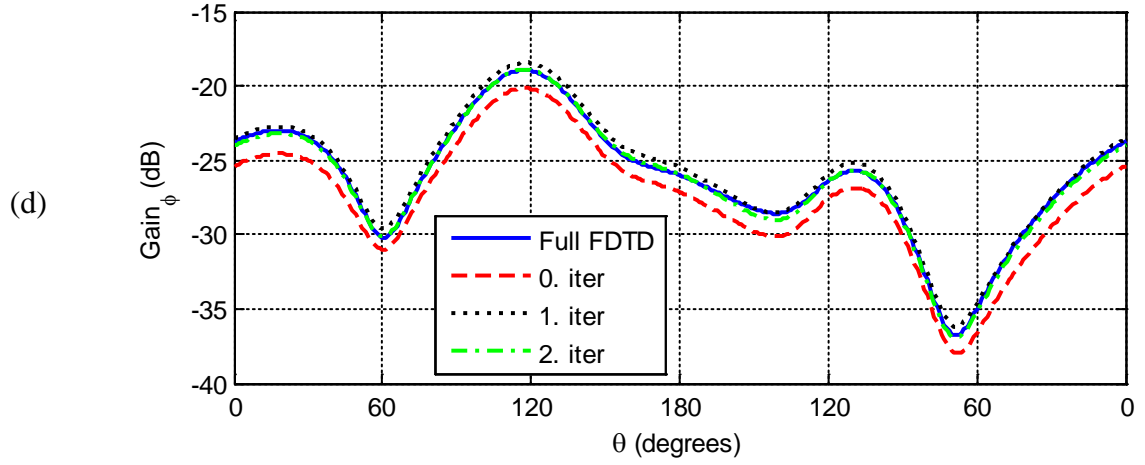
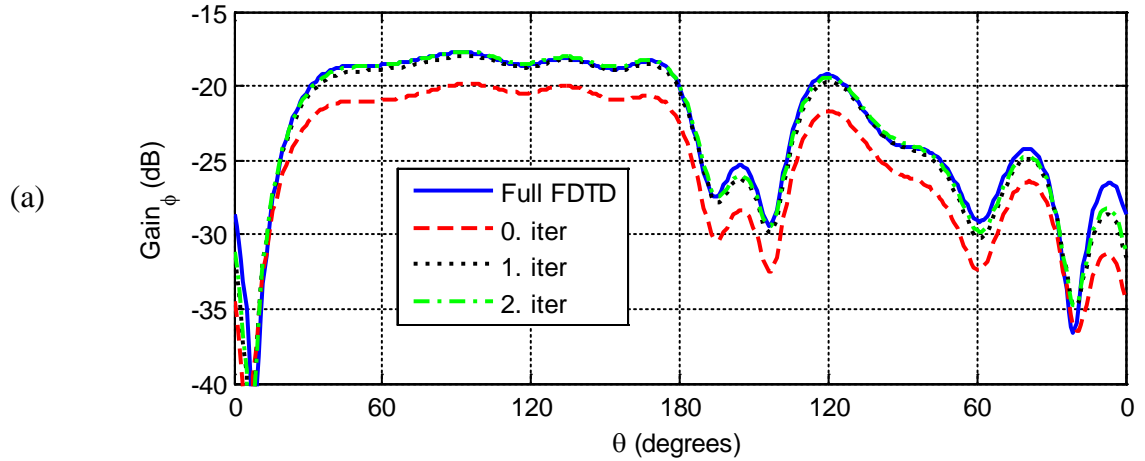
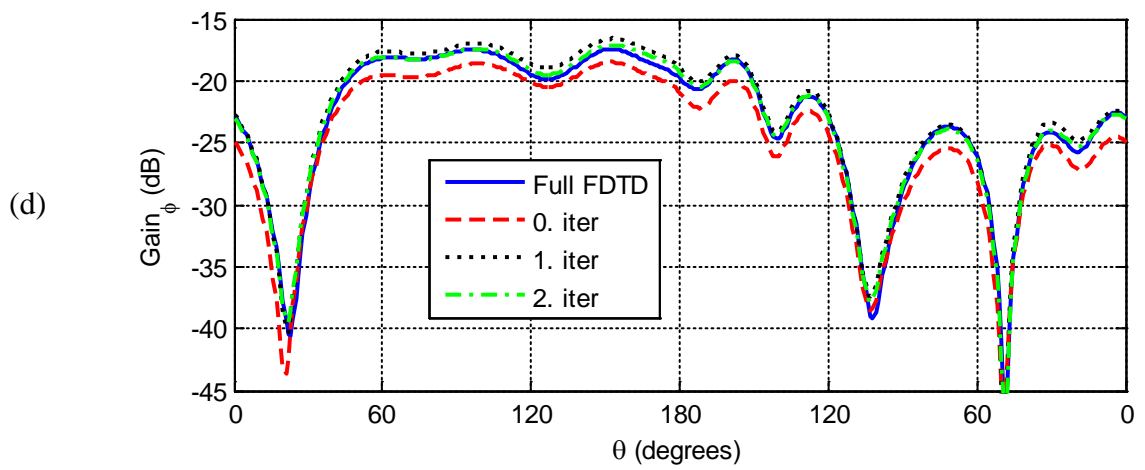
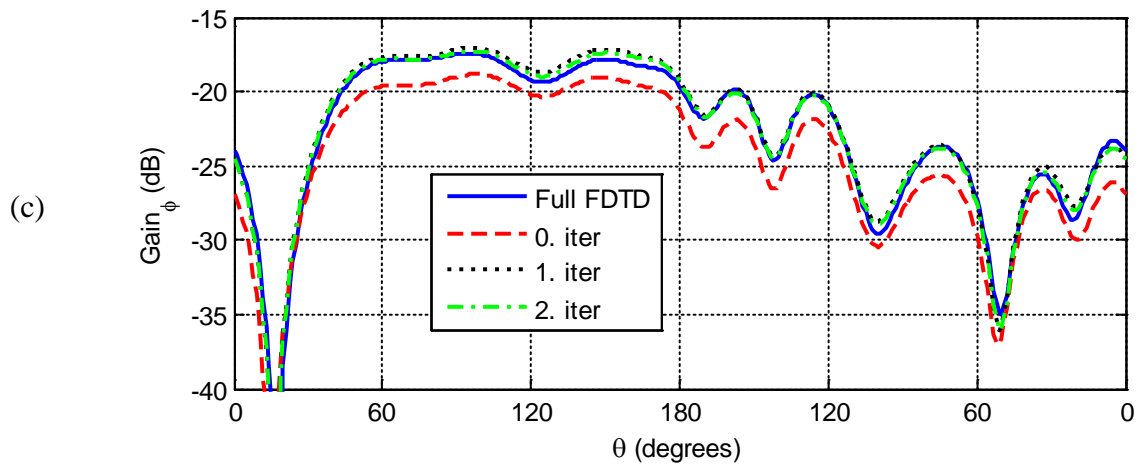
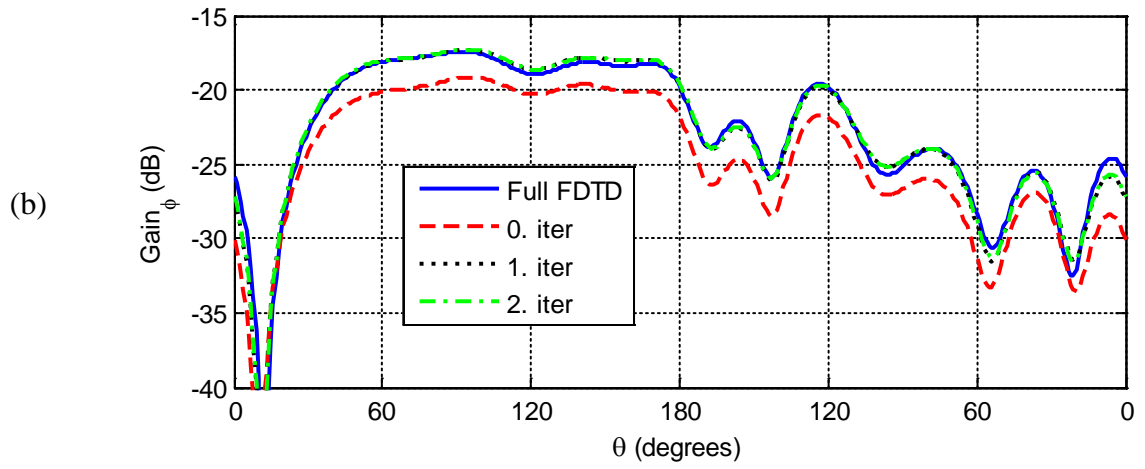


Figure 4.9: Radiation pattern (Gain_φ) for xz -plane cut at frequencies: a) 230 MHz, b) 240 MHz, c) 250 MHz, d) 260 MHz, and e) 270 MHz.





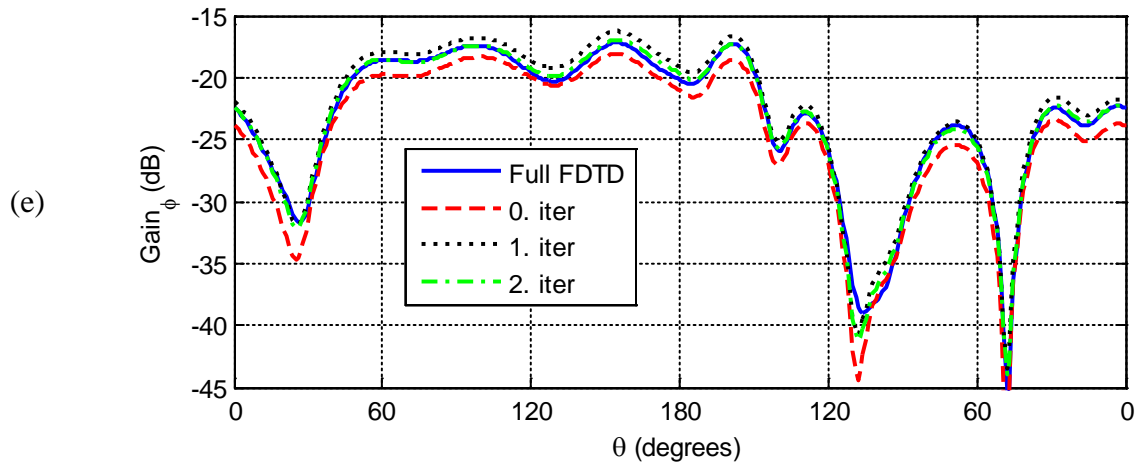
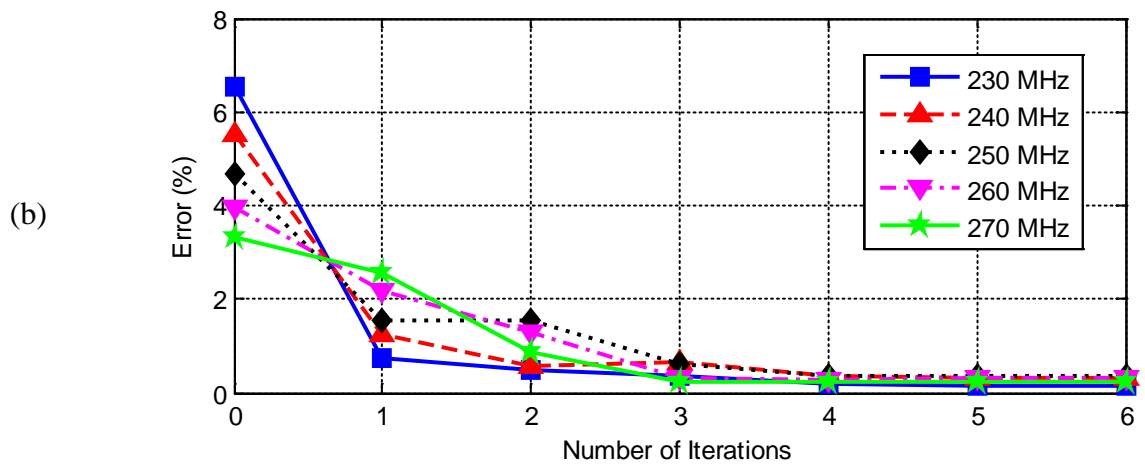
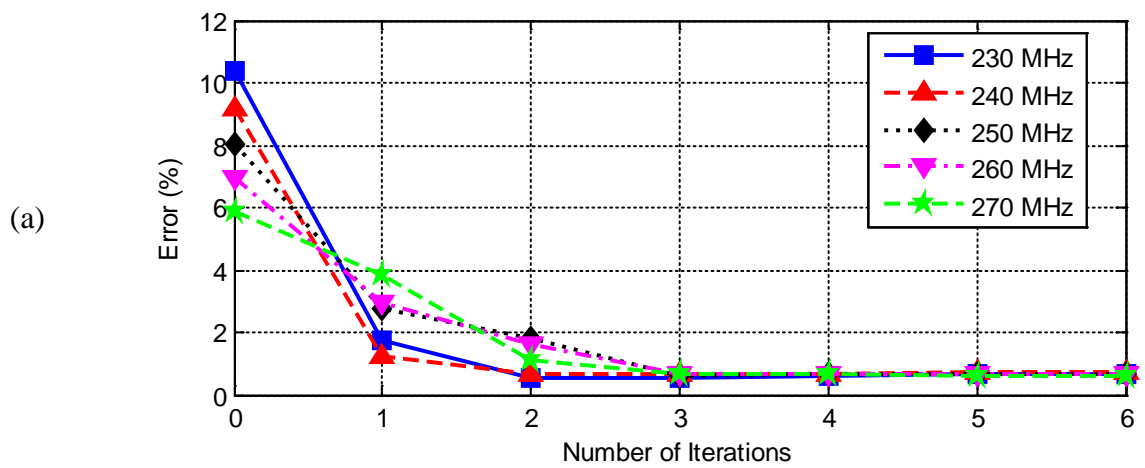


Figure 4.10: Radiation pattern (Gain_φ) for yz -plane cut at frequencies: a) 230 MHz, b) 240 MHz, c) 250 MHz, d) 260 MHz, and e) 270 MHz.



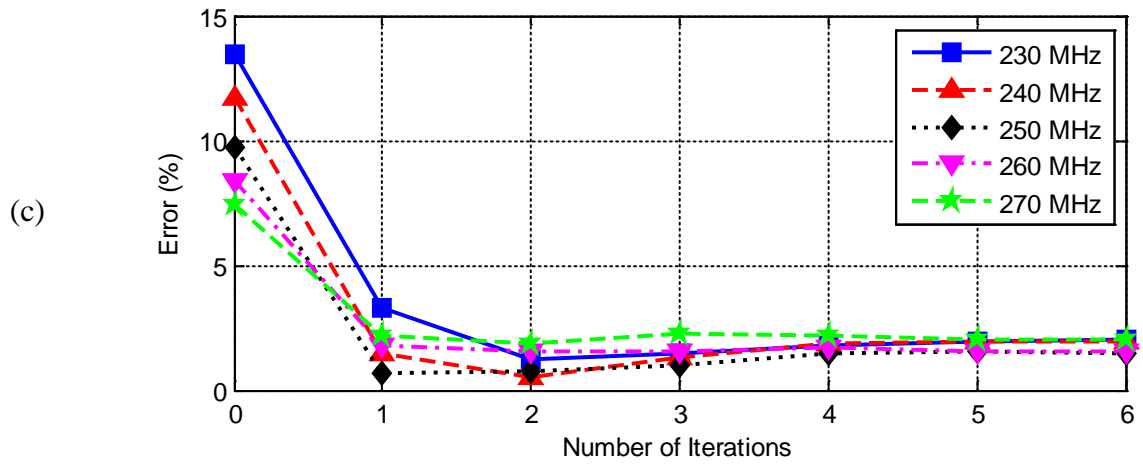
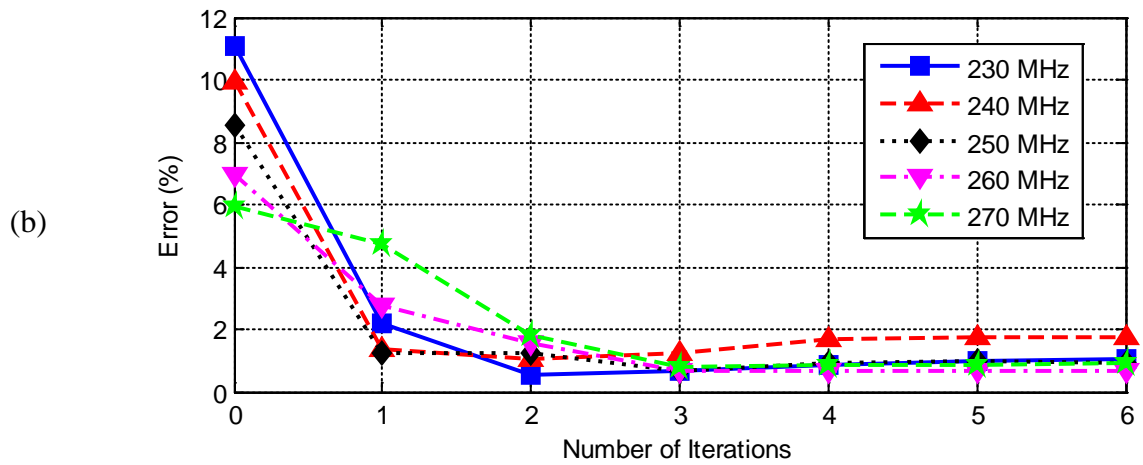
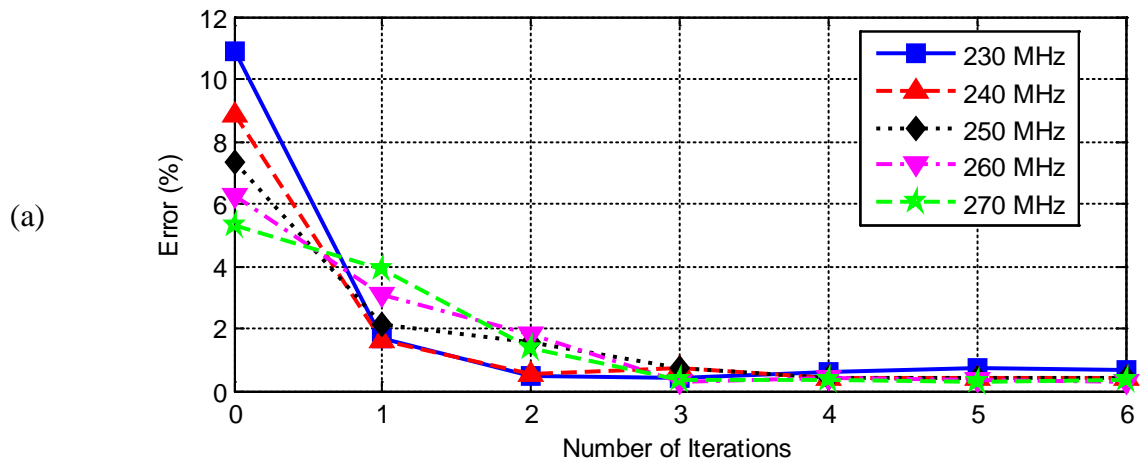


Figure 4.11: Normalized average errors for Gain_0 components in the three plane cuts: a) xy -plane, b) xz -plane, and c) yz -plane.



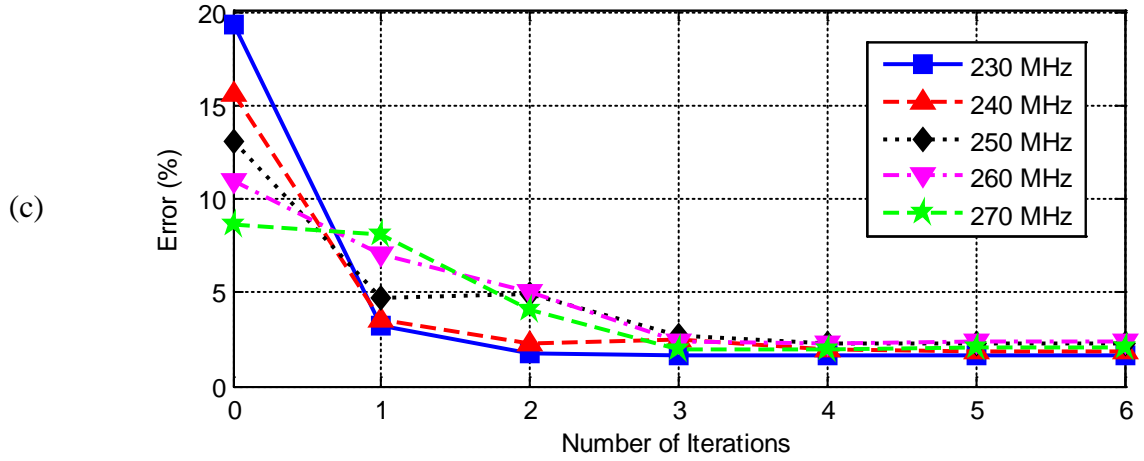


Figure 4.12: Normalized average errors for Gain_ϕ components in the three plane cuts: a) xy -plane, b) xz -plane, and c) yz -plane.

4.2 Radiation from a Dipole Antenna in the Presence of Two Objects-1

The geometry of the second problem is presented in Figure 4.13a where a 0.5 m dipole antenna is placed a distance of 0.5 m away from two conducting boxes (box-A and box-B) along the x direction. The separation between boxes is 1 m. The dimensions of the box-A are 0.25 m, 1 m, and 1 m along the x , y , and z directions, respectively. The dimensions of conducting box-B on the yz -plane is shown in Figure 4.13b. The thickness of box-B along the x direction is 25 cm. The idea of this problem is to prove the validity of the presented technique for more than one scatterer subregion. It can be seen from Figure 4.14 that the IMR algorithm reaches the convergence criterion after iteration # 4. Figures 4.15-4.20 show the radiation patterns (Gain_θ and Gain_ϕ) of the configuration for the three plane cuts. Good agreement with the full domain results is achieved for the three plane cuts after iteration # 4. To prove the convergence of the results of the IMR and the full domain,

the normalized average errors for Gain_θ and Gain_ϕ in the three plane cuts at the frequencies of interest are shown in Figures 4.21-4.22, respectively. Simulation parameters and computer resources are summarized in Table 4-2. Results in the table show a considerable reduction in the memory storage requirements, but the computation time of the IMR algorithm is more than that of the full domain because of small separation between the objects. The computation time would be less and the memory gain would be more for problems that have large separation between the objects.

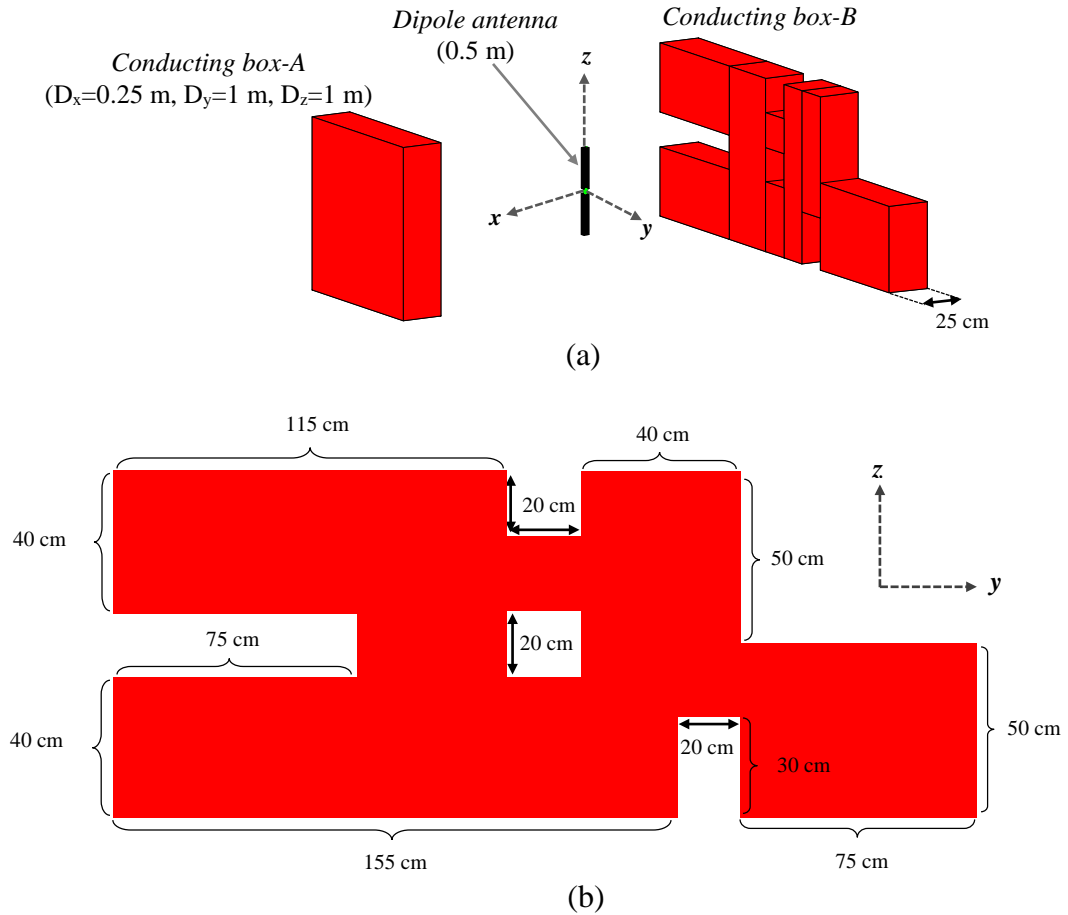


Figure 4.13: a) Geometry of the second problem and b) Geometry of the conducting box-B on the yz-plane.

Table 4-2: Simulation parameters and computer resources used by the IMR and full domain simulations.

| | Number of Domains | Total Number of Cells | Computation Time (min.) | Iteration Number | Memory (MB) |
|------------------|-------------------|-----------------------|-------------------------|------------------|-------------|
| Full FDTD | — | 13,311,552 | 345 | — | 4807 |
| IMR-FDTD | 3 | 1,699,200 | 456 | 4 | 705 |

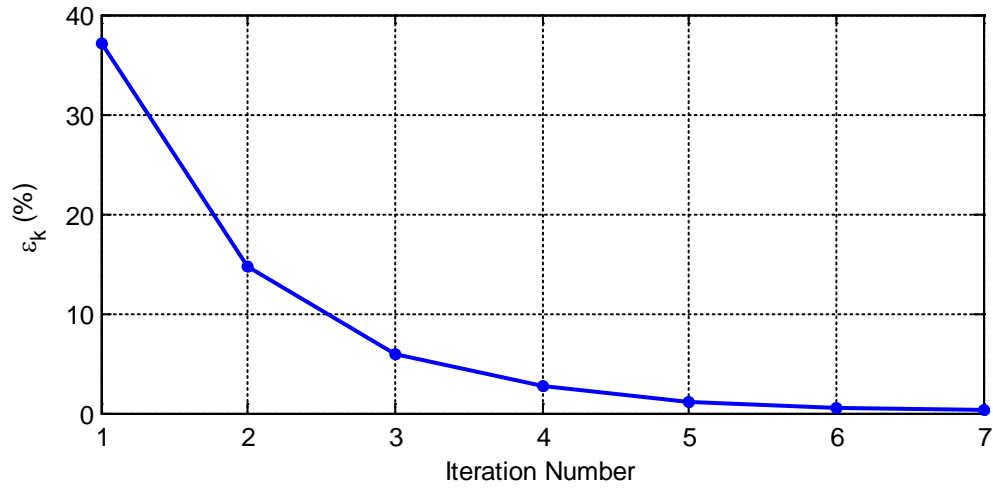
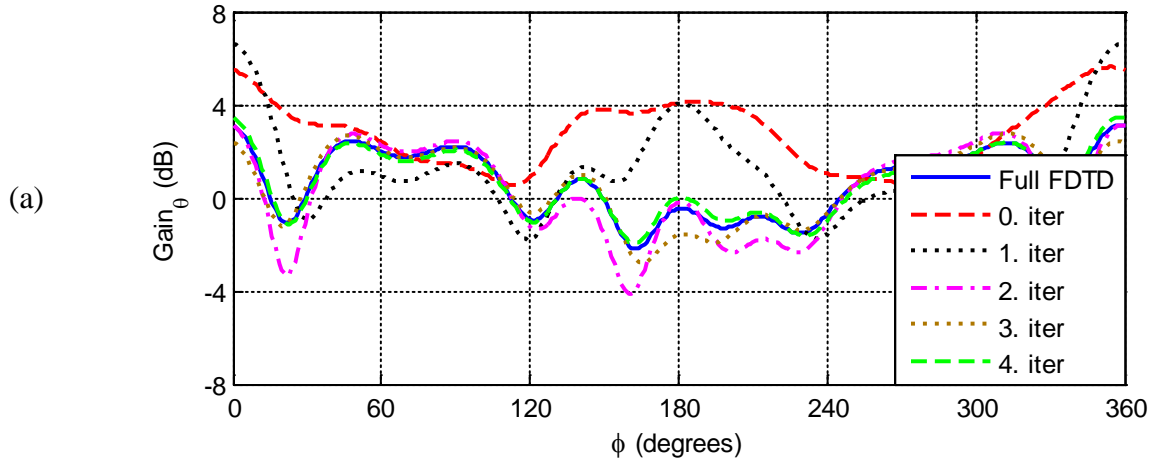
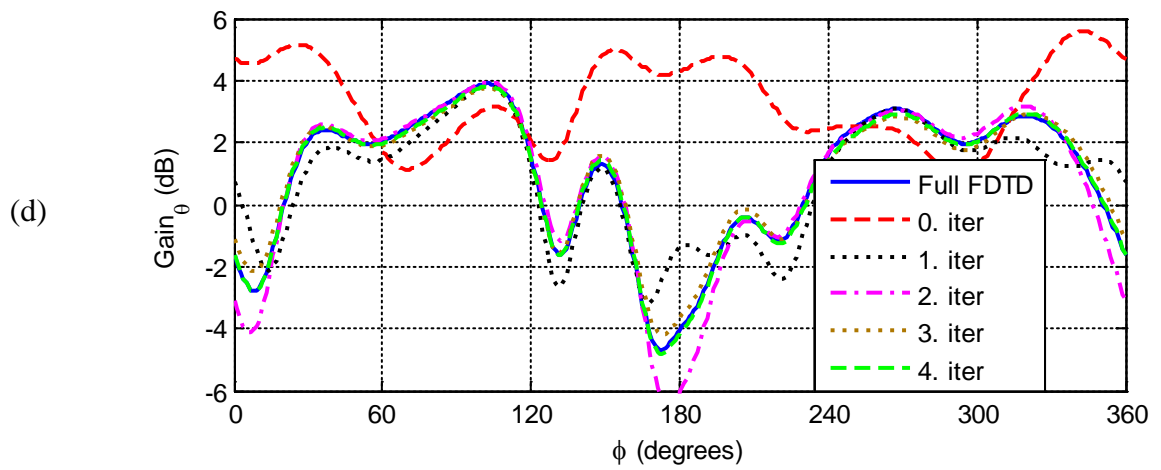
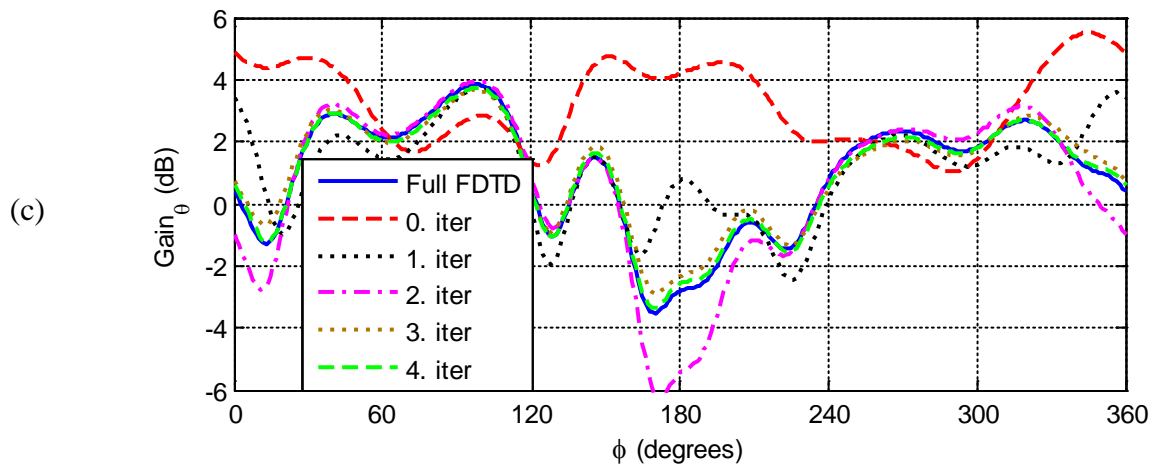
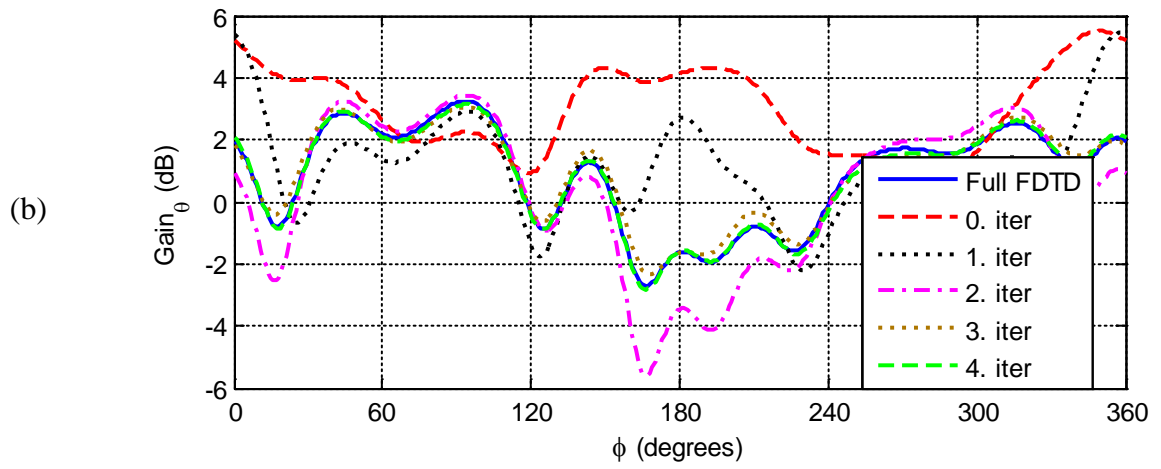


Figure 4.14: Convergence (ε_k) between iteration steps for the second problem.





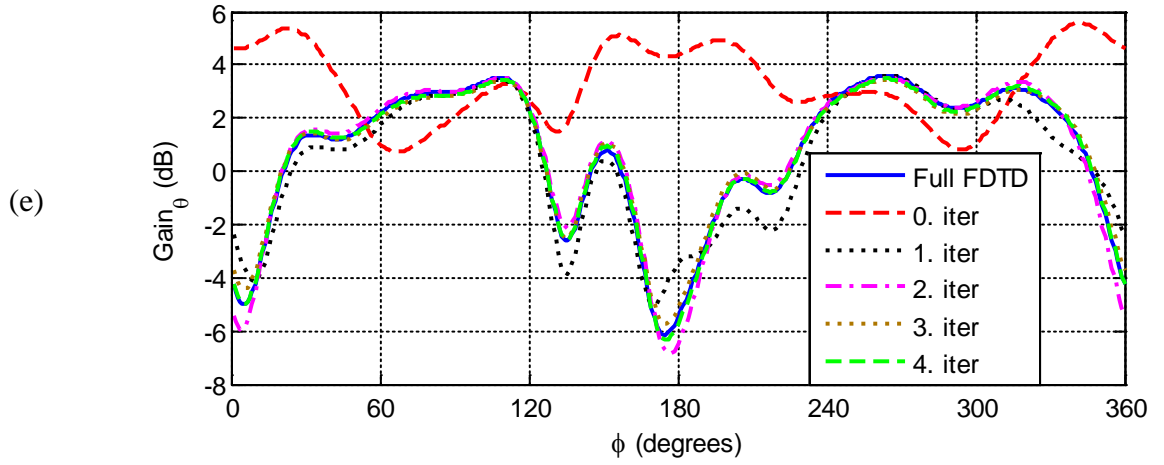
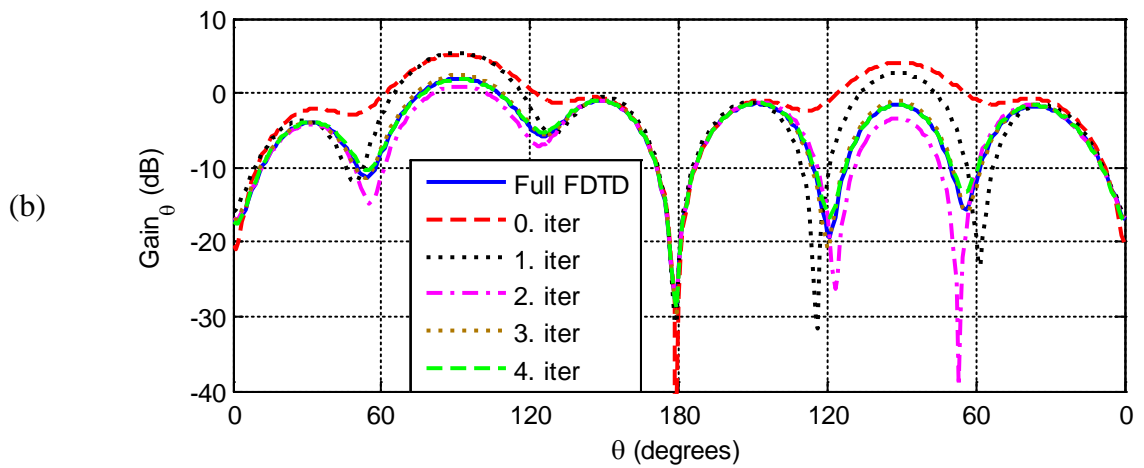
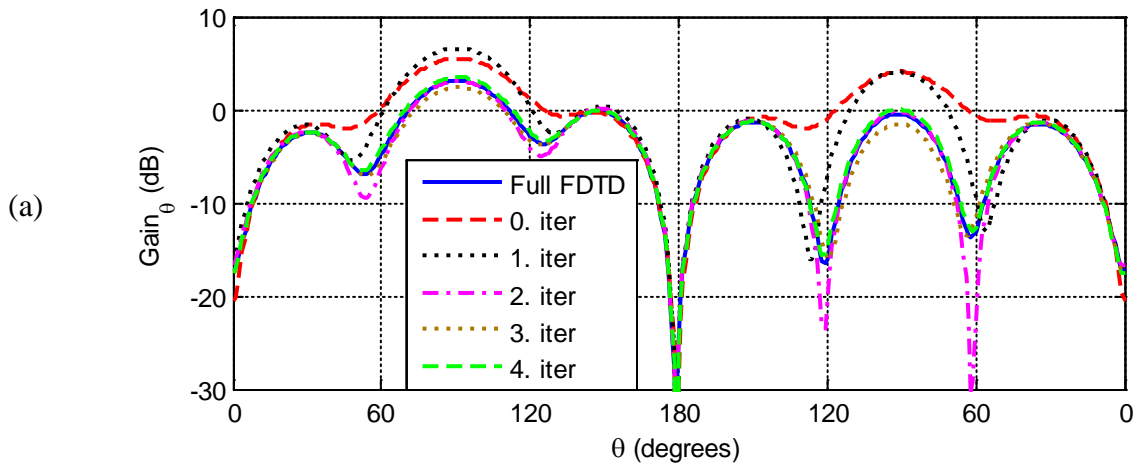


Figure 4.15: Radiation pattern (Gain_θ) for xy -plane cut at frequencies: a) 230 MHz, b) 240 MHz, c) 250 MHz, d) 260 MHz, and e) 270 MHz.



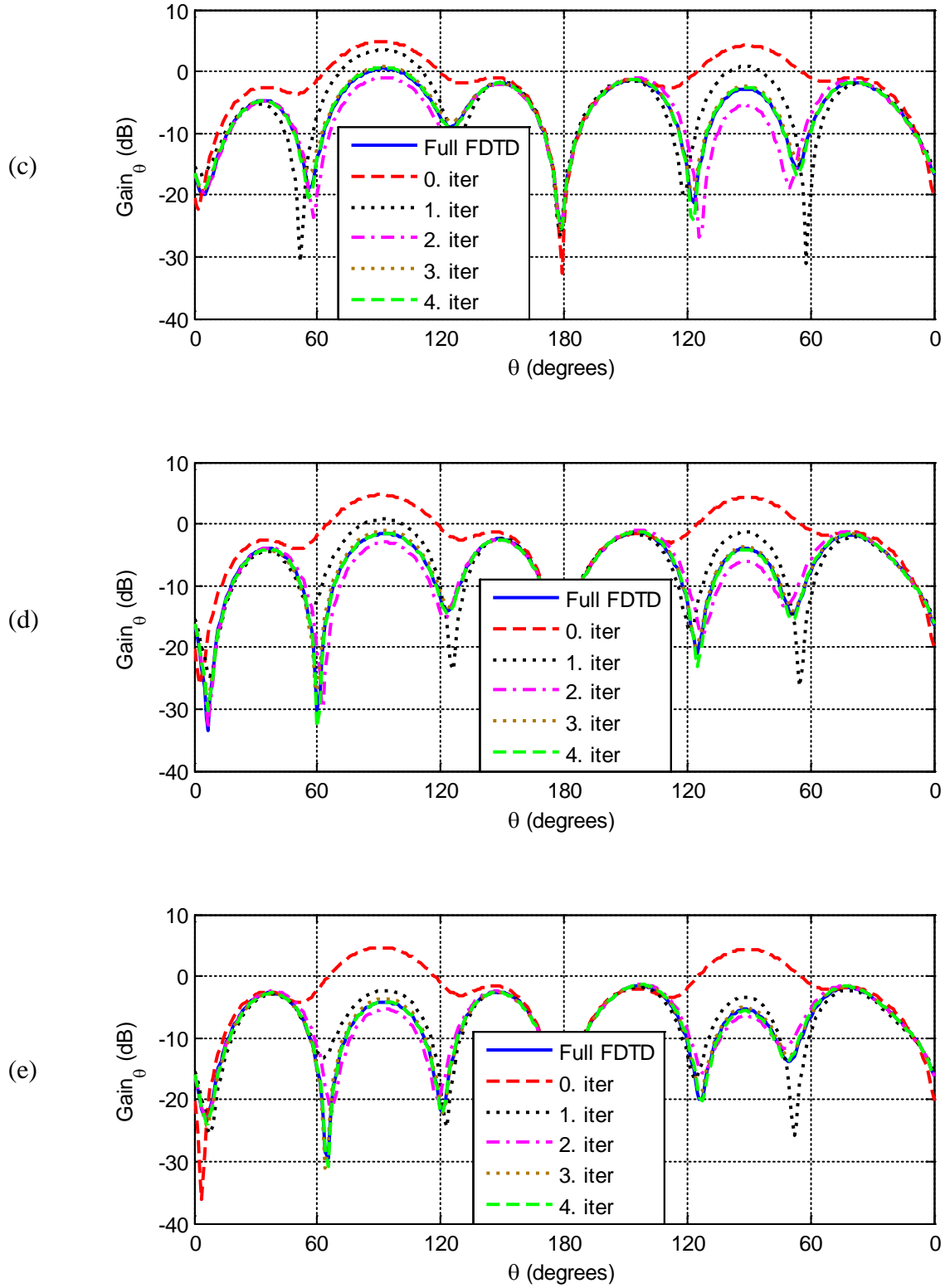
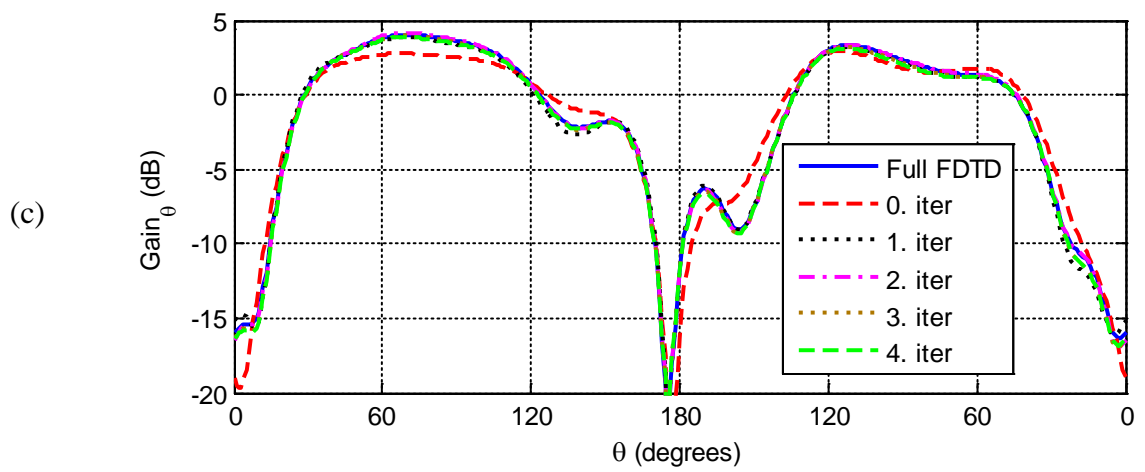
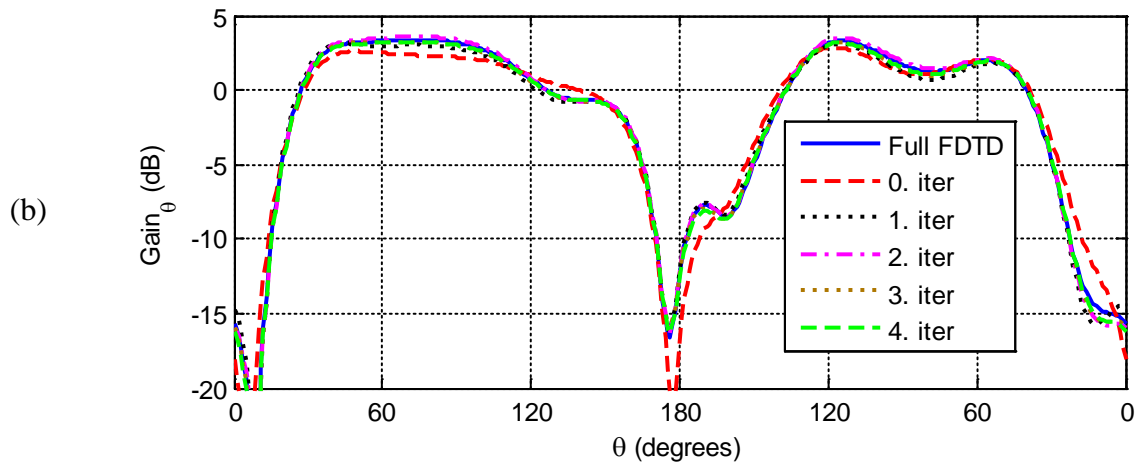
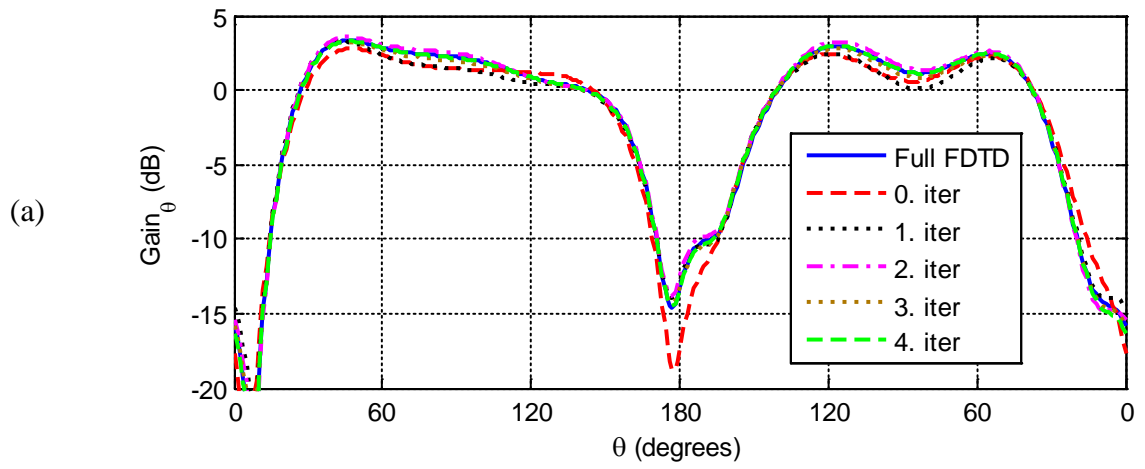


Figure 4.16: Radiation pattern (Gain_θ) for xz-plane cut at frequencies: a) 230 MHz, b) 240 MHz, c) 250 MHz, d) 260 MHz, and e) 270 MHz.



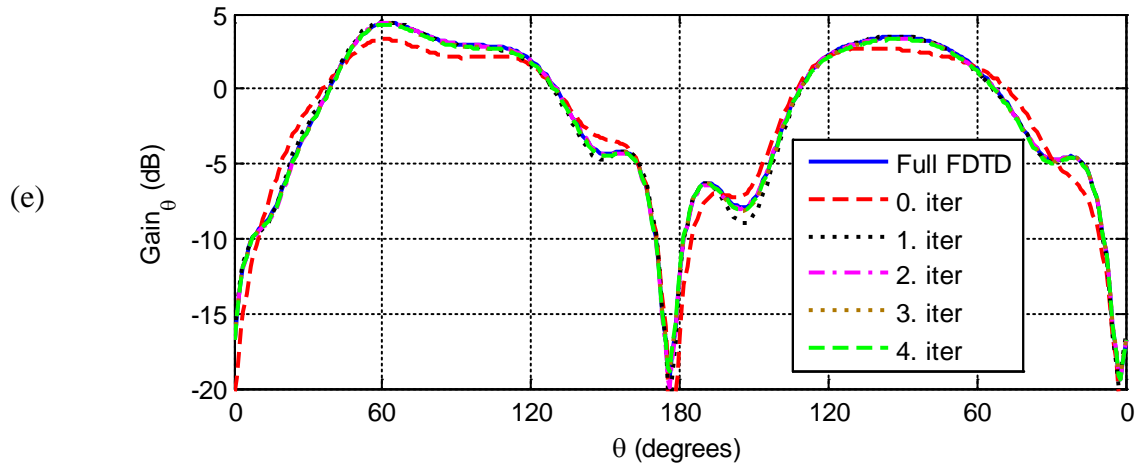
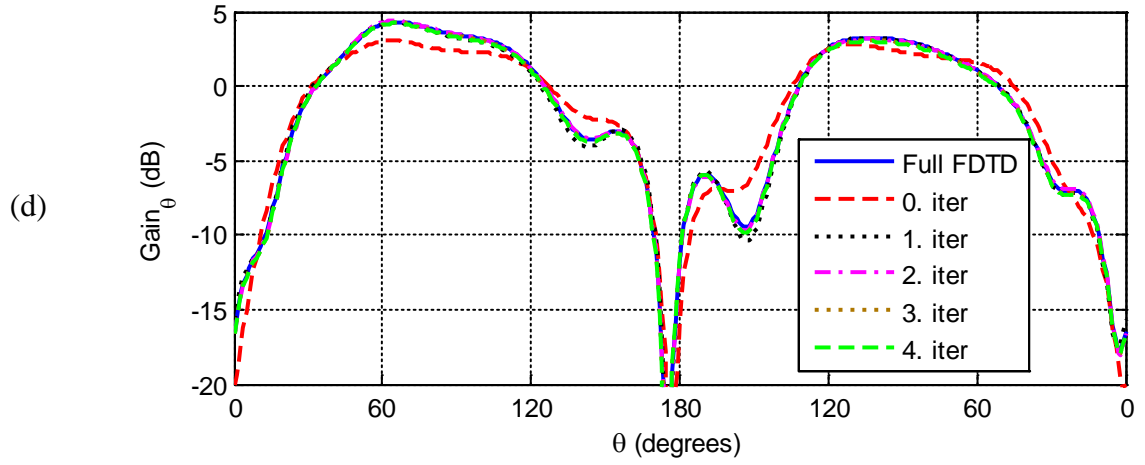
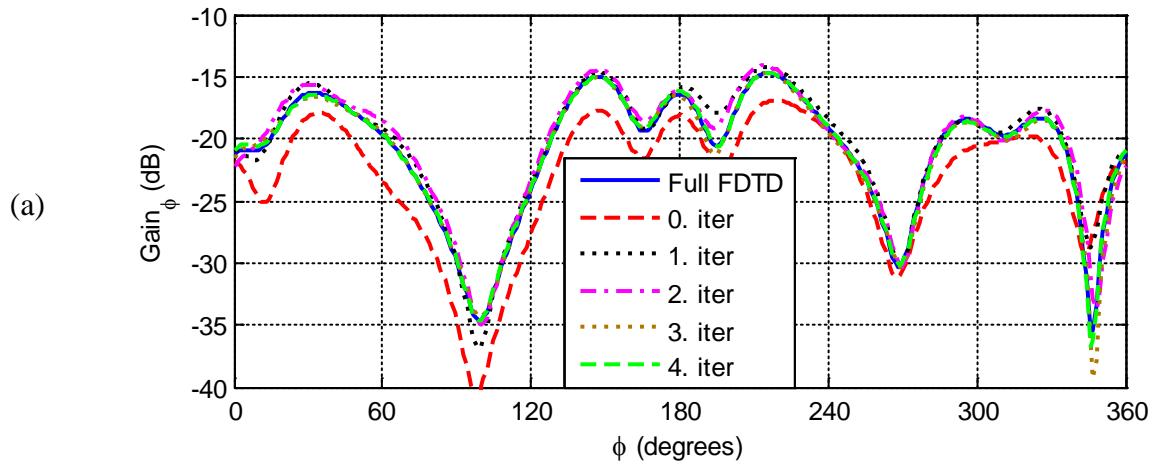
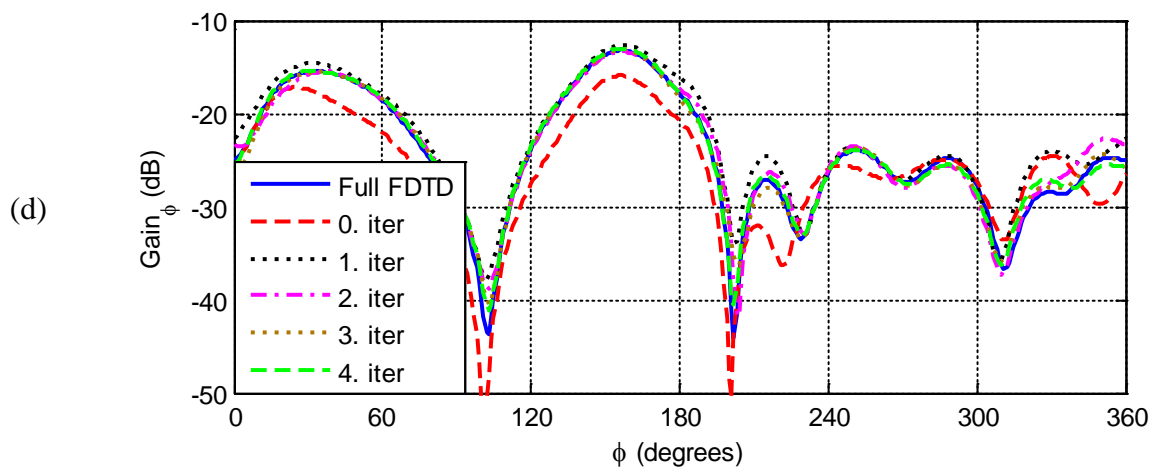
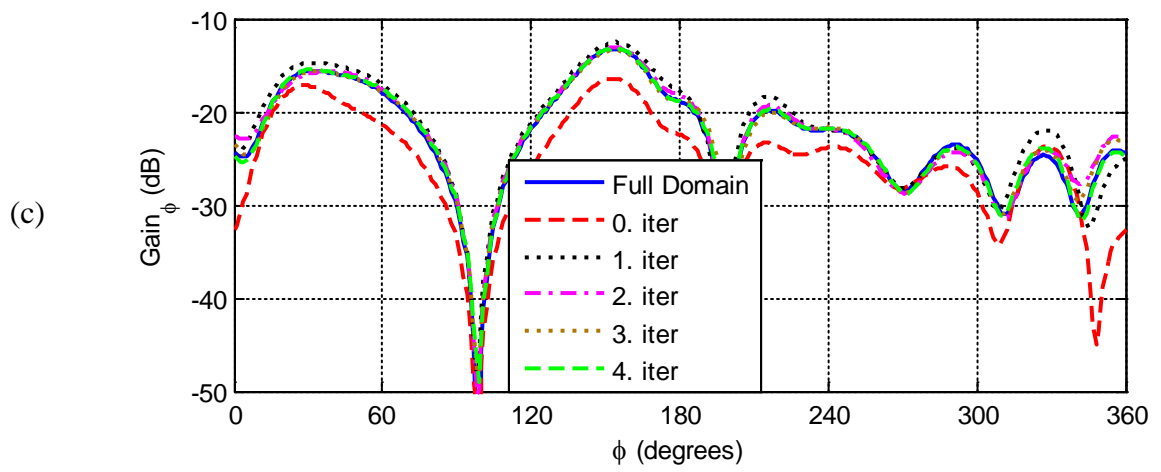
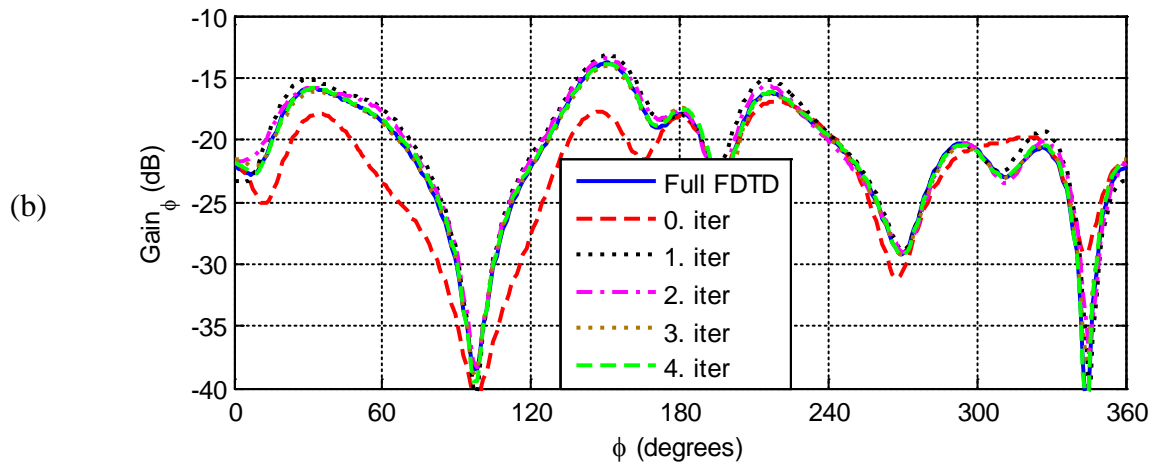


Figure 4.17: Radiation pattern (Gain_θ) for yz -plane cut at frequencies: a) 230 MHz, b) 240 MHz, c) 250 MHz, d) 260 MHz, and e) 270 MHz.





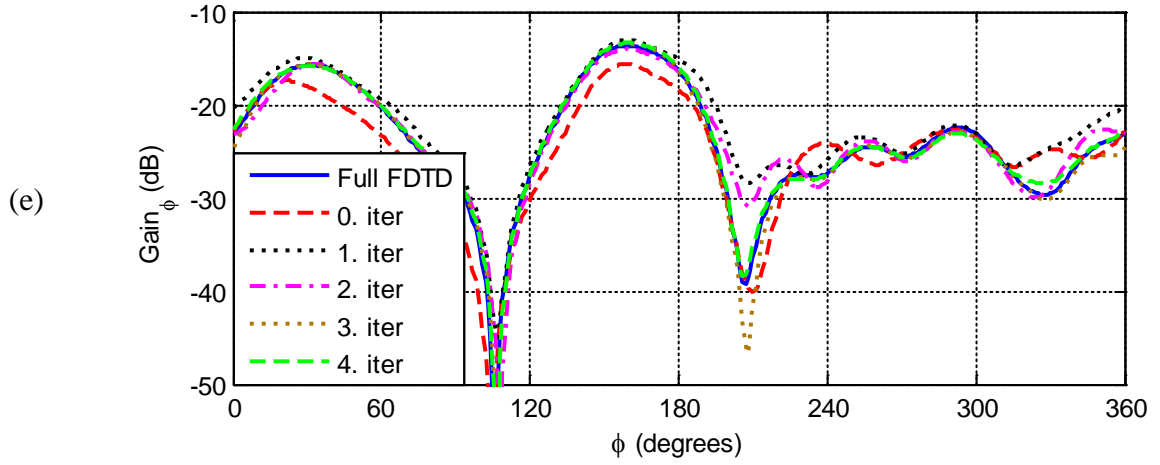
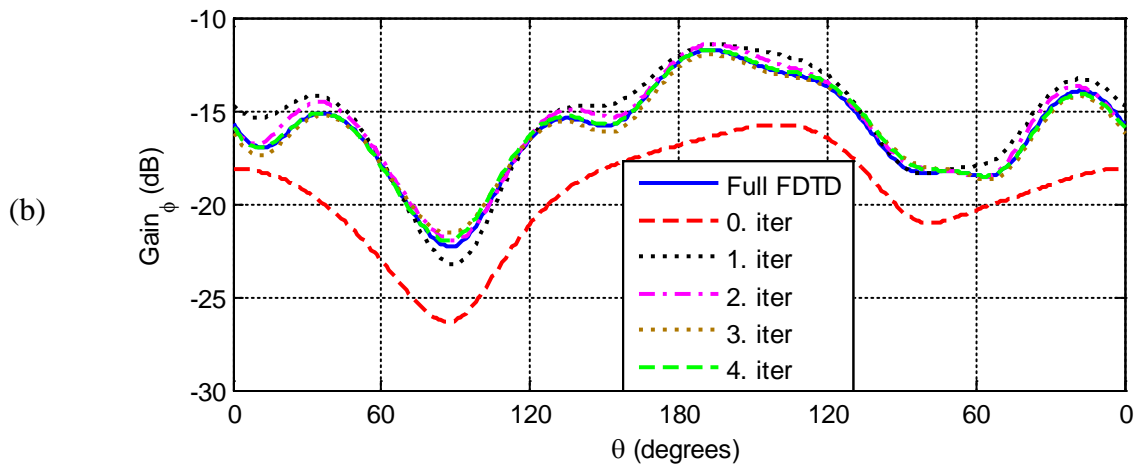
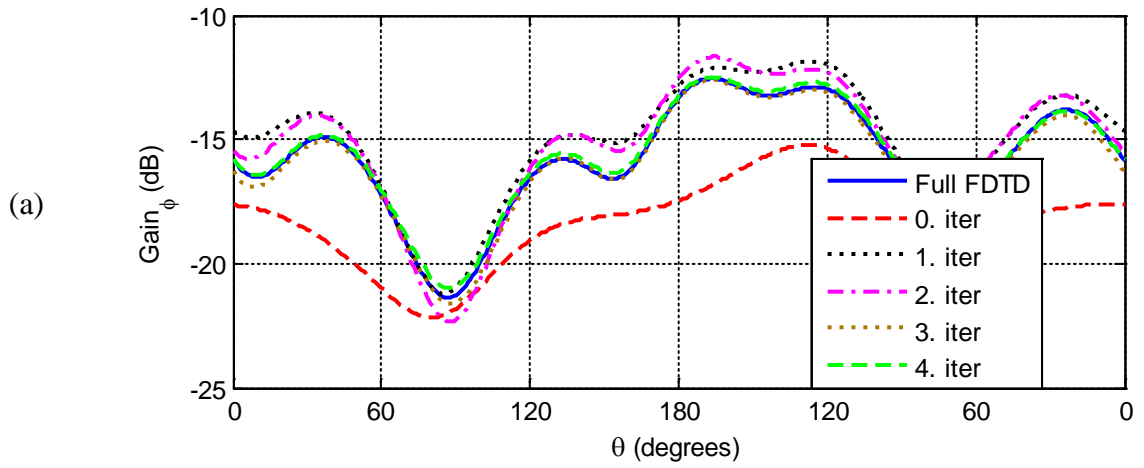


Figure 4.18: Radiation pattern (Gain_φ) for xy -plane cut at frequencies: a) 230 MHz, b) 240 MHz, c) 250 MHz, d) 260 MHz, and e) 270 MHz.



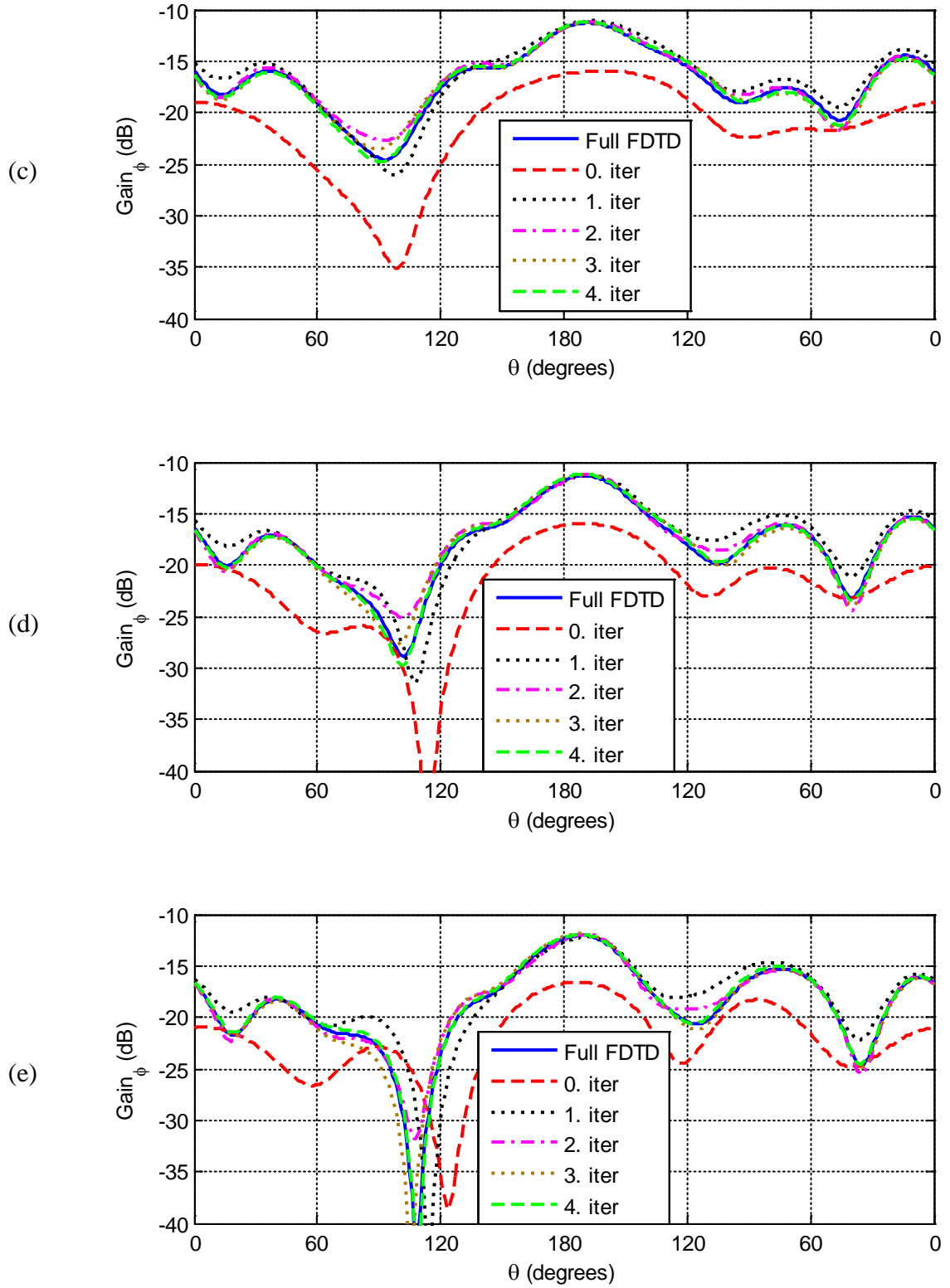
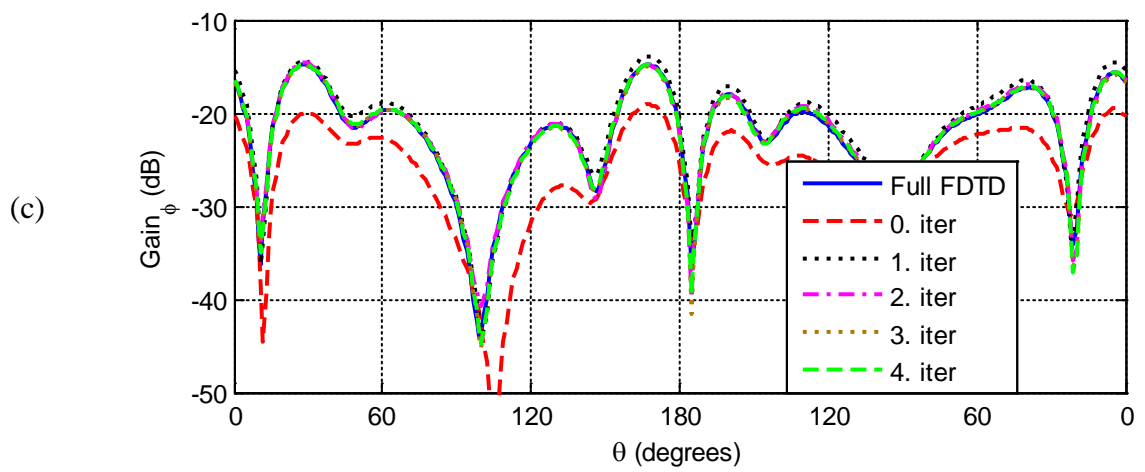
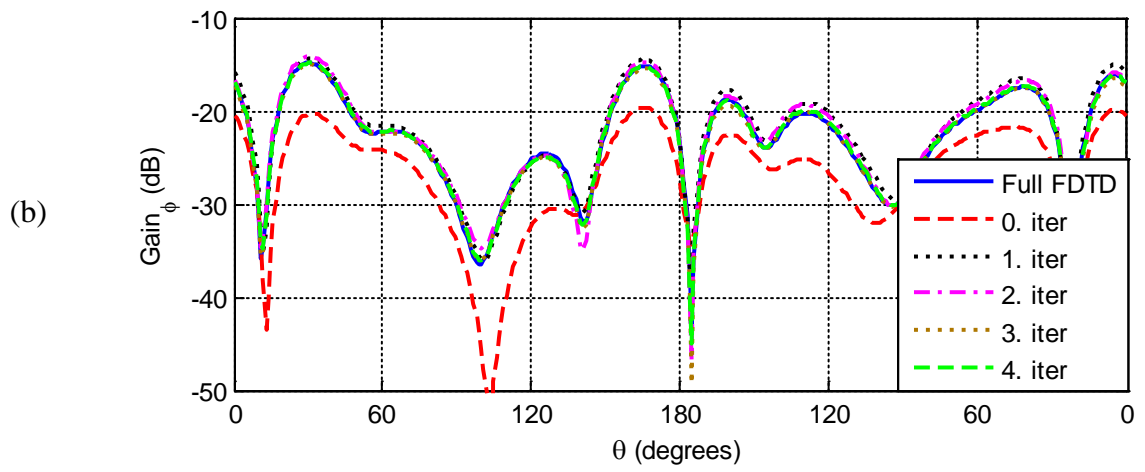
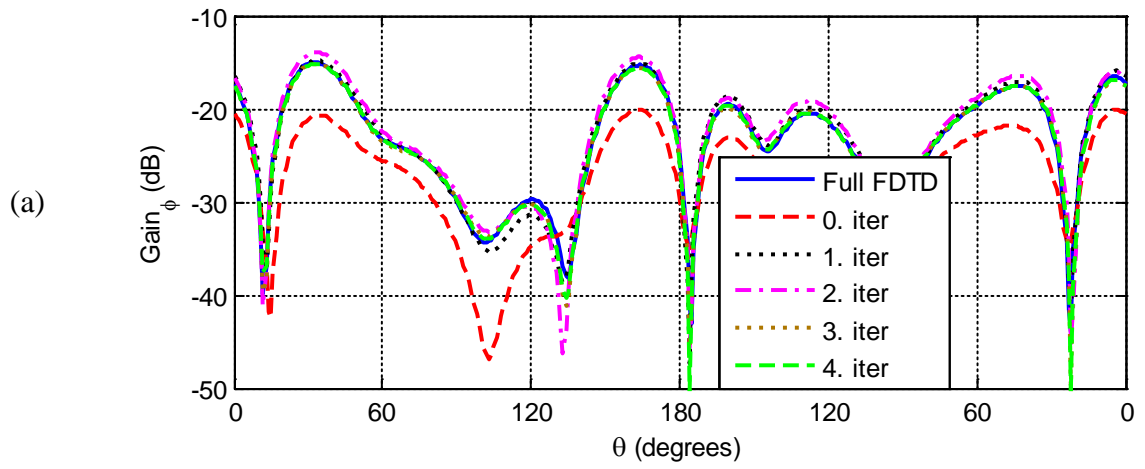


Figure 4.19: Radiation pattern (Gain_ϕ) for xz -plane cut at frequencies: a) 230 MHz, b) 240 MHz, c) 250 MHz, d) 260 MHz, and e) 270 MHz.



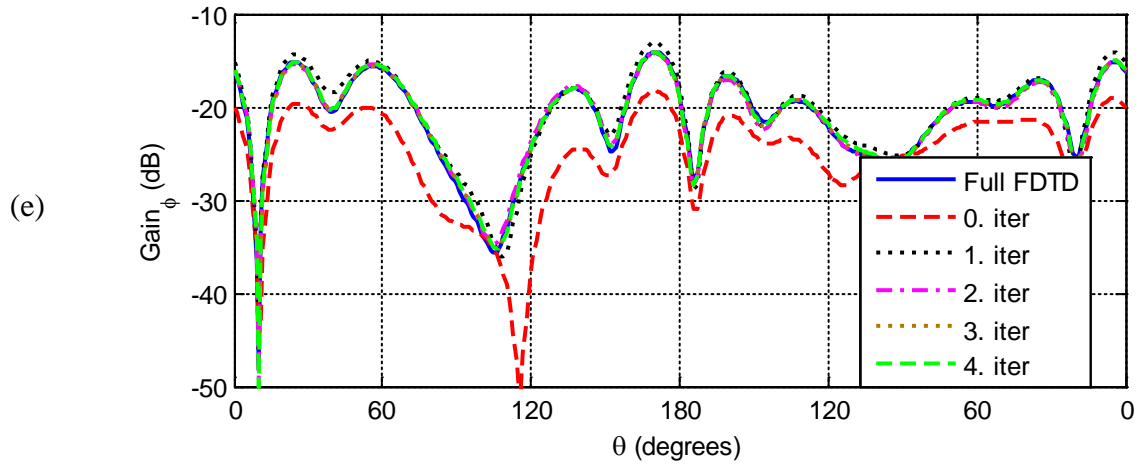
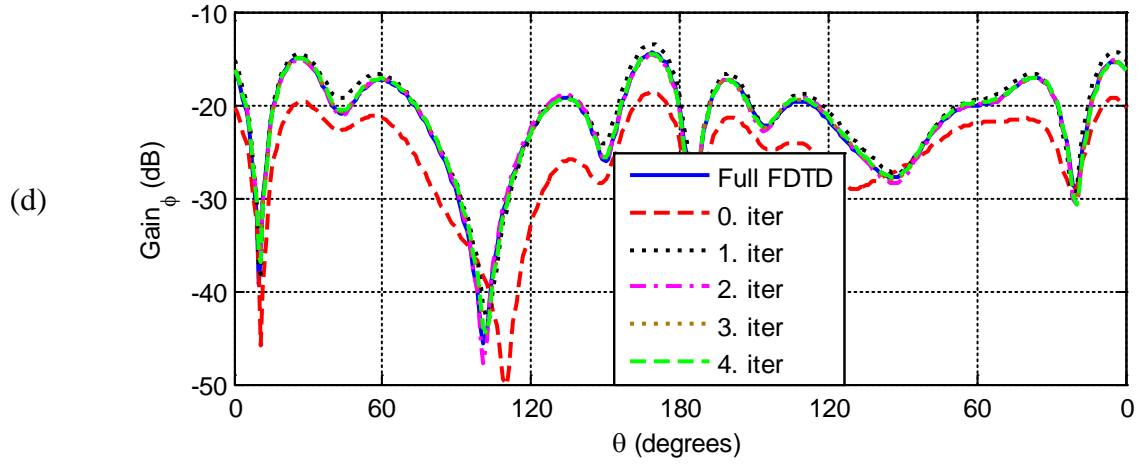
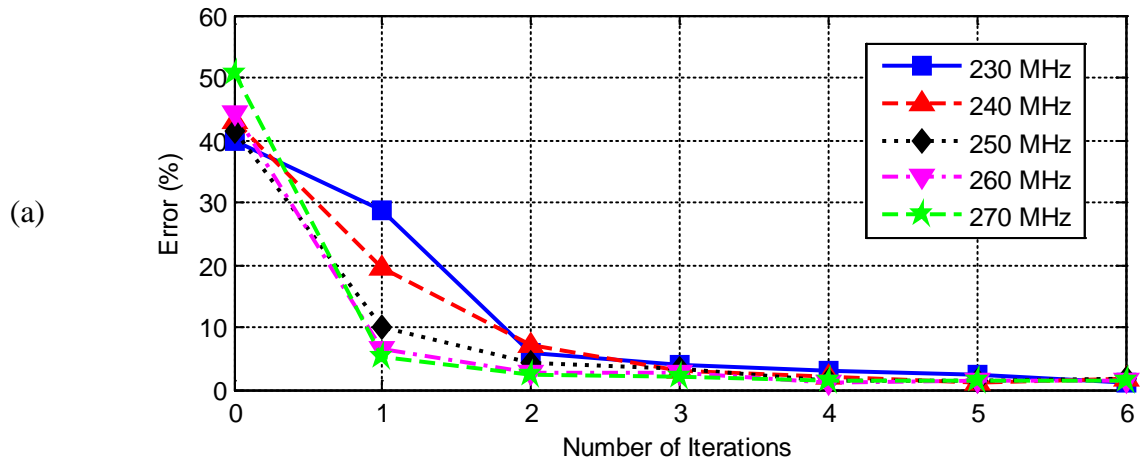


Figure 4.20: Radiation pattern (Gain_φ) for yz-plane cut at frequencies: a) 230 MHz, b) 240 MHz, c) 250 MHz, d) 260 MHz, and e) 270 MHz.



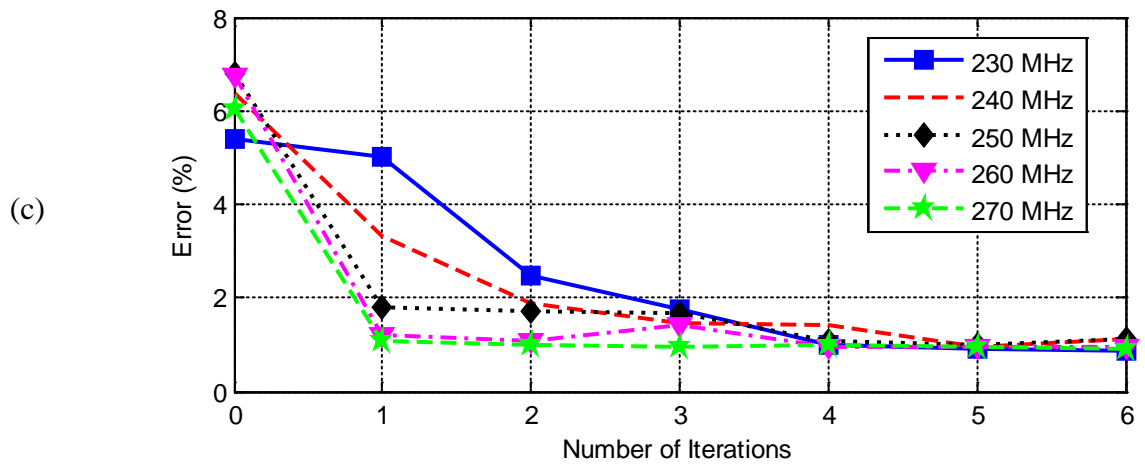
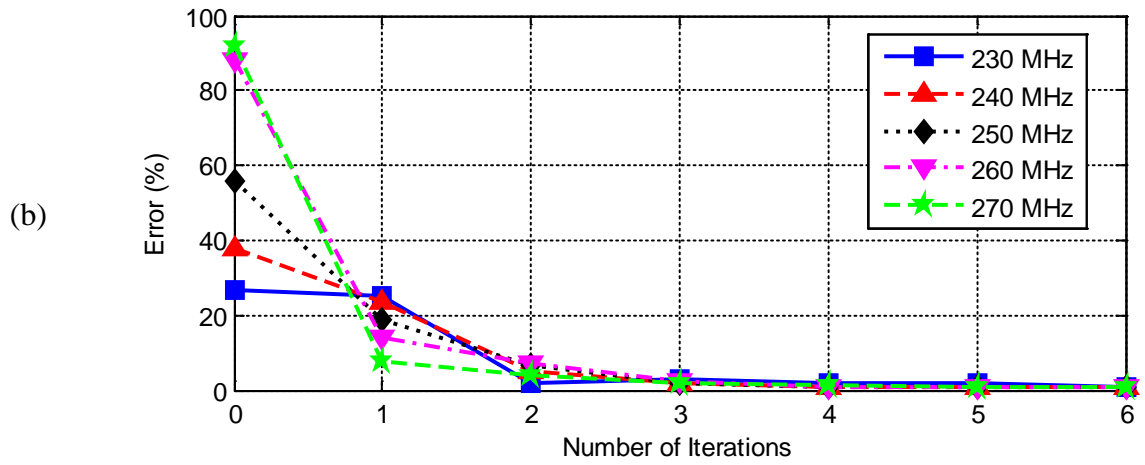
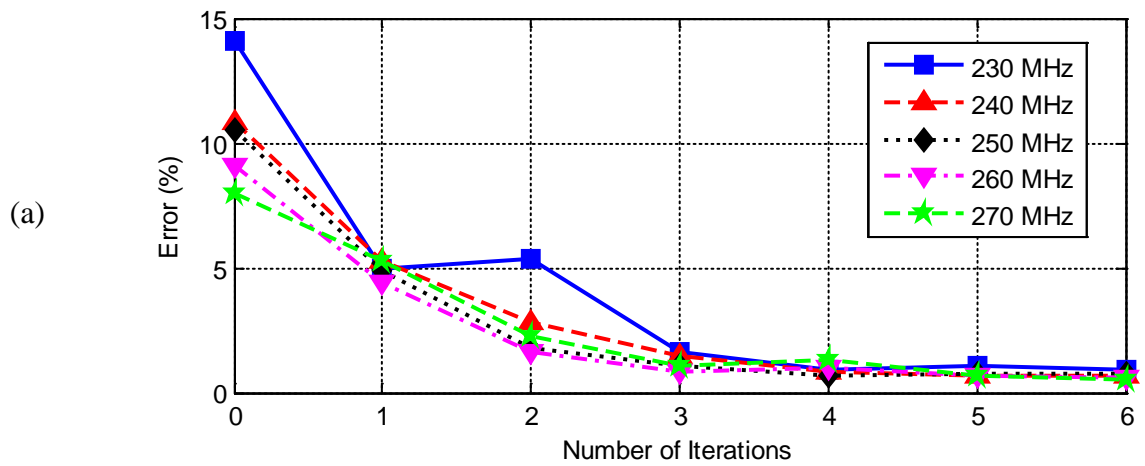


Figure 4.21: Normalized average errors for Gain_0 components in the three plane cuts: a) xy -plane, b) xz -plane, and c) yz -plane.



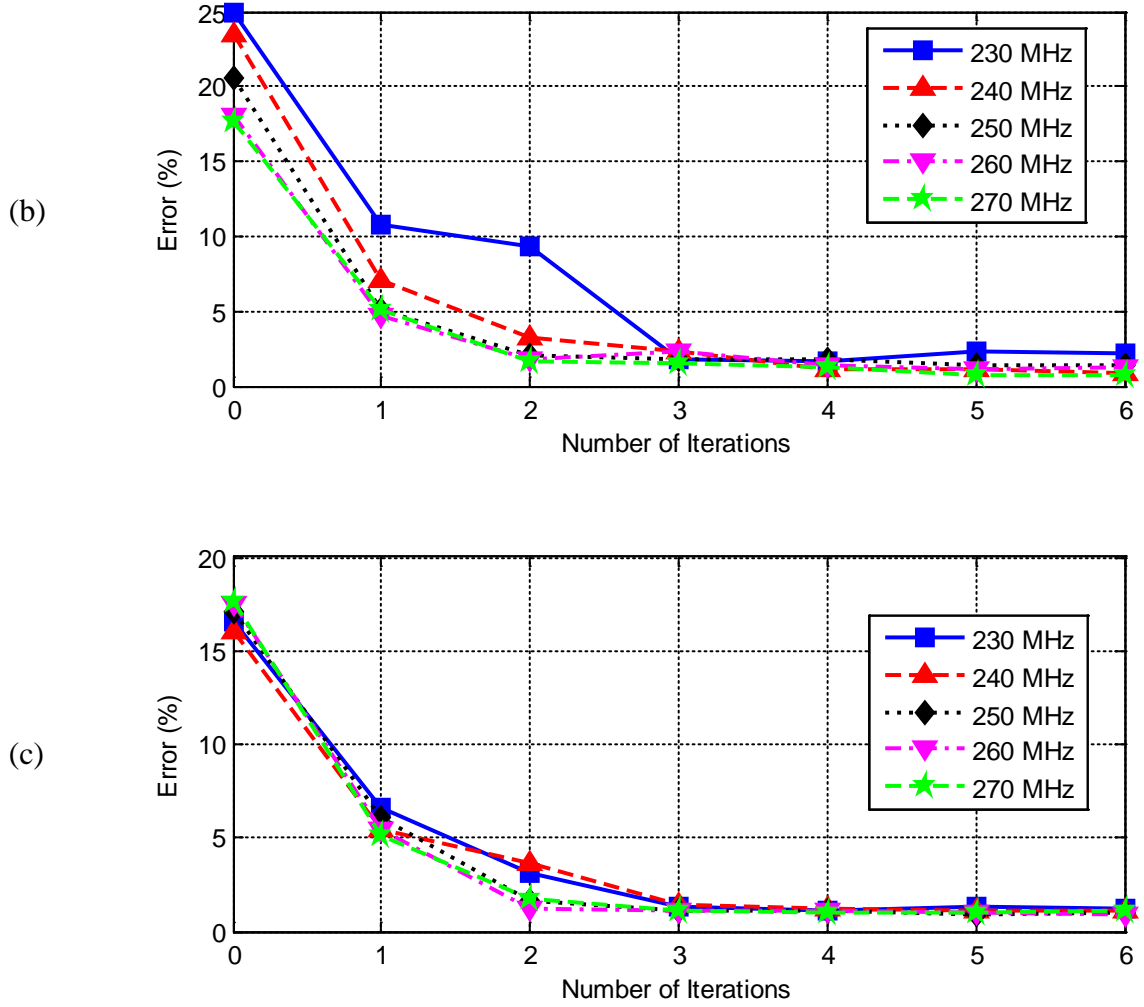


Figure 4.22: Normalized average errors for Gain_ϕ components in the three plane cuts: a) xy -plane, b) xz -plane, and c) yz -plane.

4.3 Radiation from a Dipole Antenna in the Presence of Two Objects-2

The same geometry of the second problem illustrated in Figure 4.13 is simulated as third problem with 2.5 m separation between boxes. The idea of this problem is to prove that the IMR algorithm convergences fast when the separation between the objects is large. It can be seen from Figure 4.23 that the IMR algorithm reaches the convergence criterion

after iteration # 3. Figures 4.24-4.29 show the radiation patterns (Gain_θ and Gain_ϕ) of the configuration for the three plane cuts. Good agreement with the full domain results is achieved after iteration # 3. To prove the convergence of the results of the IMR and the full domain, the normalized average errors for Gain_θ and Gain_ϕ in the three plane cuts at the frequencies of interest are shown in Figures 4.30-4.31, respectively. Simulation parameters and computer resources used are summarized in Table 4-3. The results in the table show a considerable reduction in the memory storage requirements and also computation time.

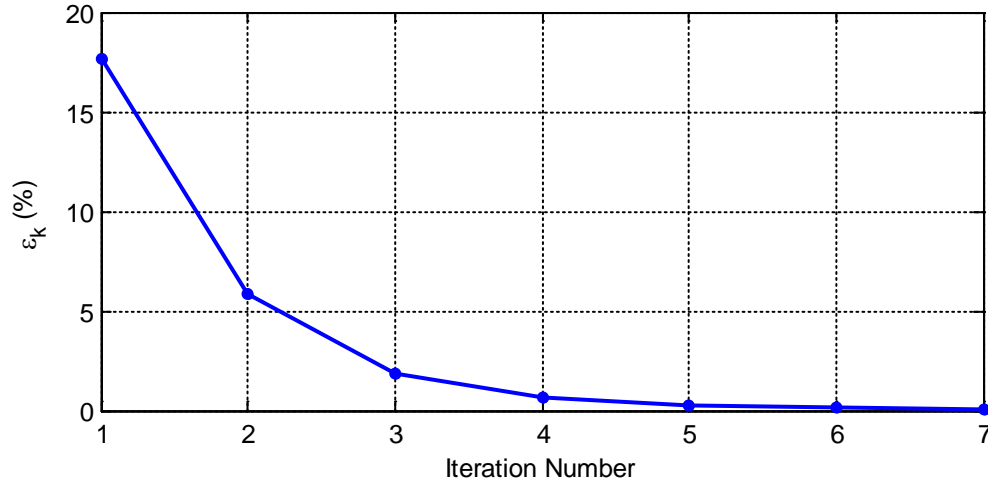
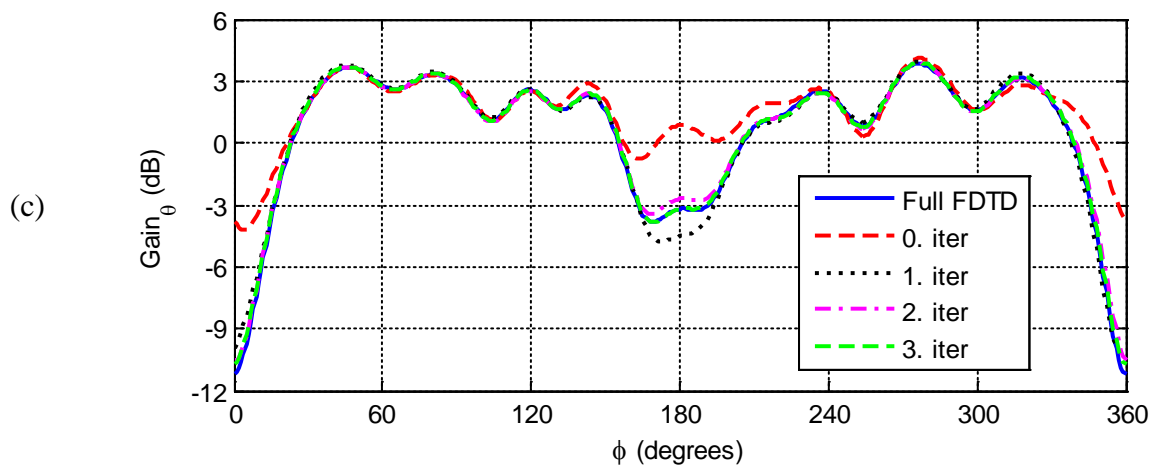
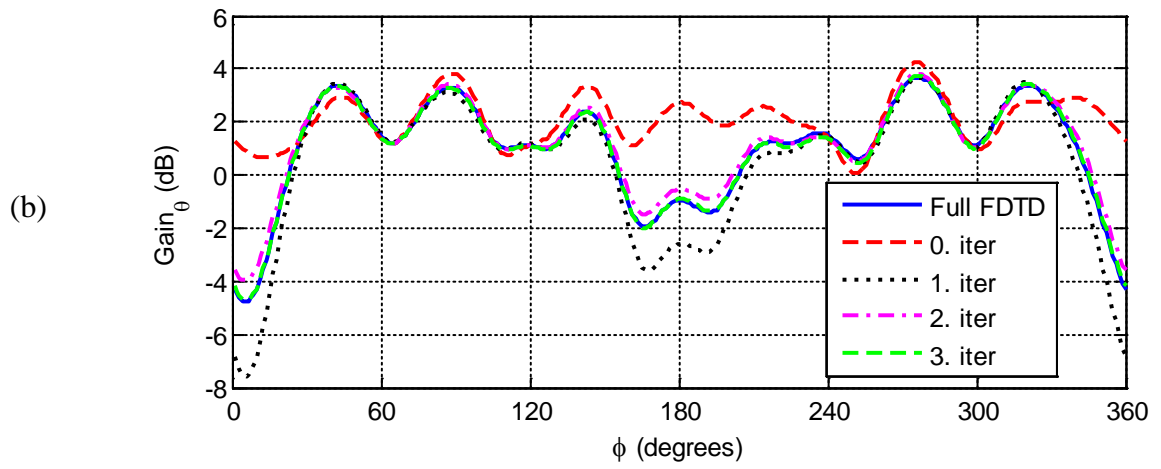
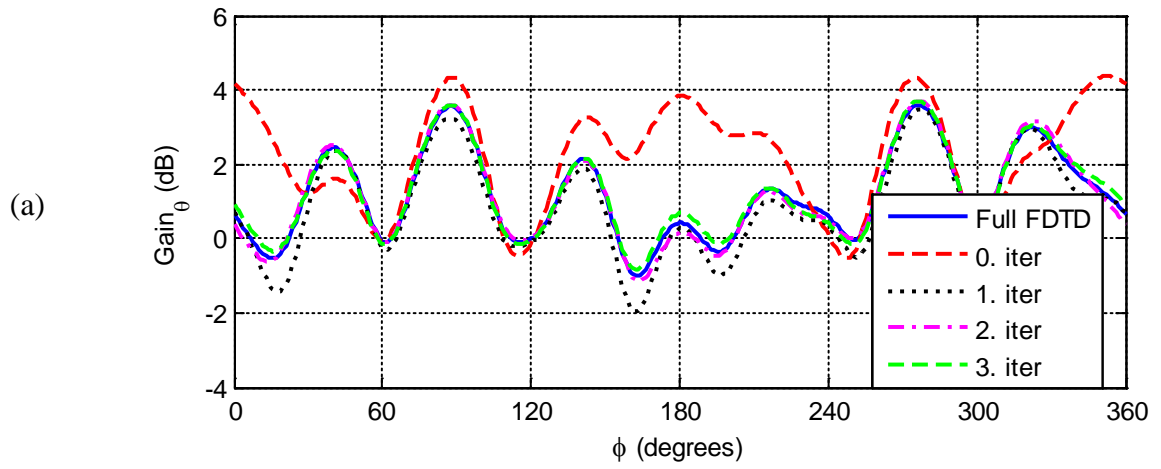


Figure 4.23: Convergence (ε_k) between iteration steps for the third problem.

Table 4-3: Simulation parameters and computer resources used by the IMR and full domain simulations.

| | Number of Domains | Total Number of Cells | Computation Time (min.) | Iteration Number | Memory (MB) |
|------------------|-------------------|-----------------------|-------------------------|------------------|-------------|
| Full FDTD | — | 24,521,280 | 651 | — | 8,375 |
| IMR-FDTD | 3 | 1,699,200 | 360 | 3 | 700 |



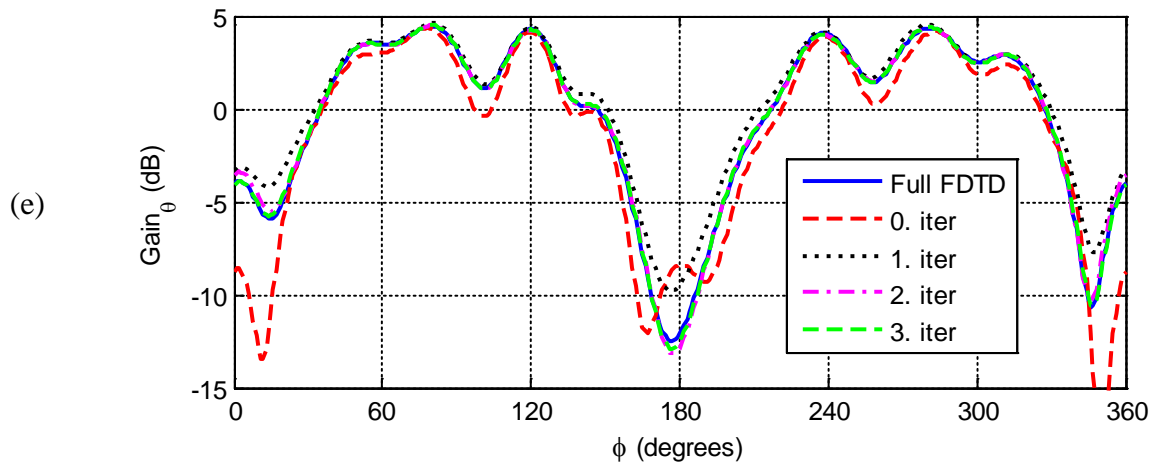
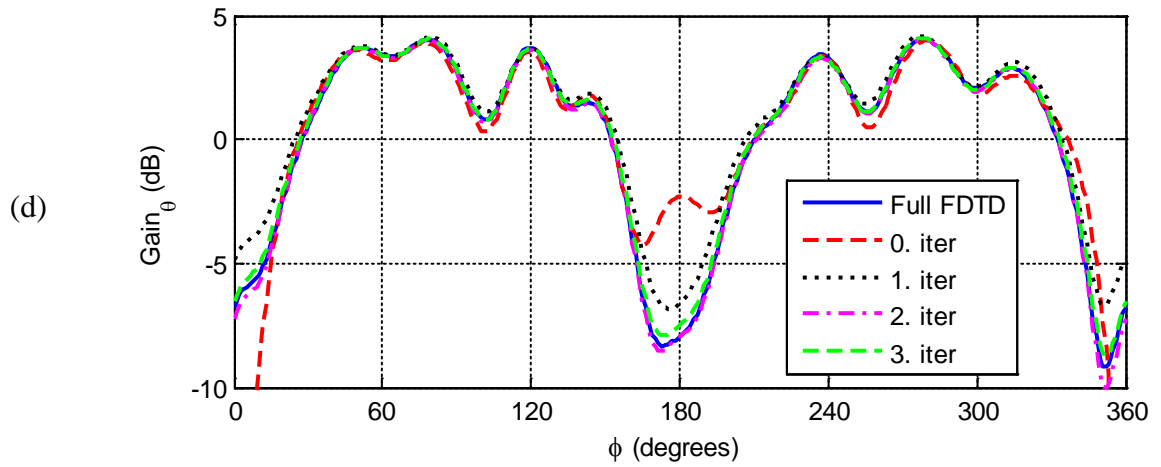
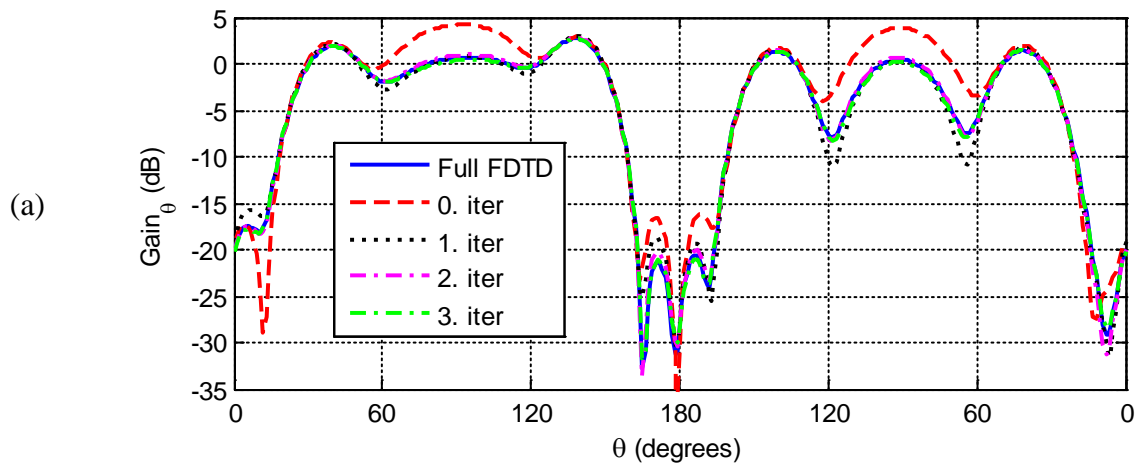
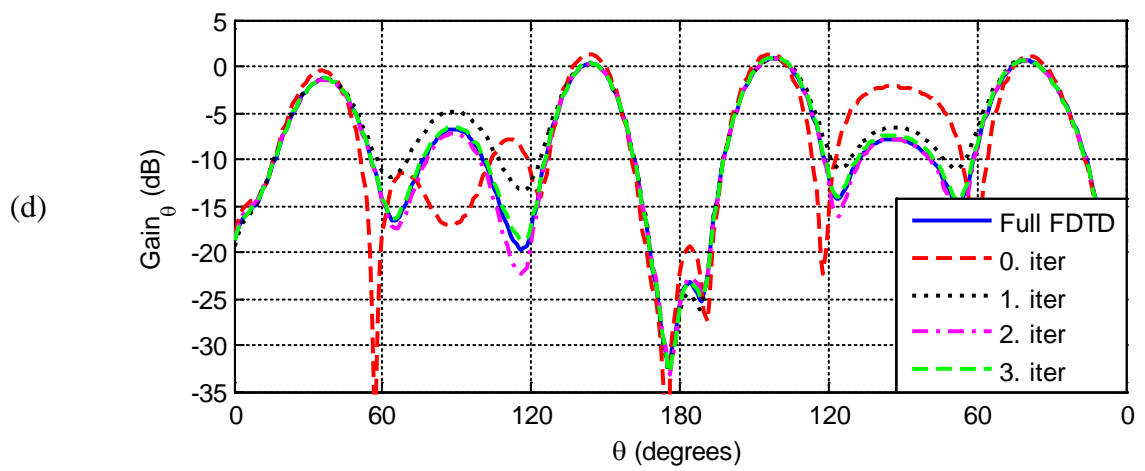
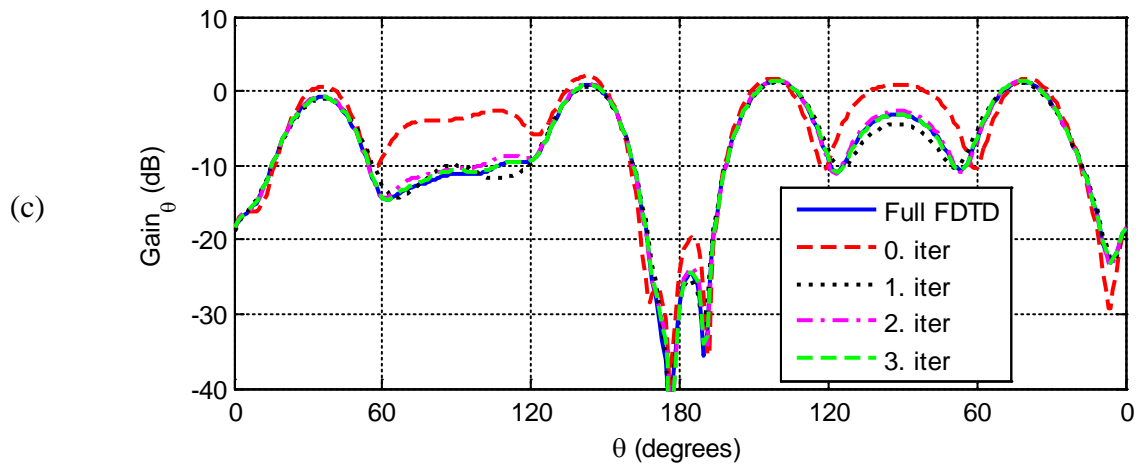
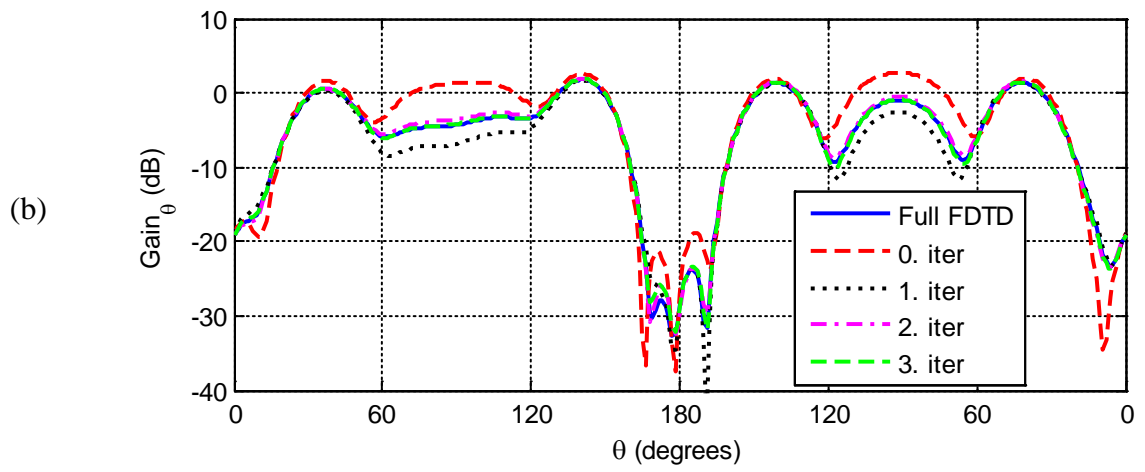


Figure 4.24: Radiation pattern (Gain_θ) for xy -plane cut at frequencies: a) 230 MHz, b) 240 MHz, c) 250 MHz, d) 260 MHz, and e) 270 MHz.





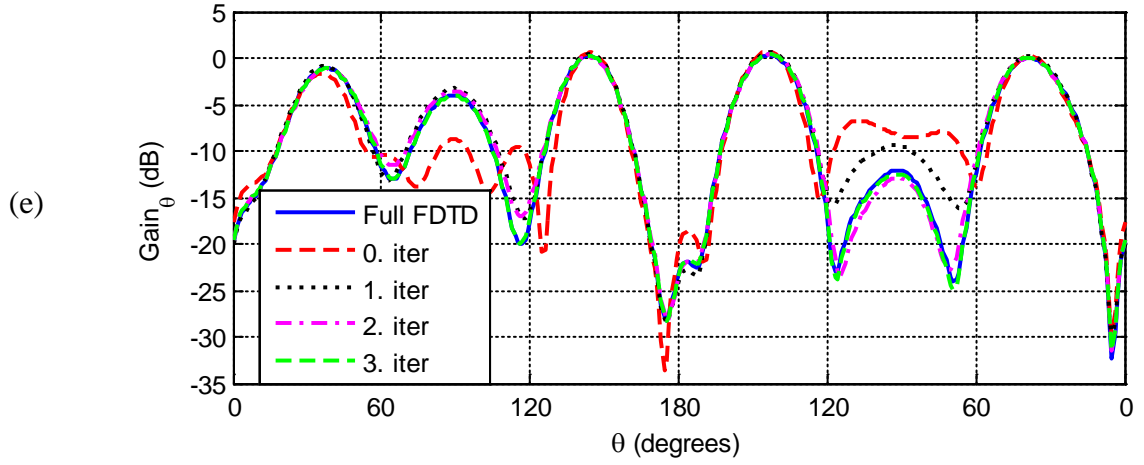
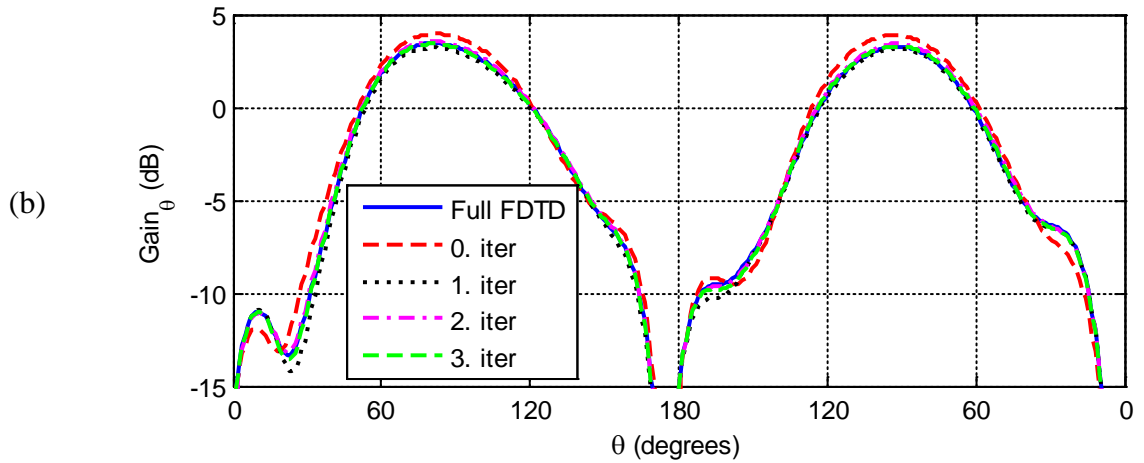
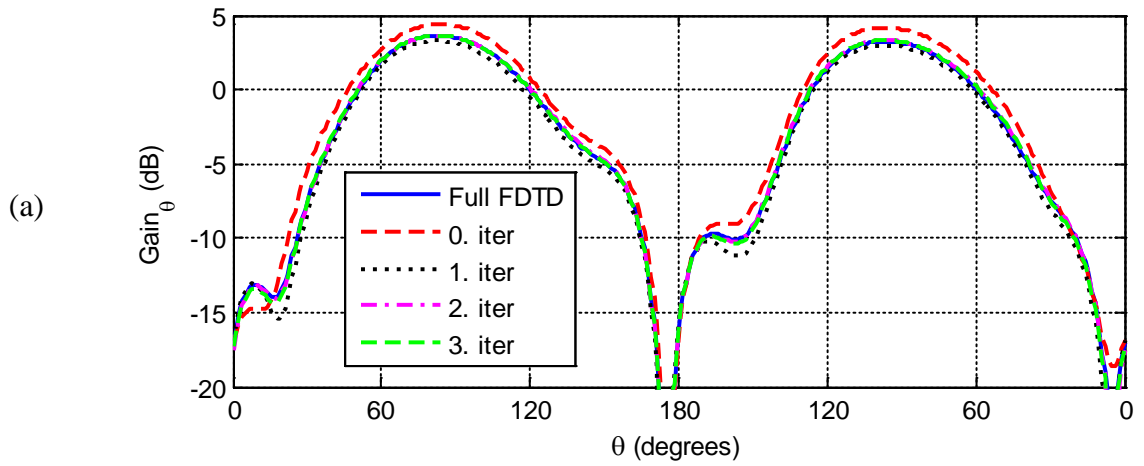


Figure 4.25: Radiation pattern (Gain_θ) for xz -plane cut at frequencies: a) 230 MHz, b) 240 MHz, c) 250 MHz, d) 260 MHz, and e) 270 MHz.



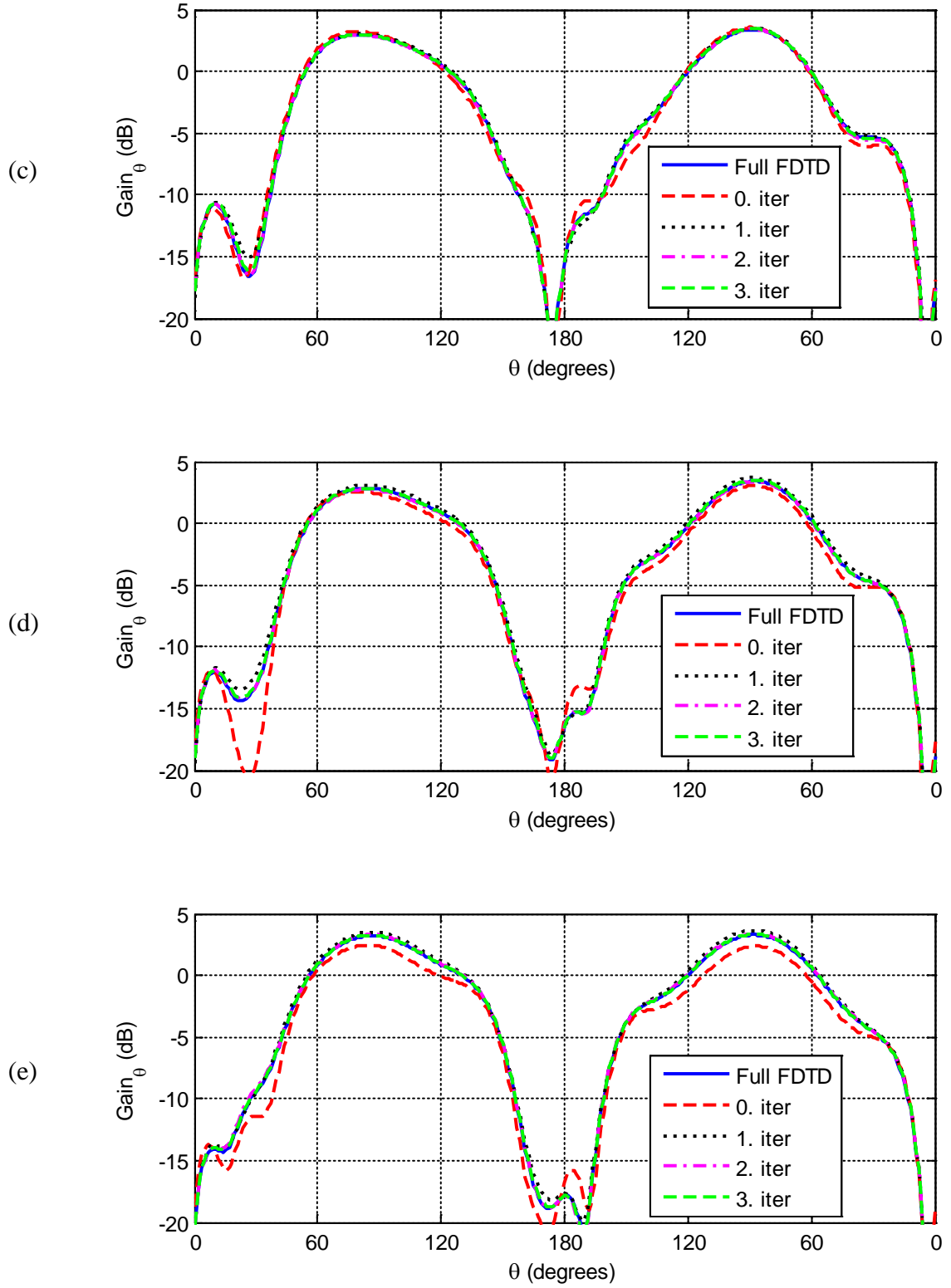
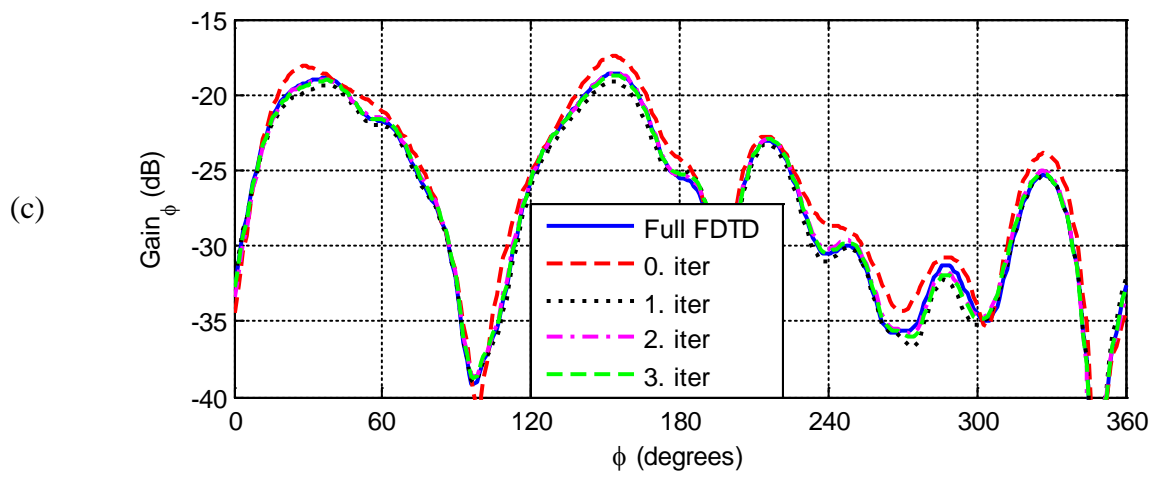
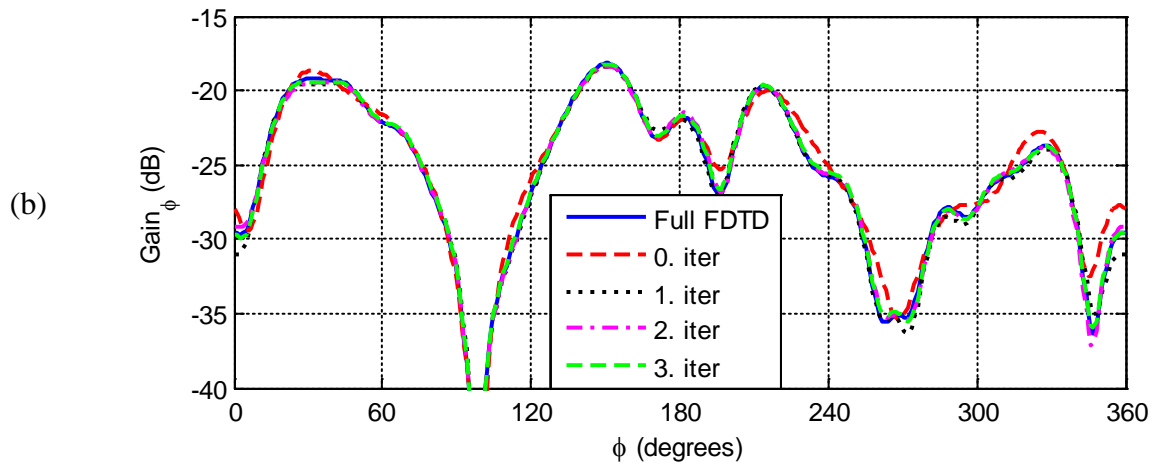
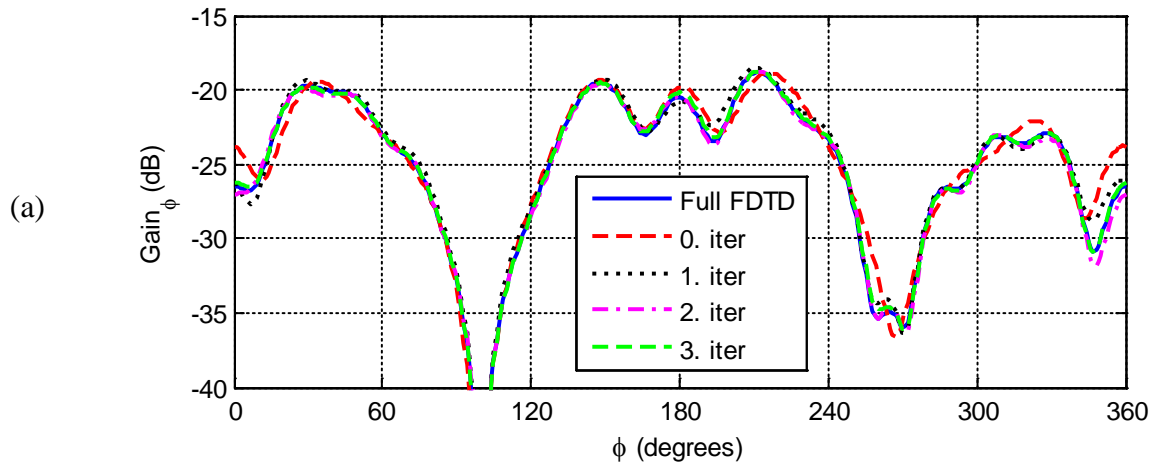


Figure 4.26: Radiation pattern (Gain_θ) for yz -plane cut at frequencies: a) 230 MHz, b) 240 MHz, c) 250 MHz, d) 260 MHz, and e) 270 MHz.



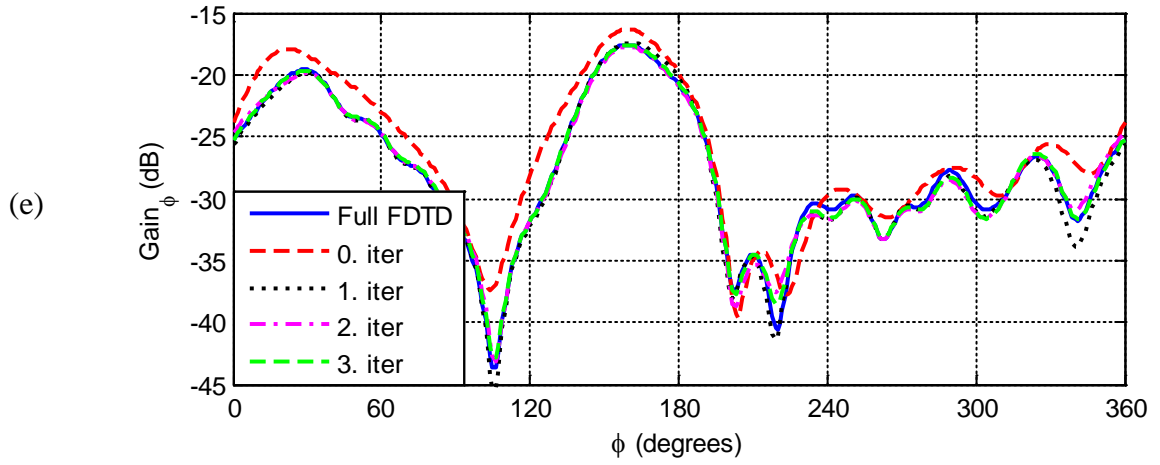
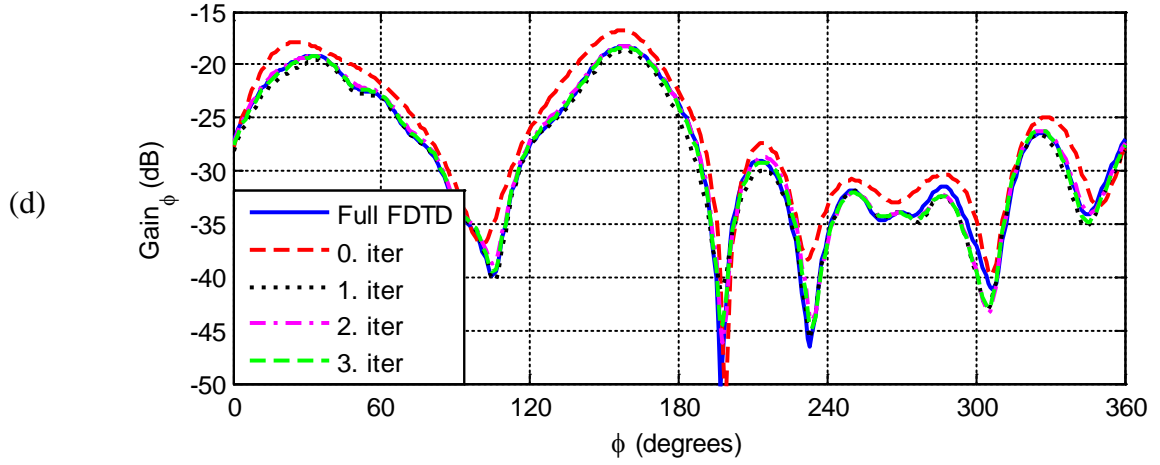
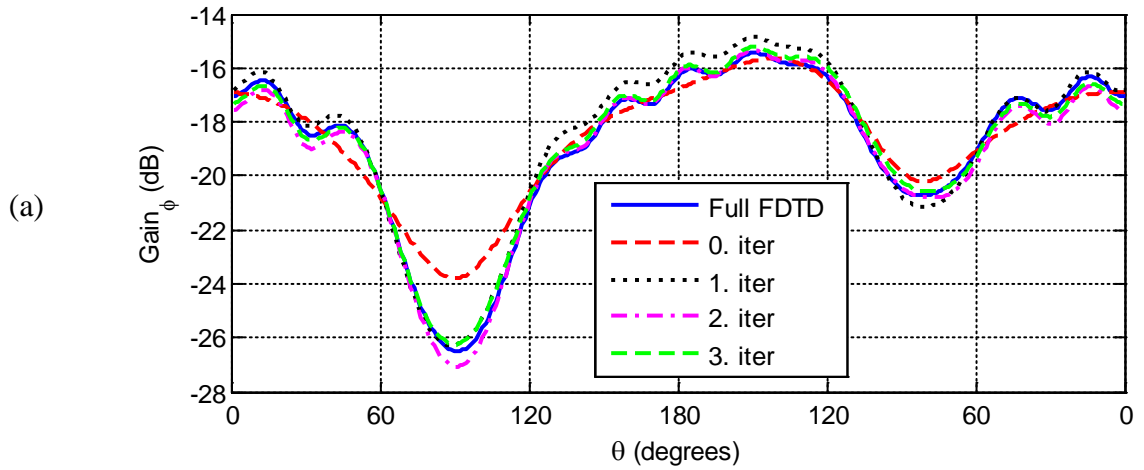
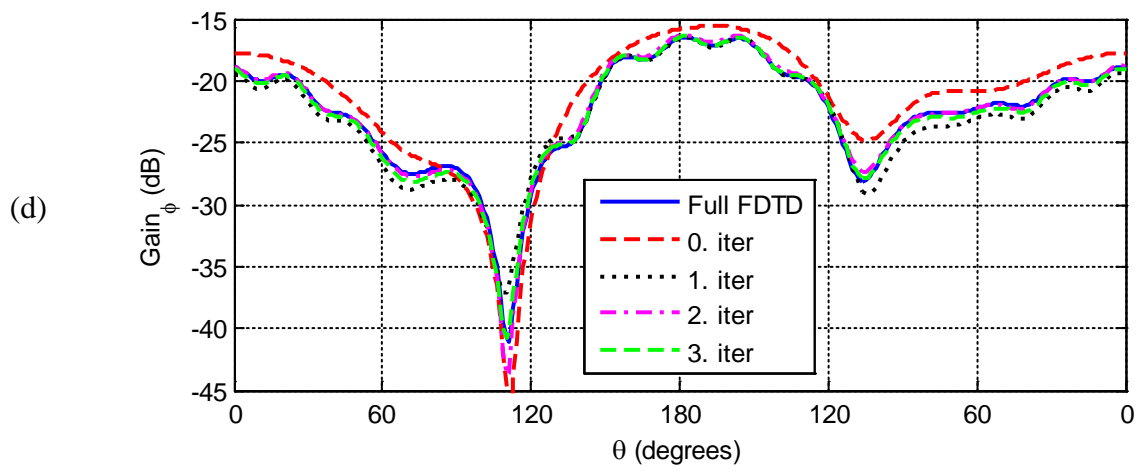
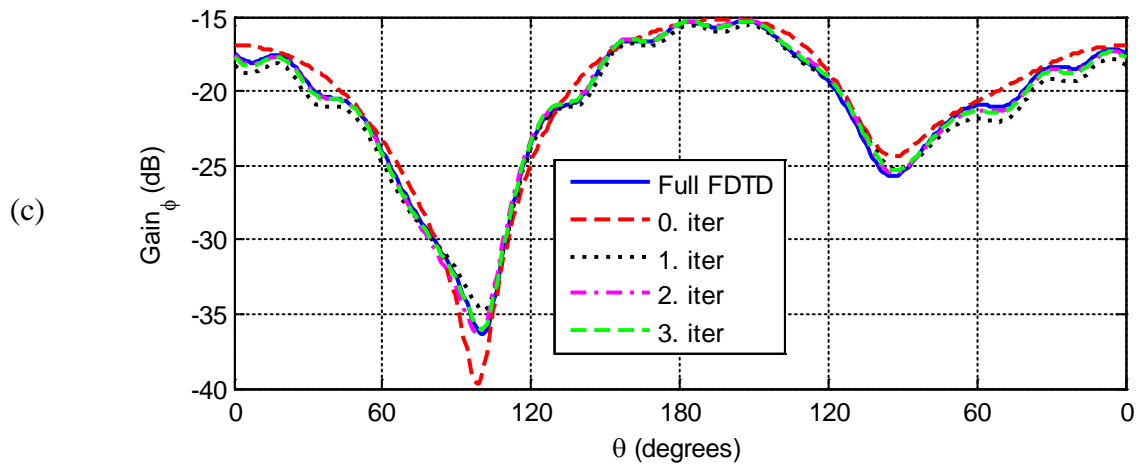
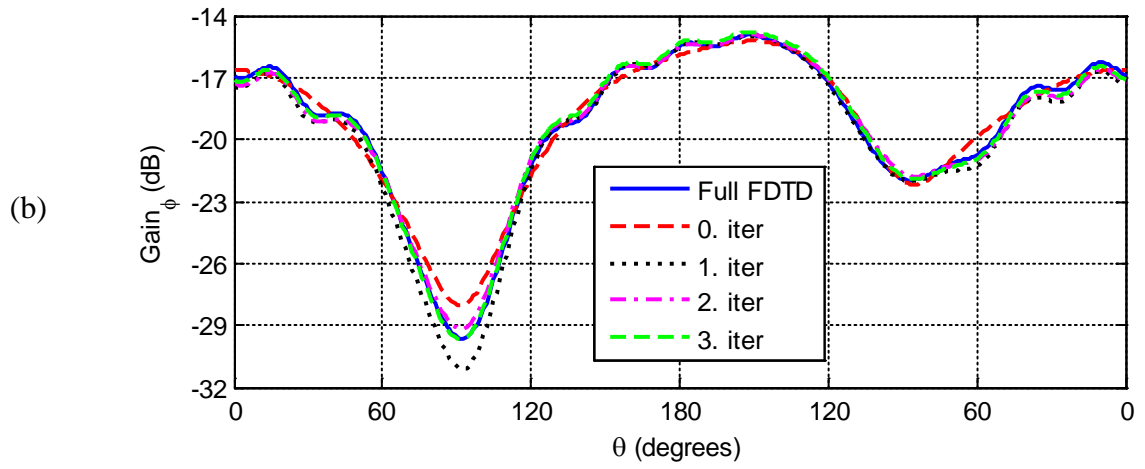


Figure 4.27: Radiation pattern (Gain_φ) for xy -plane cut at frequencies: a) 230 MHz, b) 240 MHz, c) 250 MHz, d) 260 MHz, and e) 270 MHz.





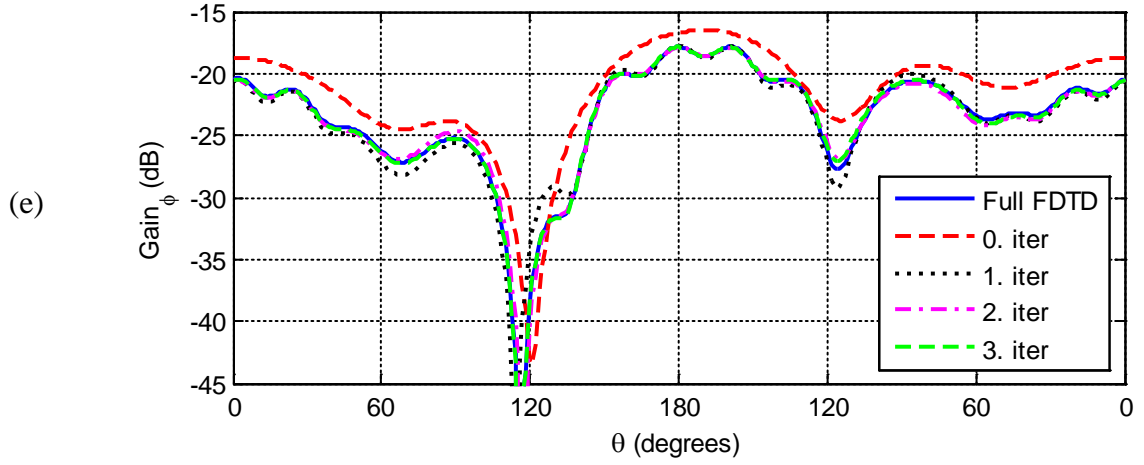
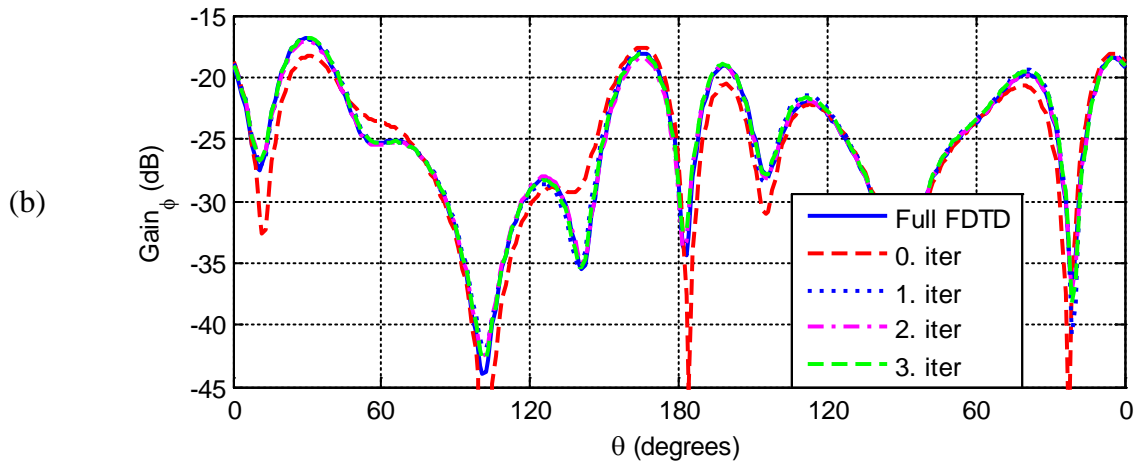
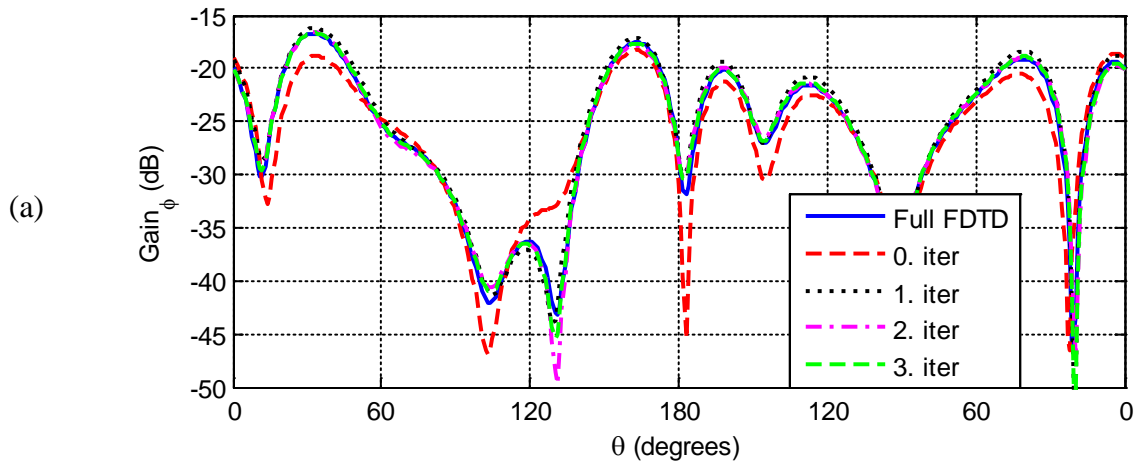


Figure 4.28: Radiation pattern (Gain_φ) for xz -plane cut at frequencies: a) 230 MHz, b) 240 MHz, c) 250 MHz, d) 260 MHz, and e) 270 MHz.



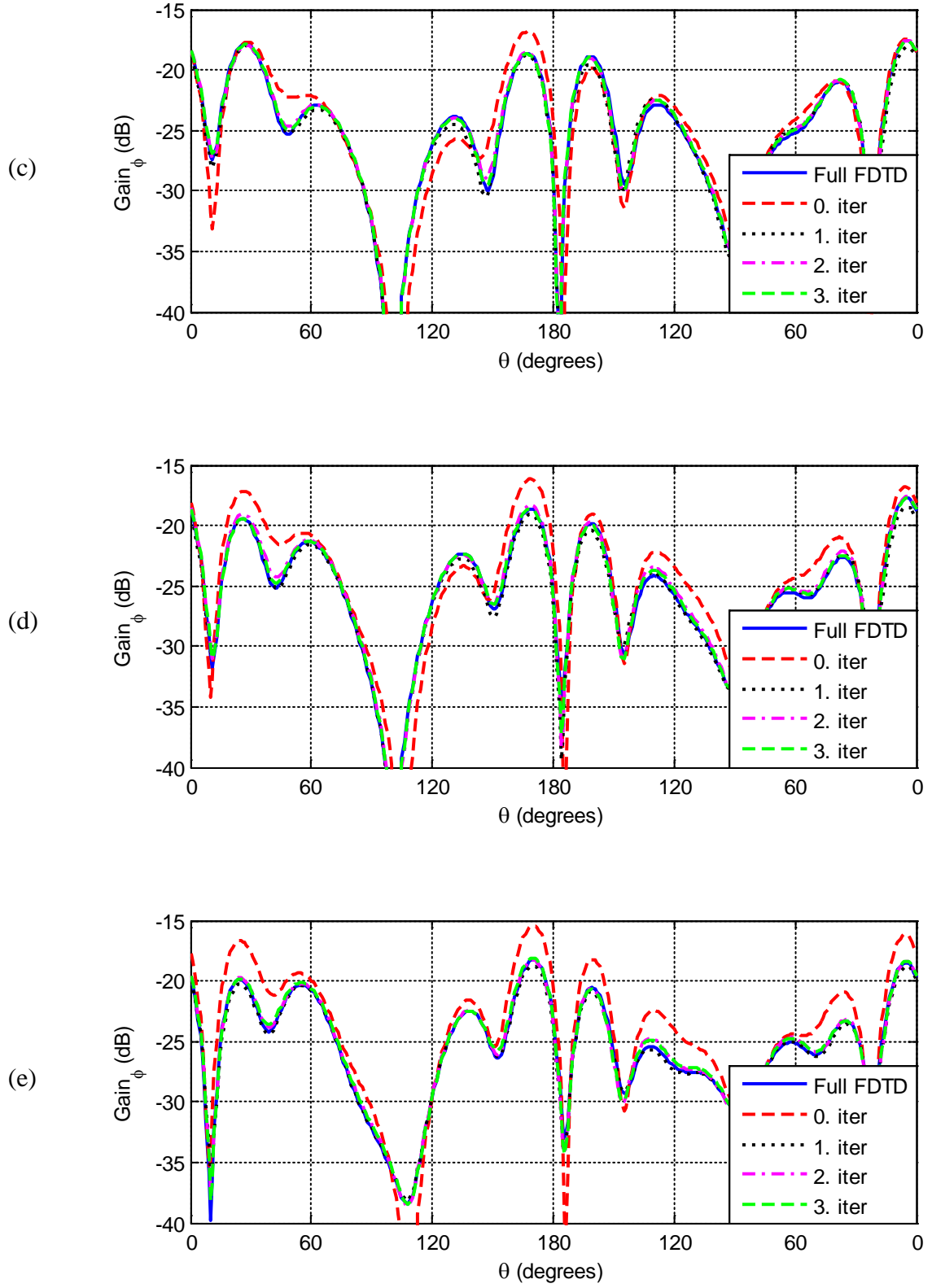


Figure 4.29: Radiation pattern (Gain_ϕ) for yz -plane cut at frequencies: a) 230 MHz, b) 240 MHz, c) 250 MHz, d) 260 MHz, and e) 270 MHz.

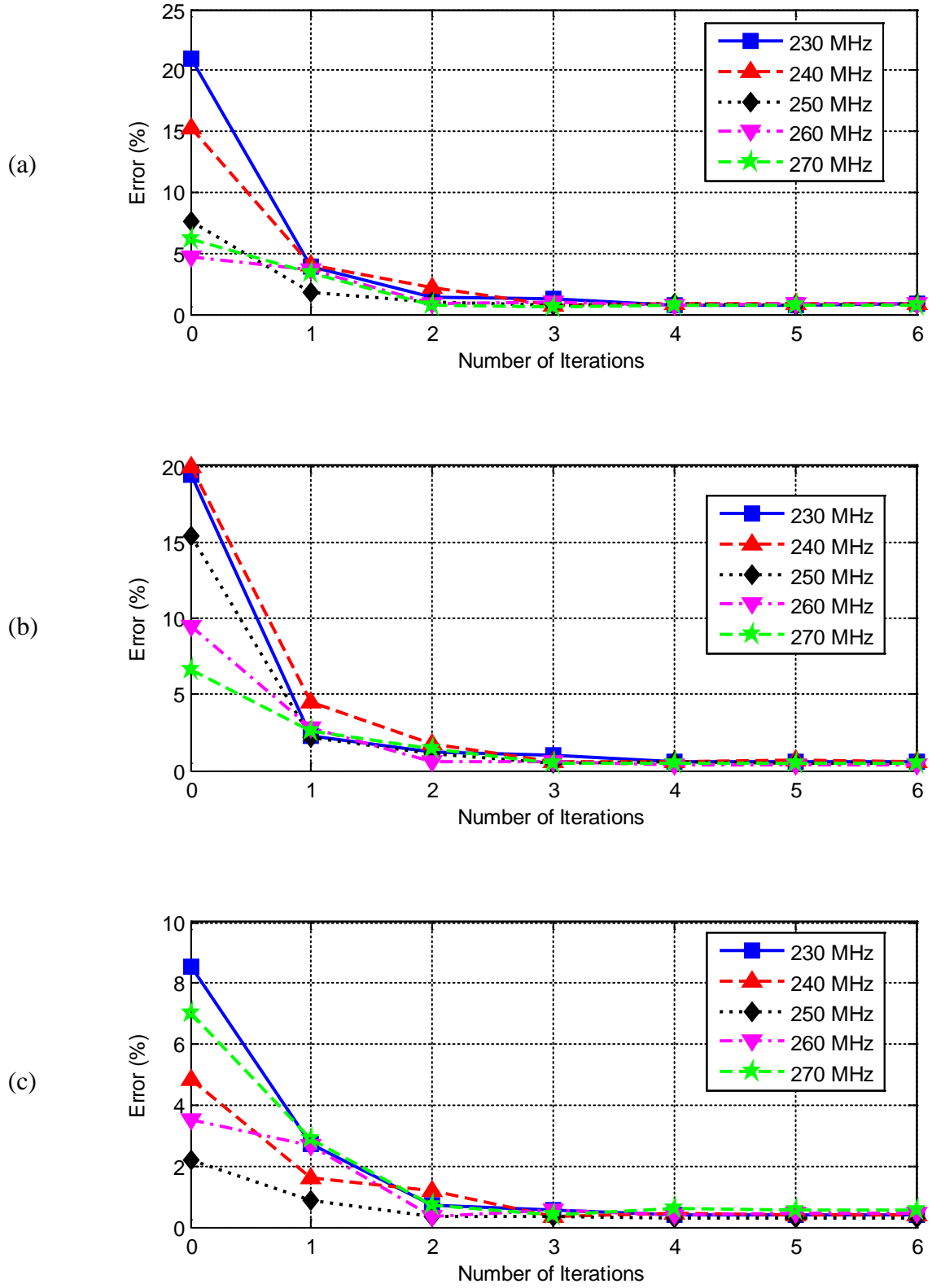


Figure 4.30: Normalized average errors for Gain_0 components in the three plane cuts: a) xy -plane, b) xz -plane, and c) yz -plane.

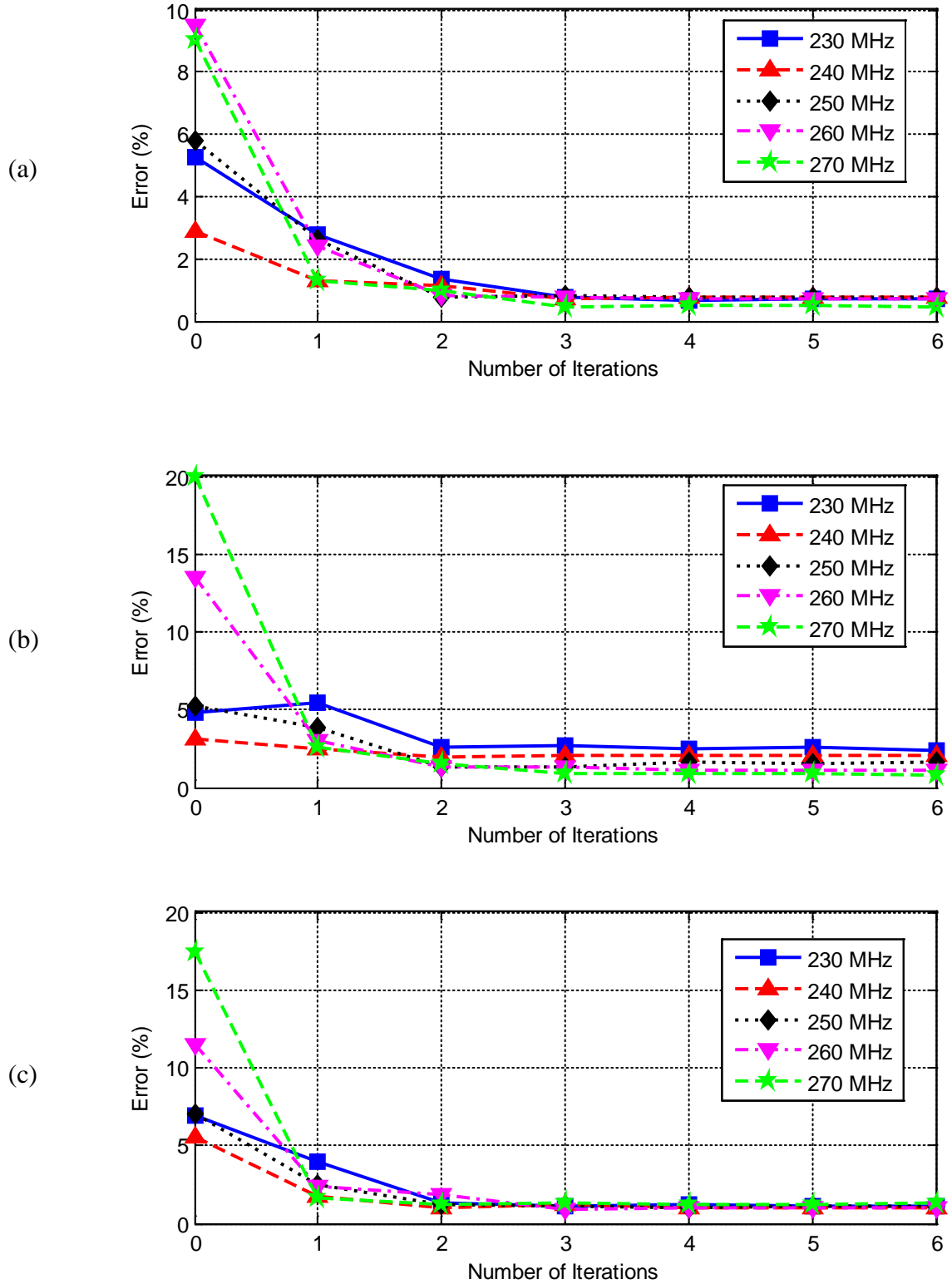


Figure 4.31: Normalized average errors for Gain_ϕ components in the three plane cuts: a) xy -plane, b) xz -plane, and c) yz -plane.

4.4 Radiation from a Dipole Antenna in the Presence of Two Objects-3

The geometry of the fourth problem is presented in Figure 4.32. This problem consists of a 0.5 m dipole antenna and two scatterer boxes. The dielectric box and conducting L-shaped box are placed a distance of 0.5 m and 3 m away from the dipole antenna on the x -axis, respectively. The dimensions of the dielectric box are 0.5 m, 2.5 m, and 1 m along the x , y , and z directions, respectively. The relative permittivity of the dielectric box is 2.2. The dimensions of the conducting L-shaped box are given in Figure 4.32. It can be seen from Figure 4.33 that the IMR algorithm reaches the convergence criterion after iteration # 3. Figures 4.34-4.39 show the radiation patterns (Gain_θ and Gain_ϕ) of the problem for the three plane cuts. Good agreement with the full domain results is achieved after iteration # 3. To prove the convergence of the results of the IMR and the full domain, the normalized average errors for Gain_θ and Gain_ϕ in the three plane cuts at the frequencies of interest are shown in Figures 4.40-4.41, respectively. Simulation parameters and computer resources are summarized in Table 4-4. The results in the table show a considerable reduction in the memory storage requirements and also computation time.

Table 4-4: Simulation parameters and computer resources used by the IMR and full domain simulations.

| | Number of Domains | Total Number of Cells | Computation Time (min.) | Iteration Number | Memory (MB) |
|------------------|-------------------|-----------------------|-------------------------|------------------|-------------|
| Full FDTD | — | 18,172,512 | 390 | — | 6,700 |
| IMR-FDTD | 3 | 1,737,600 | 267 | 3 | 632 |

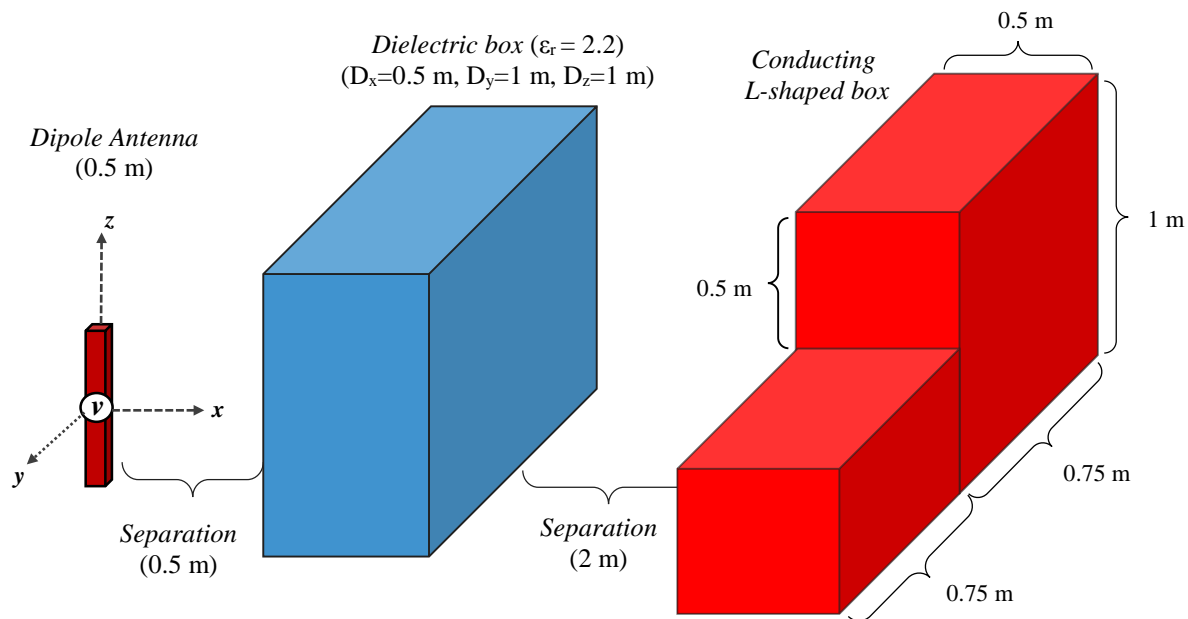


Figure 4.32: Geometry of the fourth problem.

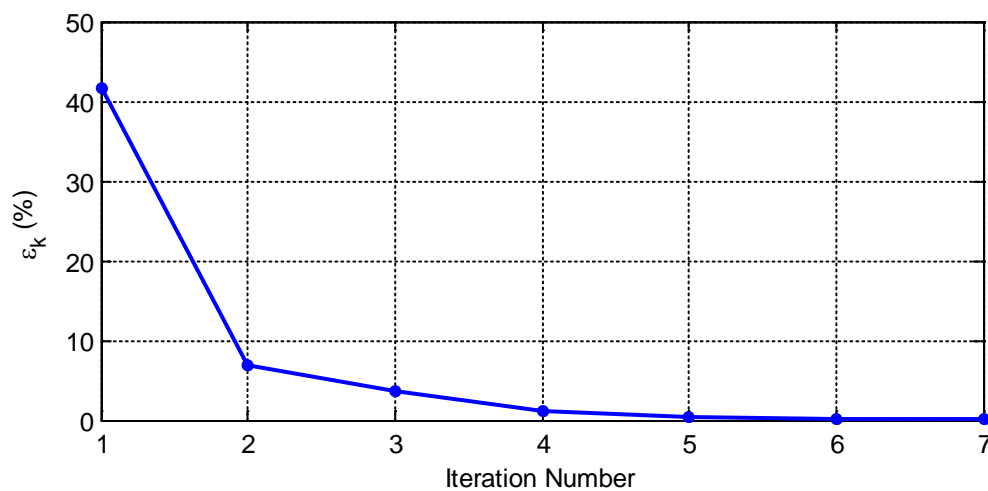
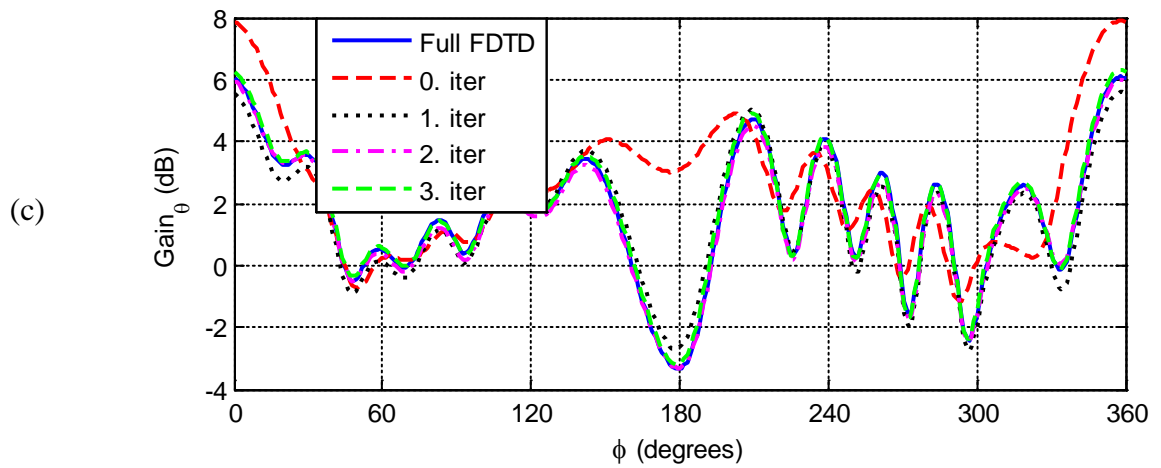
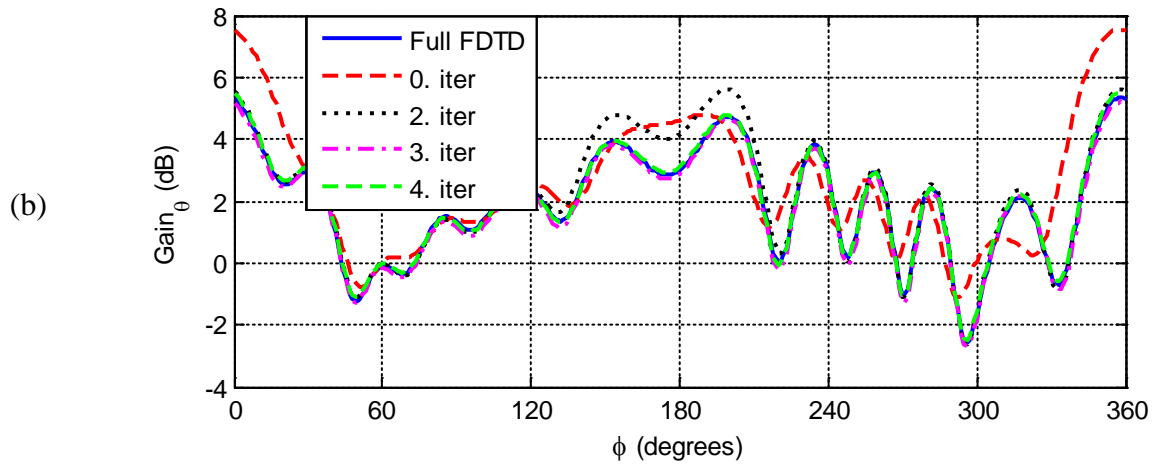
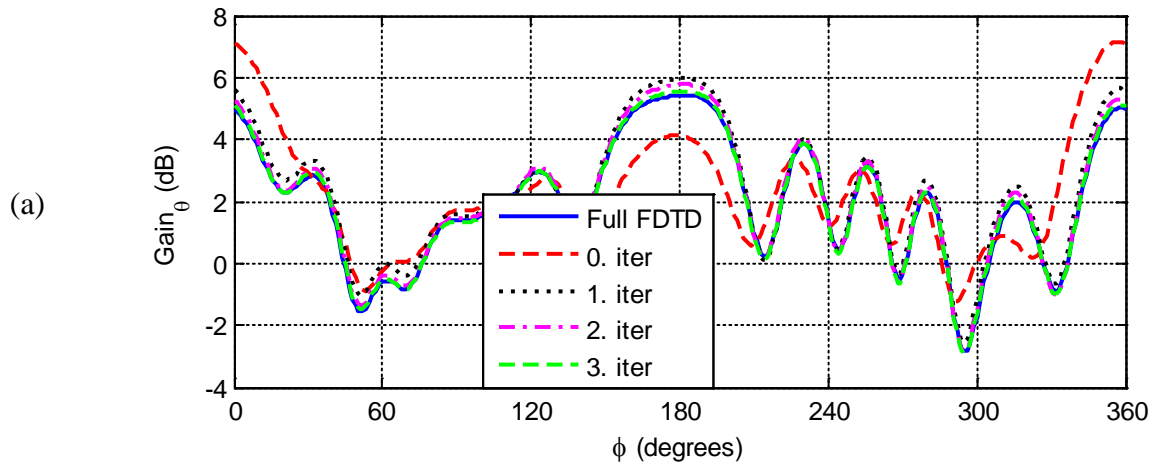


Figure 4.33: Convergence (ϵ_k) between iteration steps for the fourth problem.



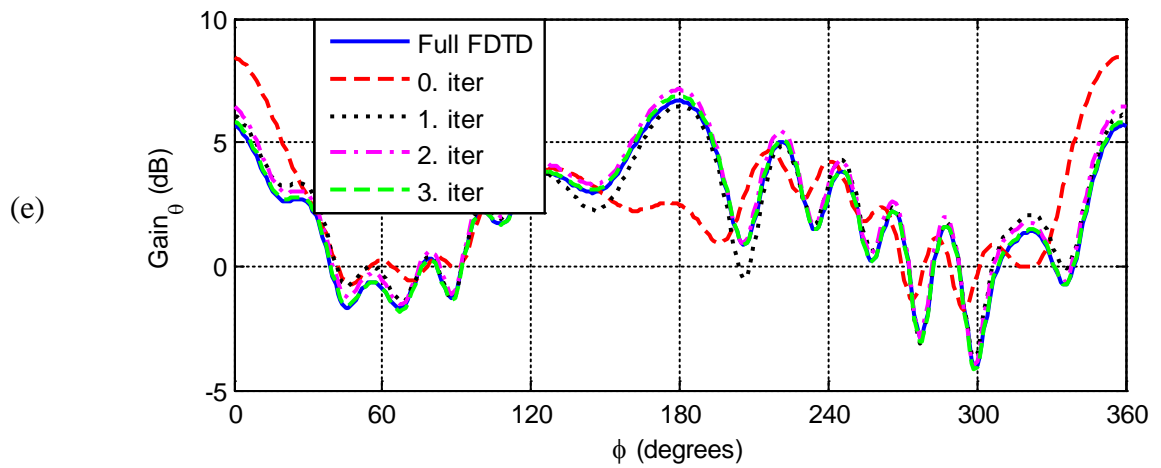
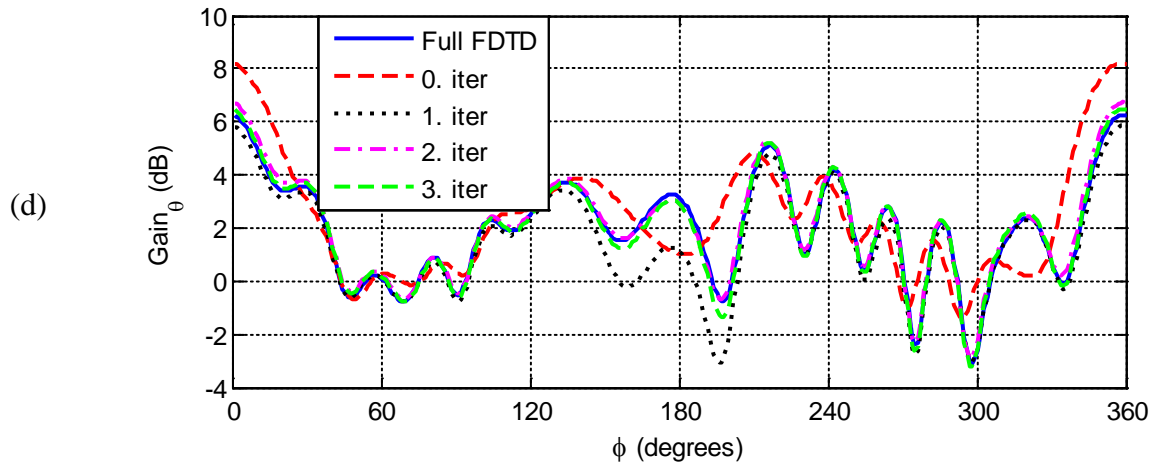
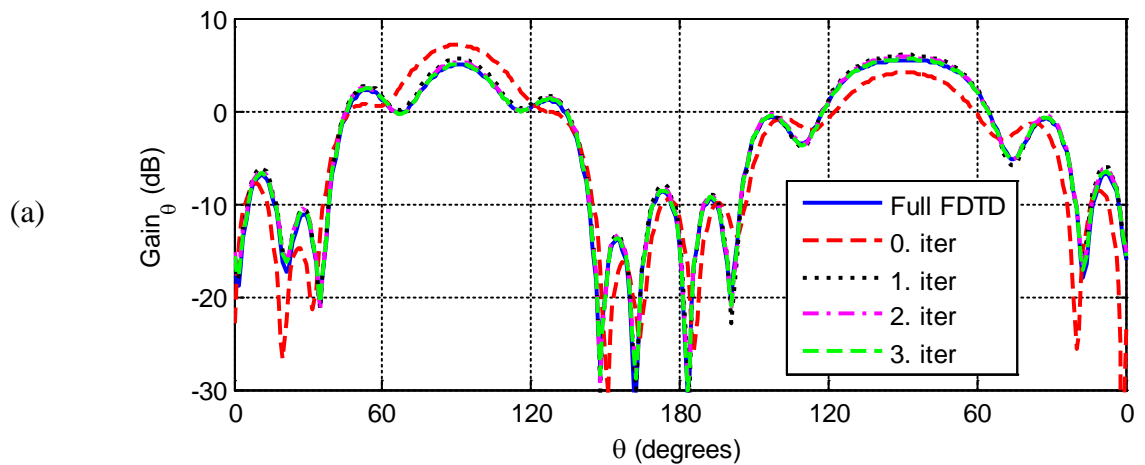
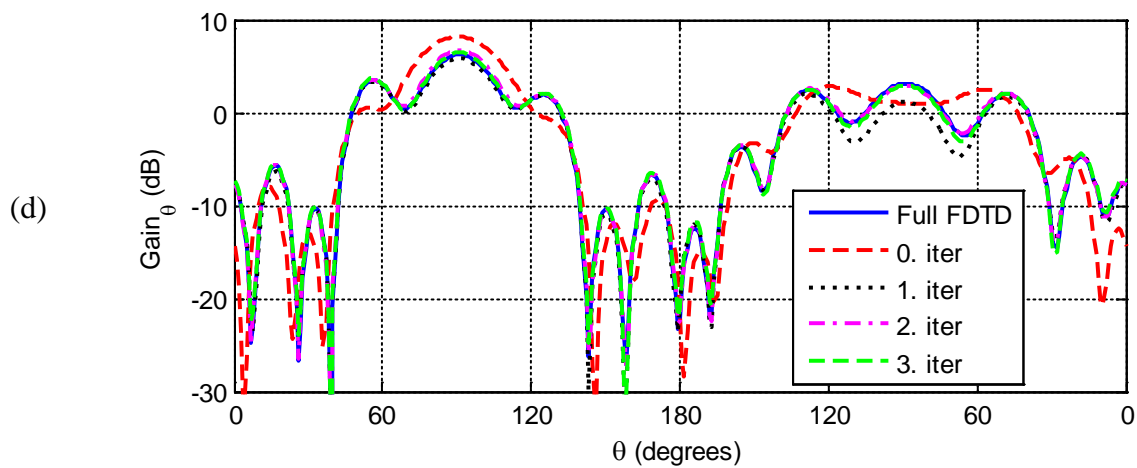
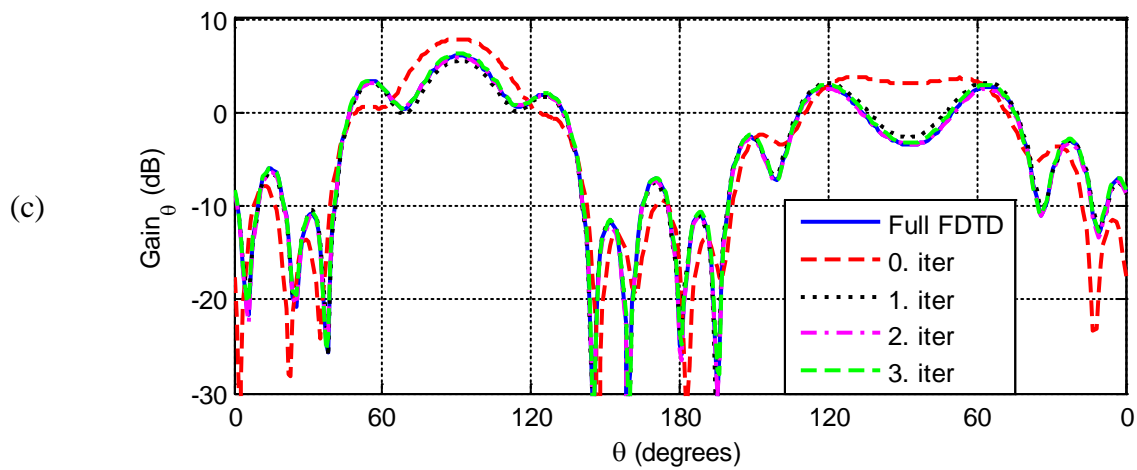
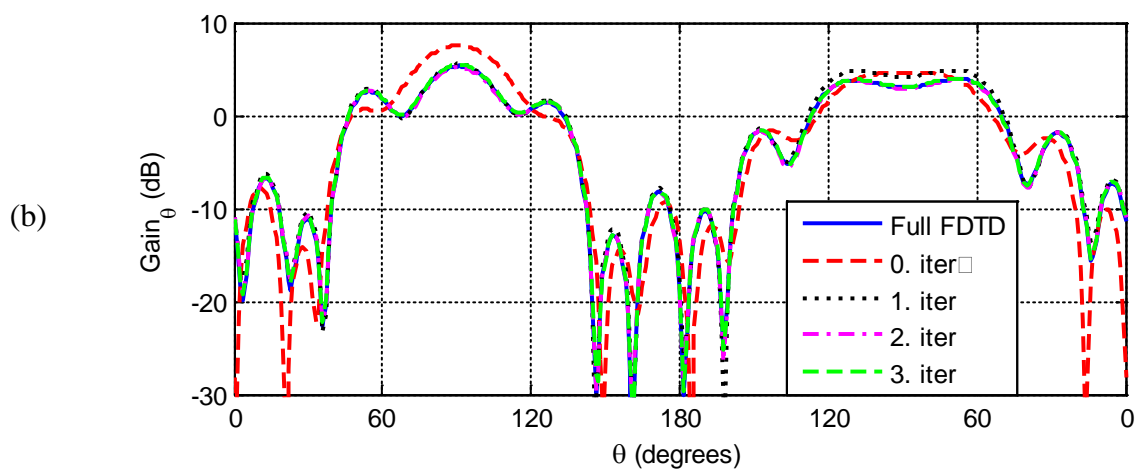


Figure 4.34: Radiation pattern (Gain_θ) for xy -plane cut at frequencies: a) 230 MHz, b) 240 MHz, c) 250 MHz, d) 260 MHz, and e) 270 MHz.





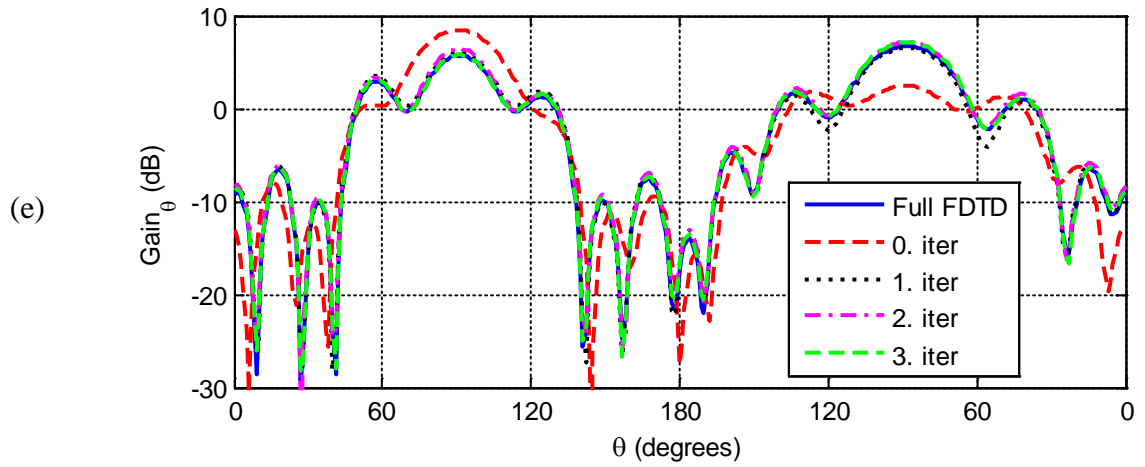
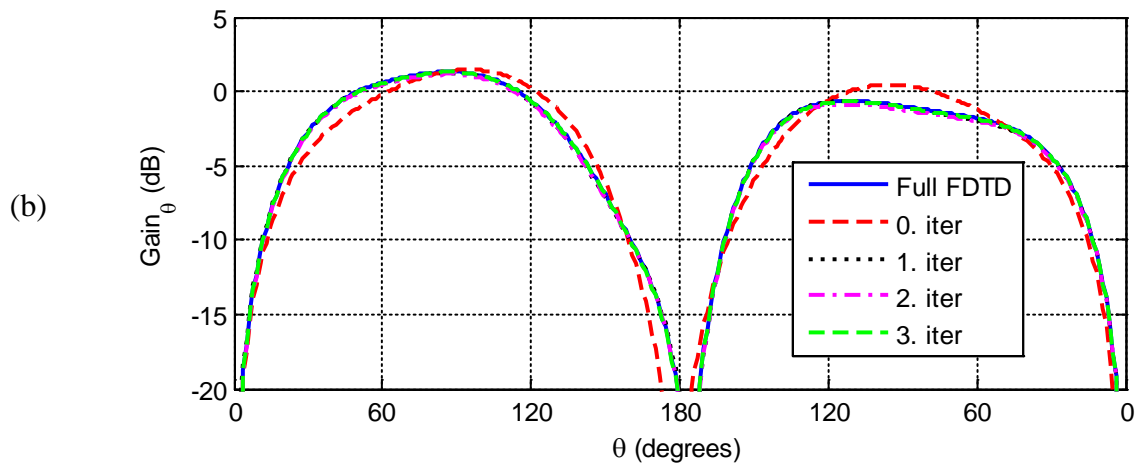
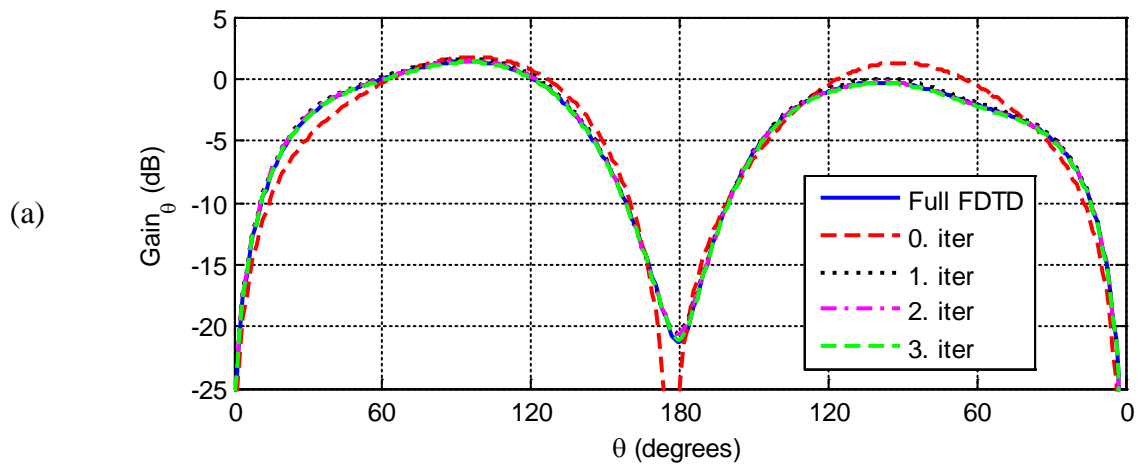


Figure 4.35: Radiation pattern (Gain_θ) for xz -plane cut at frequencies: a) 230 MHz, b) 240 MHz, c) 250 MHz, d) 260 MHz, and e) 270 MHz.



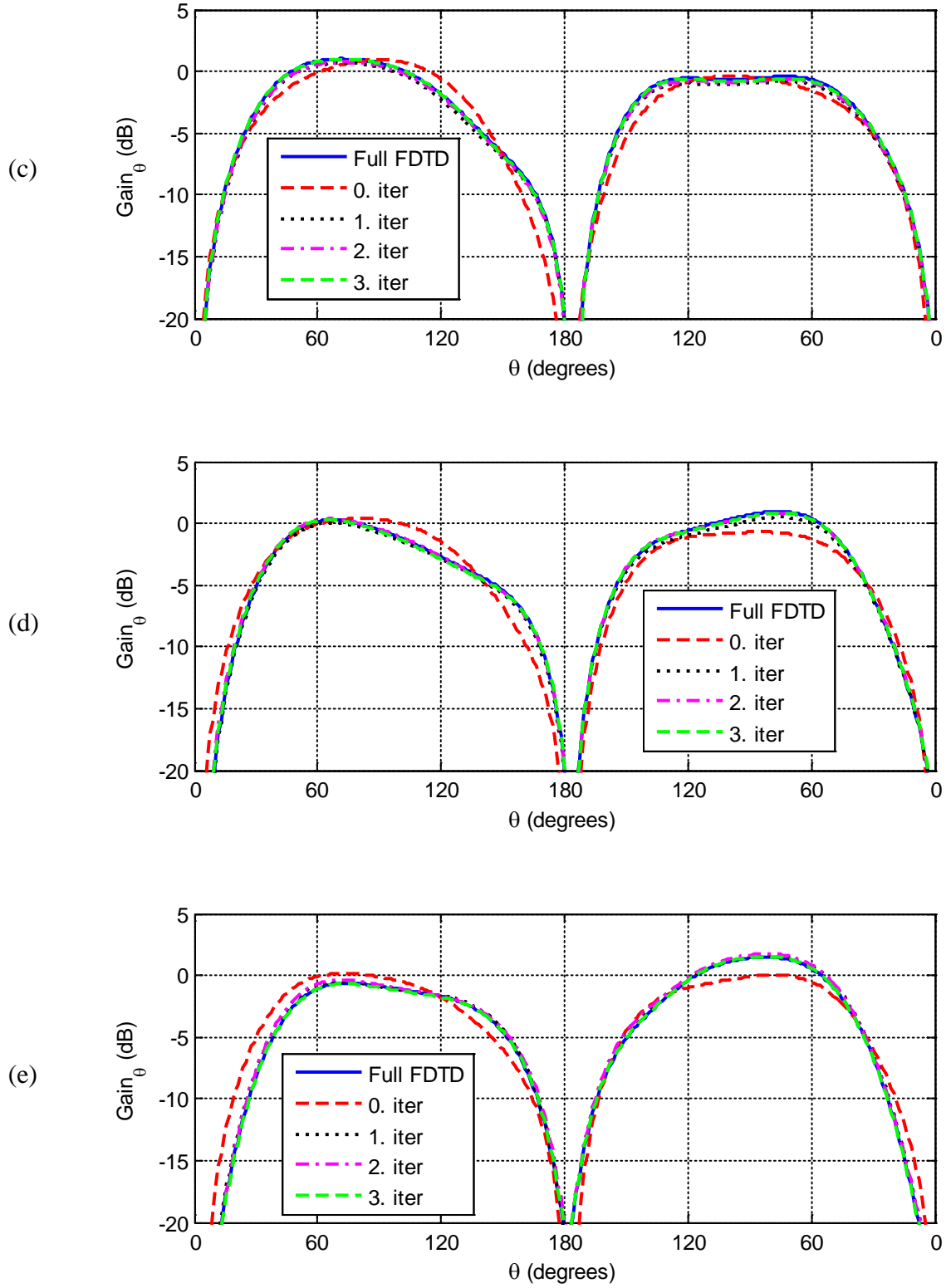
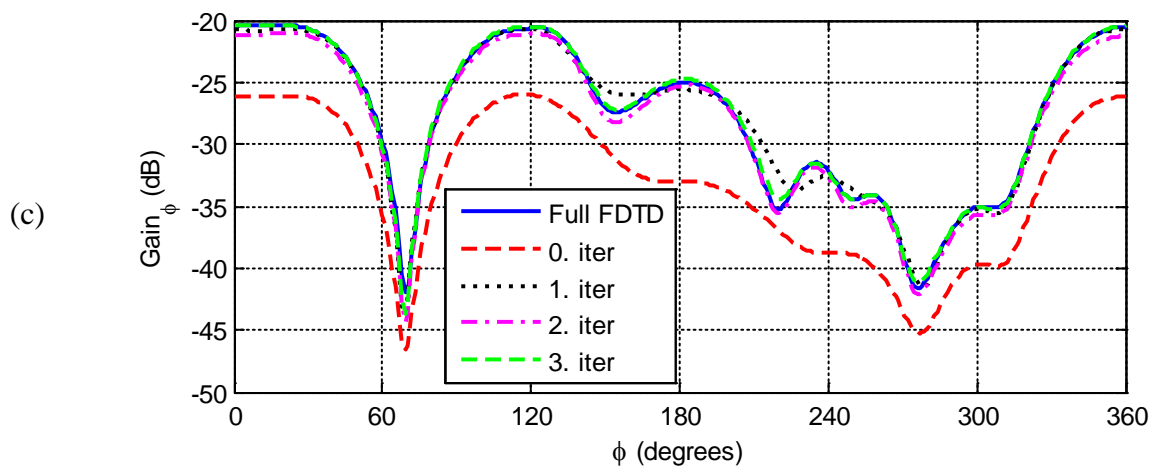
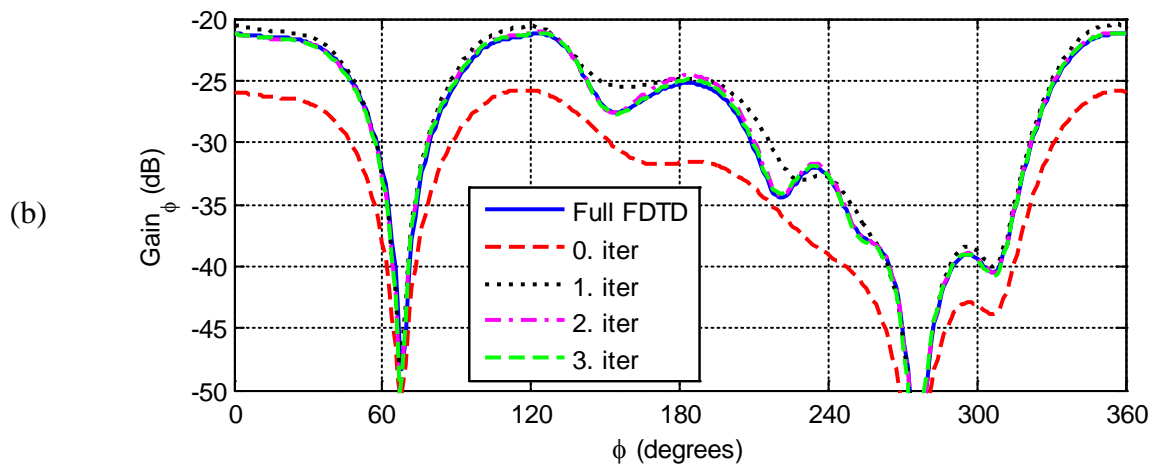
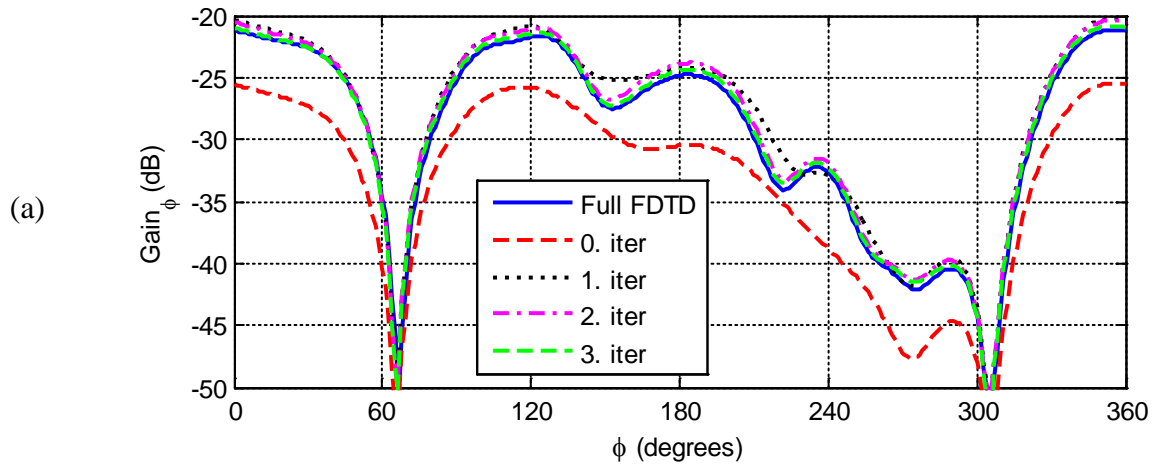


Figure 4.36: Radiation pattern (Gain_θ) for yz-plane cut at frequencies: a) 230 MHz, b) 240 MHz, c) 250 MHz, d) 260 MHz, and e) 270 MHz.



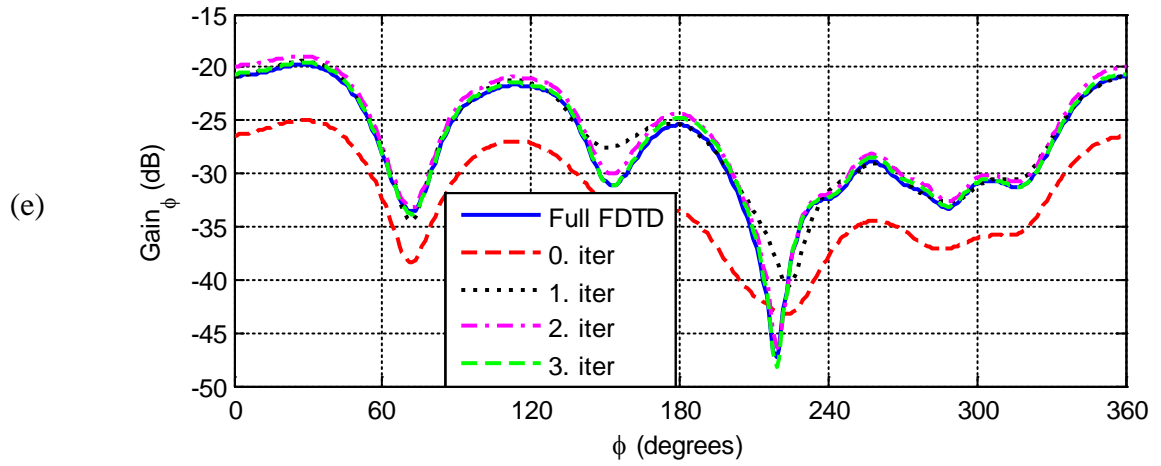
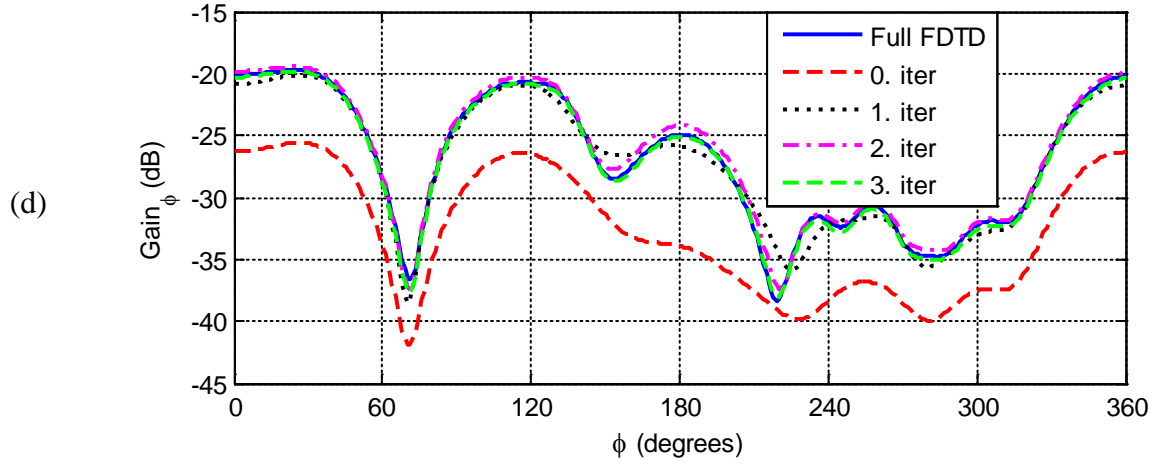
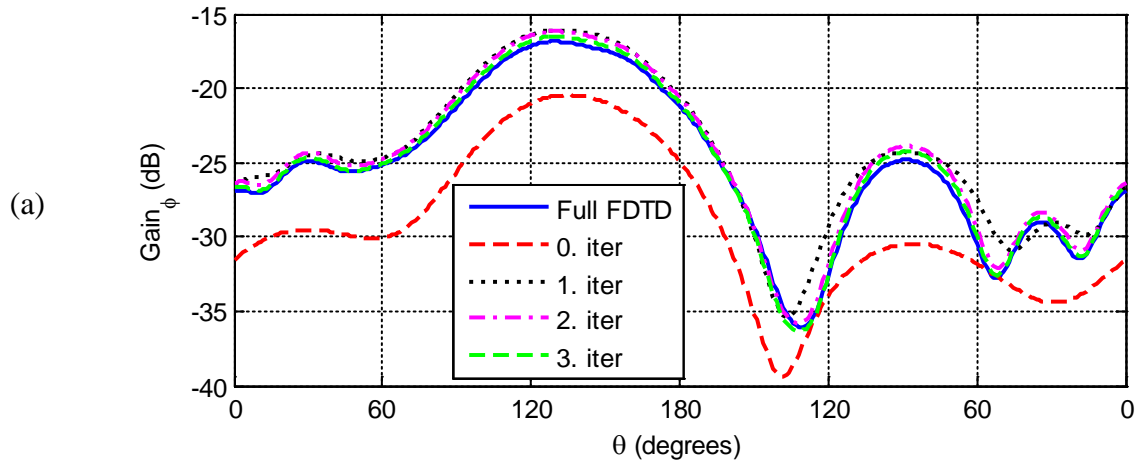
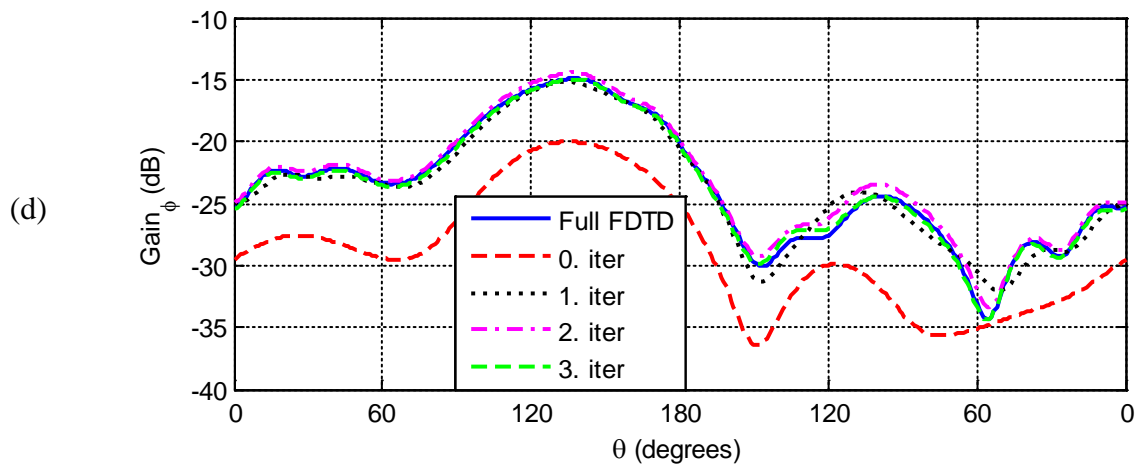
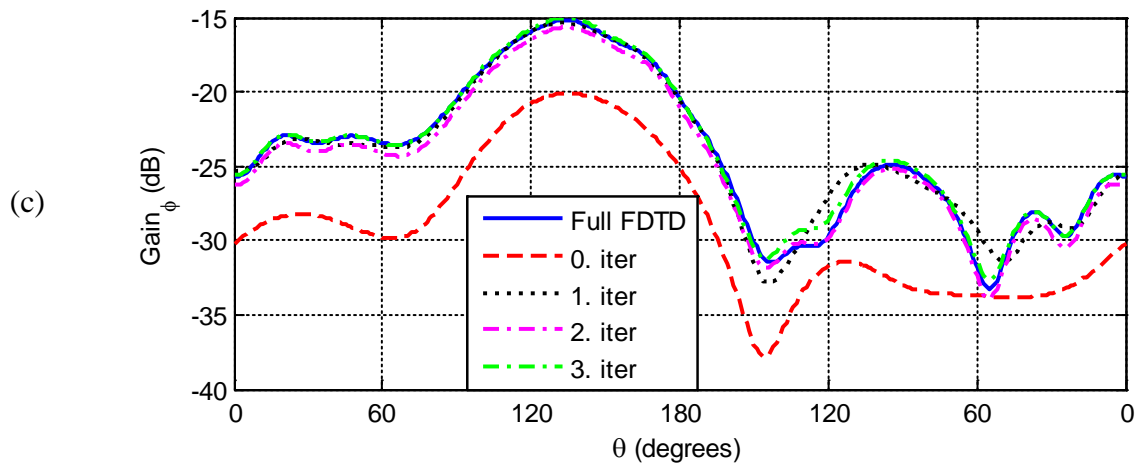
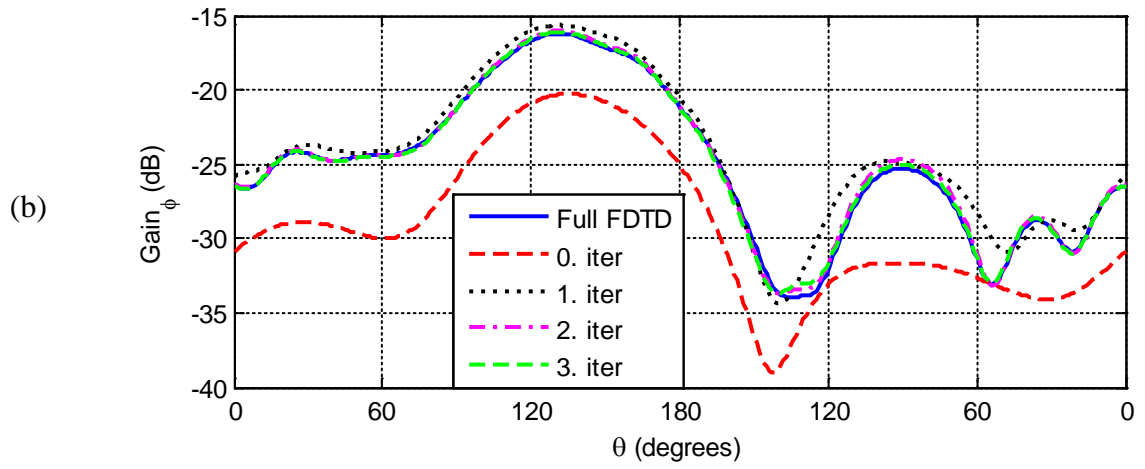


Figure 4.37: Radiation pattern (Gain_ϕ) for xy -plane cut at frequencies: a) 230 MHz, b) 240 MHz, c) 250 MHz, d) 260 MHz, and e) 270 MHz.





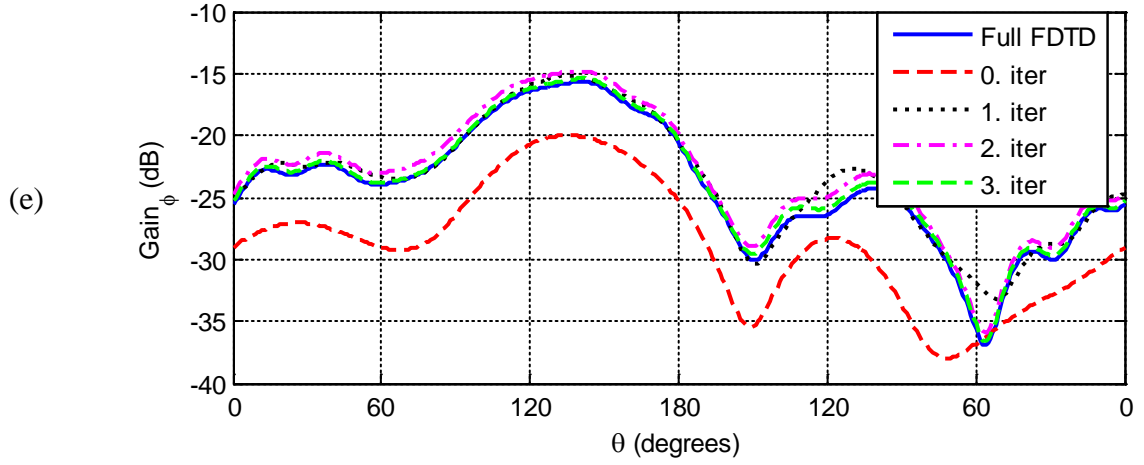
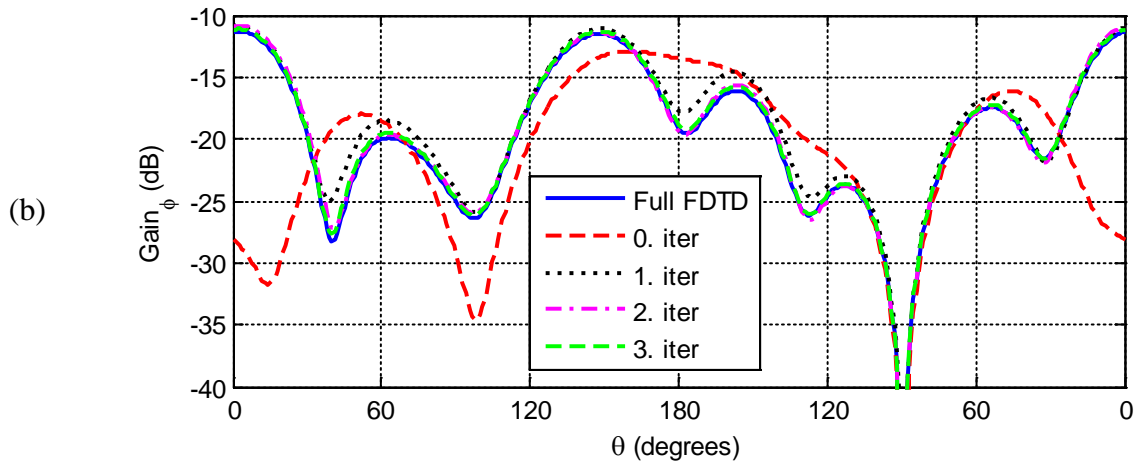
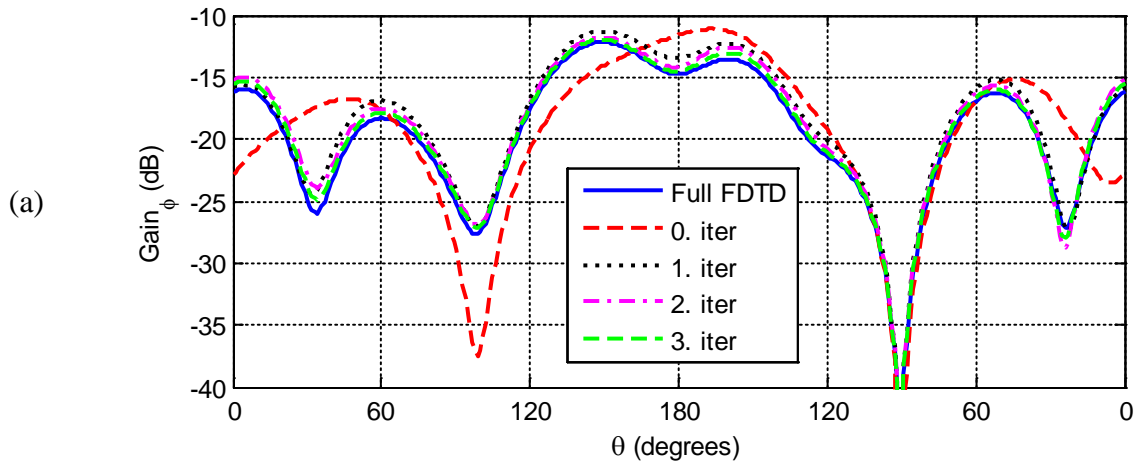


Figure 4.38: Radiation pattern (Gain_φ) for xz -plane cut at frequencies: a) 230 MHz, b) 240 MHz, c) 250 MHz, d) 260 MHz, and e) 270 MHz.



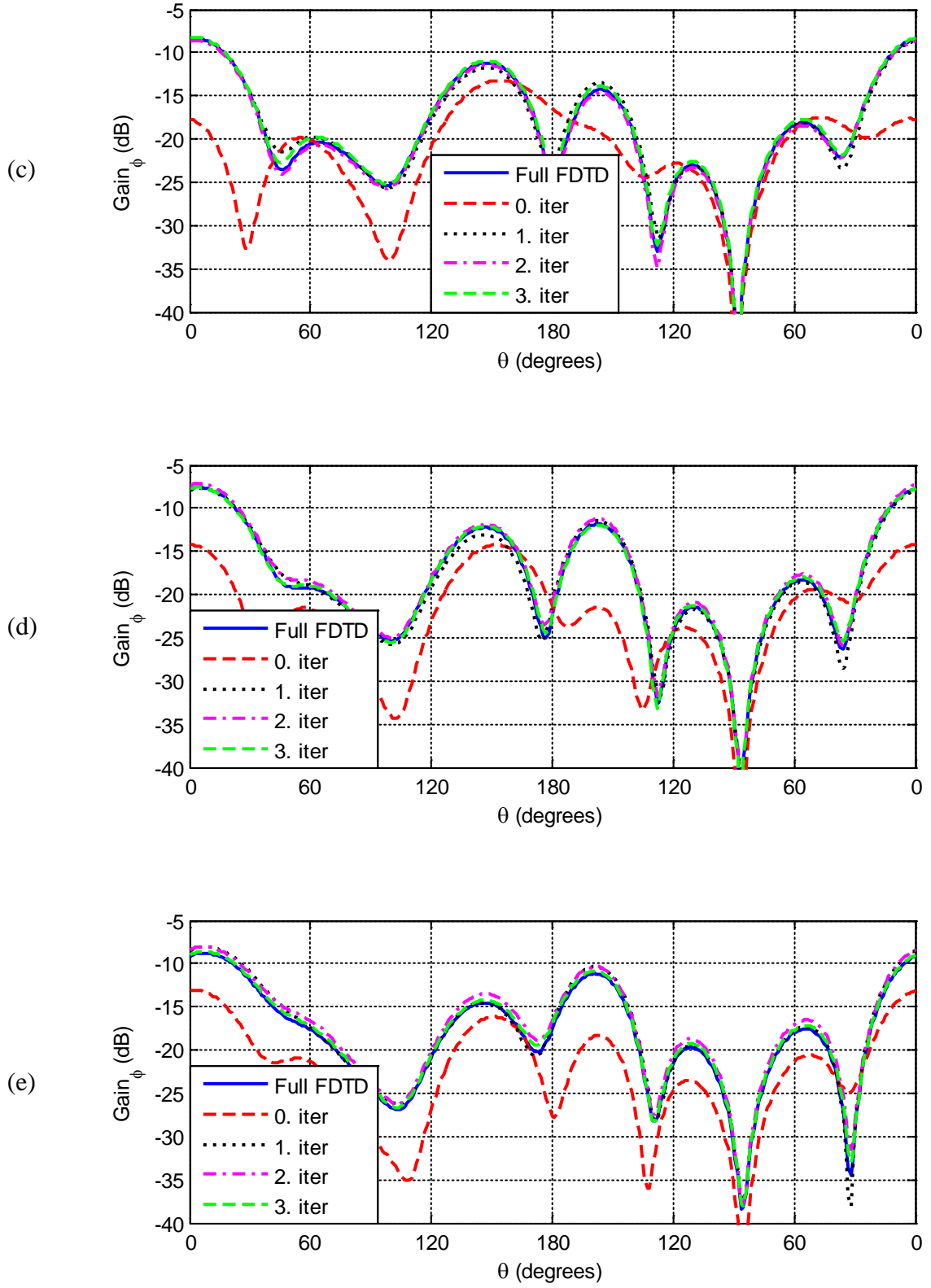


Figure 4.39: Radiation pattern (Gain_ϕ) for yz -plane cut at frequencies: a) 230 MHz, b) 240 MHz, c) 250 MHz, d) 260 MHz, and e) 270 MHz.

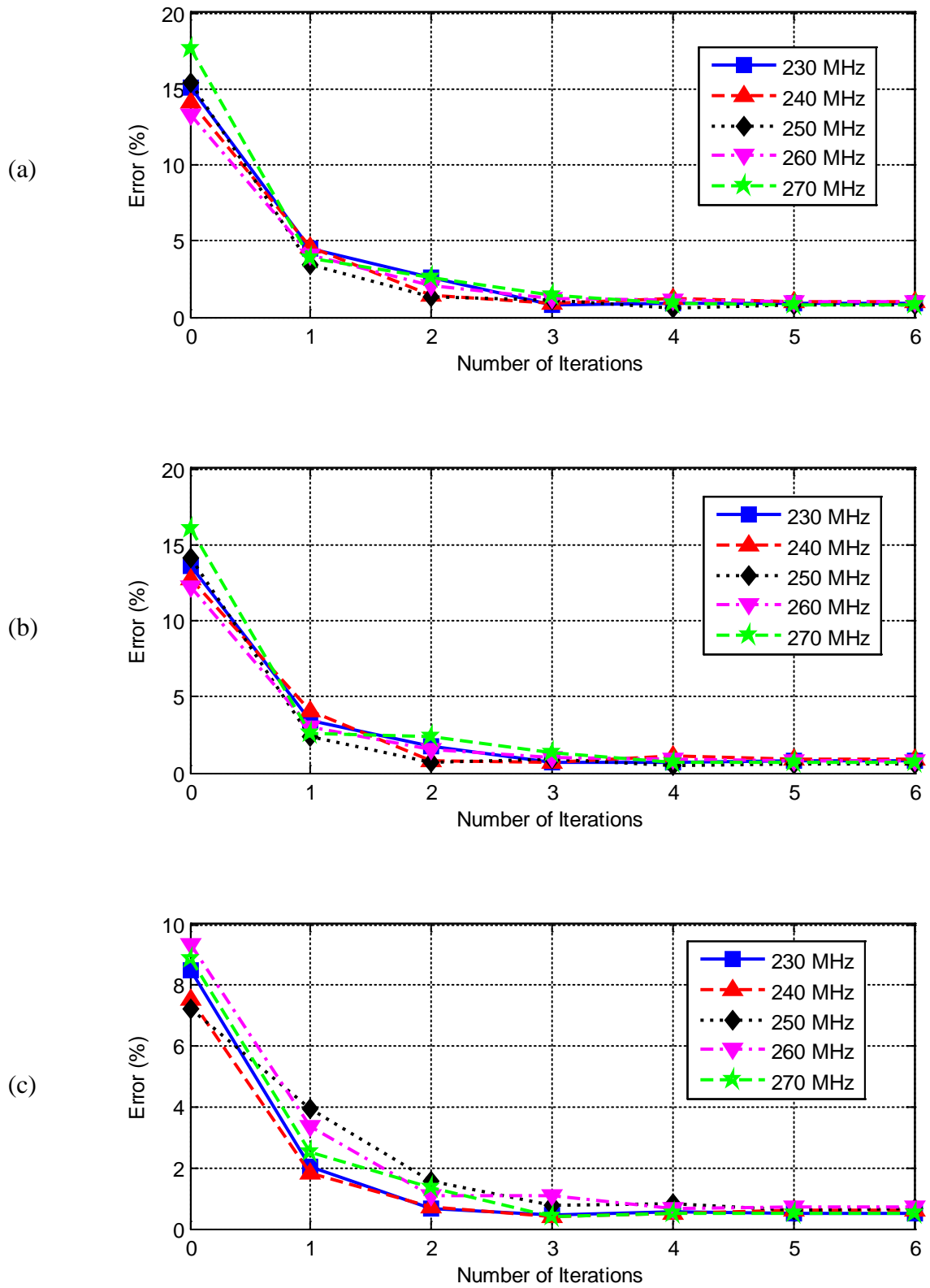


Figure 4.40: Normalized average errors for Gain_0 components in the three plane cuts: a) xy -plane, b) xz -plane, and c) yz -plane.

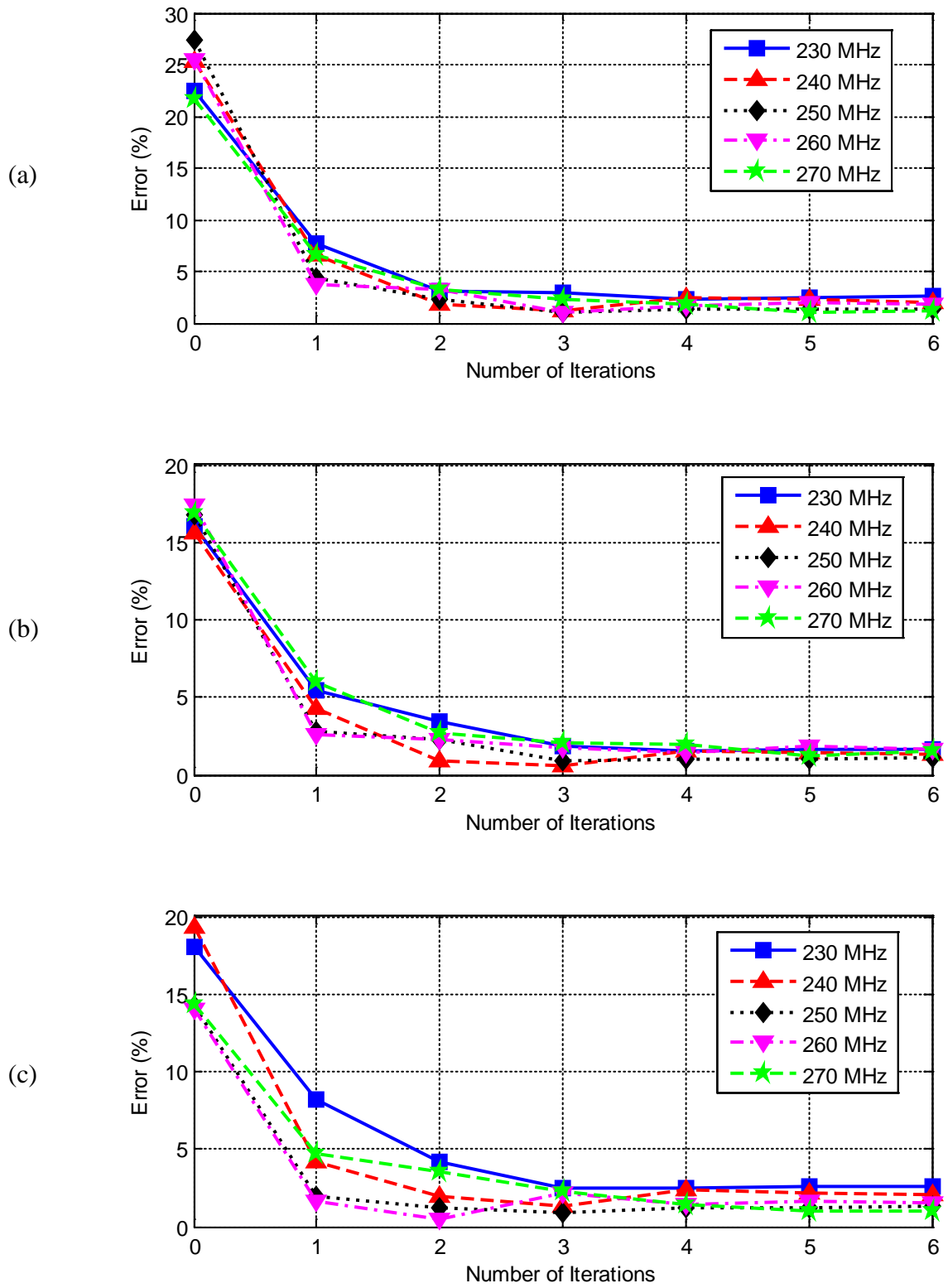


Figure 4.41: Normalized average errors for Gain_ϕ components in the three plane cuts: a) xy -plane, b) xz -plane, and c) yz -plane.

4.5 Radiation from a Dipole Antenna in the Presence of Three Objects

The geometry of a more complex radiation problem is shown as the fifth example in Figure 4.42 to prove the idea of the IMR technique based on the FDTD method for three scatterer subregions, where more coupling is involved between subregions. The problem includes a 0.5 m dipole antenna and three scatterer objects which are a dielectric ellipsoid with relative permittivity of 2.2, a conducting ellipsoid, and a conducting L-shaped box. The semi-axes of the dielectric ellipsoid are 0.25 m, 0.5 m, and 0.25 m along the x , y , and z directions, respectively. The dielectric ellipsoid is placed 0.5 m away from the antenna on the x -axis and 0.5 m away from the antenna on the y -axis. The semi-axes of the conducting ellipsoid are 0.25 m, 0.25 m, and 1 m along the x , y , and z directions, respectively. The conducting ellipsoid is placed 0.5 m away from the antenna on the x -axis and 0.5 m away from the antenna on the negative y -axis. The conducting L-shaped box is placed 0.5 m away from the antenna on the negative x -axis and its dimensions are given in Figure 4.42. It can be seen from Figure 4.43 that the IMR algorithm reaches the convergence criterion after iteration # 3. Figures 4.44-4.49 show the radiation patterns (Gain_θ and Gain_ϕ) of the configuration for the three plane cuts. Good agreement with the full domain results is achieved after iteration # 3. The normalized average errors for Gain_θ and Gain_ϕ in the three plane cuts at each frequency of interest are shown in Figures 4.50-4.51, respectively. Simulation parameters and computer resources are summarized in Table 4-5. Results in the table show a considerable reduction in the memory storage requirements and computation time.

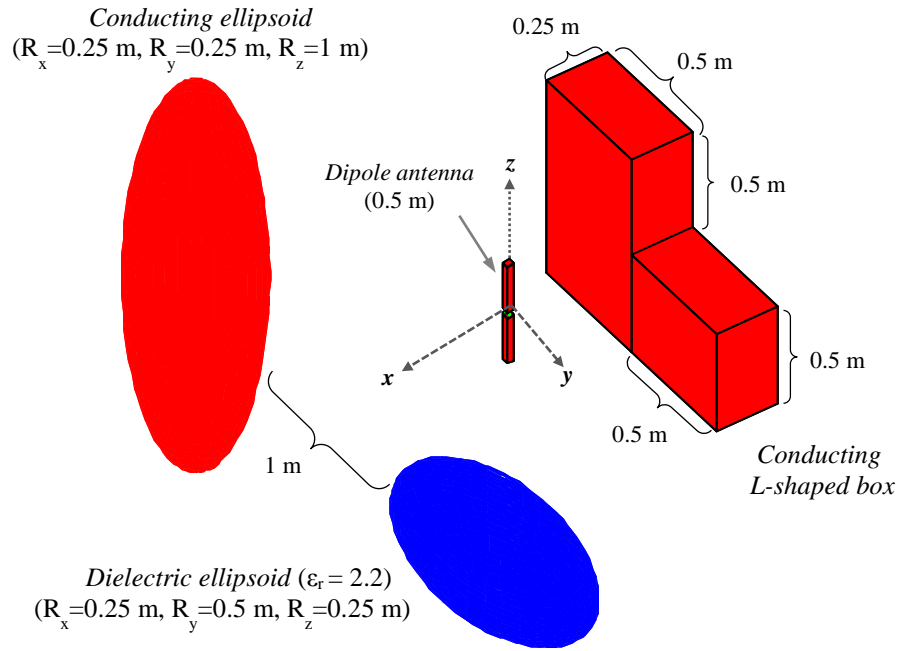


Figure 4.42: Geometry of the fifth problem.

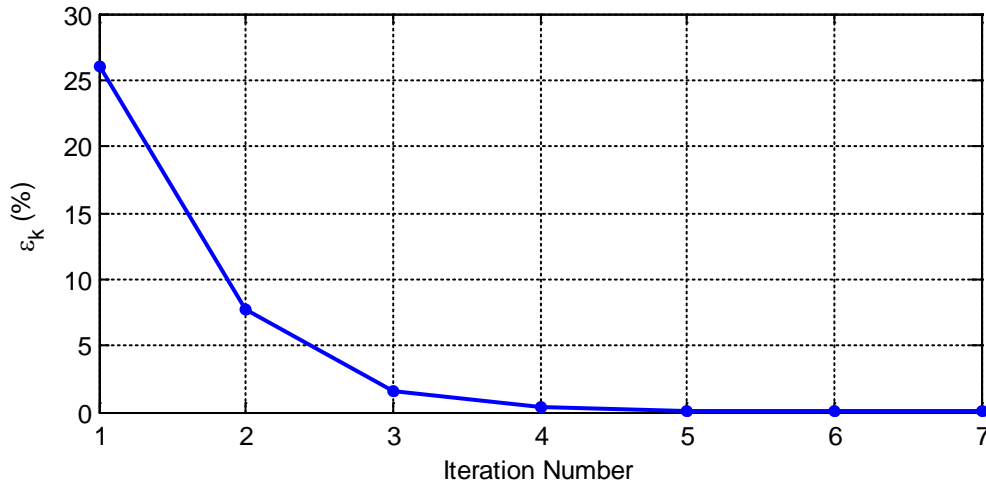
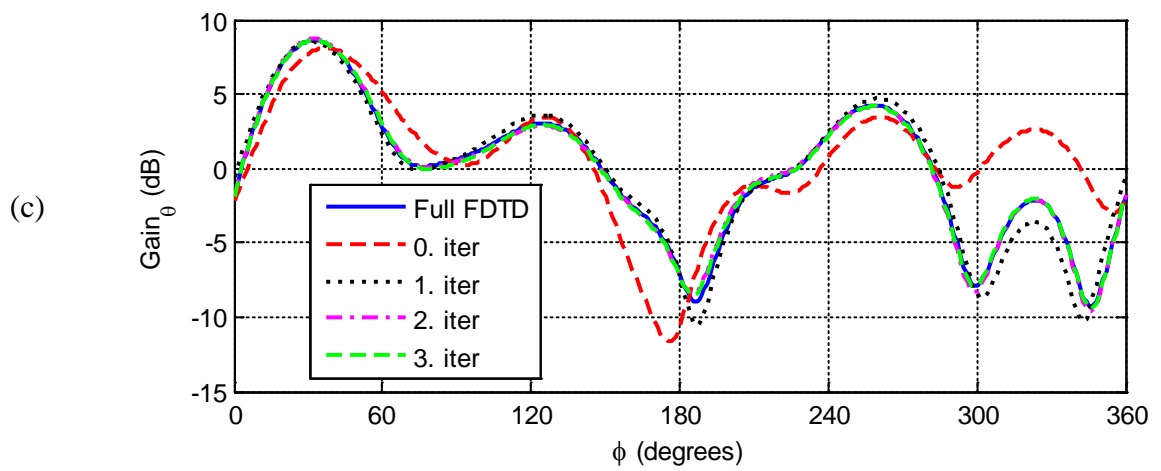
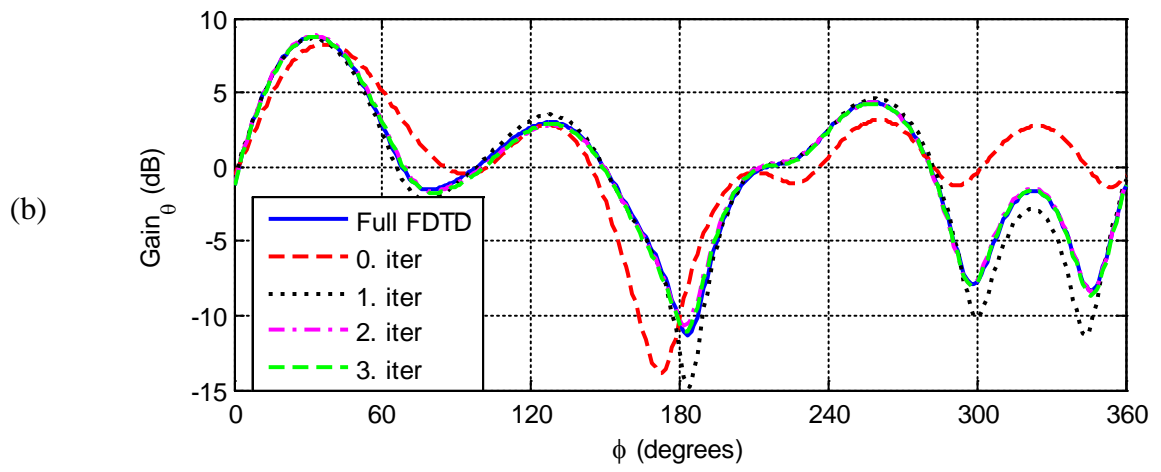
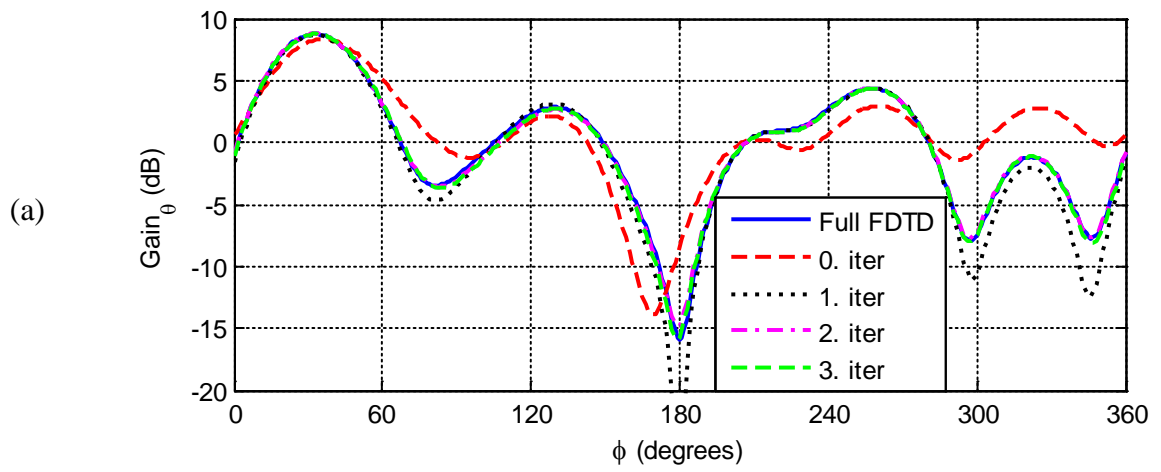


Figure 4.43: Convergence (ϵ_k) between iteration steps for the fifth problem.

Table 4-5: Simulation parameters and computer resources used by the IMR and full domain simulations.

| | Number of Domains | Total Number of Cells | Computation Time (min.) | Iteration Number | Memory (MB) |
|------------------|-------------------|-----------------------|-------------------------|------------------|-------------|
| Full FDTD | — | 27,027,520 | 437 | — | 9,390 |
| IMR-FDTD | 4 | 1,900,736 | 357 | 3 | 800 |



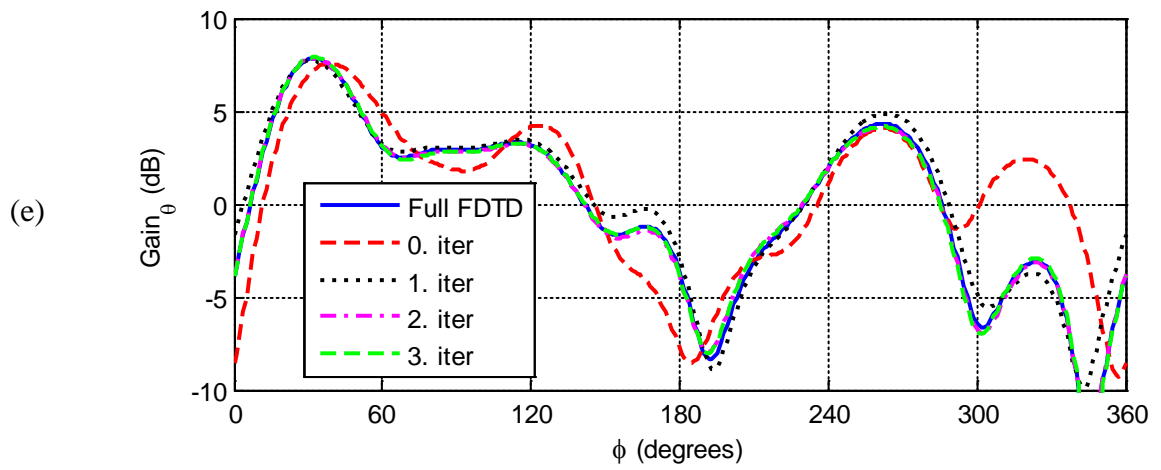
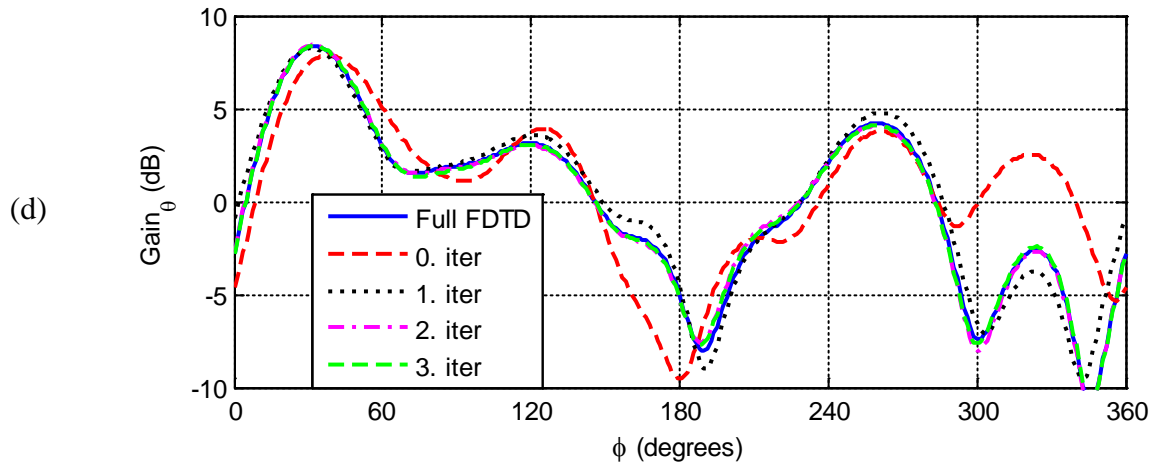
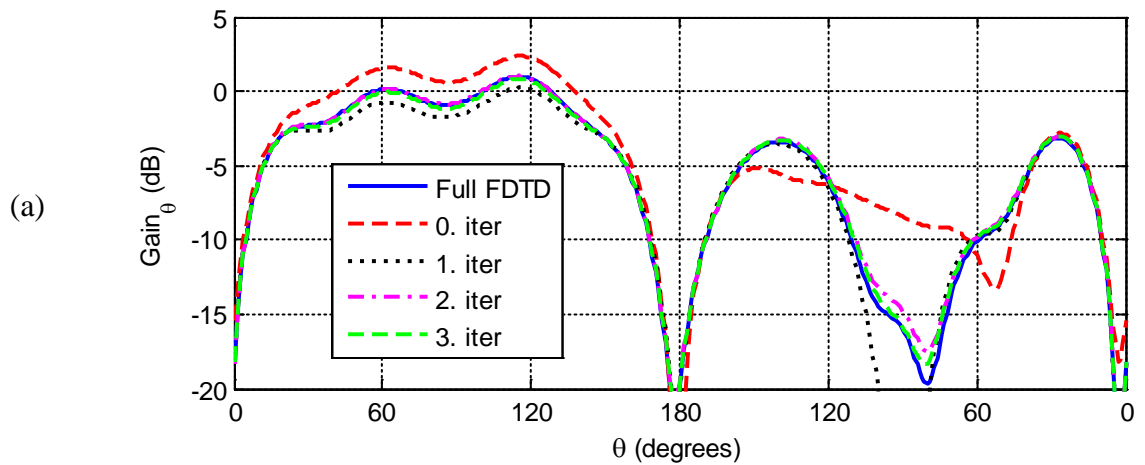
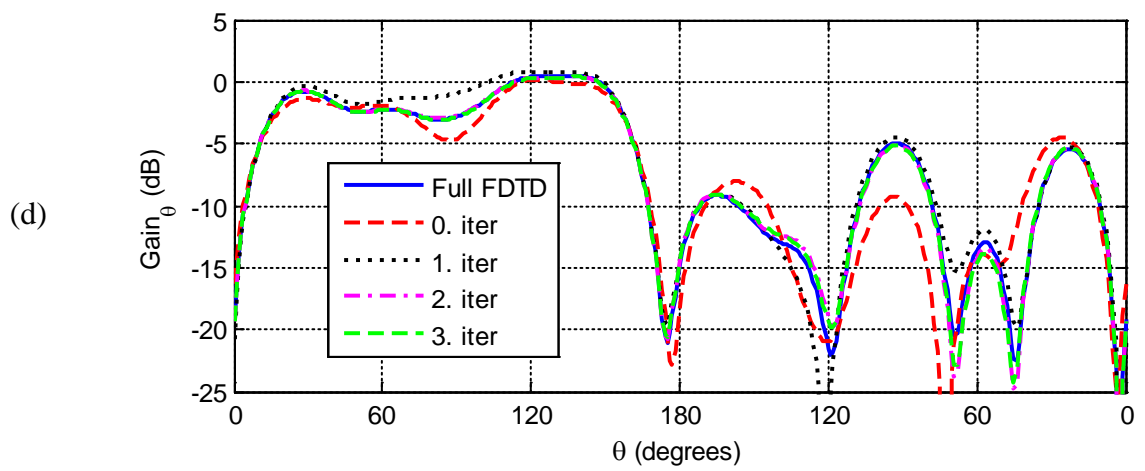
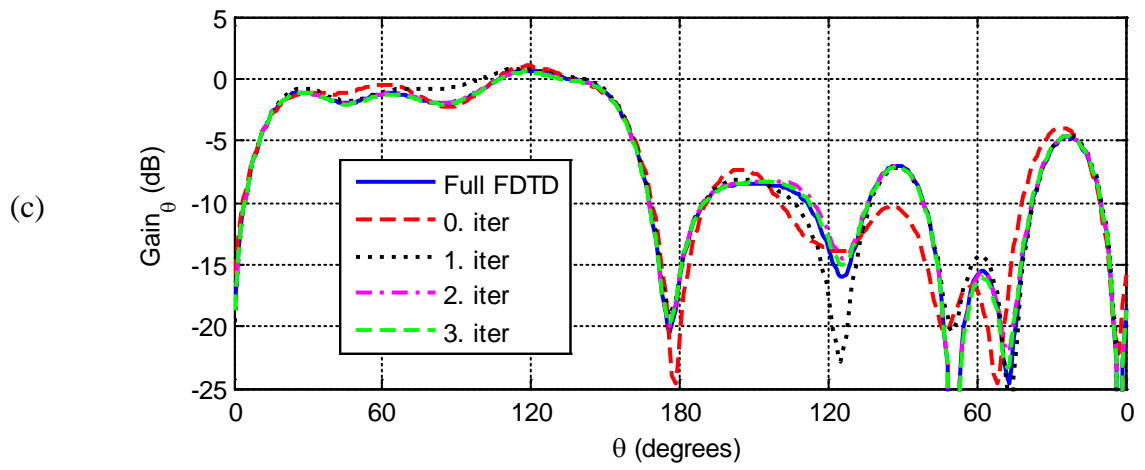
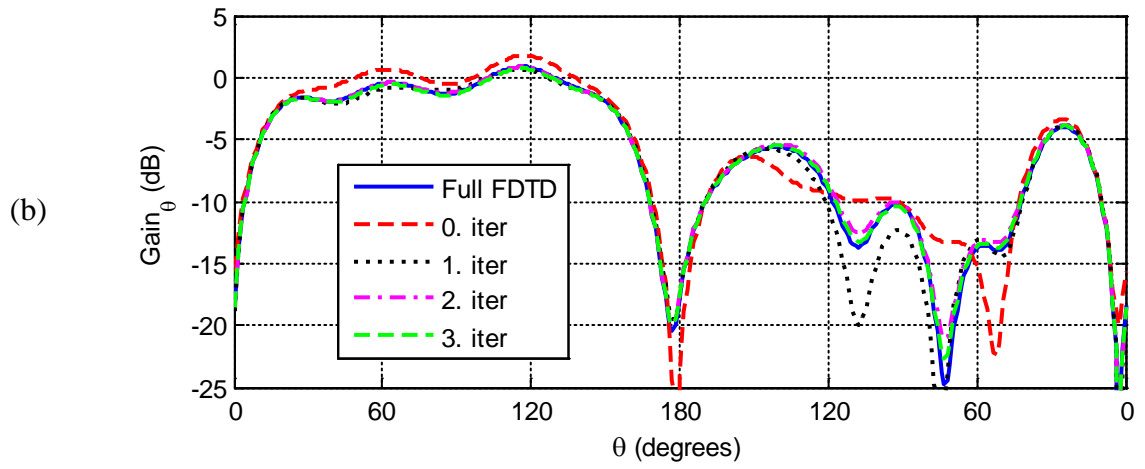


Figure 4.44: Radiation pattern (Gain_θ) for *xy*-plane cut at frequencies: a) 230 MHz, b) 240 MHz, c) 250 MHz, d) 260 MHz, and e) 270 MHz.





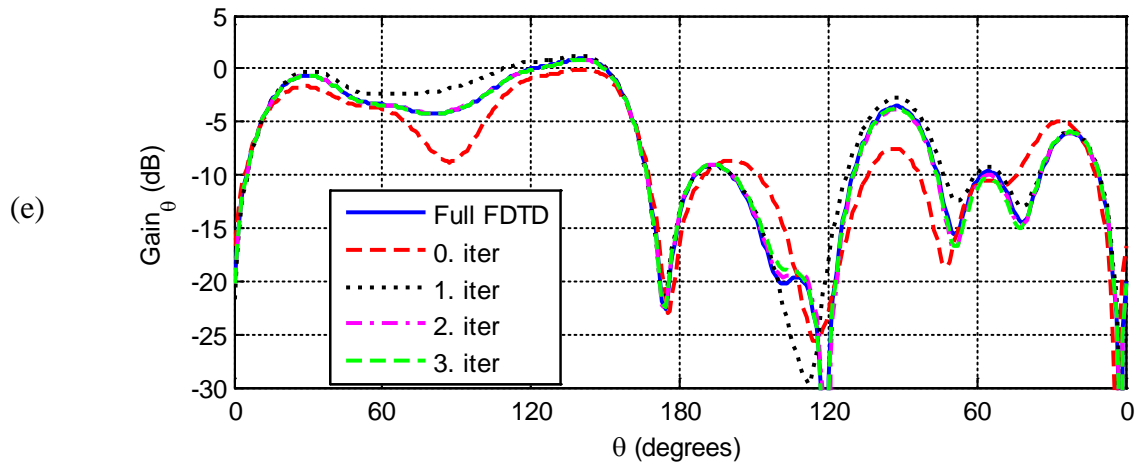
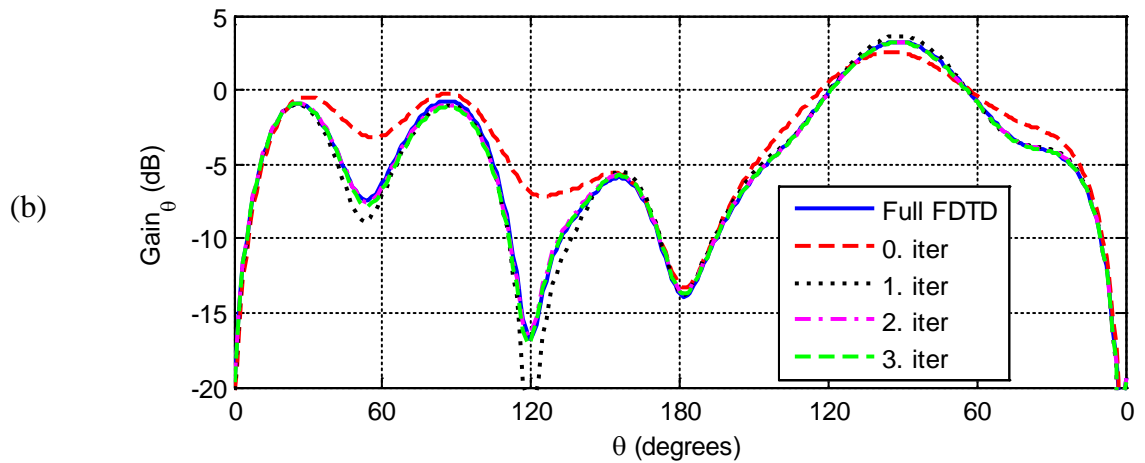
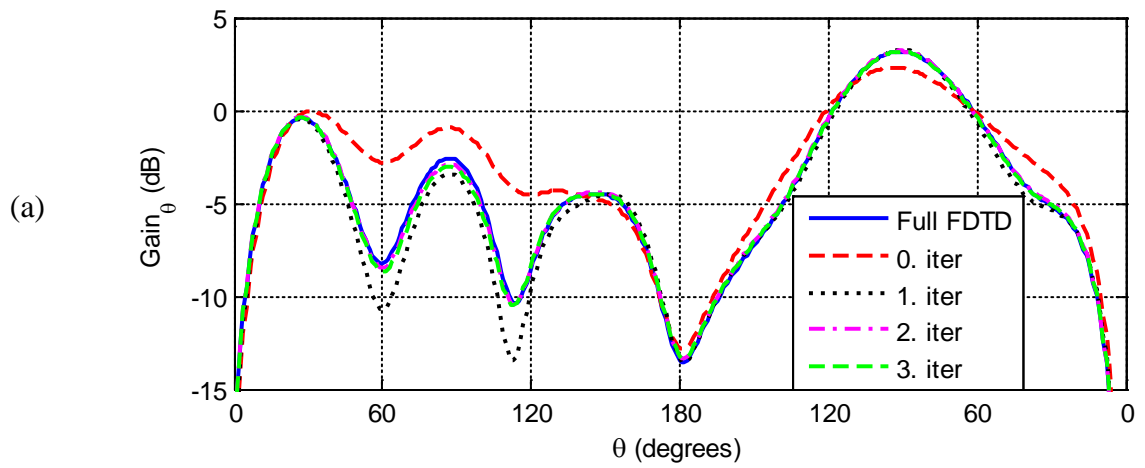


Figure 4.45: Radiation pattern (Gain_θ) for xz -plane cut at frequencies: a) 230 MHz, b) 240 MHz, c) 250 MHz, d) 260 MHz, and e) 270 MHz.



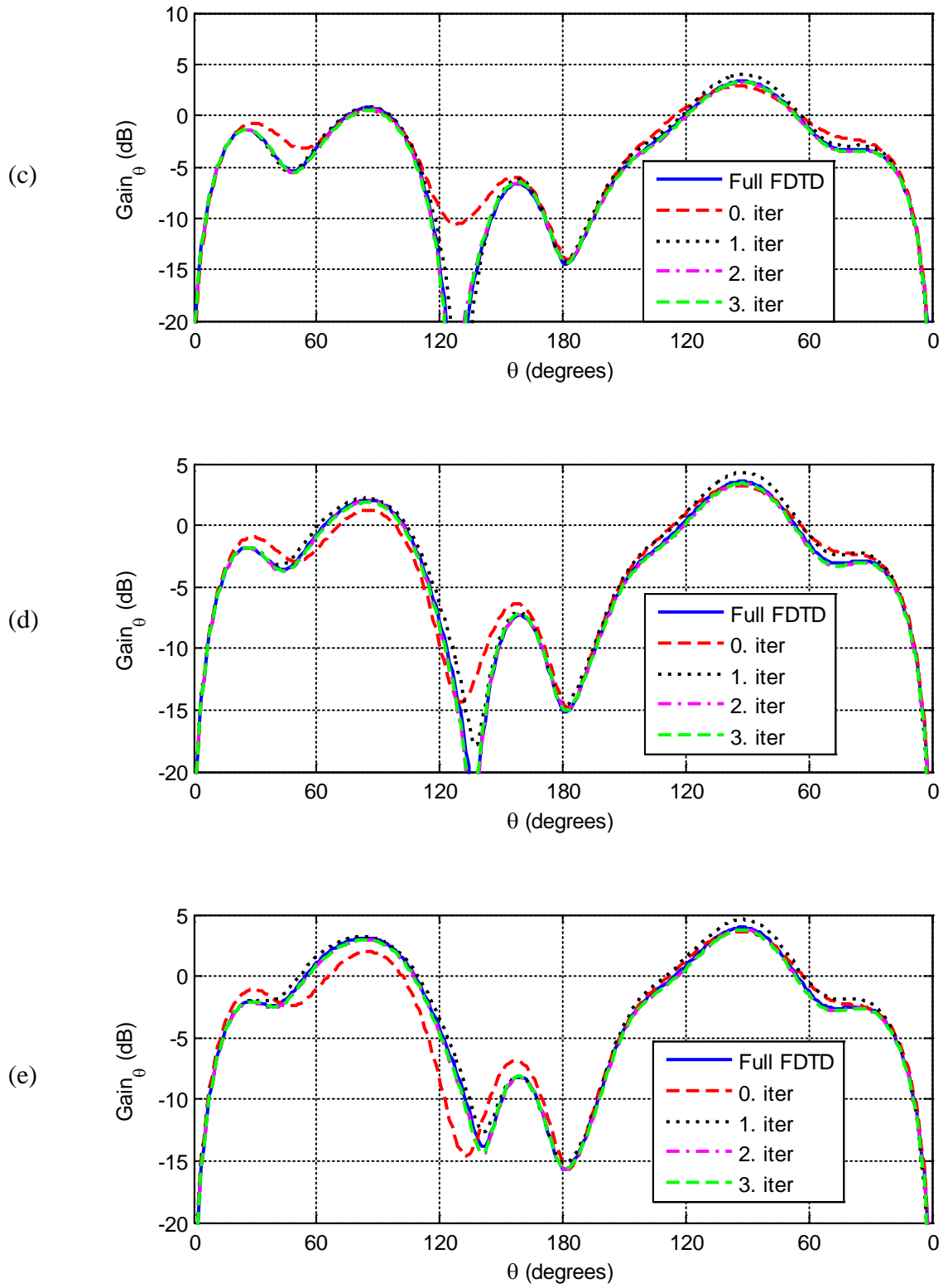
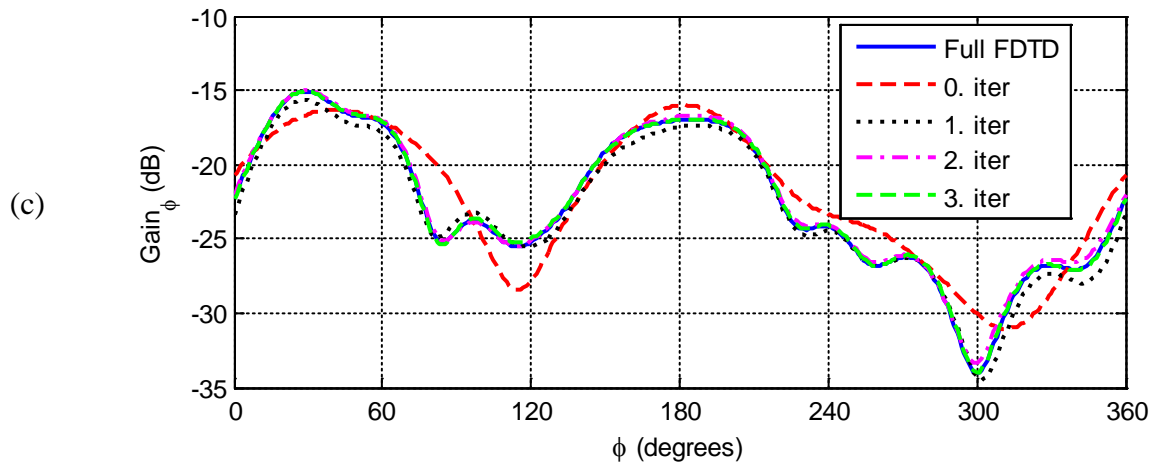
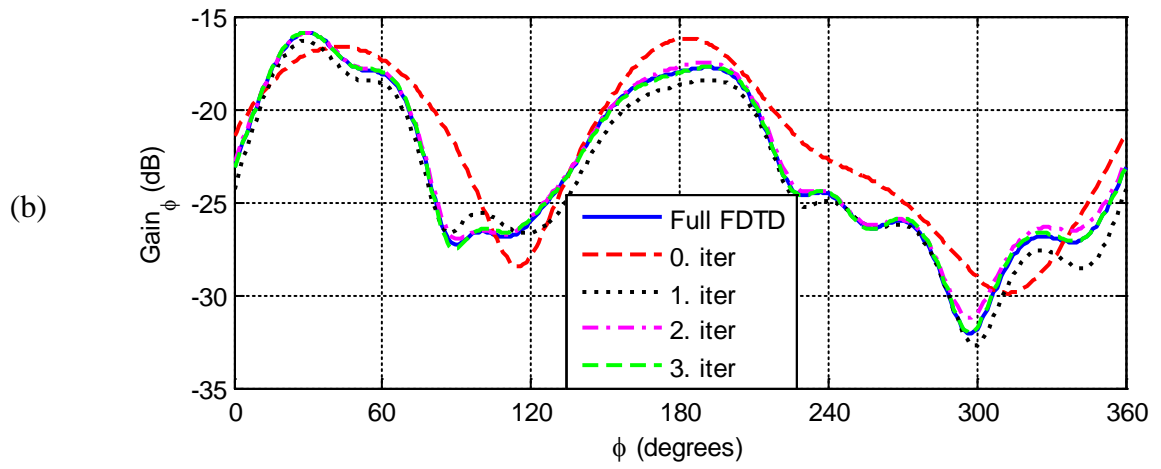
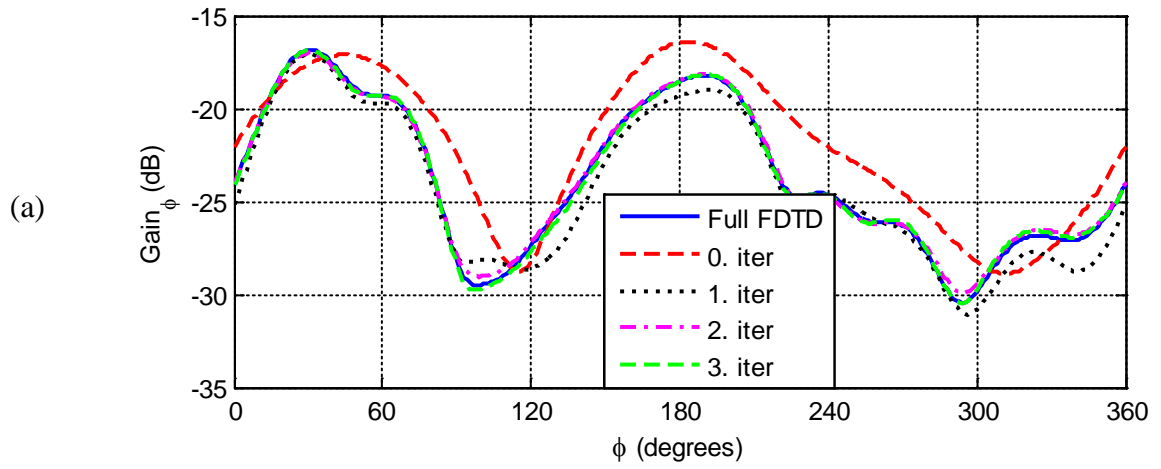


Figure 4.46: Radiation pattern (Gain_θ) for yz -plane cut at frequencies: a) 230 MHz, b) 240 MHz, c) 250 MHz, d) 260 MHz, and e) 270 MHz.



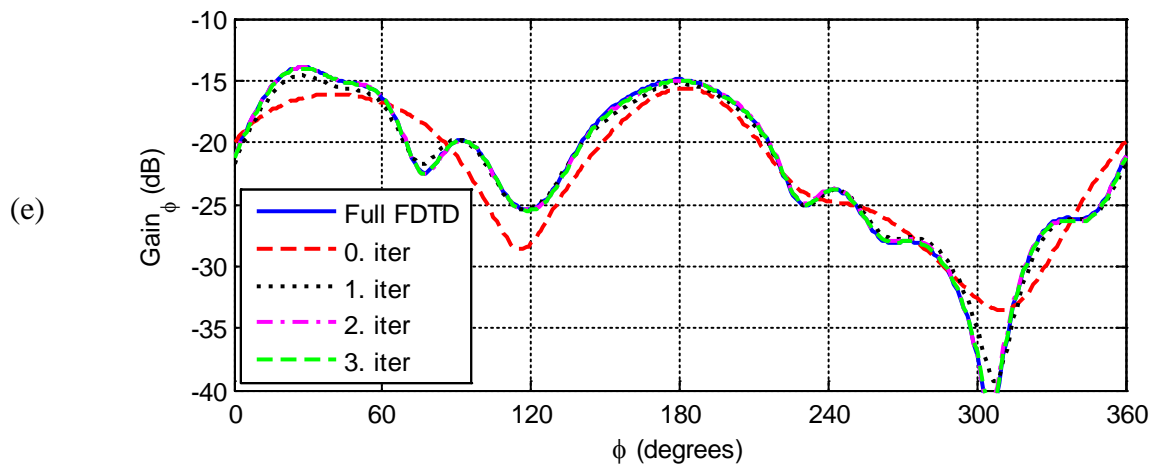
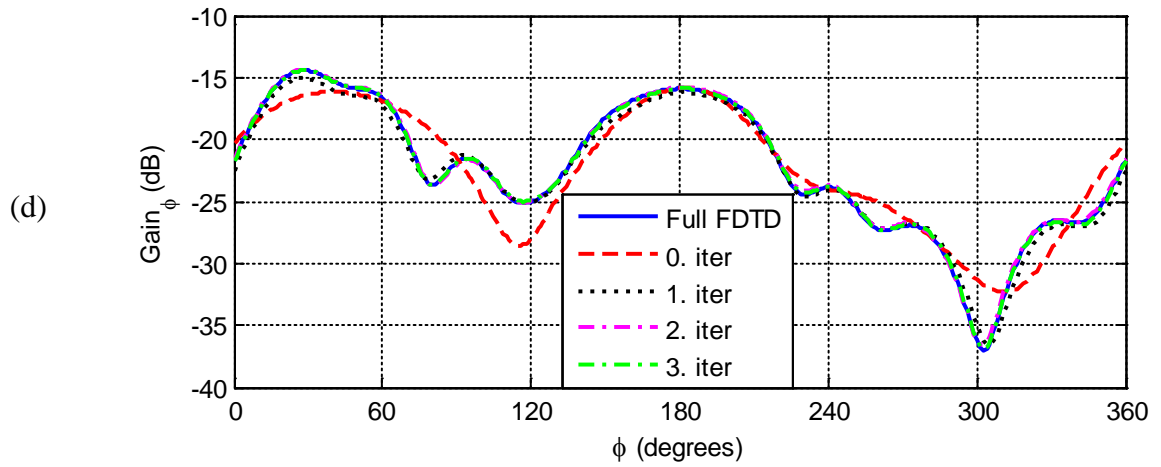
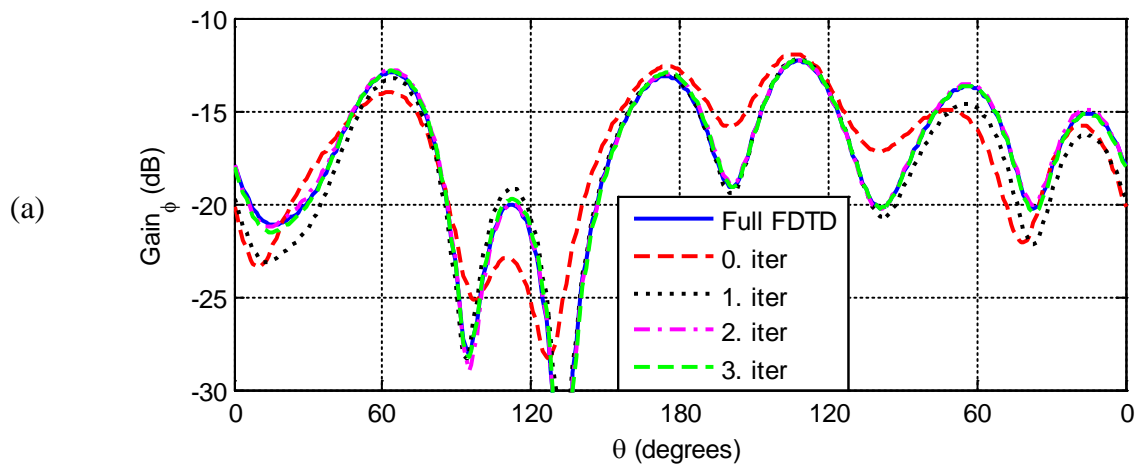
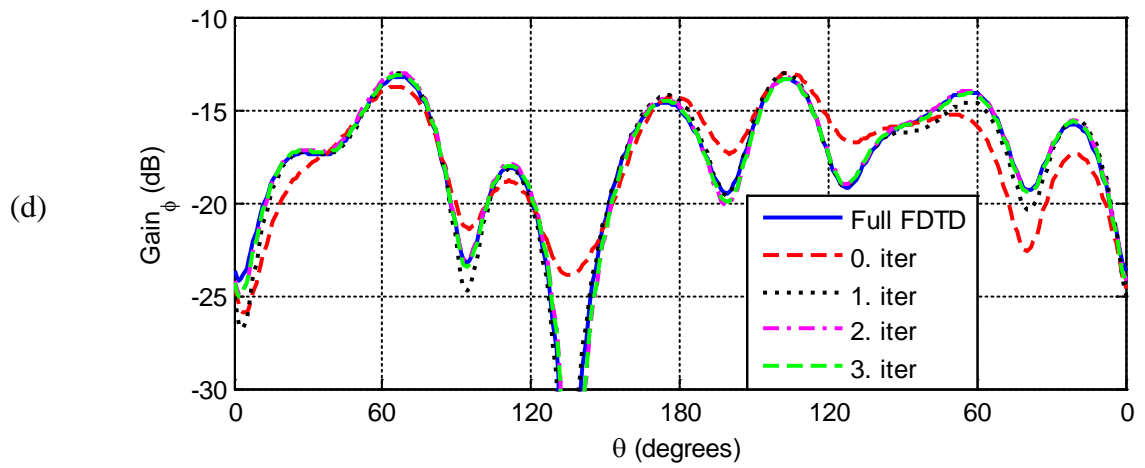
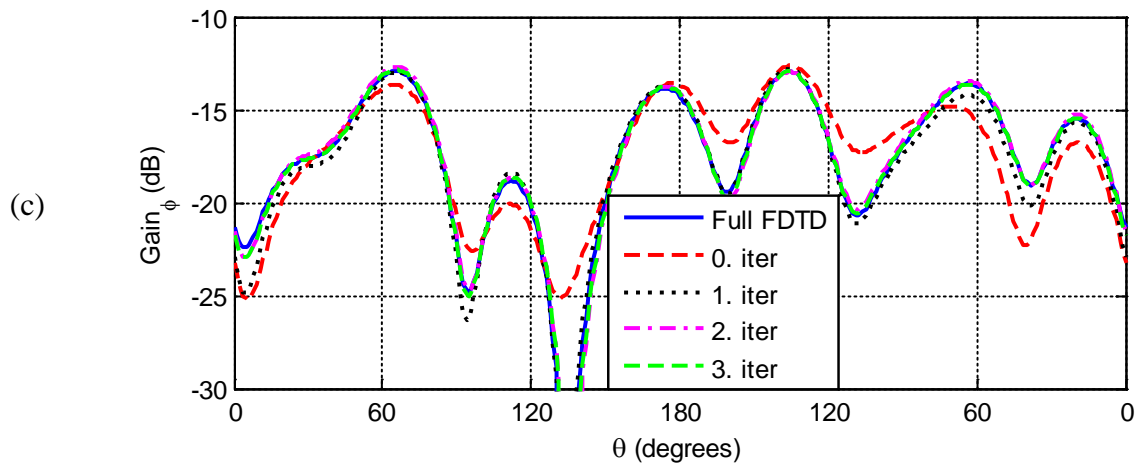
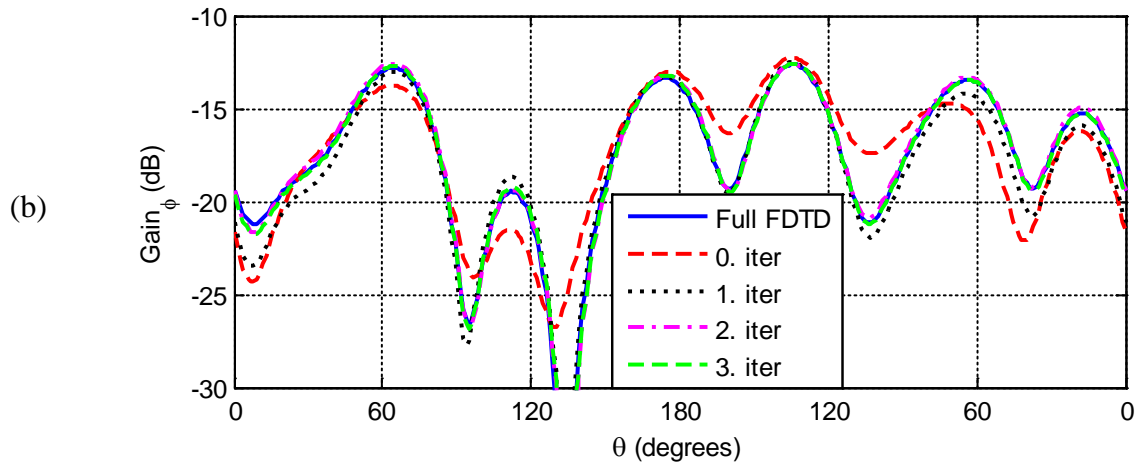


Figure 4.47: Radiation pattern (Gain _{ϕ}) for xy -plane cut at frequencies: a) 230 MHz, b) 240 MHz, c) 250 MHz, d) 260 MHz, and e) 270 MHz.





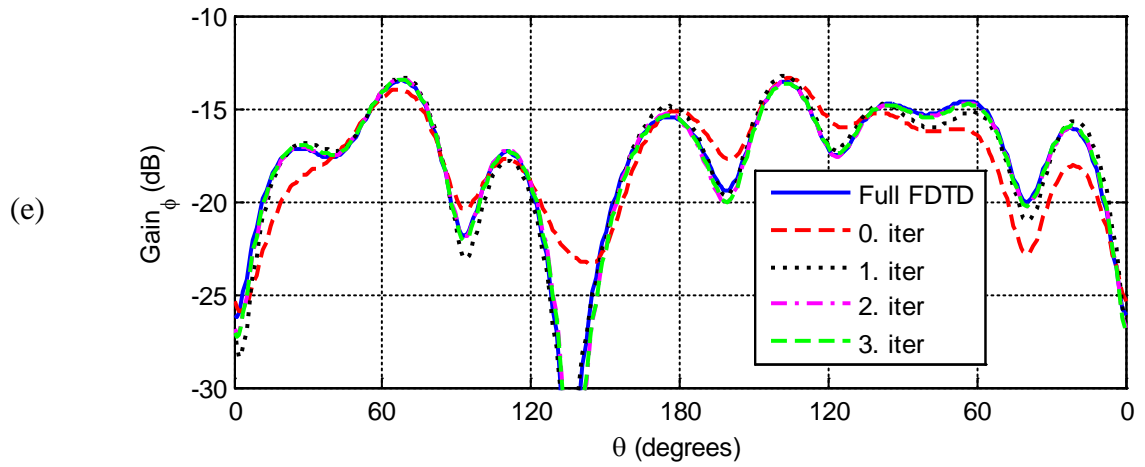
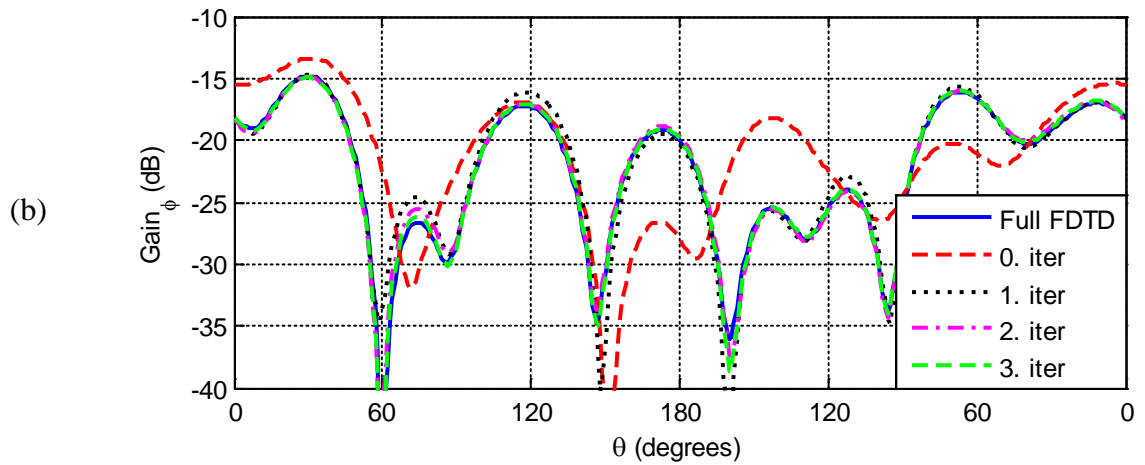
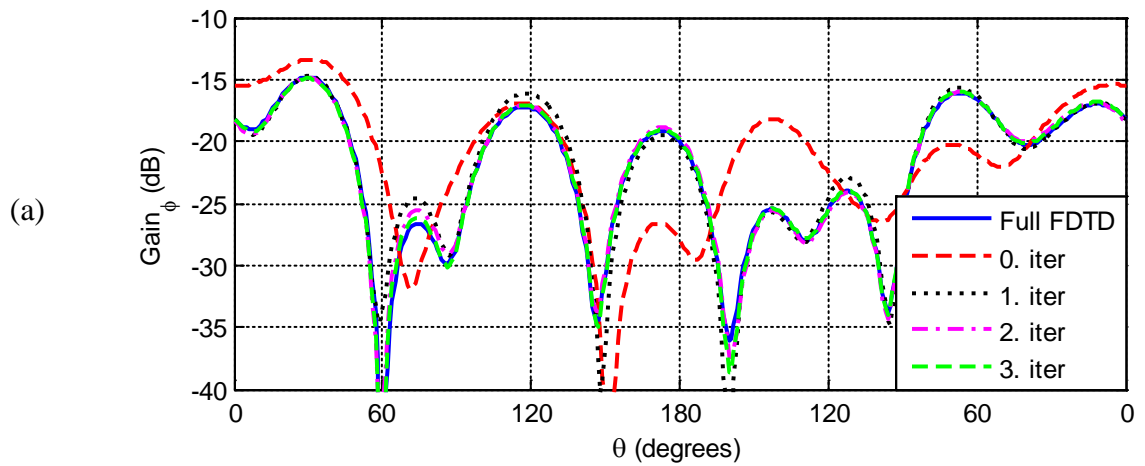


Figure 4.48: Radiation pattern (Gain_φ) for xz -plane cut at frequencies: a) 230 MHz, b) 240 MHz, c) 250 MHz, d) 260 MHz, and e) 270 MHz.



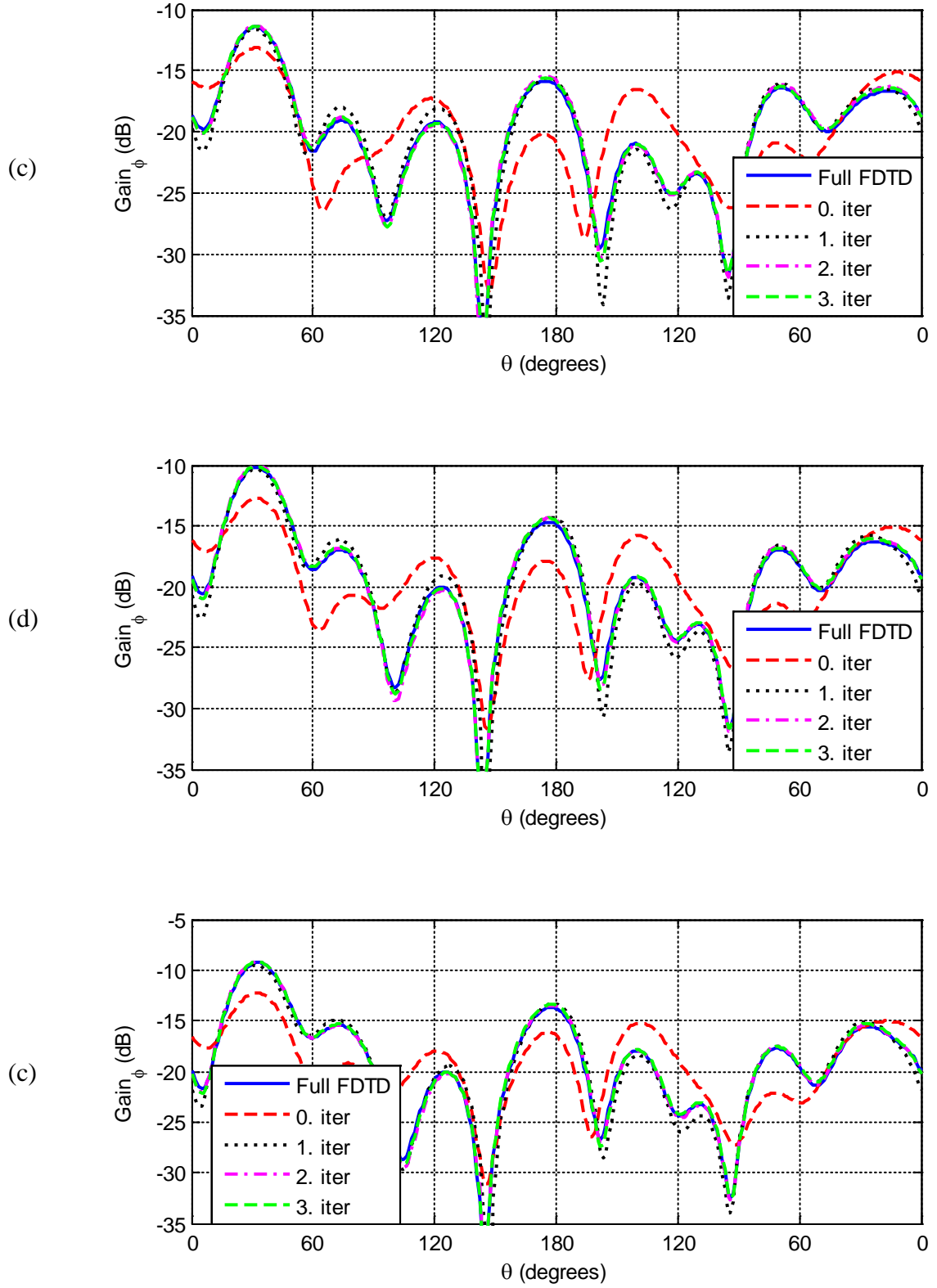


Figure 4.49: Radiation pattern (Gain_φ) for yz-plane cut at frequencies: a) 230 MHz, b) 240 MHz, c) 250 MHz, d) 260 MHz, and e) 270 MHz.

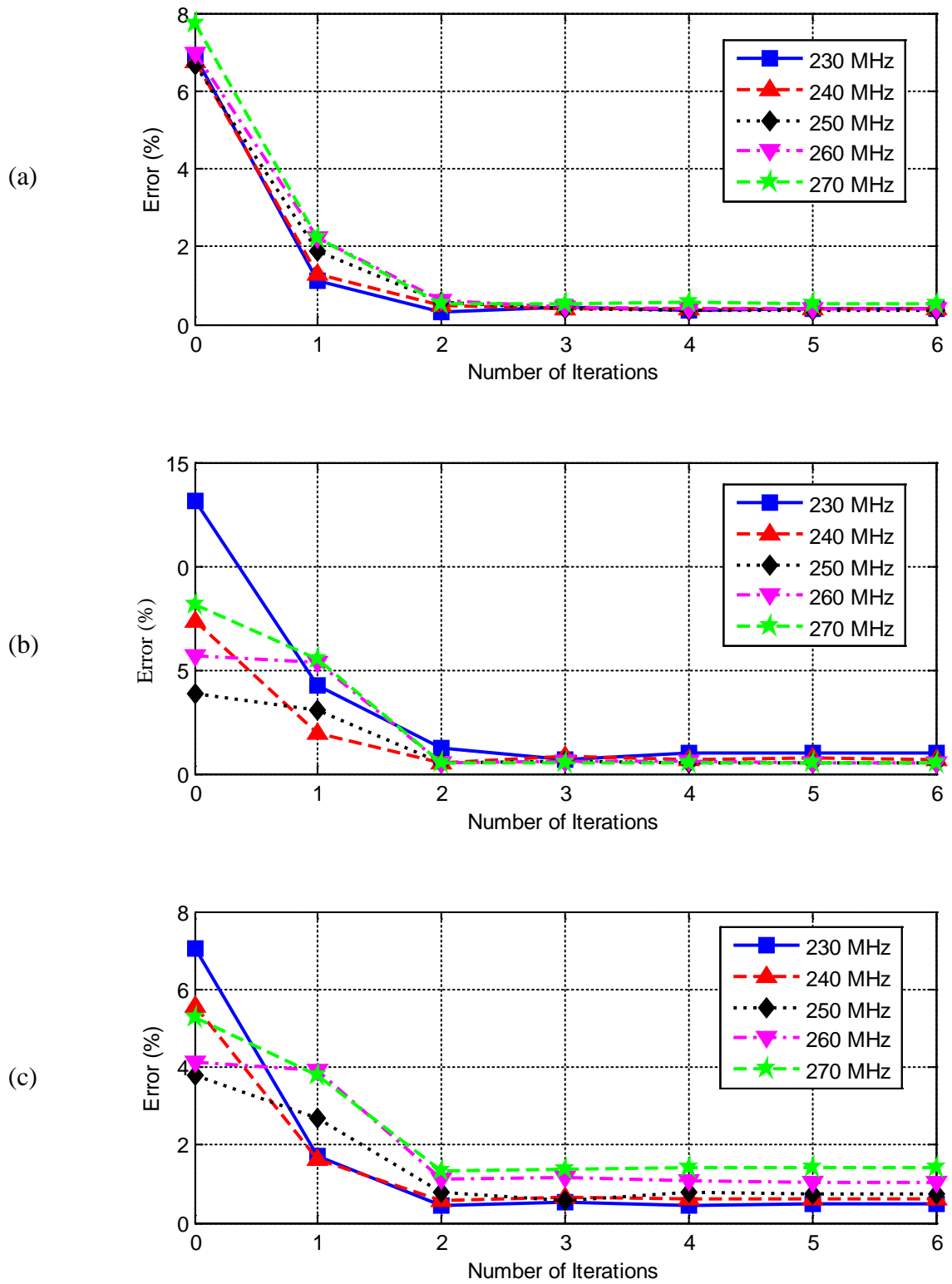


Figure 4.50: Normalized average errors for Gain_0 components in the three plane cuts: a) xy -plane, b) xz -plane, and c) yz -plane.

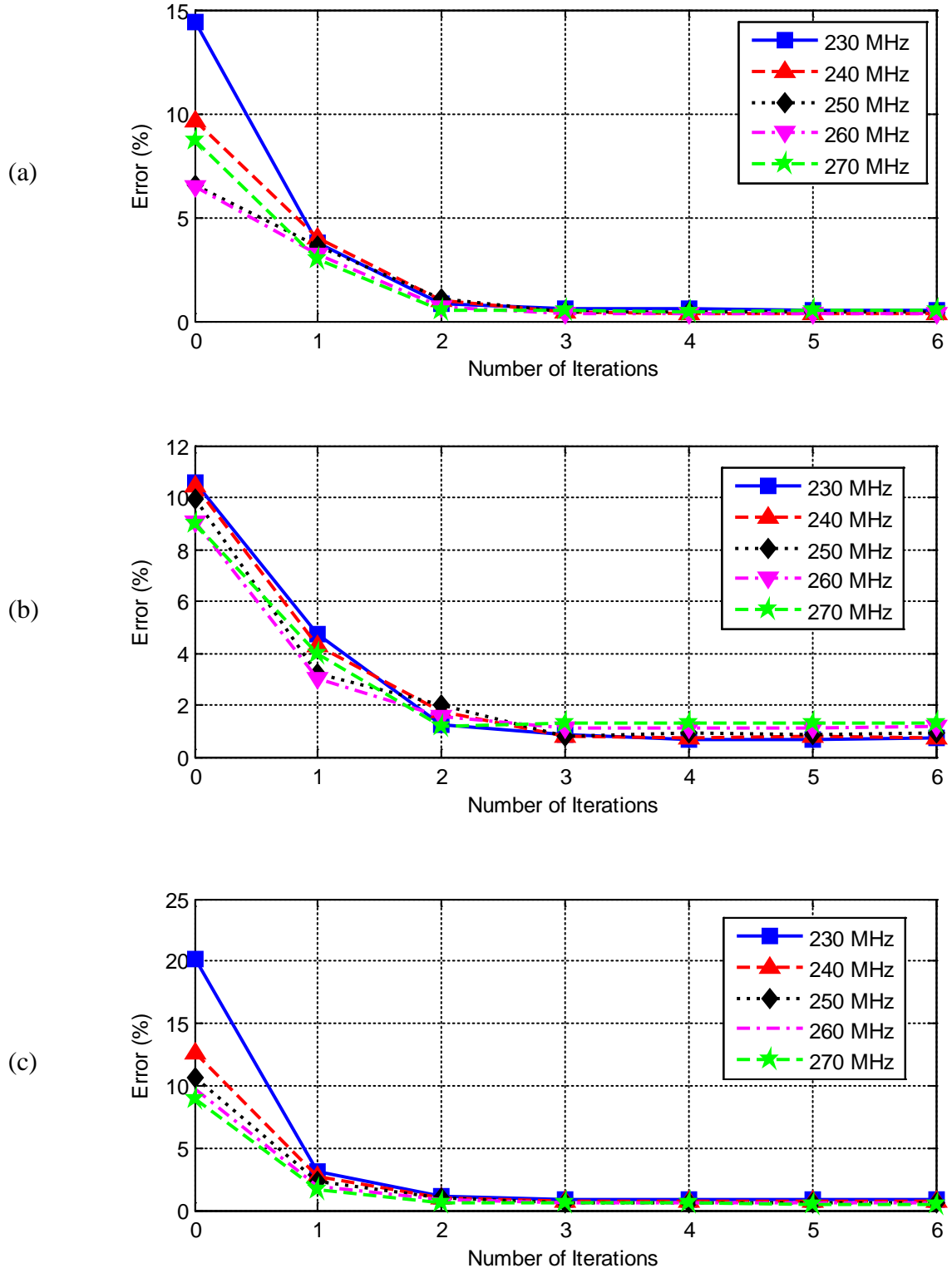


Figure 4.51: Normalized average errors for Gain_ϕ components in the three plane cuts: a) xy -plane, b) xz -plane, and c) yz -plane.

4.6 Radiation from a Dipole Antenna in the Presence of Four Objects

The geometry of another more complex radiation problem is shown as the sixth example in Figure 4.52. The problem includes a 0.5 m dipole antenna and four scatterer objects which are a conducting ellipsoid and sphere, a dielectric box with the relative permittivity of 2.2, and a conducting box. The conducting ellipsoid is placed 1.5 m away from the antenna on the x -axis. The semi-axes of conducting ellipsoid are 0.25 m, 0.25 m, and 1 m along the x , y , and z directions, respectively. The conducting sphere with a radius of 0.25 m is placed 0.5 m away from the antenna on the x -axis and 0.75 m away from the antenna on the y -axis. The dielectric box is placed 0.5 m away from the antenna on the x -axis and 0.25 m away from the antenna on the negative y -axis. The dimensions of the dielectric box are 0.25 m, 1 m, and 1 m along the x , y , and z directions, respectively. The conducting box is placed 0.5 m away from the antenna on the negative x -axis. The dimensions of the conducting box are the same as those of the box-B in Figure 4.13b. It can be seen from Figure 4.53 that the IMR algorithm reaches the convergence criterion after iteration # 3. Figures 4.54-4.59 show the gain patterns (Gain_θ and Gain_ϕ) of the configuration for the three plane cuts. Good agreement with the full domain results is achieved after iteration # 3. To prove the convergence of the results of the IMR and the full domain, the normalized average errors for Gain_θ and Gain_ϕ in the three plane cuts at each frequency are shown in Figures 4.60-4.61, respectively. Simulation parameters and computer resources are summarized in Table 4-6. Results in the table show a considerable reduction in the memory storage requirements and computation time.

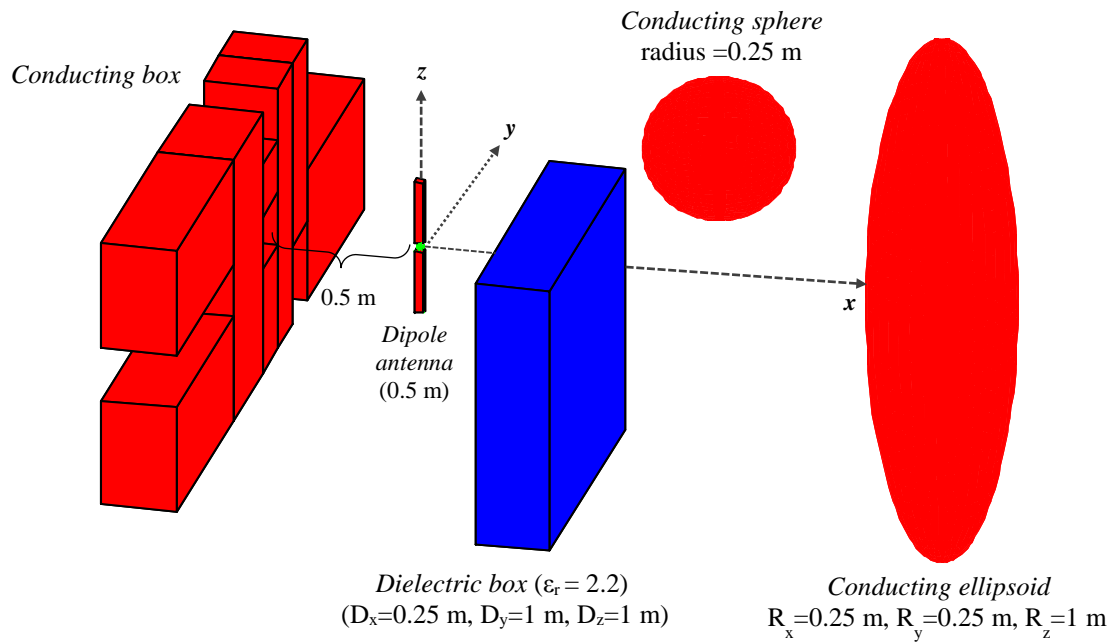


Figure 4.52: Geometry of the sixth problem.

Table 4-6: Simulation parameters and computer resources used by the IMR and full domain simulations.

| | Number of Domains | Total Number of Cells | Computation Time (min.) | Iteration Number | Memory (MB) |
|------------------|-------------------|-----------------------|-------------------------|------------------|-------------|
| Full FDTD | — | 40,333,376 | 1,065 | — | 14,750 |
| IMR-FDTD | 5 | 2,771,968 | 747 | 3 | 1,650 |

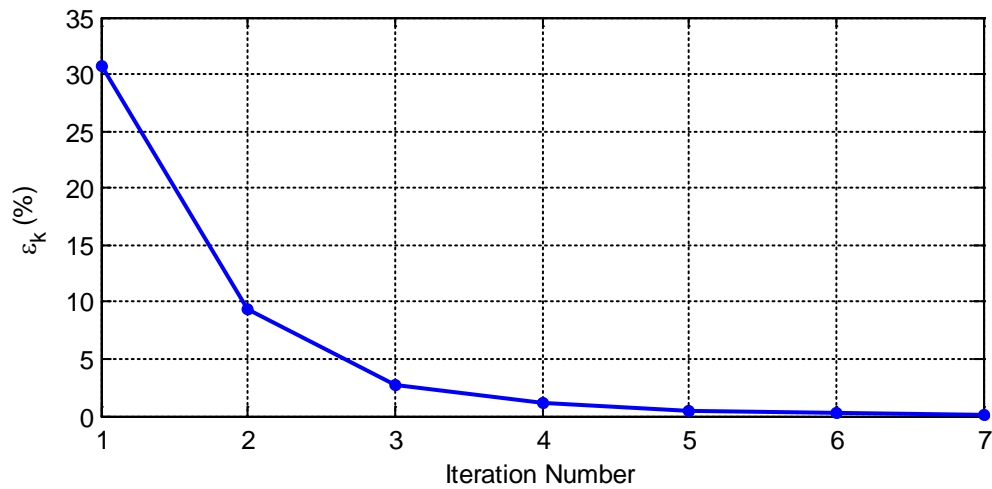
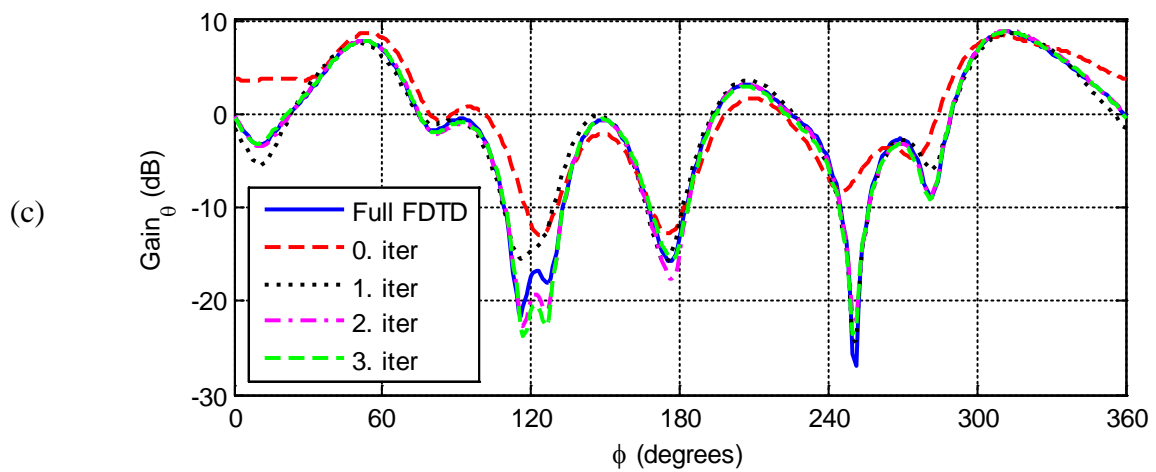
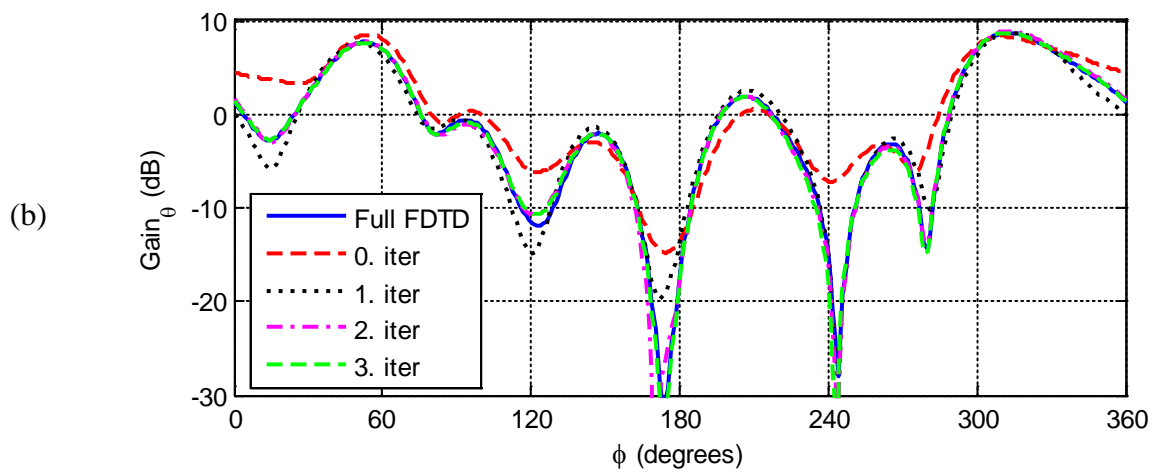
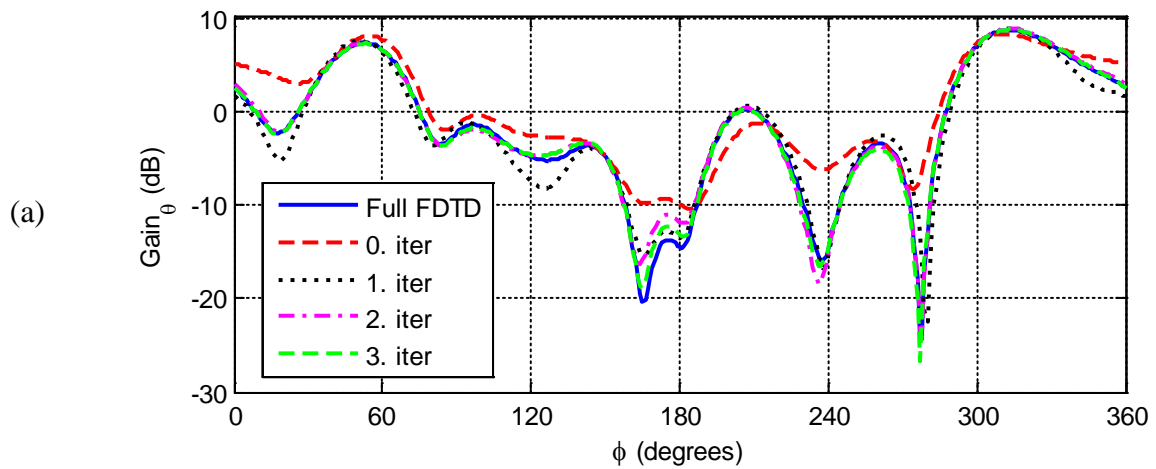


Figure 4.53: Convergence (ϵ_k) between iteration steps for the sixth problem.



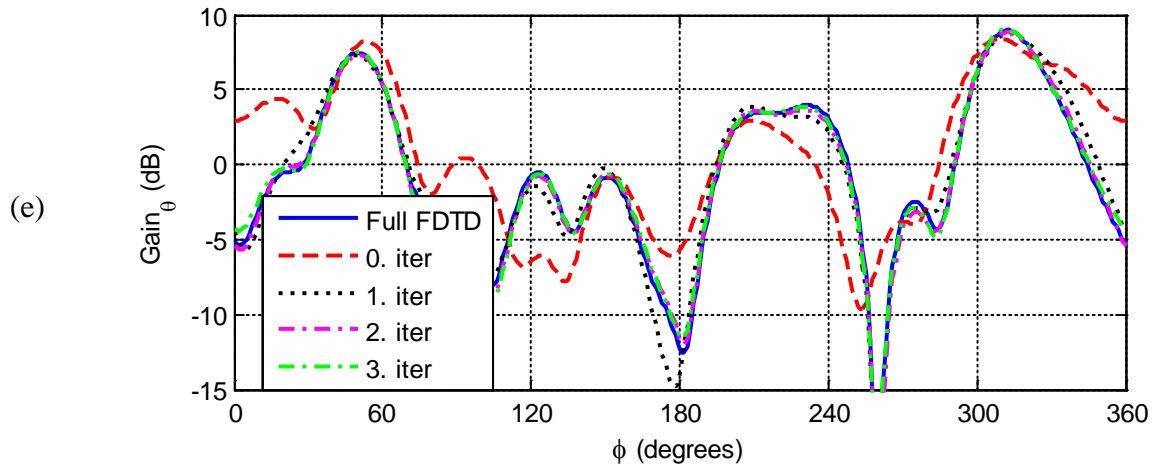
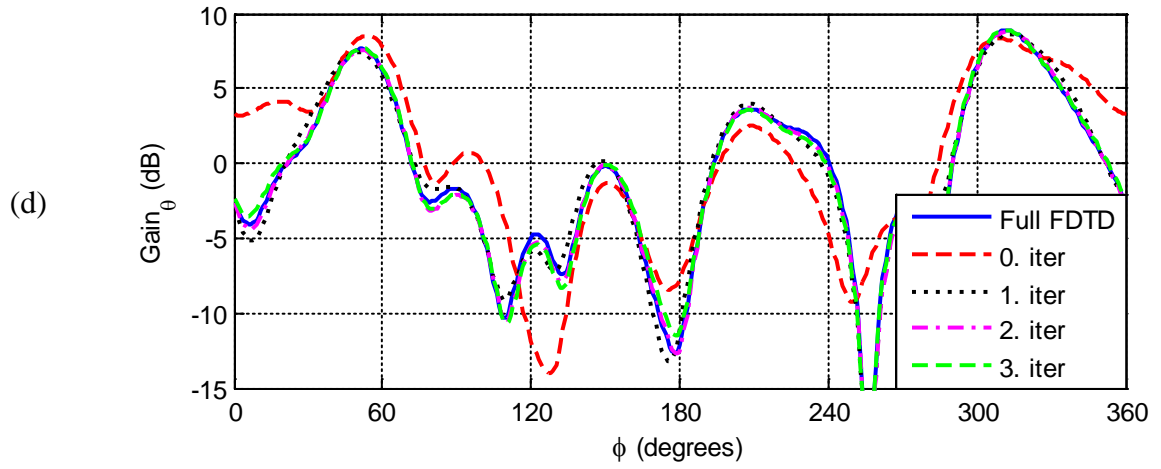
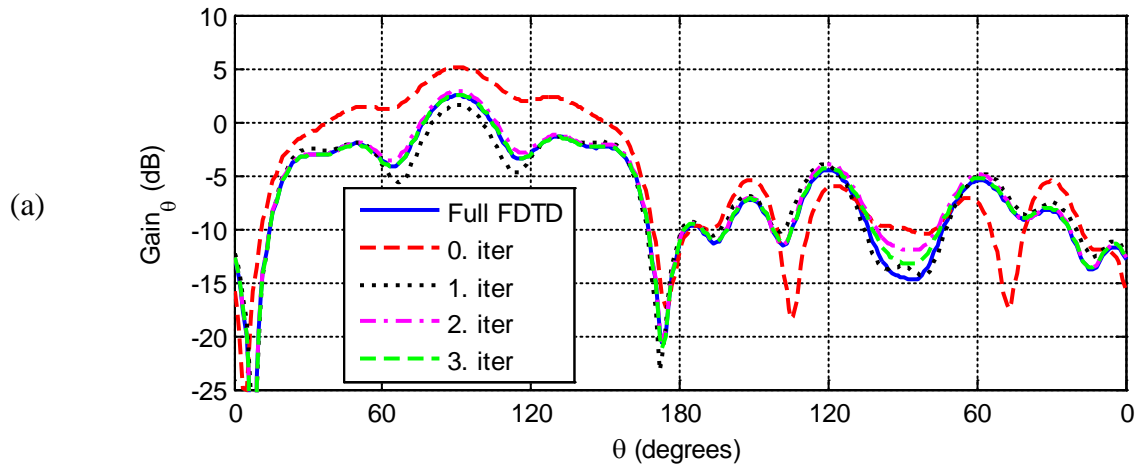
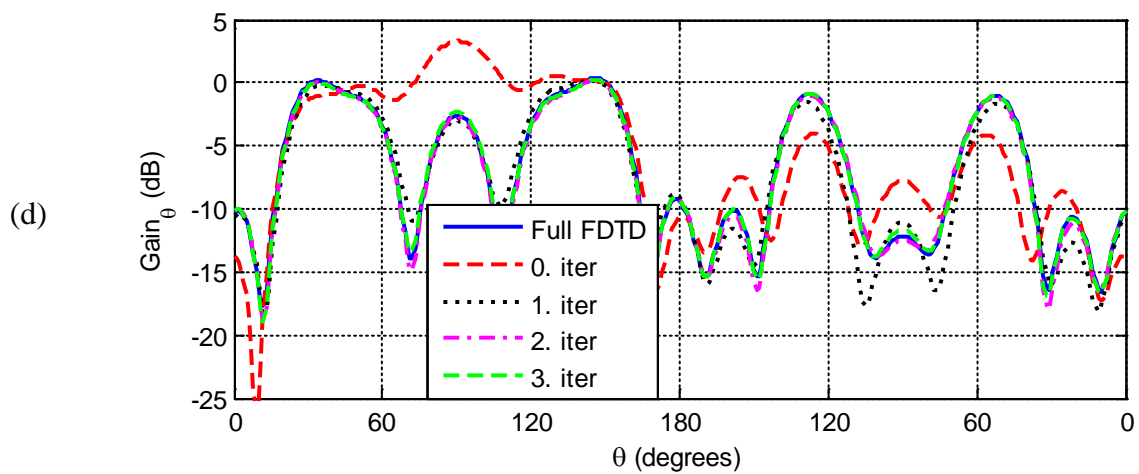
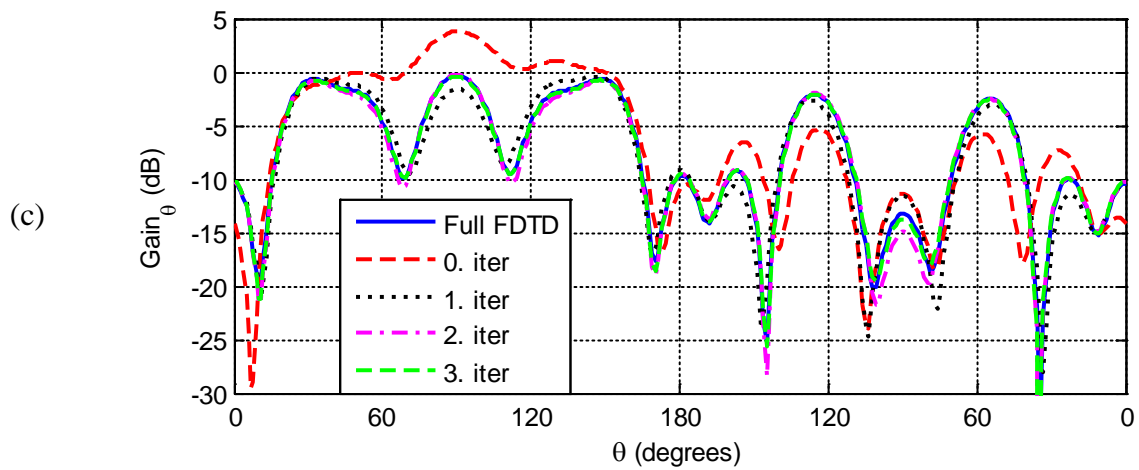
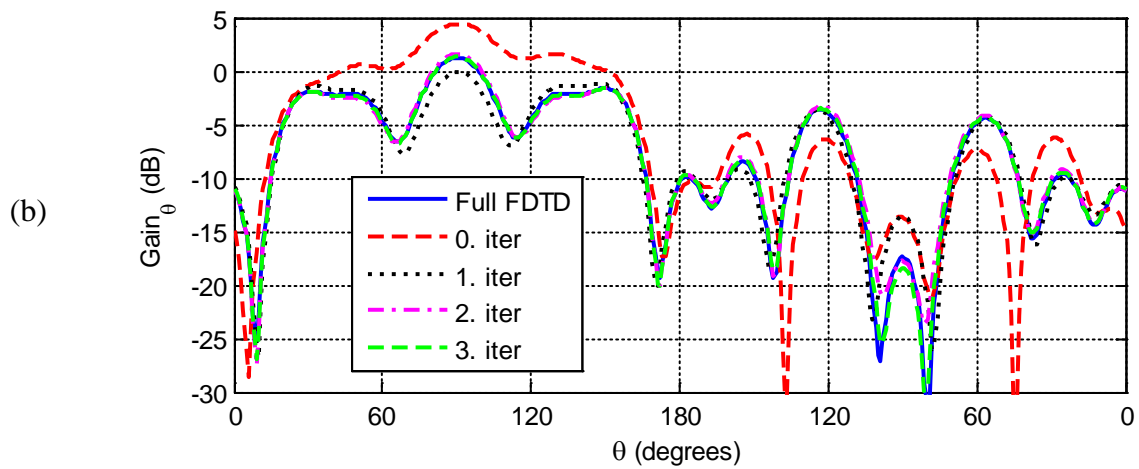


Figure 4.54: Radiation pattern (Gain_θ) for *xy*-plane cut at frequencies: a) 230 MHz, b) 240 MHz, c) 250 MHz, d) 260 MHz, and e) 270 MHz.





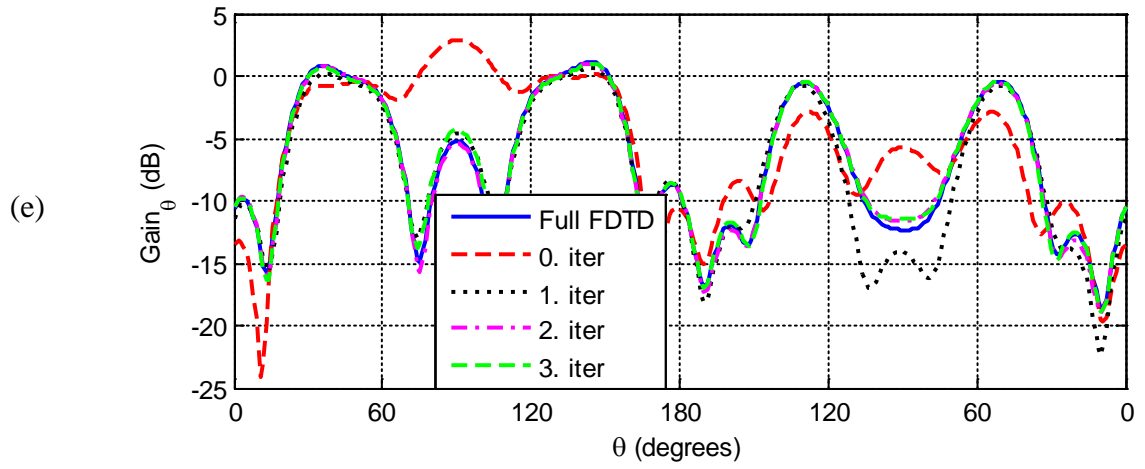
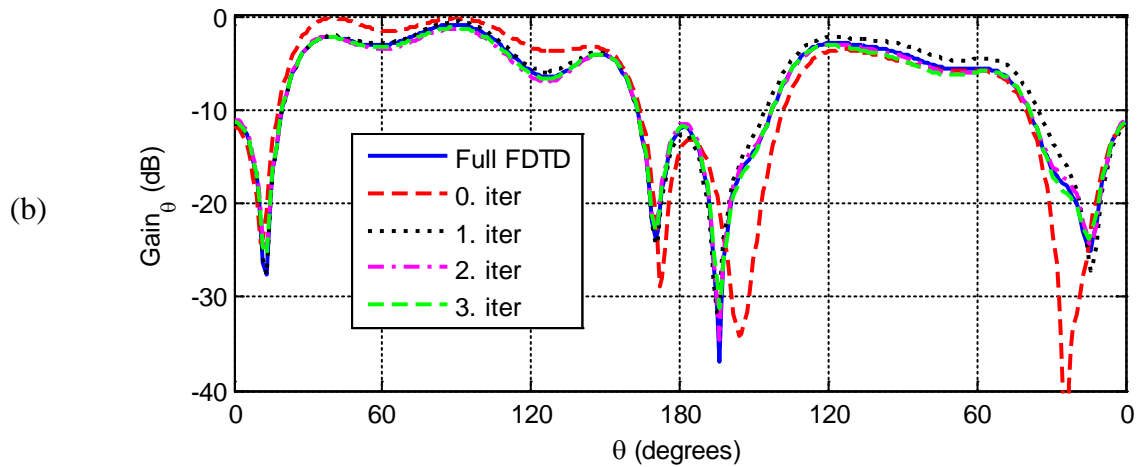
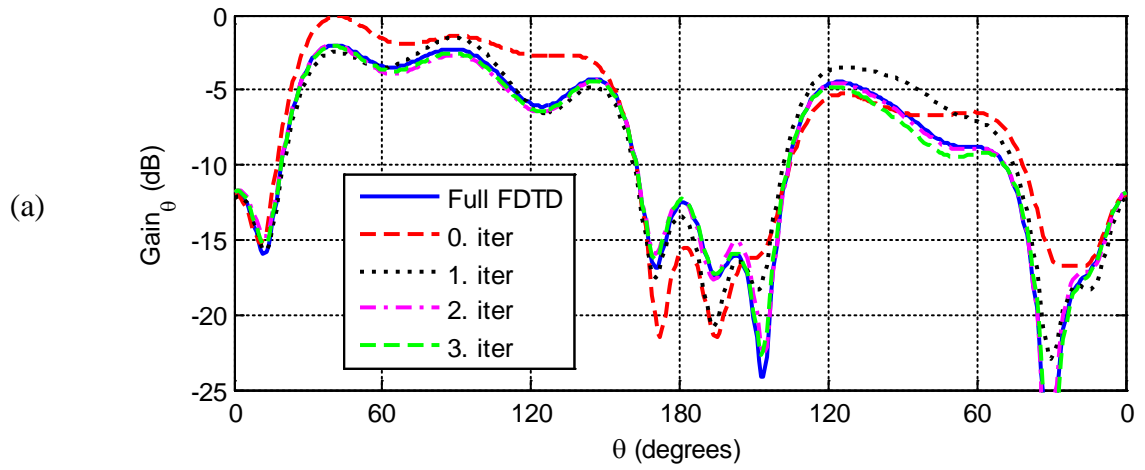


Figure 4.55: Radiation pattern (Gain_θ) for xz -plane cut at frequencies: a) 230 MHz, b) 240 MHz, c) 250 MHz, d) 260 MHz, and e) 270 MHz.



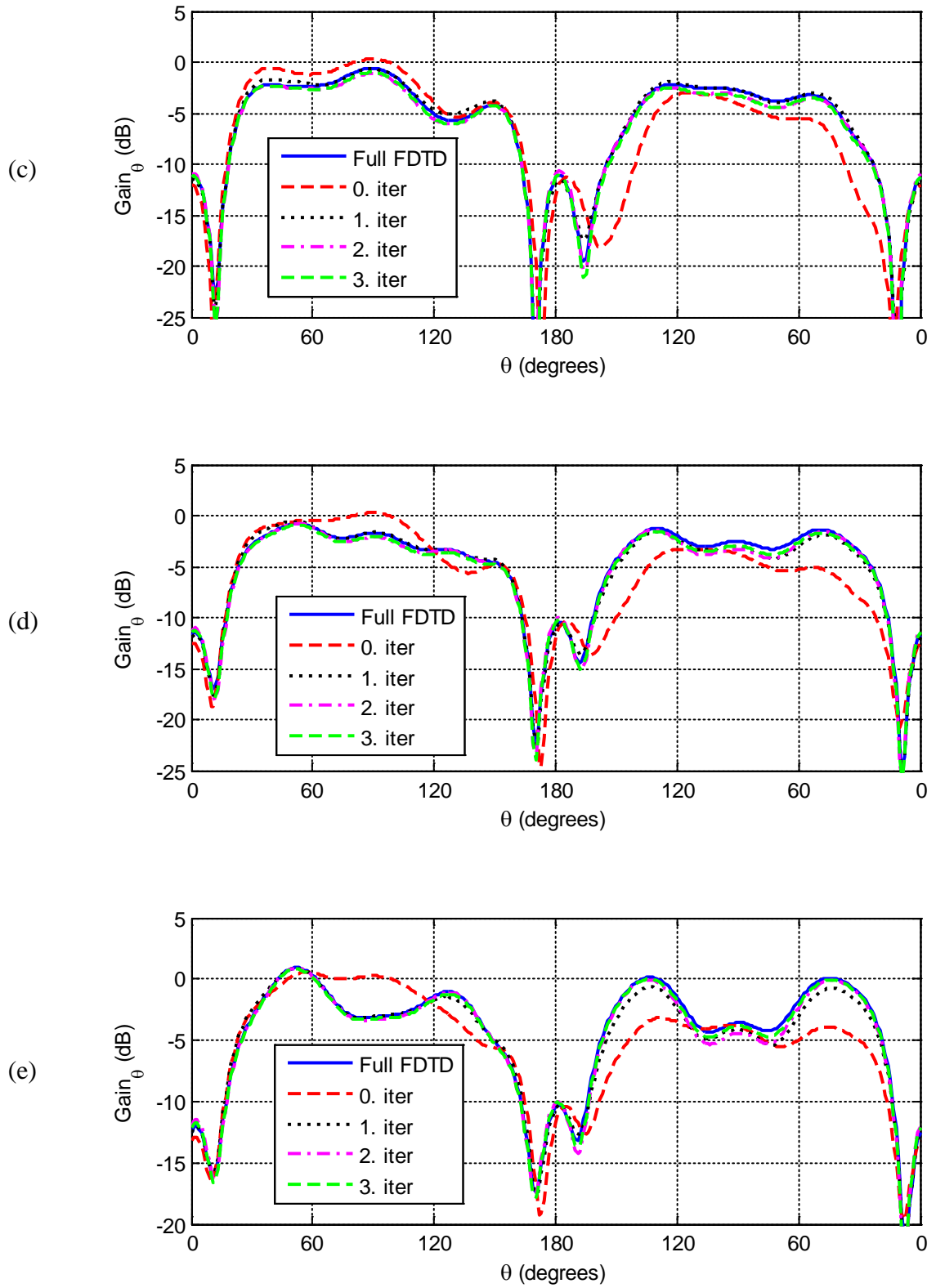
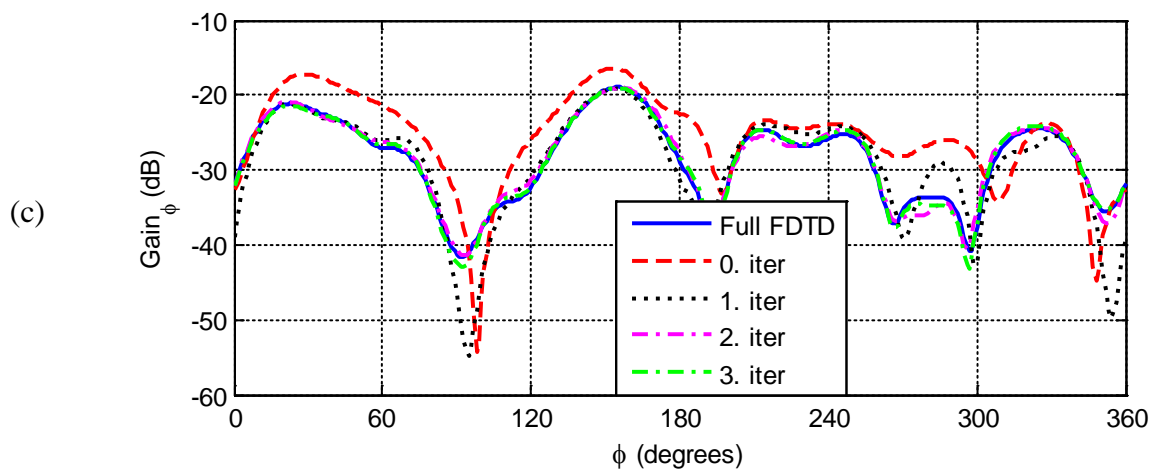
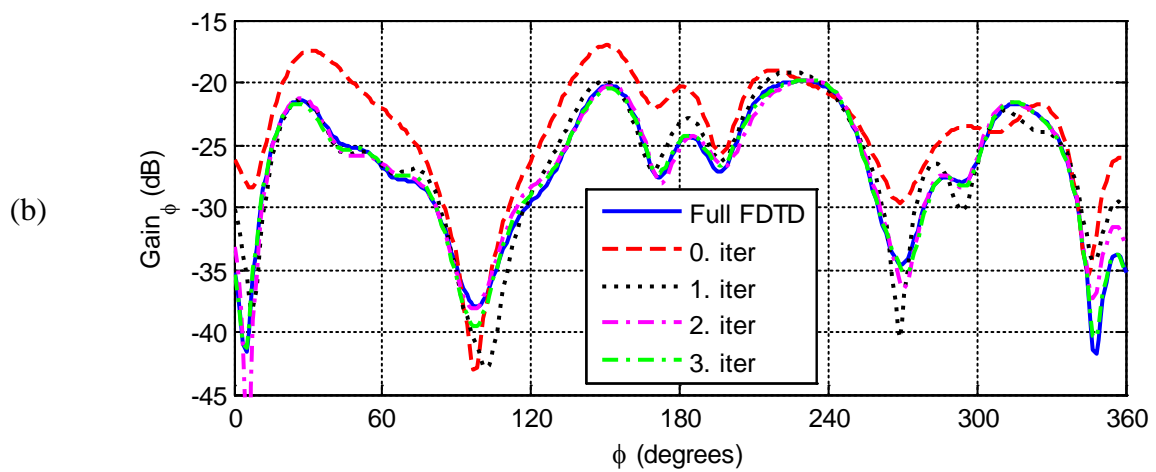
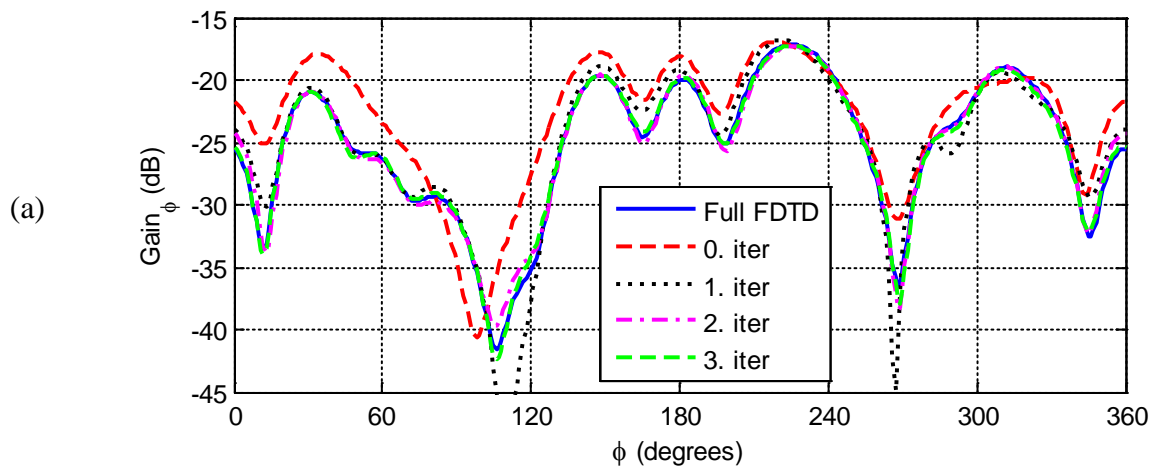


Figure 4.56: Radiation pattern (Gain_θ) for yz -plane cut at frequencies: a) 230 MHz, b) 240 MHz, c) 250 MHz, d) 260 MHz, and e) 270 MHz.



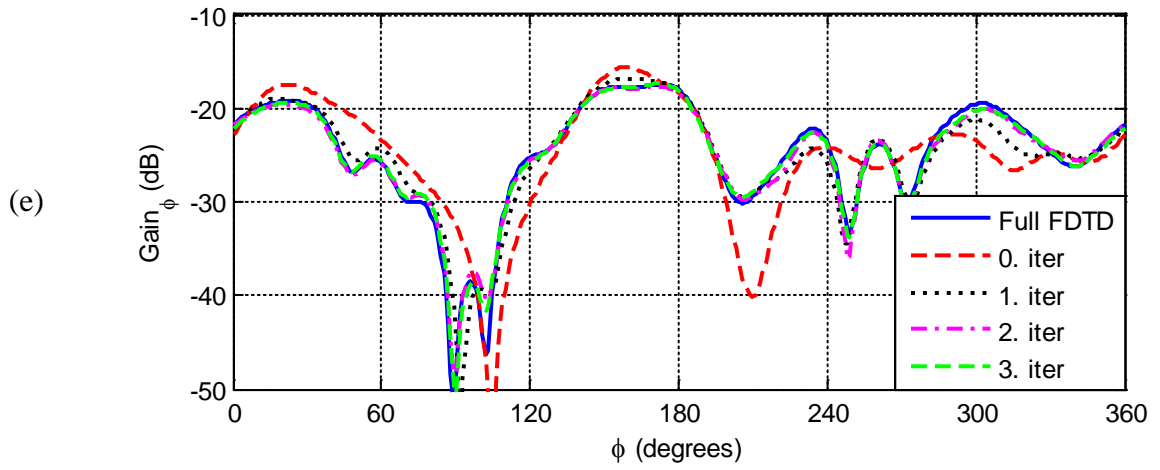
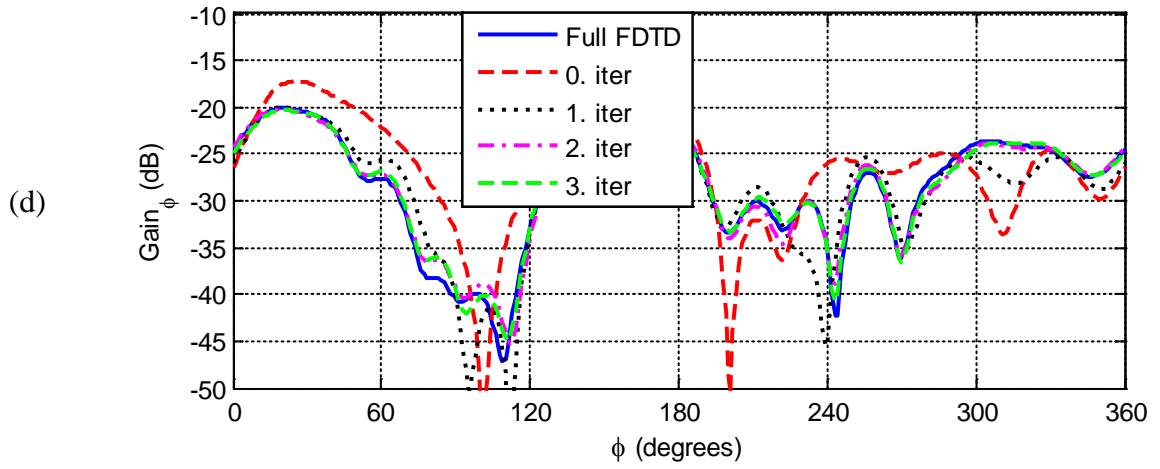
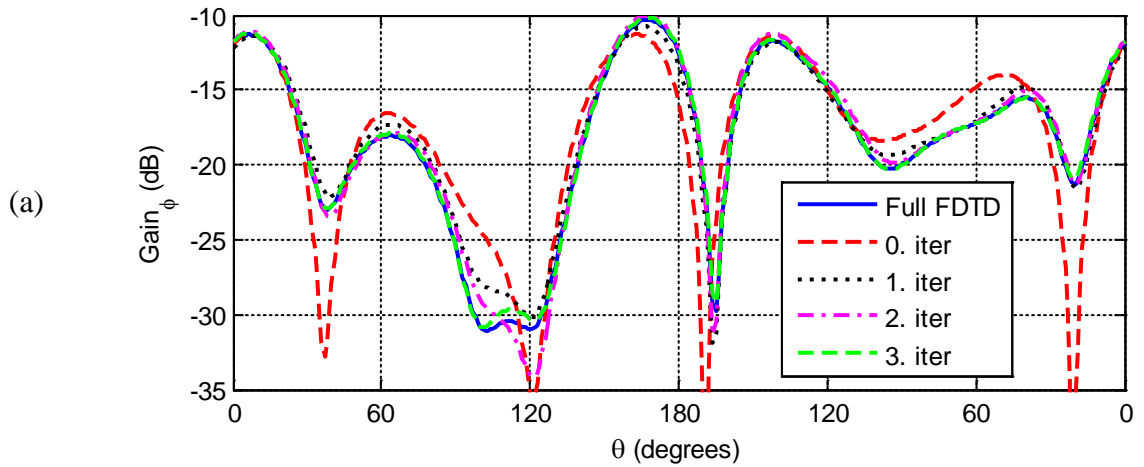
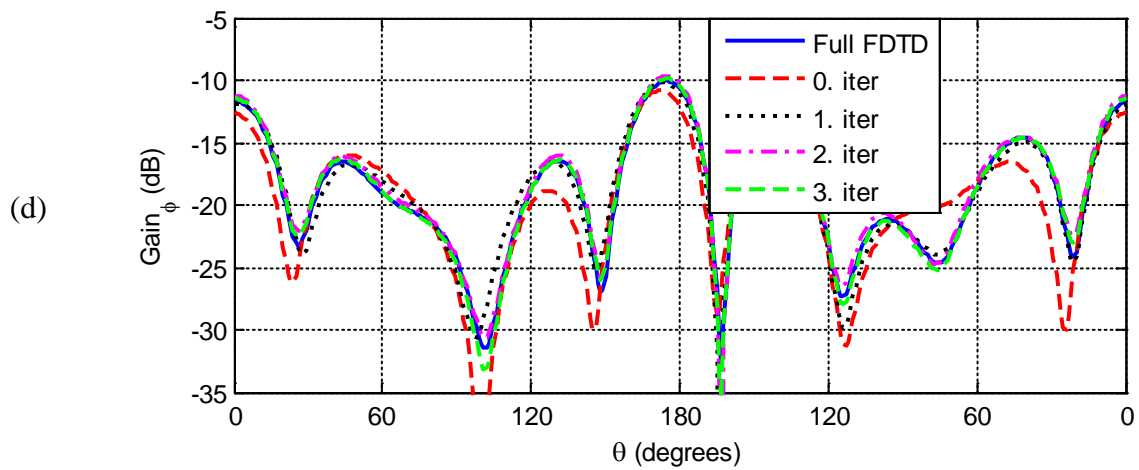
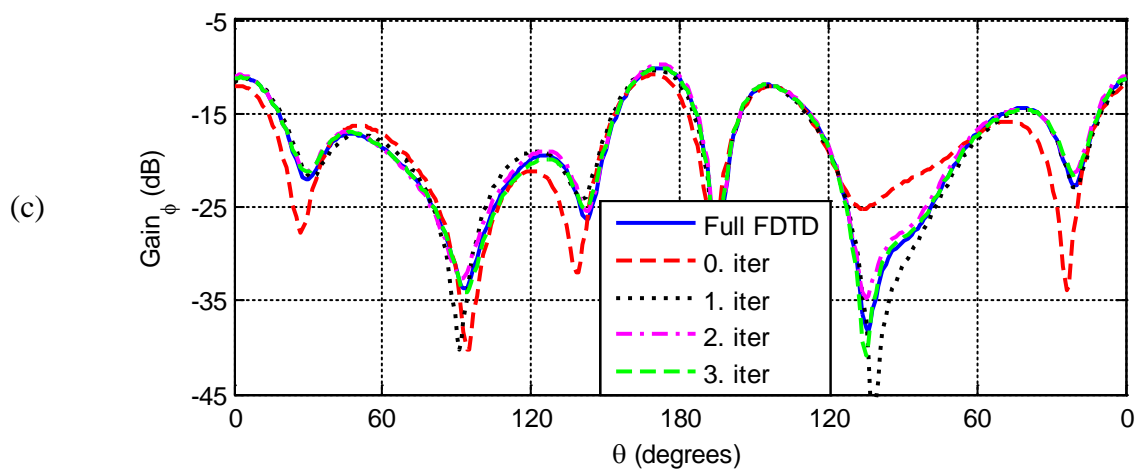
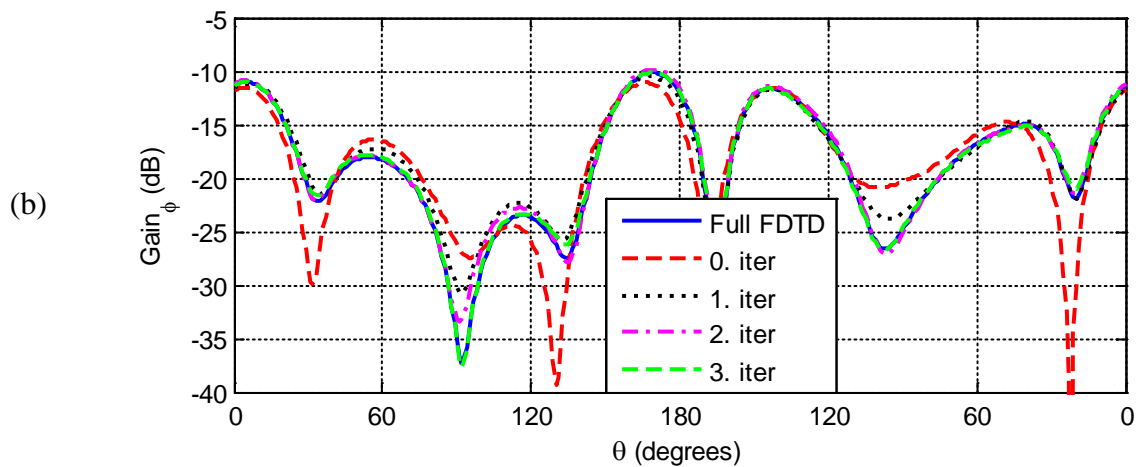


Figure 4.57: Radiation pattern (Gain_ϕ) for xy -plane cut at frequencies: a) 230 MHz, b) 240 MHz, c) 250 MHz, d) 260 MHz, and e) 270 MHz.





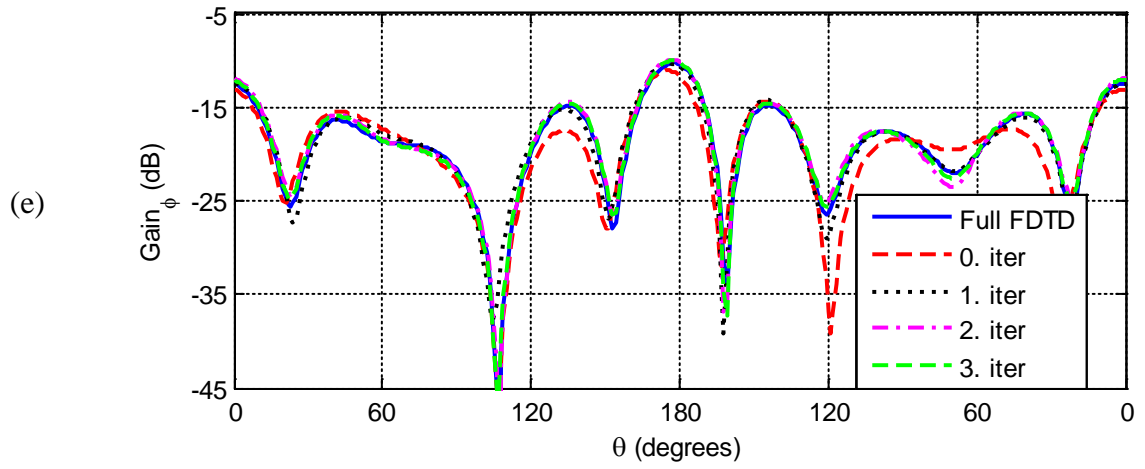
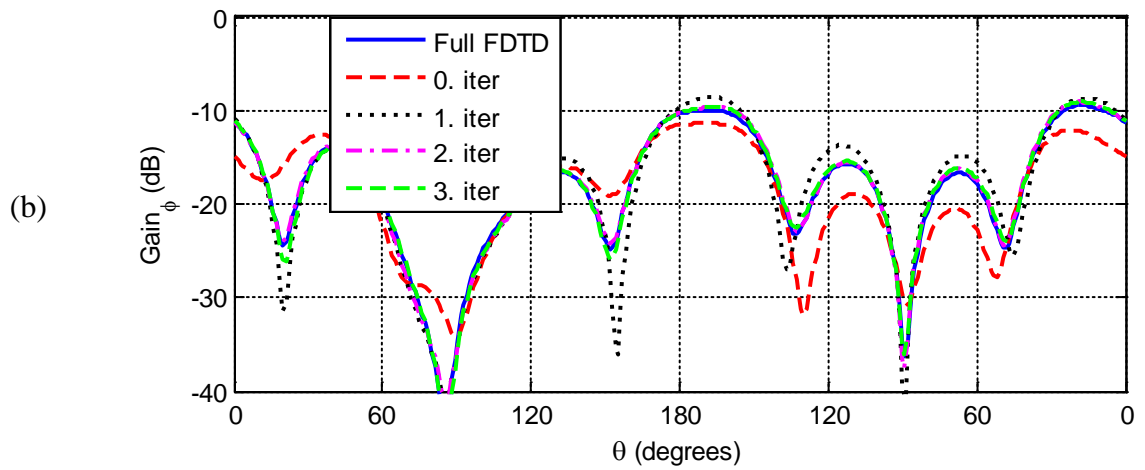
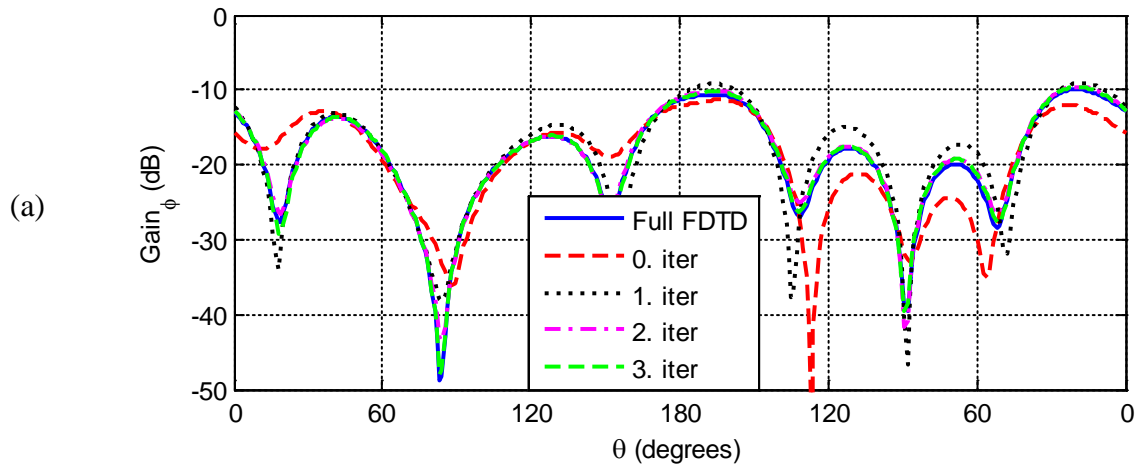


Figure 4.58: Radiation pattern (Gain_φ) for xz -plane cut at frequencies: a) 230 MHz, b) 240 MHz, c) 250 MHz, d) 260 MHz, and e) 270 MHz.



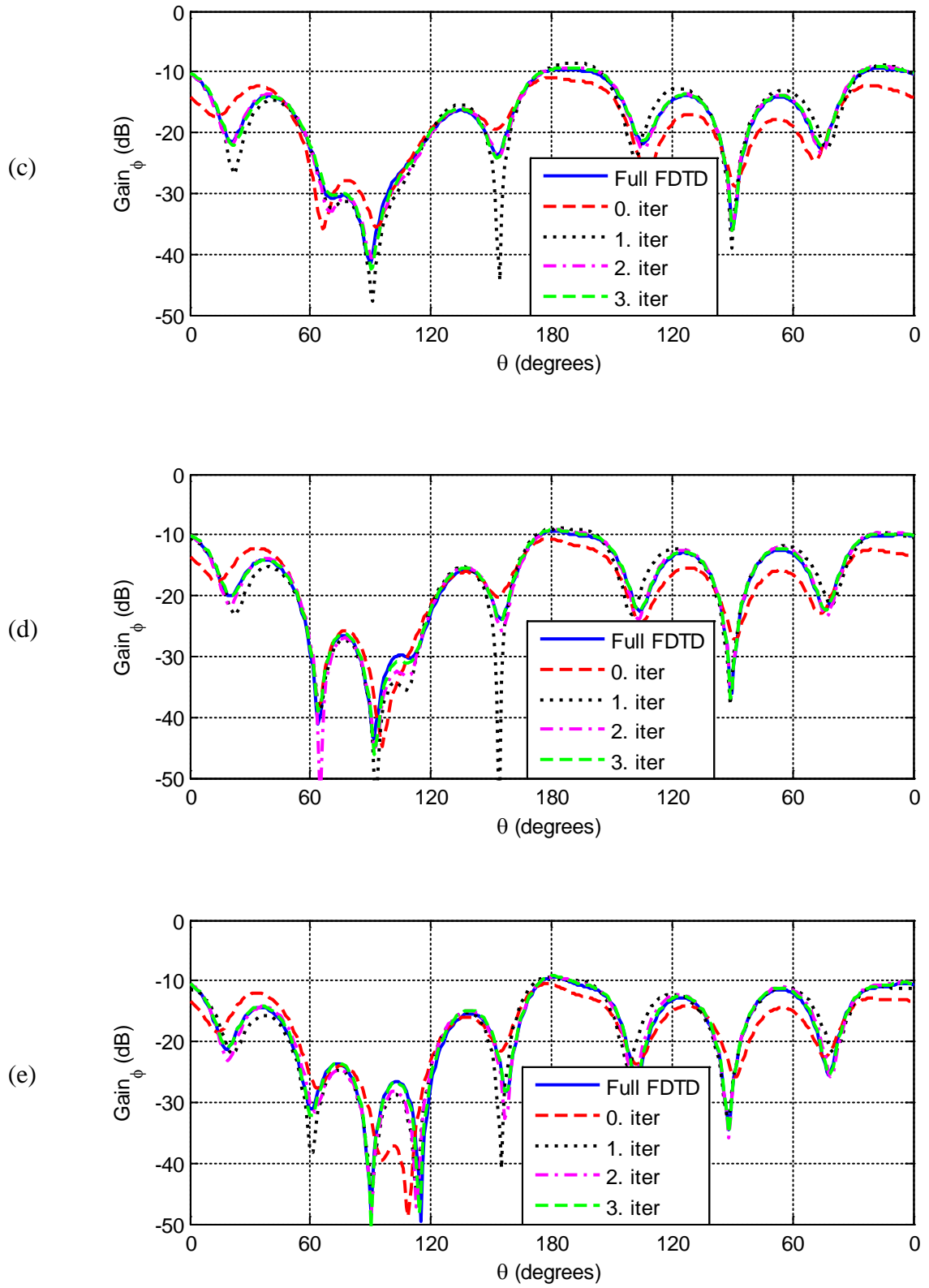


Figure 4.59: Radiation pattern (Gain_φ) for yz-plane cut at frequencies: a) 230 MHz, b) 240 MHz, c) 250 MHz, d) 260 MHz, and e) 270 MHz.

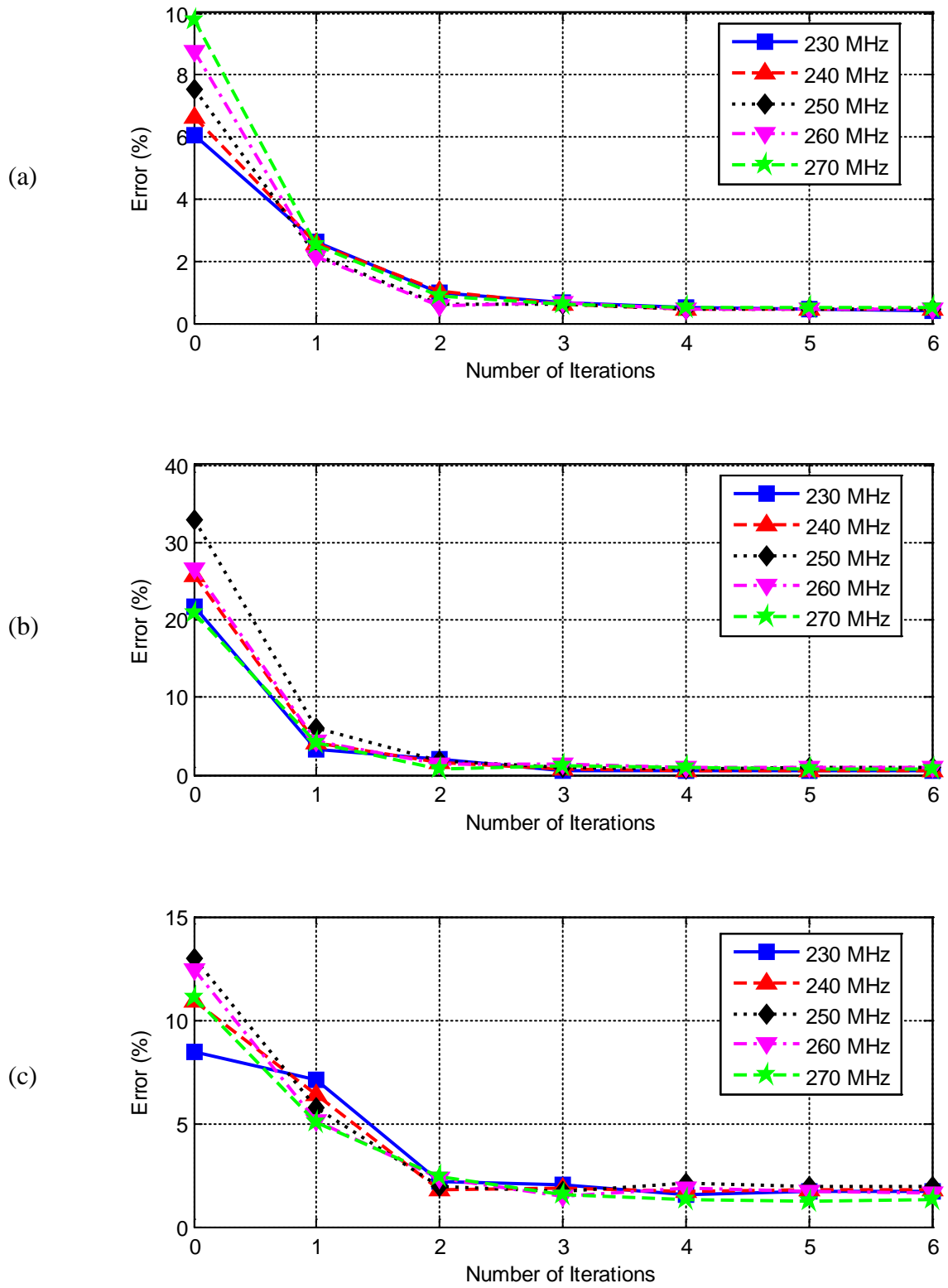


Figure 4.60: Normalized average errors for Gain_0 components in the three plane cuts: a) xy -plane, b) xz -plane, and c) yz -plane.

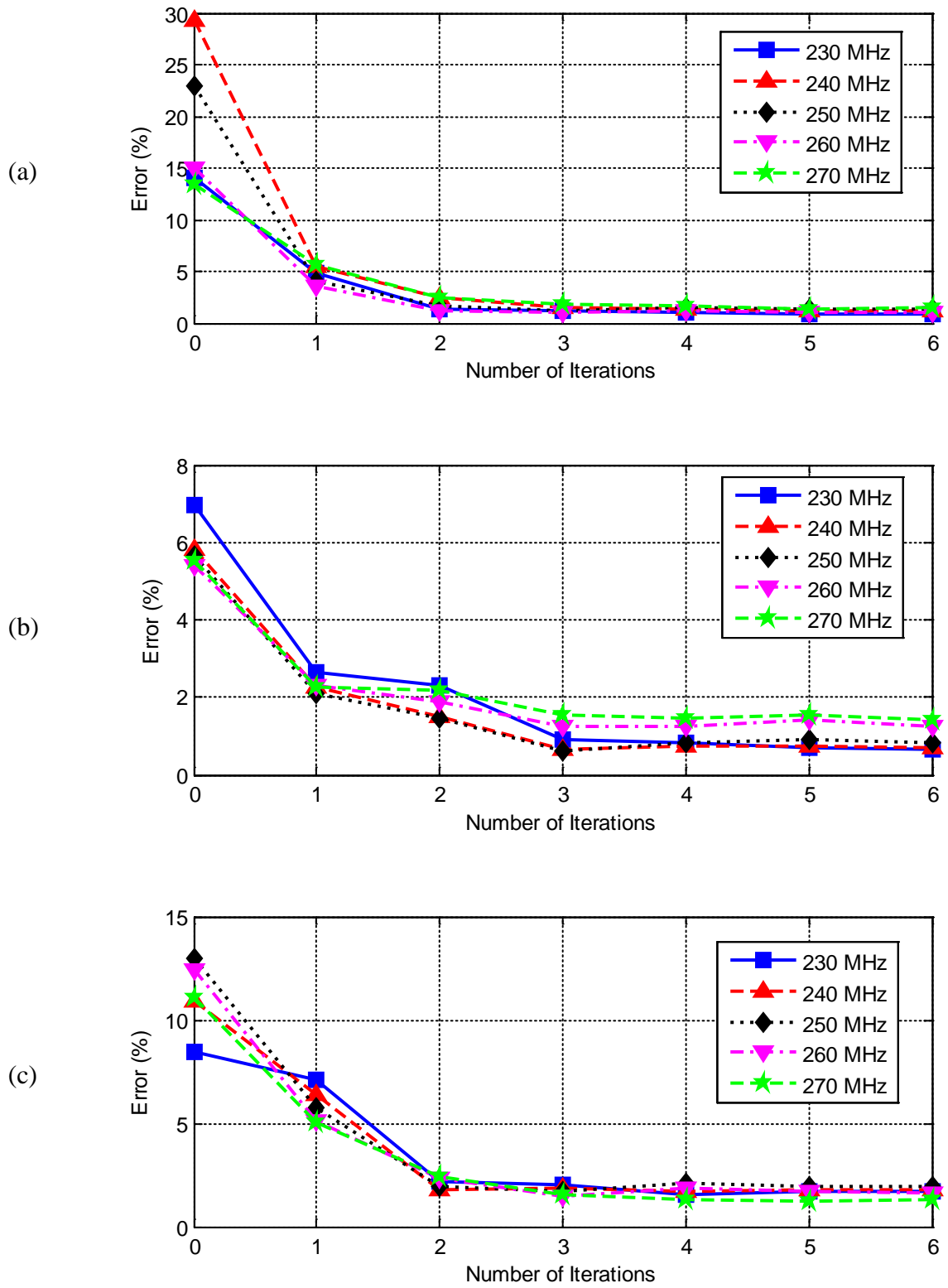


Figure 4.61: Normalized average errors for Gain_ϕ components in the three plane cuts: a) xy -plane, b) xz -plane, and c) yz -plane.

5 IMR ALGORITHM AS HYBRID TECHNIQUE

In this chapter, integration of the method of moments (MoM) and the finite-difference time-domain (FDTD) method into the iterative multi-region (IMR) technique is presented. This hybrid method combines the desirable features of the MoM and the FDTD method to solve large-scale radiation problems more efficiently. The idea of this hybrid method based on the IMR technique is to divide an original problem domain into multiple unconnected subregions and use the more appropriate method in each subregion. For instance, if a problem domain is composed of a thin wire antenna and an arbitrary shaped inhomogeneous scatterer, each of these objects can be placed in a separate subregion, the thin wire antenna can be solved using the MoM while the other region can be solved using the FDTD method, and their solutions can be combined in an iterative algorithm to achieve the combined subregions solution. The interaction between the subregions is based on the radiated fields due to current distribution on the antenna from the MoM region and equivalent currents on the surface of a Huygens' box from FDTD region. Since the FDTD method is a time domain solver, the fields originated from the MoM region that excite the FDTD region need to be converted into time-limited waveforms, which are achieved by the aforementioned time-limited waveform construction (TWC) algorithm. The steady-state solution for the interaction between the MoM and FDTD regions is obtained through an iterative procedure by solving each region due to the excitations from the opposing regions in each iteration until a convergence criterion, that indicates the convergence of the global solution, is achieved. It is observed that convergence is achieved after several iterations. The most prominent feature of this technique is the combination of MoM simulations at multiple frequencies with single FDTD simulations by constructing time-

limited waveforms. Furthermore, considerable reduction in the memory storage requirements and computation time can be achieved especially with larger separation between subregions. After developing the analytical background of this method, we present some numerical results related to the three dimensional electrically large radiation problems.

5.1 Hybrid (MoM/FDTD) Method

A hybrid method, which combines the MoM and FDTD method, has been developed previously to analyze the radiation problems [35–39], where the solution is achieved at a single frequency. In this chapter, we present a hybrid MoM/FDTD approach to obtain solutions at multiple frequencies in a single hybrid simulation by taking the advantage of the capability of the FDTD to analyze inhomogeneous bodies with arbitrary material properties, and that of the MoM to model a thin wire antenna with less memory storage requirements.

As an example, a problem domain as shown in Figure 5.1 is divided into two subregions: one is the MoM subregion including a thin wire antenna, and the other is the FDTD subregion including a dielectric object. The iterative procedure between subregions, as shown in Figure 5.2, consists of iteration # 0 and iteration # k for $\{k=1, 2, \dots, K\}$ where K is an integer depending on how many iterations are necessary.

In iteration # 0, the thin wire antenna in the MoM subregion is analyzed to obtain the current distributions at all frequencies of interest on the antenna surface, using the well-known matrix equation [41] of MoM:

$$[J_{MoM}^k(\omega_i)] = [Z^{-1}(\omega_i)][V^k(\omega_i)], \{k = 0, 1, \dots, K - 1\}, \quad (5.1)$$

where I_{MoM}^k is the current distribution in iteration # k , Z^{-1} is the inverse of the moment matrix, and $V^k(\omega_i)$ is the total voltage vector in iteration # k . The details of the moment matrix [42] and voltage vector, $V^0(\omega_i)$, used for the current distributions calculation are given in Appendix C. The current distributions at all frequencies of interest obtained in iteration # 0 are used to start the iteration # 1.

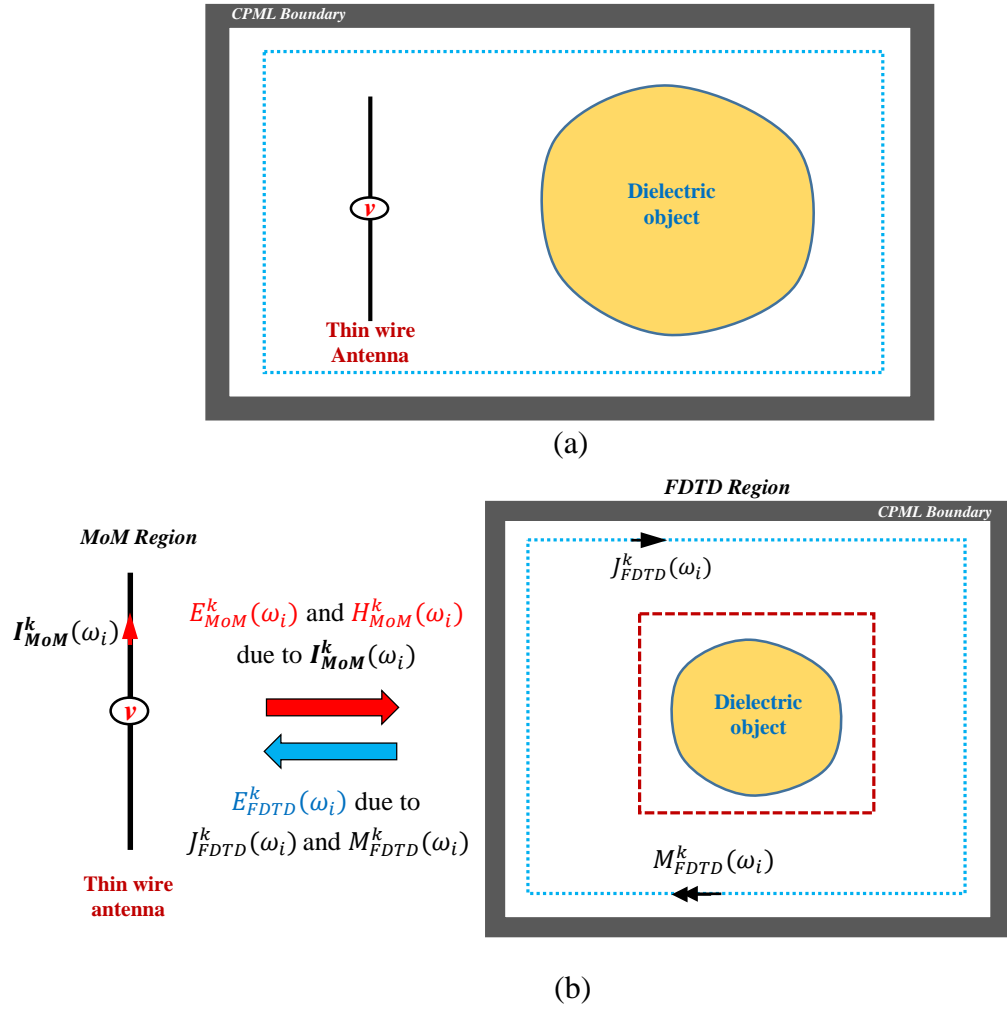


Figure 5.1: Radiation from multiple objects: a) original problem and b) MoM and FDTD subregions. (dotted line: imaginary surface, dashed line: TF/SF boundary)

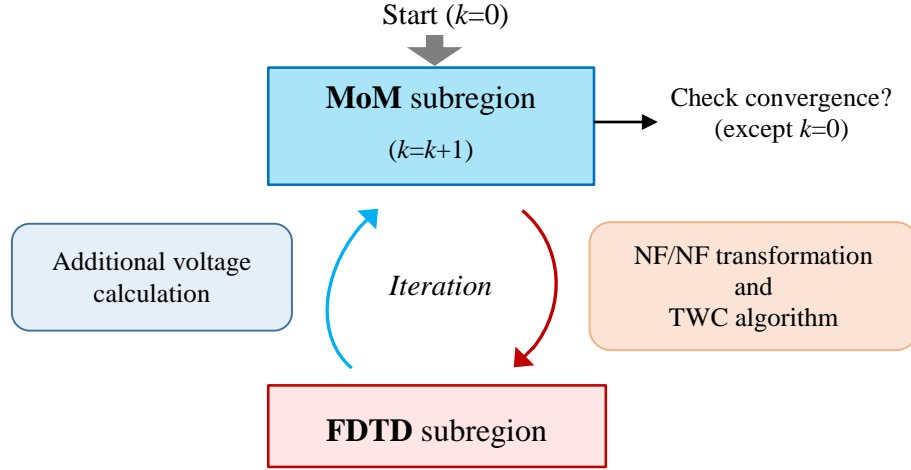


Figure 5.2: Iterative procedure between subregions using the hybrid method.

At the beginning of iteration # 1, radiated fields, $E_{MoM}^1(\omega_i)$ and $H_{MoM}^1(\omega_i)$, due to current distributions, $I_{MoM}^0(\omega_i)$, on the antenna are calculated on the field points of TF/SF boundary in the FDTD subregion at all frequencies of interest, using the near field formulation of a thin wire antenna [43–44]. The details of near field formulation of the thin wire antenna is provided in Appendix D. These fields are considered as the excitation fields for the FDTD subregion. Since the FDTD method is a time domain solver, the excitation fields originated from the MoM subregion need to be converted into time-limited waveforms. Therefore, the TWC algorithm in section 2.3 is used to construct time-limited waveforms which include the desired frequencies of solution with the required magnitudes and phases in their frequency spectrums. The constructed time-limited waveforms imposed on the TF/SF boundary start a FDTD procedure to capture the scattered fields on the imaginary surface. Then fictitious electric and magnetic surface are calculated from the scattered fields on the imaginary surface, using the equivalence principle. These fictitious current values in the time domain are converted into the fictitious currents (J_{FDTD}^1 and M_{FDTD}^1) in the frequency domain, using the NFT in (2.5). For each frequency of interest,

the NFT is performed with the corresponding frequency value. After the FDTD procedure is completed, the induced voltages at all frequencies of interest on each segment of the antenna are calculated from these fictitious currents, using the NF/NF transformation provided in Appendix A. These voltages are considered as additional feeding voltages, $V_{additional}^1(\omega_i)$, and expressed as

$$V_{additional}^1(\omega_i) = \langle E_{FDTD}^1 \left(\mathbf{r} \middle| J_{FDTD}^1(\omega_i), M_{FDTD}^1(\omega_i) \right), t(\mathbf{r} - \mathbf{r}_m) \rangle. \quad (5.2)$$

where $E_{FDTD}^1(\mathbf{r} | J_{FDTD}^1(\omega_i), M_{FDTD}^1(\omega_i))$ is the electric field generated by the fictitious electric and magnetic currents on the imaginary surface in the FDTD subregion, $t(\mathbf{r} - \mathbf{r}_m)$ is the m^{th} testing function of the MoM, and $(\mathbf{r} - \mathbf{r}_m)$ is the distance from each segment on the antenna to the gap where the voltage source is placed. $V_{additional}^1(\omega_i)$ at each frequency of interest is calculated by using the inner product of the electric field, $E_{FDTD}^1(\omega_i)$, and the testing function, $t(\mathbf{r} - \mathbf{r}_m)$.

In general, the additional voltages $V_{additional}^k(\omega_i)$ in iteration # k are added to the voltage vector, $V^{k-1}(\omega_i)$, used in the previous iteration to calculate the current distributions. The total voltage vector, expressed in (5.3), is used for the next MoM calculation. After the new current distributions at all frequencies of interest on the antenna are calculated using (5.1), the iteration # 1 is completed. The procedure for the subsequent iterations is the same as iteration # 1.

$$V^k(\omega_i) = V^{k-1}(\omega_i) + V_{additional}^k(\omega_i). \quad \{k = 1, 2, \dots, K-1\}. \quad (5.3)$$

Iteration # 1 is repeated $K-1$ times until a convergence (stopping) criterion is achieved. The iterations are terminated when the Euclidean norm of the difference in the current distributions at all frequencies of interest from one iteration to the next iteration is

smaller than the convergence criterion. The calculation of convergence is defined as follows:

$$\varepsilon_k = \text{average}_{i=1,\dots,N} \left(\left\| \frac{I_{MoM}^k(\omega_i) - I_{MoM}^{k-1}(\omega_i)}{I_{MoM}^{k-1}(\omega_i)} \right\| \right) \times 100 \%, \quad (5.4)$$

where $I_{MoM}^k(\omega_i)$ is the current distribution at k^{th} iteration for ω_i frequency, and N is the number of frequencies. Based on the numerical experiments, 1 % is found sufficient to indicate that convergence is achieved since the current distributions at desired frequencies do not change significantly for smaller values.

5.2 Numerical Results

In this section we demonstrate some examples to show the validity of the proposed hybrid method. The problems presented here have been simulated in [37–38] to obtain solution at a single frequency, whereas our proposed hybrid method provides solutions at multiple frequencies instead of a single frequency in a single simulation. In all simulation of the radiation problems, a 16.65 cm thin wire antenna with a radius of 0.27 mm is used. The single thin wire antenna is performed to determine the frequency band in which it radiates well. The frequencies 840, 860, and 880 MHz are found to be in the band of operation. Figure 5.3 shows the magnitude of the reflection coefficient of the antenna. The specifications of the computer used for the simulations are given in Appendix B.

In order to show the difference between the results generated by the MoM and the FDTD method, the input impedances of the antenna at frequencies of interest are shown in Table 5-1. The thin wire antenna is divided into 51 segments for the MoM simulation, and the discretization of the thin wire antenna is 1.665 mm in all Cartesian directions for the FDTD simulation.

Table 5-1: Antenna input impedances at frequencies of interest of a single thin wire.

| Method\Frequency | 840 MHz | 860 MHz | 880 MHz |
|------------------|----------------|---------------|----------------|
| FDTD | 66.97 -j 21.19 | 72.14 +j 0.96 | 77.73 +j 23.17 |
| MoM | 67.63 -j 19.15 | 72.56 +j 3.03 | 77.82 +j 25.12 |

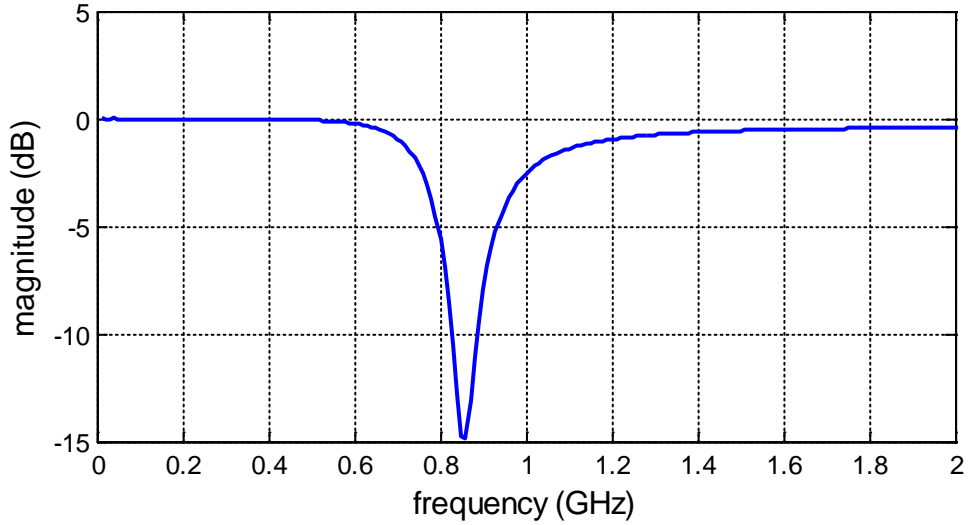


Figure 5.3: Magnitude of the reflection coefficient of a single thin wire antenna.

5.2.1 Current Distributions on an Antenna in the Presence of an Obstacle-1

Figure 5.4 shows the first problem that is used to validate the proposed hybrid method. A thin wire antenna is placed a distance of 2 cm away from a dielectric sphere. The dielectric sphere has a radius of 10 cm, relative permittivity of 43, and conductivity of 0.83 S/m. A cell size of the FDTD subregion that contains the dielectric sphere is 2.5 mm in all directions in hybrid simulation, whereas a cell size is 1.665 mm for the full domain FDTD simulation. Figure 5.5 shows the convergence of the IMR iteration calculated by (5.4). It can be seen that the IMR algorithm reaches the convergence criterion ($\epsilon_k < 1\%$) after iteration # 4. The current distributions obtained using the hybrid method over the

antenna surface at frequencies of interest are shown in Figure 5.6. The antenna input impedances at frequencies of interest after four iterations using the hybrid method and the conventional FDTD method are listed in Table 5-2. Comparison shows that the proposed hybrid results are in good agreement with the conventional FDTD method results. Simulation parameters and computer resources are summarized in Table 5-3. Results in the table show a considerable reduction in the memory requirements and computation time.

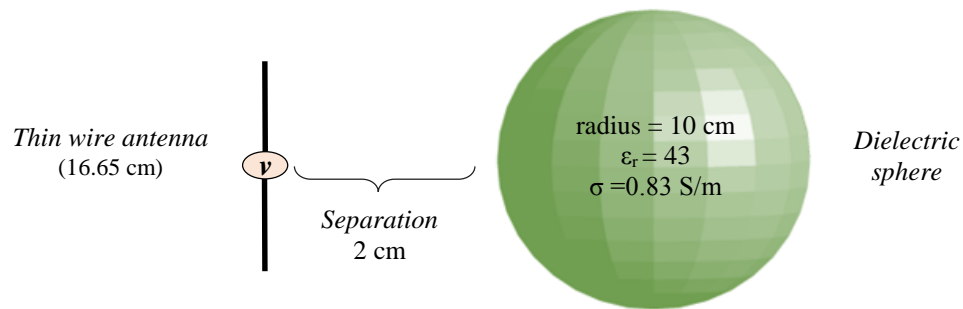


Figure 5.4: The geometry of the first problem.

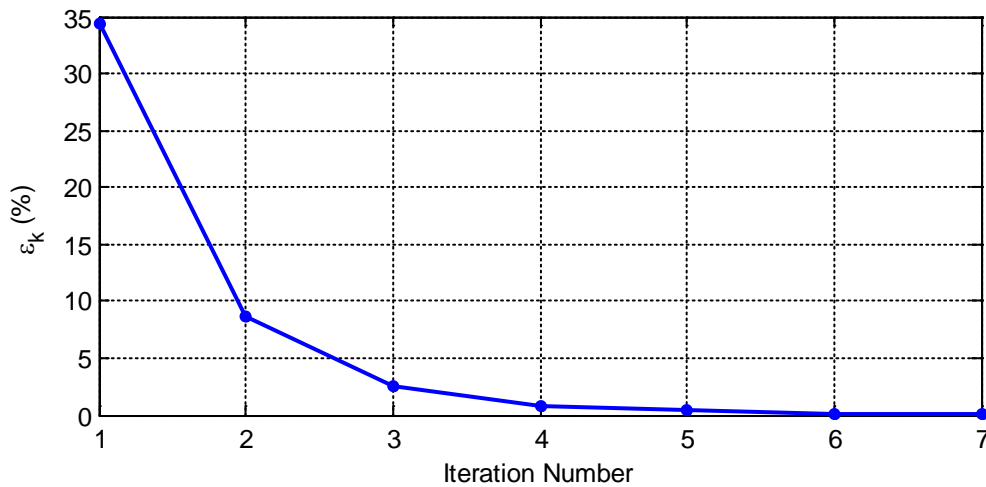


Figure 5.5: Convergence (ϵ_k) between iteration steps.

Table 5-2: Antenna input impedances at the frequencies of interest.

| Method\Frequency | 840 MHz | 860 MHz | 880 MHz |
|---------------------------|----------------|---------------|----------------|
| FDTD (Full Domain) | 40.44 -j 28.58 | 43.15 -j 6.74 | 46.09 +j 15.21 |
| Hybrid (MoM/FDTD) | 40.15 -j 24.04 | 43.05 -j 5.29 | 44.00 +j 14.02 |

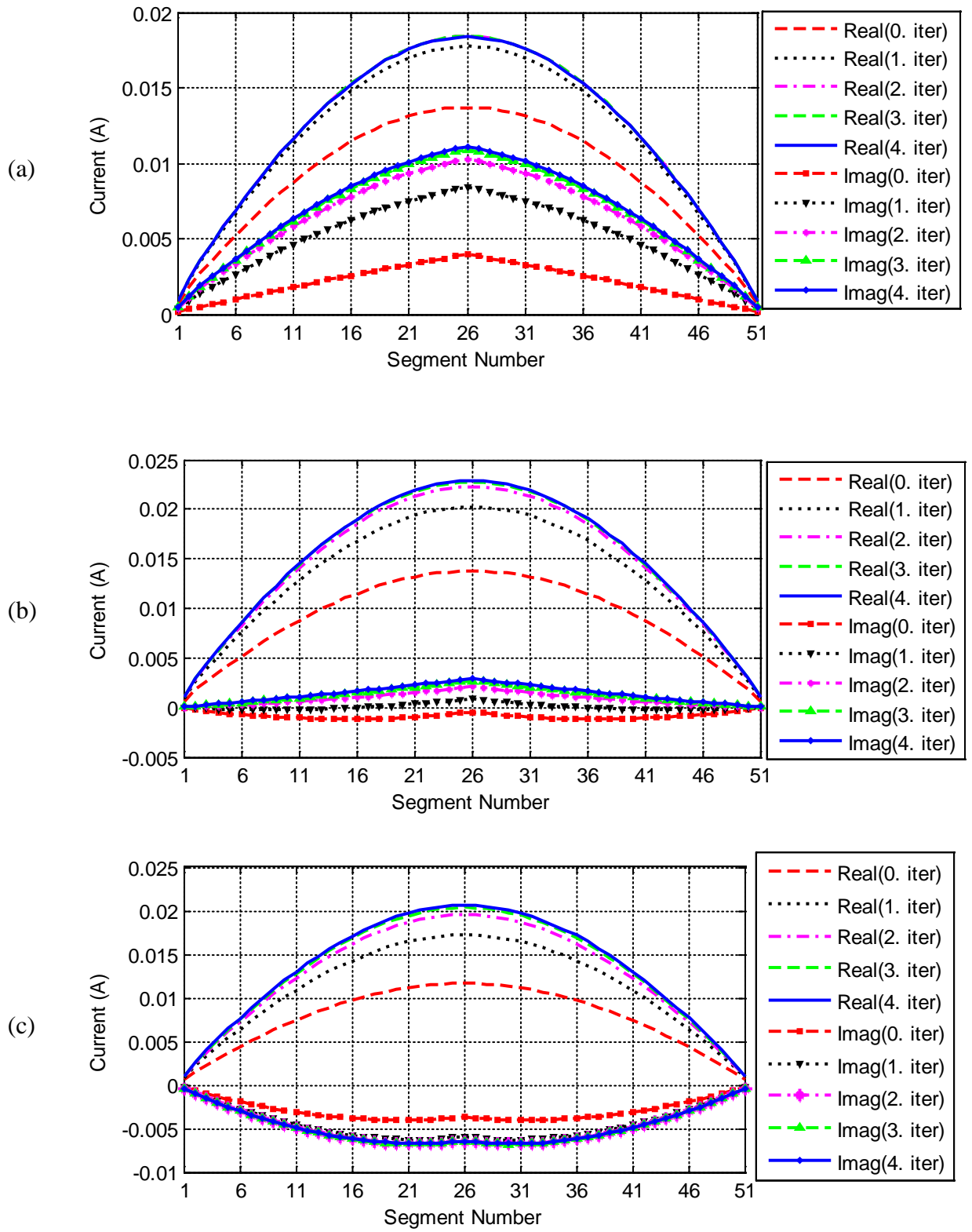


Figure 5.6: Convergence of current distribution versus segment number at frequencies: a) 840, b) 860, and c) 880 MHz. (0-4): represents the iteration number.

Table 5-3: Simulation parameters and computer resources used by the IMR and full domain simulations.

| | Total Number of Cells | Computation Time (min.) | Iteration Number | Memory (MB) |
|---------------------------|------------------------------|--------------------------------|-------------------------|--------------------|
| FDTD (Full Domain) | 4,403,200 | 113 | — | 1765 |
| Hybrid (MoM/FDTD) | 1,560,896 | 87 | 4 | 540 |

The same geometry of the first problem illustrated in Figure 5.4 is simulated with different separations (6, 8, 10 and 12 cm) between the antenna and the dielectric sphere. The idea of this problem is to prove that the hybrid-IMR algorithm convergences fast when the separation between the antenna and object is large. The antenna input impedances at all frequencies of interest using the hybrid method and the conventional FDTD method are listed for different separations in Table 5-4. Results in the table show that the hybrid method results are in good agreement with the conventional FDTD method results. Simulation parameters and computer resources are summarized in Table 5-5. Results in the table show that a considerable reduction in the memory storage requirements and computation time are achieved especially with larger separation between the antenna and the dielectric sphere.

Table 5-4: Antenna input impedances at the frequencies of interest for different separations.

| Separation | Method\Frequency | 840 MHz | 860 MHz | 880 MHz |
|-------------------|-------------------------|----------------|----------------|----------------|
| 6 cm | FDTD (Full Domain) | 58.16 -j 7.48 | 63.64 +j 16.25 | 69.71 +j 40.04 |
| | Hybrid (MoM/FDTD) | 57.45 -j 7.68 | 61.20 +j 16.83 | 66.92 +j 43.00 |
| 8 cm | FDTD (Full Domain) | 67.51 -j 8.81 | 73.84 +j 14.19 | 80.77 +j 37.10 |
| | Hybrid (MoM/FDTD) | 67.28 -j 7.23 | 72.56 +j 16.40 | 79.30 +j 40.43 |
| 10 cm | FDTD (Full Domain) | 72.91 -j 13.68 | 79.35 +j 8.39 | 86.28 +j 30.25 |
| | Hybrid (MoM/FDTD) | 73.08 -j 11.49 | 78.93 +j 11.10 | 85.87 +j 33.50 |
| 12 cm | FDTD (Full Domain) | 74.25 -j 19.21 | 80.24 +j 2.18 | 86.56 +j 23.36 |
| | Hybrid (MoM/FDTD) | 74.87 -j 16.97 | 80.40 +j 4.78 | 86.64 +j 26.29 |

Table 5-5: Simulation parameters and computer resources used by the IMR and full domain simulations.

| Separation | Method | Total Number of Cells | Computation Time (min.) | Iteration Number | Memory (MB) |
|-------------------|------------------------------|------------------------------|--------------------------------|-------------------------|--------------------|
| 6 cm | FDTD (Full Domain) | 5,171,200 | 132 | – | 1995 |
| | Hybrid (MoM/FDTD) | 1,560,896 | 87 | 4 | 540 |
| 8 cm | FDTD (Full Domain) | 5,324,800 | 133 | – | 2100 |
| | Hybrid (MoM/FDTD) | 1,560,896 | 68 | 3 | 540 |
| 10 cm | FDTD (Full Domain) | 5,632,000 | 142 | – | 2210 |
| | Hybrid (MoM/FDTD) | 1,560,896 | 68 | 3 | 540 |
| 12 cm | FDTD (Full Domain) | 5,939,200 | 152 | – | 2330 |
| | Hybrid (MoM/FDTD) | 1,560,896 | 49 | 2 | 540 |

5.2.2 Current Distributions on an Antenna in the Presence of an Obstacle-2

The geometry of the second problem illustrated in Figure 5.7 includes the thin wire antenna and a dielectric cube. The thin wire antenna is placed a distance of 2 cm away from the dielectric cube. The dimension of the dielectric cube is 20 cm on a side. It can be seen from Figure 5.8 that the results of the hybrid method converges after iteration # 4. The current distributions over the antenna surface at frequencies of interest obtained using the hybrid method are shown in Figure 5.9. The antenna input impedances at the frequencies of interest after four iterations using the hybrid method and the conventional FDTD method are listed in Table 5-6. Comparison shows that the hybrid method results are in good agreement with the conventional FDTD method results. Simulation parameters and

computer resources are summarized in Table 5-7. Results in the table show a considerable reduction in the memory storage requirements and computation time.

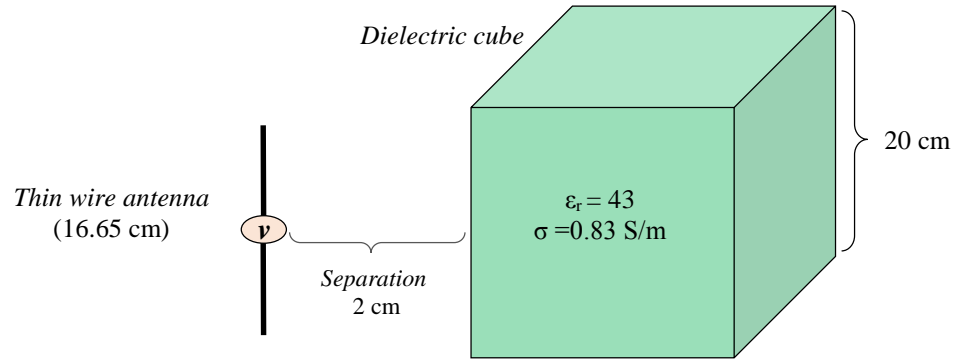


Figure 5.7: The geometry of the second problem.

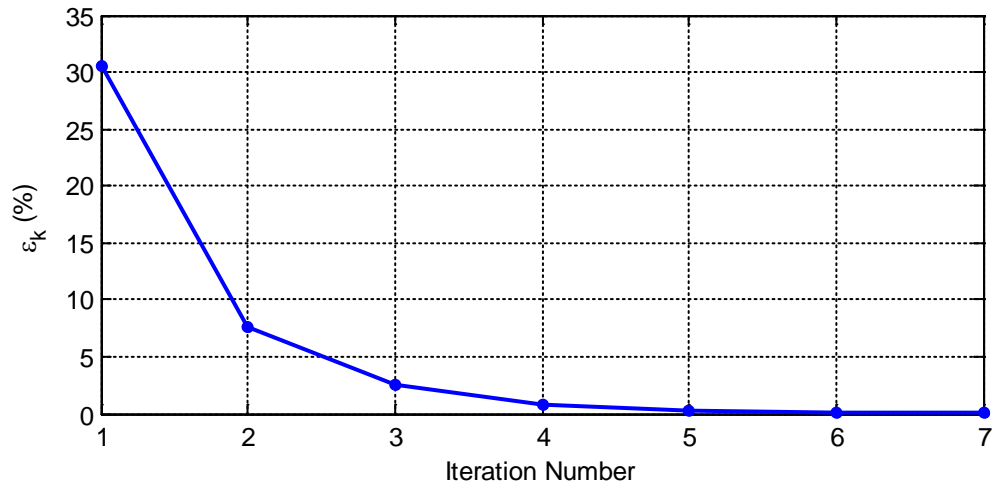


Figure 5.8: Convergence (ϵ_k) between iteration steps.

Table 5-6: Antenna input impedances at the frequencies of interest.

| Method\Frequency | 840 MHz | 860 MHz | 880 MHz |
|---------------------------|----------------|---------------|----------------|
| FDTD (Full Domain) | 39.37 -j 15.71 | 41.68 +j 5.74 | 44.18 +j 27.32 |
| Hybrid (MoM/FDTD) | 42.47 -j 13.87 | 44.31 +j 5.46 | 44.70 +j 25.33 |

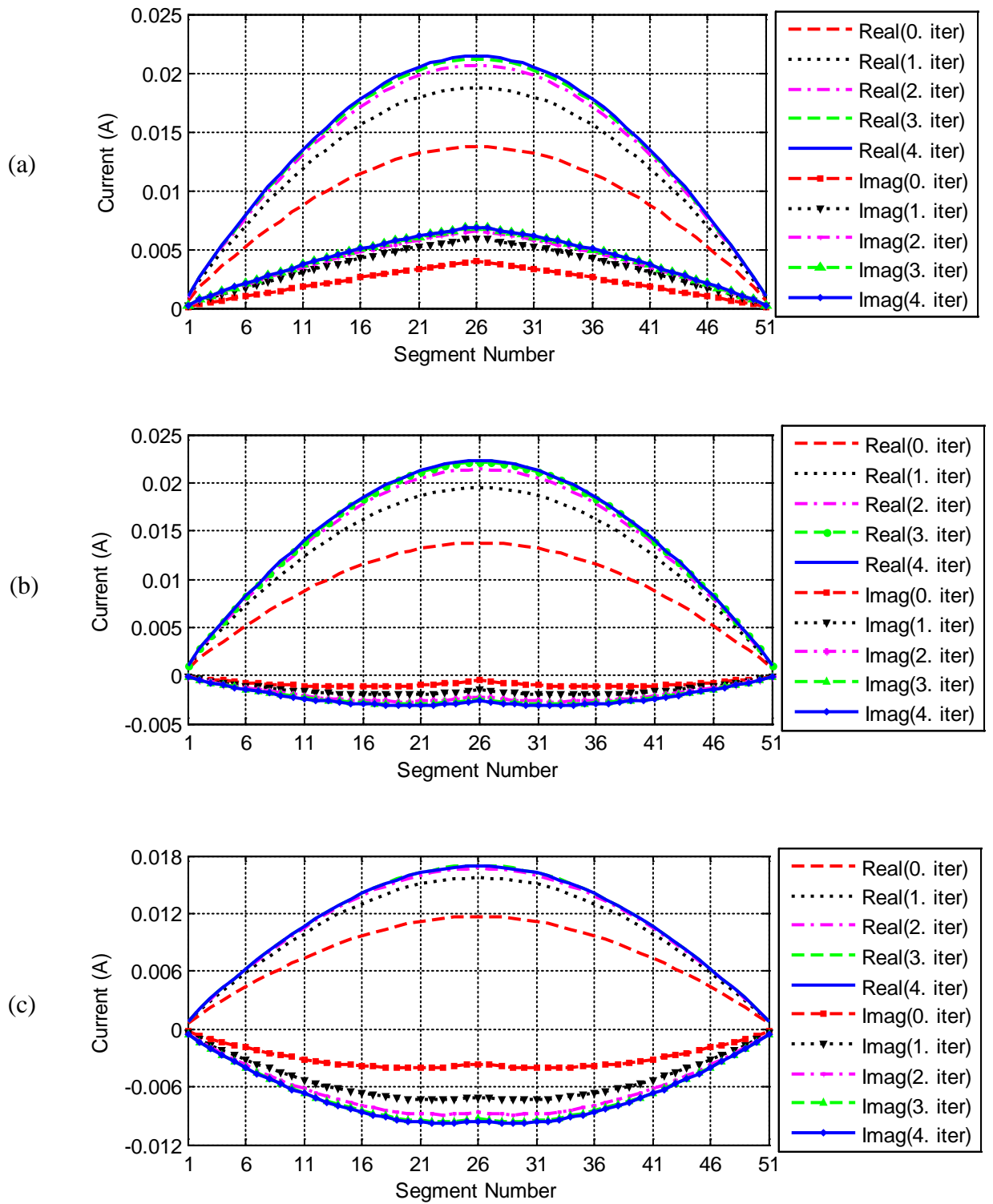


Figure 5.9: Convergence of current distribution versus segment number at frequencies: a) 840, b) 860, and c) 880 MHz. (0-4): represents the iteration number.

Table 5-7: Simulation parameters and computer resources used by the IMR and full domain simulations.

| | Total Number of Cells | Computation Time (min.) | Iteration Number | Memory (MB) |
|---------------------------|------------------------------|--------------------------------|-------------------------|--------------------|
| FDTD (Full Domain) | 4,403,200 | 109 | — | 1740 |
| Hybrid (MoM/FDTD) | 1,560,896 | 88 | 4 | 585 |

The same geometry of the second problem, as illustrated in Figure 5.7, is simulated with different separations (6, 8, 10, and 12 cm) between the antenna and the dielectric cube. The antenna input impedances at frequencies of interest using the hybrid method and the conventional FDTD method are listed for different separations in Table 5-8. Results in the table show that the hybrid method results are in good agreement with the conventional FDTD method results. Simulation parameters and computer resources are summarized in Table 5-9.

Table 5-8: Antenna input impedances at the frequencies of interest for different separations.

| Separation | Method\Frequency | 840 MHz | 860 MHz | 880 MHz |
|-------------------|---------------------------|----------------|----------------|----------------|
| 6 cm | FDTD (Full Domain) | 53.89 +j 4.76 | 59.74 +j 29.31 | 66.21 +j 53.99 |
| | Hybrid (MoM/FDTD) | 54.16 +j 3.86 | 57.06 +j 29.06 | 63.68 +j 57.23 |
| 8 cm | FDTD (Full Domain) | 69.02 +j 3.76 | 76.36 +j 27.23 | 84.36 +j 50.60 |
| | Hybrid (MoM/FDTD) | 69.54 +j 5.12 | 75.28 +j 28.52 | 82.43 +j 53.28 |
| 10 cm | FDTD (Full Domain) | 79.86 -j 4.28 | 87.47 +j 17.51 | 95.60 +j 39.02 |
| | Hybrid (MoM/FDTD) | 79.98 -j 2.43 | 86.86 +j 19.97 | 94.86 +j 42.10 |
| 12 cm | FDTD (Full Domain) | 83.97 -j 15.26 | 90.75 +j 5.18 | 97.80 +j 25.33 |
| | Hybrid (MoM/FDTD) | 84.60 -j 13.07 | 90.70 +j 7.59 | 97.54 +j 28.31 |

Table 5-9: Simulation parameters and computer resources used by the IMR and full domain simulations.

| Separation | Method | Total Number of Cells | Computation Time (min.) | Iteration Number | Memory (MB) |
|-------------------|------------------------------|------------------------------|--------------------------------|-------------------------|--------------------|
| 6 cm | FDTD (Full Domain) | 5,171,200 | 132 | – | 1995 |
| | Hybrid (MoM/FDTD) | 1,560,896 | 88 | 4 | 540 |
| 8 cm | FDTD (Full Domain) | 5,324,800 | 141 | – | 2140 |
| | Hybrid (MoM/FDTD) | 1,560,896 | 88 | 4 | 540 |
| 10 cm | FDTD (Full Domain) | 5,632,000 | 149 | – | 2310 |
| | Hybrid (MoM/FDTD) | 1,560,896 | 87 | 4 | 540 |
| 12 cm | FDTD (Full Domain) | 5,939,200 | 157 | – | 2480 |
| | Hybrid (MoM/FDTD) | 1,560,896 | 67 | 3 | 540 |

5.2.3 Antenna Input Impedance in the Presence of Two Obstacles

A more complex configuration is presented as the third problem in Figure 5.10 to prove the validity of the proposed hybrid method for a problem which has multiple scattering objects near to the thin wire antenna. A conducting box and dielectric sphere are placed a distance of 5 cm and 15 cm away from the thin wire antenna on the x -axis, respectively. The dimensions of conducting box are 5 cm in the x -axis and 10 cm in the y and z -axis. The dielectric sphere has a radius of 10 cm with relative permittivity of 43 and conductivity of 0.83 S/m. A cell size of the FDTD subregion that contains the dielectric sphere is 2.5 mm in all directions in hybrid simulation, whereas a cell size is 1.665 mm for the full domain FDTD simulation. Figure 5.11 shows the convergence of the IMR iteration. It can be seen that the IMR algorithm reaches the convergence criterion ($\epsilon_k < 1\%$) after

iteration # 8. The antenna input impedances at the frequencies of interest after eight iterations using the hybrid method and conventional FDTD method are listed in Table 5-10. Comparison shows that the proposed hybrid results are in good agreement with the conventional FDTD method results. Simulation parameters and computer resources are summarized in Table 5-11. Results in the table show that a considerable reduction in the memory storage requirements is achieved, but the computation time of the IMR algorithm is more than that of the full domain because of small separation between the objects. The computation time would be less and the memory gain would be more for problems that have large separation between the objects and antenna.

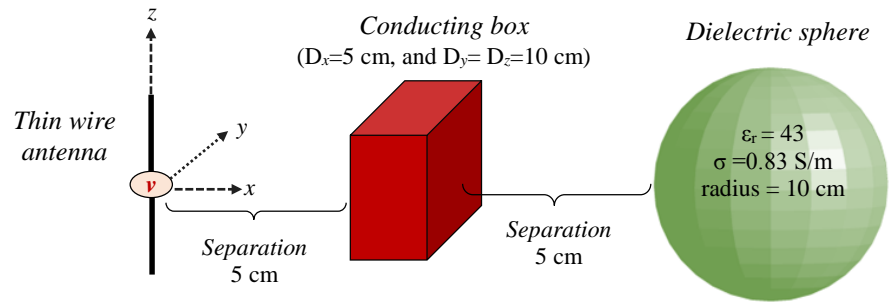


Figure 5.10: The geometry of the third problem.

Table 5-10: Antenna input impedances at the frequencies of interest.

| Method\Frequency | 840 MHz | 860 MHz | 880 MHz |
|---------------------------|----------------|---------------|----------------|
| FDTD (Full Domain) | 25.01 -j 18.74 | 26.68 +j 7.51 | 29.11 +j 34.55 |
| Hybrid (MoM/FDTD) | 24.13 -j 20.10 | 25.87 +j 5.88 | 27.24 +j 33.67 |

Table 5-11: Simulation parameters and computer resources used by the IMR and full domain simulations.

| | Total Number of Cells | Computation Time (min.) | Iteration Number | Memory (MB) |
|---------------------------|-----------------------|-------------------------|------------------|-------------|
| FDTD (Full Domain) | 6,400,000 | 176 | — | 2660 |
| Hybrid (MoM/FDTD) | 1,884,352 | 269 | 8 | 1140 |

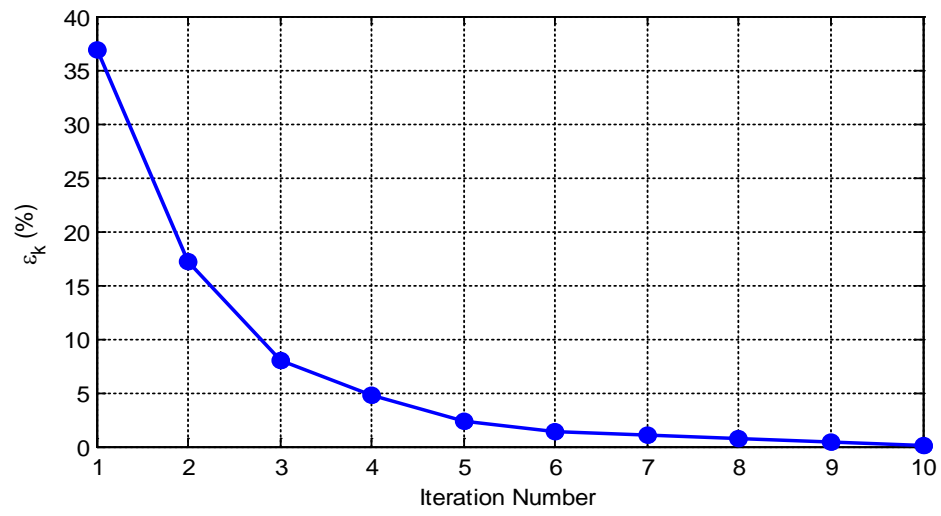


Figure 5.11: Convergence (ϵ_k) between iteration steps.

6 CONCLUSION

In this dissertation, the integration of the FDTD method into the IMR technique is presented to solve large-scale electromagnetic scattering and radiation problems. The IMR technique procedure is based on dividing the original computational domain into smaller subregions, and analyzing each subregion separately, using the FDTD method. Then the solutions of subregions, after following the iterative interaction process between subregions, are combined to obtain solutions at multiple frequencies for the complete domain. To prove the validity of the IMR technique integrated into the FDTD method, numerical results of the scattering and radiation problems are presented. Two techniques are proposed to speed up the calculation of the excitation fields between interacting domains; the use of TF/SF formulation, and interpolation process at current points on the imaginary surface and field points on the TF/SF boundary in each domain.

The most distinguished feature of this technique is to obtain solutions at multiple frequencies in a single IMR simulation by constructing time-limited waveforms, using the TWC algorithm. Furthermore, the considerable reduction in the memory storage requirements and computation time is achieved especially if the separation between subregions is large and coarser grids are used in some subregions.

To provide efficient and desirable solution to large-scale electromagnetic radiation problems, a hybrid method is integrated into the IMR procedure by combining the desirable features of the two different numerical methods: MoM and FDTD method. This procedure starts by dividing the original computational domain into separated subregions where the solution is easily performed using either the MoM or the FDTD method in each subregion followed by an iterative interaction process between the subregions. The most prominent

feature of this proposed technique is the combination of MoM simulations with single FDTD simulations to obtain solutions at multiple frequencies by constructing time-limited waveforms. Furthermore, considerable reduction in the memory storage requirements and computation time can be achieved especially with larger separation between regions.

Finally, we believe that the integration of the FDTD method and hybrid method into the IMR technique in this research will provide as efficient solutions at a number of frequencies for the large-scale electromagnetic scattering and radiation problems.

Appendix A

Near-Field to Near-Field (NF/NF) Transformation

The formulation for the NF/NF transformation [32] is derived here. A vector potential approach is developed to compute the unknown near electric and magnetic fields from the known fictitious electric and magnetic currents obtained by the scattered fields on the imaginary surface. The expression for the radiated fields is obtained at a field point on TF/SF boundary, as illustrated in Figure A.1, close to fictitious currents at all current points on the imaginary surface.

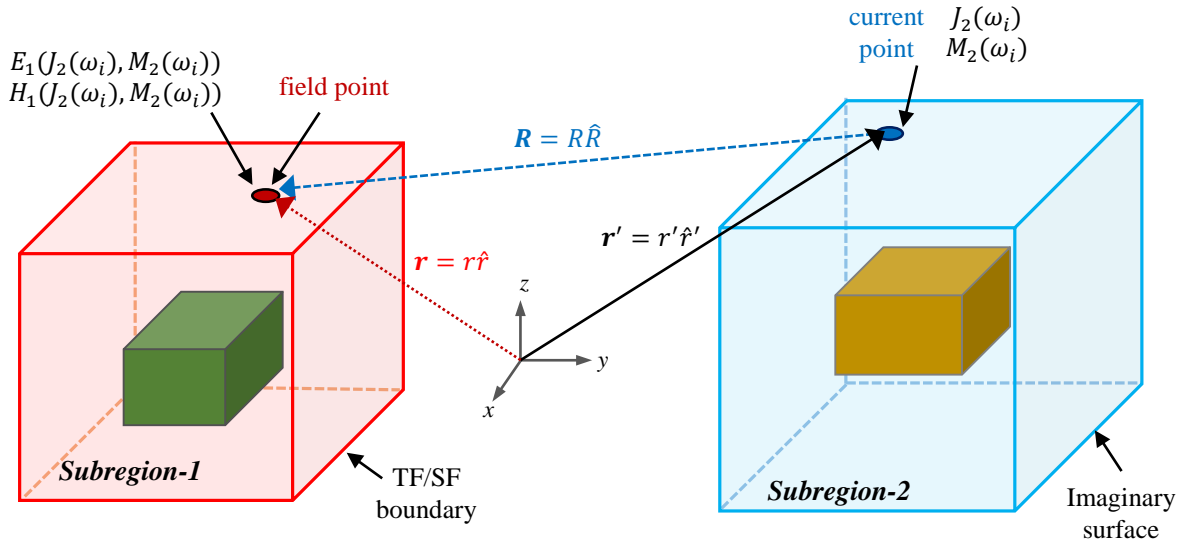


Figure A.1: NF/NF transformation between two subregions.

The magnetic vector potential A can be written in (A.1) in terms of the fictitious electric current J and the Green's function $G(\mathbf{r}, \mathbf{r}')$.

$$\mathbf{A}(\mathbf{r}) = \mu \iiint_V \mathbf{J}(\mathbf{r}') G(\mathbf{r}, \mathbf{r}') d\mathbf{r}' = \mu \iiint_V \mathbf{J}(\mathbf{r}') \frac{e^{-jk|\mathbf{r}-\mathbf{r}'|}}{4\pi|\mathbf{r}-\mathbf{r}'|} d\mathbf{r}', \quad (\text{A.1})$$

where \mathbf{r} and \mathbf{r}' represent the coordinates of a field point on the TF/SF boundary and a current point on the imaginary surface, respectively. Here, the magnetic field (\mathbf{H}) that is due to potential of (A.1) can be written

$$\mathbf{H}(\mathbf{r}) = \frac{1}{\mu} \nabla \times \mathbf{A}(\mathbf{r}) = \nabla \times \iiint_V \mathbf{J}(\mathbf{r}') \frac{e^{-jkR}}{4\pi R} d\mathbf{r}', \quad (\text{A.2})$$

where $R = |\mathbf{r} - \mathbf{r}'|$. Moving the curl operator under the integral sign and using the vector identity

$$\nabla \times [g\mathbf{F}] = (\nabla g) \times \mathbf{F} + g(\nabla \times \mathbf{F}), \quad (\text{A.3})$$

we can write

$$\mathbf{H}(\mathbf{r}) = - \iiint_V \mathbf{J}(\mathbf{r}') \times \nabla \left(\frac{e^{-jkR}}{4\pi R} \right) d\mathbf{r}', \quad (\text{A.4})$$

where $\nabla \times \mathbf{J}(\mathbf{r}') = 0$. Taking the gradient of the Green's function yields

$$\nabla \left(\frac{e^{-jkR}}{4\pi R} \right) = -(\mathbf{r} - \mathbf{r}') \left(\frac{1+jkR}{4\pi R^3} \right) e^{-jkR}. \quad (\text{A.5})$$

Using (A.5), we can write (A.4) as

$$\mathbf{H}(\mathbf{r}) = - \iiint_V [(\mathbf{r} - \mathbf{r}') \times \mathbf{J}(\mathbf{r}')] \left(\frac{1+jkR}{4\pi R^3} \right) e^{-jkR} d\mathbf{r}', \quad (\text{A.6})$$

which can be expanded into its rectangular coordinates. (A.6) can be written as

$$H_x(\mathbf{r}) = \iiint_V [(z - z')J_y - (y - y')J_z] \frac{1+jkR}{4\pi R^3} e^{-jkR} dx' dy' dz', \quad (\text{A.7a})$$

$$H_y(\mathbf{r}) = \iiint_V [(x - x')J_z - (z - z')J_x] \frac{1+jkR}{4\pi R^3} e^{-jkR} dx' dy' dz', \quad (\text{A.7b})$$

$$H_z(\mathbf{r}) = \iiint_V [(y - y')J_x - (x - x')J_y] \frac{1+jkR}{4\pi R^3} e^{-jkR} dx' dy' dz', \quad (\text{A.7c})$$

and using (A.8) the corresponding electric fields can written in (A.9)

$$\mathbf{E} = \frac{1}{j\omega\epsilon} \nabla \times \mathbf{H}, \quad (\text{A.8})$$

$$E_x(\mathbf{r}) = \frac{1}{j\omega\epsilon} \iiint_V [G_1 J_x + P_j(x - x')G_2] \frac{e^{-jkR}}{4\pi} dx' dy' dz', \quad (\text{A.9a})$$

$$E_y(\mathbf{r}) = \frac{1}{j\omega\epsilon} \iiint_V [G_1 J_y + P_j(y - y')G_2] \frac{e^{-jkR}}{4\pi} dx' dy' dz', \quad (\text{A.9b})$$

$$E_z(\mathbf{r}) = \frac{1}{j\omega\epsilon} \iiint_V [G_1 J_z + P_j(z - z')G_2] \frac{e^{-jkR}}{4\pi} dx' dy' dz', \quad (\text{A.9c})$$

where

$$P_j = (x - x')J_x + (y - y')J_y + (z - z')J_z, \quad (\text{A.10})$$

$$G_1 = \frac{-1 - jkR + k^2 R^2}{R^3}, \quad (\text{A.11})$$

$$G_2 = \frac{3 + j3kR - k^2 R^2}{R^5}, \quad (\text{A.12})$$

In the same manner, we can write the electric vector potential \mathbf{F} in terms of the fictitious magnetic current \mathbf{M} and the Green's function $G(\mathbf{r}, \mathbf{r}')$ in (A.13).

$$\mathbf{F}(\mathbf{r}) = \epsilon \iiint_V \mathbf{M}(\mathbf{r}') G(\mathbf{r}, \mathbf{r}') d\mathbf{r}' = \epsilon \iiint_V M(\mathbf{r}') \frac{e^{-jk|\mathbf{r}-\mathbf{r}'|}}{4\pi|\mathbf{r}-\mathbf{r}'|} d\mathbf{r}', \quad (\text{A.13})$$

The electric field (\mathbf{E}) that is due to potential of (A.13) can be written as

$$\mathbf{E}(\mathbf{r}) = -\frac{1}{\epsilon} \nabla \times \mathbf{F}(\mathbf{r}) = -\nabla \times \iiint_V \mathbf{M}(\mathbf{r}') \frac{e^{-jkR}}{4\pi R} d\mathbf{r}', \quad (\text{A.14})$$

Then we can write (A.15) by moving the curl operator under the integral sign and using the vector identity in (A.3).

$$\mathbf{E}(\mathbf{r}) = \iiint_V \mathbf{M}(\mathbf{r}') \times \nabla \left(\frac{e^{-jkR}}{4\pi R} \right) d\mathbf{r}', \quad (\text{A.15})$$

where $\nabla \times \mathbf{M}(\mathbf{r}') = 0$. We can write (A.16) by taking the gradient of the Green's function.

$$\mathbf{E}(\mathbf{r}) = \iiint_V [(\mathbf{r} - \mathbf{r}') \times \mathbf{M}(\mathbf{r}')] \left(\frac{1 + jkR}{4\pi R^3} \right) e^{-jkR} d\mathbf{r}', \quad (\text{A.16})$$

which can be expanded into its rectangular coordinates. (A.16) can be written as

$$E_x(\mathbf{r}) = - \iiint_V [(z - z')M_y - (y - y')M_z] \frac{1 + jkR}{4\pi R^3} e^{-jkR} dx' dy' dz', \quad (\text{A.17a})$$

$$E_y(\mathbf{r}) = - \iiint_V [(x - x')M_z - (z - z')M_x] \frac{1 + jkR}{4\pi R^3} e^{-jkR} dx' dy' dz', \quad (\text{A.17b})$$

$$E_z(\mathbf{r}) = - \iiint_V [(y - y')M_x - (x - x')M_y] \frac{1 + jkR}{4\pi R^3} e^{-jkR} dx' dy' dz', \quad (\text{A.17c})$$

and using (A.18) the corresponding magnetic fields can be written in (A.19)

$$\mathbf{H} = -\frac{1}{j\omega\mu} \nabla \times \mathbf{E}, \quad (\text{A.18})$$

$$H_x(\mathbf{r}) = \frac{1}{j\omega\mu} \iiint_V [G_1 M_x + P_m(x - x') G_2] \frac{e^{-jkR}}{4\pi} dx' dy' dz', \quad (\text{A.19a})$$

$$H_y(\mathbf{r}) = \frac{1}{j\omega\mu} \iiint_V [G_1 M_y + P_m(y - y') G_2] \frac{e^{-jkR}}{4\pi} dx' dy' dz', \quad (\text{A.19b})$$

$$H_z(\mathbf{r}) = \frac{1}{j\omega\mu} \iiint_V [G_1 M_z + P_m(z - z') G_2] \frac{e^{-jkR}}{4\pi} dx' dy' dz', \quad (\text{A.19c})$$

where G_1 and G_2 are given by (A.11) and (A.12), and

$$P_m = (x - x')M_x + (y - y')M_y + (z - z')M_z. \quad (\text{A.20})$$

Therefore, the radiated fields at any field point close to fictitious electric and magnetic currents can be calculated numerically using (A.7), (A.9), (A.17), and (A.19).

Appendix B

The Computing System Information

All of the simulations presented in this dissertation are done with a system whose specifications are given in Table B-1 below.

Table B-1: The computer specifications.

| | |
|----------------------------|--|
| Memory | Intel(R) Core (TM) i7-4770 CPU @ 3.40 GHz |
| Processor | 32.00 GB |
| System Type | 64-bit Operating System, x64-based processor |
| Operating System | Windows 8 |
| Programing Language | Matlab Version 7.5.0.342 (R2007b) |

Appendix C

Moment Matrix of a Thin Wire Antenna

In this appendix, the moment matrix and the voltage vector used in the calculation of the current distribution over a thin wire antenna are expressed. The antenna is divided into 51 segments. When piecewise sinusoids are chosen as expansion functions and point matching is used for testing function, the moment matrix and the voltage vector can be found analytically given in [42].

The moment matrix is expressed as follows:

$$Z_{mn} = \frac{-j30}{\sin(kd)} \left(\frac{e^{-jkR_1}}{R_1} + \frac{e^{-jkR_2}}{R_2} - 2\cos(kd) \frac{e^{-jkr}}{r} \right), \quad (\text{C.1})$$

where

$$r = \sqrt{a^2 + h^2}, R_1 = \sqrt{a^2 + (h - d)^2}, \text{ and } R_2 = \sqrt{a^2 + (h + d)^2},$$

where R_1 , R_2 , and r are defined for each segment of the thin wire antenna as illustrated in Figure C.1, d is the length of a segment of the wire, a is the radius of the wire, and k is the wave number.

The delta gap source model used as thin wire excitation assumes that the impressed electric field in the gap between the antenna terminals can be expressed as

$$E^i = \hat{z} \frac{V}{\Delta_z}, \quad (\text{C.2})$$

where Δ_z is the width of the gap, and V is set to unity. This is shown in Figure C.2. For the thin wire excited in the i^{th} interval, the voltage vector (V^0) used for iteration # 0 in (5.1) is defined as

$$V^0 = \begin{bmatrix} 0 \\ \vdots \\ E^i \\ \vdots \\ 0 \end{bmatrix}, \quad (C.3)$$

that is, all elements zero except the i^{th} , which is equal to source voltage.

Once the moment matrix in (C.1) and voltage vector in (C.3) are calculated, the current distribution (I_{MoM}) is determined using the matrix equation of MoM in (5.1).

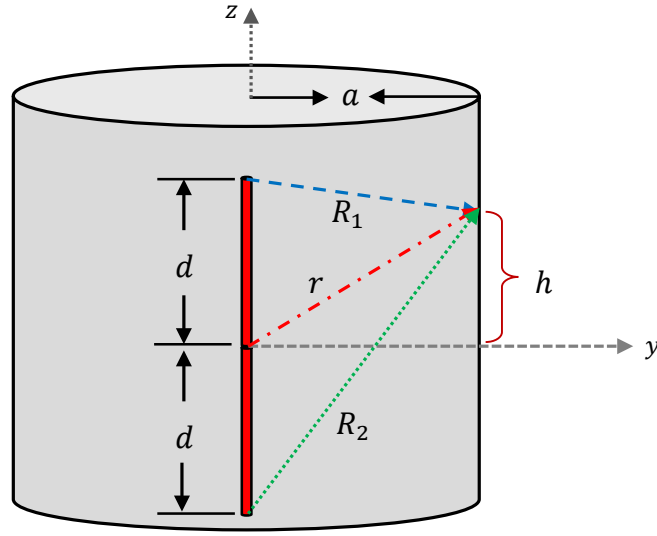


Figure C.1: Geometry of a thin wire antenna for the moment matrix calculation.

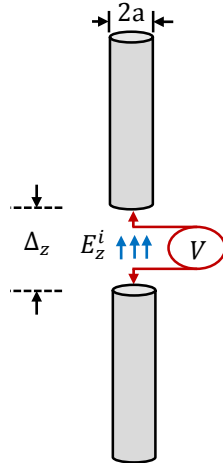


Figure C.2: The delta gap source model with impressed field.

Appendix D

Near Fields of a Thin Wire Antenna

A thin wire antenna can be considered many wire segments connected end-to-end. A single wire segment with current (I_0), as illustrated in Figure D.1, is considered as an electric dipole (ideal dipole) that is electrically small ($dz \ll \lambda$) and very thin (radius $\ll \lambda$). The amplitude of the current is assumed to be constant and given by

$$I(z') = \hat{a}_z I_0, \quad (\text{D.1})$$

where $I_0 = \text{constant}$.

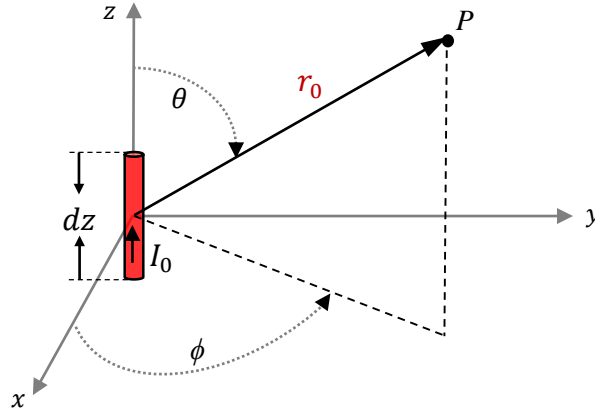


Figure D.1: The electric dipole (ideal dipole).

The near electric and magnetic fields at point P generated by a single electric dipole are expressed in [43] and [44] as follows

$$E_r = \frac{I_0 dz}{2\pi} \eta_0 k^2 \cos(\theta) \left[\frac{1}{k^2 r_0^2} - \frac{j}{k^3 r_0^3} \right] e^{-jkr_0}, \quad (\text{D.2a})$$

$$E_\theta = \frac{I_0 dz}{4\pi} \eta_0 k^2 \sin(\theta) \left[\frac{j}{kr_0} + \frac{1}{k^2 r_0^2} - \frac{j}{k^3 r_0^3} \right] e^{-jkr_0}, \quad (\text{D.2b})$$

$$E_\phi = 0, H_r = 0, H_\theta = 0, \quad (\text{D.2c})$$

$$H_\phi = \frac{I_0 dz}{4\pi} k^2 \sin(\theta) \left[\frac{j}{kr_0} + \frac{1}{k^2 r_0^2} \right] e^{-jkr_0}, \quad (\text{D.2d})$$

where $\eta_0 = \sqrt{\mu_0/\epsilon_0}$ is the intrinsic impedance of the free space, $k = 2\pi/\lambda$ is the wave number, and dz is the length of the electric dipole. The components of electric and magnetic fields are valid under the conditions,

$$dz \ll r_0 \text{ and } dz \ll \lambda. \quad (\text{D.3})$$

Similarly, the total near electric and magnetic fields at point P generated by the thin wire antenna can be expressed as follows

$$E_{r,total} = \hat{r} \cdot \vec{E}_i \text{ and } E_{\theta,total} = \hat{\theta} \cdot \vec{E}_i, \quad (\text{D.4a})$$

$$E_{\phi,total} = 0, H_{r,total} = 0, \text{ and } H_{\theta,total} = 0, \quad (\text{D.4b})$$

$$H_{\phi,total} = \sum_{i=1}^N \frac{I_i dz}{4\pi} k^2 \sin(\theta_i) \left[\frac{j}{kr_i} + \frac{1}{k^2 r_i^2} \right] e^{-jkr_i}, \quad (\text{D.4c})$$

where N is the number of the segments on the thin wire antenna and

$$\vec{E}_i = \sum_{i=1}^N I_i dz \eta_0 k^2 \left(\frac{\hat{r}_i}{2\pi} \cos\theta_i \left[\frac{1}{k^2 r_i^2} - \frac{j}{k^3 r_i^3} \right] + \frac{\hat{\theta}_i}{4\pi} \sin\theta_i \left[\frac{j}{kr_i} + \frac{1}{k^2 r_i^2} - \frac{j}{k^3 r_i^3} \right] \right) e^{-jkr_i}, \quad (\text{D.5a})$$

$$r_i = \sqrt{(z - z_i)^2 + r^2 \sin^2 \theta}, \cos\theta_i = \frac{z - z_i}{r_i}, \text{ and } \sin\theta_i = \frac{r \sin\theta}{r_i}, \quad (\text{D.5b})$$

$$\hat{r}_i = \hat{z} \cos\theta_i + \hat{e} \sin\theta_i, \text{ and } \hat{\theta}_i = \hat{e} \cos\theta_i - \hat{z} \sin\theta_i, \quad (\text{D.5c})$$

where z_i is the z coordinate of the location of the i^{th} electrical dipole and $\hat{e} = \frac{\vec{r} - \hat{z}z}{|\vec{r} - \hat{z}z|}$.

BIBLIOGRAPHY

- [1] B. Despres, "Domain decomposition method and the Helmholtz problem," in *Proc. Int. Symp. Math. Numer. Aspects Wave Propagat. Phenomena*, Strasbourg, France, 1992, pp. 44–52.
- [2] B. Stupfel and B. Despres, "A domain decomposition method for the solution of large electromagnetic scattering problems," *J. Electromagn. Waves and Applicat.*, vol. 13, no. 11, pp. 1553–1568, 1999.
- [3] B. Stupfel, "A fast-domain decomposition method for the solution of electromagnetic scattering by large objects," *IEEE Trans. Antennas Propag.*, vol. 44, no. 10, pp. 1375–1385, Oct. 1996.
- [4] B. Stupfel and M. Mognot, "A domain decomposition method for the vector wave equation," *IEEE Trans. Antennas Propag.*, vol. 48, no. 5, pp. 653–660, May 2000.
- [5] J. Wang and W. Hong, "A fast-domain decomposition method for electromagnetic scattering analysis of 3-D objects," in *Proc. Asia-Pacific Microwave Confer.*, 2000, pp. 424–427.
- [6] B. Stupfel, "A hybrid finite element and integral equation domain decomposition method for the solution of the 3-D scattering problem," *J. Computational Phys.*, vol. 172, no. 2, pp. 451–471, Sept. 2001.
- [7] Z. Qian, L. Yin, and W. Hong, "Application of domain decomposition and finite element method to electromagnetic compatible analysis," in *IEEE Antennas and Propagation Society, AP-S Int. Symp. Dig.*, vol. 4, 2001, pp. 642–645.
- [8] P. Liu and Y.-Q. Jin, "The finite-element method with domain decomposition for electromagnetic bistatic scattering from the comprehensive model of a ship on and a target above a large-scale rough sea surface," *IEEE Trans. Geosci. Remote Sensing*, vol. 42, no. 5, pp. 950–956, May 2004.
- [9] W. Hong, X. X. Yin, X. An, Z. Q. Lv, and T. J. Cui, "A mixed algorithm of domain decomposition method and the measured equation of invariance for the electromagnetic problems," in *Proc. IEEE Antennas and Propagation Society, AP-S Int. Symp. Dig.*, vol. 3, 2004, pp. 2255–2258.
- [10] K. Zhao, V. Rawat, S.-C. Lee, and J.-F. Lee, "A domain decomposition method with nonconformal meshes for finite periodic and semiperiodic structures," *IEEE Trans. Antennas Propag.*, vol. 55, no. 9, pp. 2559–2570, Sep. 2007.
- [11] P. Paul and J. P. Webb, "Reducing computational cost using a multi-region finite element method for electromagnetic scattering problems," *IET Microw., Antennas Propag.*, vol. 2, no. 5, pp. 427–433, Aug. 2008.

- [12] O. Ozgun and M. Kuzuoglu, "Iterative leap-field domain decomposition method—A domain decomposition finite element algorithm for 3D electromagnetic boundary value problems," *IET Microw. Antenna Propag.*, vol. 4, no. 4, pp. 543–552, Apr. 2010.
- [13] A. Takei, S. Sugimoto, M. Ogino, S. Yoshimura, and H. Kanayama, "Full wave analysis of electromagnetic fields with an iterative domain decomposition method," *IEEE Trans. Magn.*, vol. 46, no. 8, pp. 2860–2863, Aug. 2010.
- [14] L. Yin and W. Hong, "Domain decomposition method: a direct solution of Maxwell equations," in *Proc. IEEE Antennas and Propagation Society, AP-S Int. Symp. Dig.*, vol. 2, 1999, pp. 1290–1293.
- [15] C. T. Spring and A. C. Cangellaris, "Parallel implementation of domain decomposition methods for the electromagnetic analysis of guided wave systems," *J. Electromagn. Waves and Applicat.*, vol. 9, no. 1–2, pp. 175–192, 1995.
- [16] C. T. Wolfe, U. Navsariwala, and S. D. Gedney, "A parallel finite-element tearing and interconnecting algorithm for solution of the vector wave equation with PML absorbing medium," *IEEE Trans. Antennas Propag.*, vol. 48, no. 2, pp. 278–284, Feb. 2000.
- [17] L. Yin and W. Hong, "A fast algorithm based on the domain decomposition method for scattering analysis of electrically large objects," *Radio Sci.*, vol. 37, no. 1, pp. 31–39, Jan.–Feb. 2002.
- [18] L. Yin, J. Wang, and W. Hong, "A novel algorithm based on the domain-decomposition method for the full-wave analysis of 3-D electromagnetic problems," *IEEE Trans. Microwave Theory Tech.*, vol. 50, no. 8, pp. 2011–2017, Aug. 2002.
- [19] M. H. Al Sharkawy, V. Demir, and A. Z. Elsherbeni, "Iterative Multi-Region Technique for large scale electromagnetic scattering problems – Two-dimensional case," *Radio Science*, vol. 40, no. 5, September 2005.
- [20] M. H. Al Sharkawy, V. Demir, and A. Z. Elsherbeni, "Scattering from two dimensional problems using the iterative multi-region technique for large scale problems based on the FDFD method," 2005 IEEE Antennas and Propagation Society International Symposium, vol. 3B, pp. 188-191, 3-8 July 2005.
- [21] M. H. Al Sharkawy, V. Demir, and A. Z. Elsherbeni, "The FDFD with the Iterative Multi-Region Technique for the Scattering from Multiple Three Dimensional Objects," IEEE/ACES International Conference Proceedings, Honolulu-HI, USA, 2005.
- [22] M. H. Al Sharkawy, V. Demir, and A. Z. Elsherbeni, "Plane wave scattering from three dimensional multiple objects using the iterative multiregion technique based on the FDFD method," *IEEE Trans. Antenna Propag.*, 2006, 54, (2), pp. 666–673.
- [23] G. Zheng and B.-Z. Wang, "Analysis of scattering from multiple objects by the finite-difference frequency-domain method with an iteration-free multiregion technique," *IEEE Antennas and Wireless Propag. Letters*, Vol. 8, 794–797, 2009.

- [24] M. Carr and J. L. Volakis, "Domain decomposition by iterative field bouncing," *IEEE Antennas and Propagation Society, AP-S International Symposium (Digest)*, San Antonio, TX, vol. 3, pp. 298–301, 2001.
- [25] D. D. Reuster, and G. A. Thiele, "A field iterative method for computing the scattered electric fields at the apertures of large perfectly conducting cavities," *IEEE Trans. Antennas Propag.*, vol. 43, no. 3, pp. 286–290, Mar. 1995.
- [26] F. Obelleiro-Basteiro, J. L. Rodriguez, and R. J. Burkholder, "An iterative physical optics approach for analyzing the electromagnetic scattering by large open-ended cavities," *IEEE Trans. Antennas Propag.*, 43, 356–361, 1995.
- [27] F. Xu, and W. Hong, "Analysis of two dimensions sparse multi-cylinder scattering problem using DD-FDTD method," *IEEE Trans. Antennas Propag.*, vol. 52, no. 10, pp. 2612–2616, Oct. 2004.
- [28] L. Yin, X. Yin, and W. Hong, "A fast algorithm based on DDM and FMM for scattering by multi-cylinder," in *Proc. ISAPE'2000*, Beijing, China, pp. 195.
- [29] J. M. Johnson and Y. Rahmat-Samii, "Multiple region FDTD (MR/FDTD) and its application to microwave analysis and modeling," in *Proc. IEEE MTT-S Symp. Dig.*, San Francisco, CA, 1996, pp. 1475–1478.
- [30] M. H. Al Sharkawy, V. Demir, and A. Z. Elsherbeni, "The iterative multi-region algorithm using a hybrid finite difference frequency domain and method of moment techniques," *Progress In Electromagnetics Research, PIER* 57, 19–32, 2006.
- [31] G. A. Thiele, "Overview of selected hybrid methods in radiating system analysis," *Proceedings of the IEEE*, vol. 80, no. 1, pp. 66–78, Jan. 1992.
- [32] C. A. Balanis, *Advanced Engineering Electromagnetics*, New York, Wiley, 1989.
- [33] A. Z. Elsherbeni and V. Demir, *The Finite-difference Time-domain Method for Electromagnetics: with MATLAB Simulations*, SciTech Publishing, 2009.
- [34] A. Taflove and S. C. Hagness, *Computational Electrodynamics: The Finite-Difference Time-Domain Method*, 2nd ed. Norwood, MA: Artech House, 2000.
- [35] G. Cerri, P. Russo, A. Schiavoni, G. Tribellini, and P. Bielli, "MoM–FDTD hybrid technique for analyzing scattering problems," *Electron. Lett.*, vol. 34, pp. 433–440, 1998.
- [36] M. A. Mangoud, R. A. Abd-Alhameed and P. S. Excell, "Simulation of human interaction with mobile telephones using hybrid techniques over coupled domains," *IEEE Trans. Microwave Theory Tech.*, Vol. 48 no. 11, pp.2014–2021, 2000.
- [37] S. Mochizuki, S. Watanabe, M. Taki, Y. Yamanaka and H. Shirai, "Novel Iteration Procedures of a Hybrid Method combining MoM and Scattered-Field FDTD Method

- for Electromagnetic Dosimetry,” *Proc. of 2003 IEEE Topical Conference on Wireless Communication Technology*, Honolulu, Hawaii, Oct. 2003.
- [38] S. Mochizuki, S. Watanabe, M. Taki and Y. Yamanaka, ”A New Hybrid MoM/FDTD Method for Antennas Located off the Yee’s Lattice,” *2004 URSI EMTS Conf. Proc.*, vol. 2 , pp. 436–438, 23-27 May 2004.
 - [39] D. Wei, Z. Peiyun, Z. Yu, and L. Changhong, “Study on human head/antenna interactions with a novel hybrid MoM–FDTD method,” in *2005 APMC Microwave Conf. Proc.*, vol. 3, 4-7 December 2005, pp. 174–178.
 - [40] Volakis, John L., Arindam Chatterjee, and Leo C. Kempel. *Finite element method electromagnetics: antennas, microwave circuits, and scattering applications*. Vol. 6. John Wiley & Sons, 1998.
 - [41] R. F. Harrington, *Field Computation by Moment Methods*. New York: Macmillan, 1968. (reprinted by IEEE press, 1993)
 - [42] E. C. Jordan and K. G. Balmain, *Electromagnetic Waves and Radiating Systems*, 2nd ed. Englewood Cliffs, NJ: Prentice-Hall Inc., 1968, pp. 333.
 - [43] C. A. Balanis, *Antenna Theory: Analysis and Design*, New York, Wiley, 2005.
 - [44] X. J. Zhang, A. Q. Liu, Y. H. Lee, and A. Alphones, “Near field and surface field analysis of thin wire antenna in the presence of conducting cube,” *Progress In Electromagnetics Research, PIER 45*, 313–333, 2004.

VITA

NAME OF AUTHOR: Fatih Kaburcuk

DATE OF BIRTH: September 27, 1984

DATE OF PLACE: Sivas, Turkey

GRADUATE AND UNDERGRADUATE SCHOOLS ATTENDED:

Syracuse University, Syracuse, NY, USA
Ondokuz Mayıs University, Samsun, Turkey

DEGREES AWARDED:

M.S. in Electrical Engineering, 2011, Syracuse University
B.S. in Electrical & Electronics Engineering, 2007, Ondokuz Mayıs University

PROFESSIONAL EXPERIENCE:

Teaching Assistant, Department of EECS, Syracuse University, 2011–2014
Intern, PPC Broadband, Inc., Summer–2013

PUBLICATIONS:

F. Kaburcuk, V. Demir, Atef Z. Elsherbeni, and E. Arvas, “IMR technique for Antenna and Scattering Problems Using Hybrid Solutions Based on the MoM and FDTD Method,” 2014 International Conference on Electromagnetics in Advanced Applications (ICEAA), Palm Beach, Aruba, August 3-9, 2014.

F. Kaburcuk, V. Demir, Atef Z. Elsherbeni, and E. Arvas, “The Integration of the FDTD Method into the Iterative Multi-Region Technique for the Scattering from Multiple Three Dimensional Objects,” 2014 IEEE International Symposium on Antennas and Propagation and USNC/URSI Radio Science Meeting, Memphis, TN USA, July 6-12, 2014.

F. Kaburcuk, M. Onur Kok, and E. Arvas, “Design of Low Noise Amplifier at 2 GHz,” The 30th International Review of Progress in Applied Computational Electromagnetics (ACES), Jacksonville, FL, USA, March 23-27, 2014.

M. Onur Kok, F. Kaburcuk, and E. Arvas, “A Wideband LNA at 2 GHz,” The 30th International Review of Progress in Applied Computational Electromagnetics (ACES), Jacksonville, FL, USA, March 23-27, 2014.

F. Kaburcuk, V. Demir, Atef Z. Elsherbeni, and E. Arvas, “The Integration of the FDTD Method into the Iterative Multi-Region Technique for the Scattering from Multiple Three Dimensional Objects,” 2014 USNC/URSI Radio Science Meeting, Boulder, CO USA, January 8-11, 2014.

Fatih Kaburcuk, Serhend Arvas, Ercument Arvas, and Jay K. Lee, “Wideband Information in MOM Obtained from Narrowband Data,” *IEEE International Conference (ICUWB)*, Syracuse, NY, Sep. 2012.